Experimental characterisation and mechanical modelling of connection details in traditional Groningen houses

Arslan, O.

DOI
10.4233/uuid:6d51ae3a-ffd8-48f1-96ee-89358d3cb5b7

Publication date
2023

Document Version
Final published version

Citation (APA)
Arslan, O. (2023). *Experimental characterisation and mechanical modelling of connection details in traditional Groningen houses*. [Dissertation (TU Delft), Delft University of Technology]. https://doi.org/10.4233/uuid:6d51ae3a-ffd8-48f1-96ee-89358d3cb5b7

Important note
To cite this publication, please use the final published version (if applicable).
Please check the document version above.

Experimental characterisation and mechanical modelling of connection details in traditional Groningen houses

Dissertation

for the purpose of obtaining the degree of doctor
at Delft University of Technology
by the authority of the Rector Magnificus, Prof. dr. ir. T.H.J.J. van der Hagen,
Chair of the Board for Doctorates,
to be defended publicly on
Monday 27 November 2023 at 15:00 o'clock

by

Onur ARSLAN

Master of Science in Civil Engineering
Istanbul Technical University, Türkiye
born in Bakırköy, Istanbul, Türkiye

This dissertation has been approved by the promotors.

Composition of the doctoral committee:

Rector Magnificus	chairperson
Prof. dr. ir. J.G. Rots	Delft University of Technology, promotor
Dr. F. Messali	Delft University of Technology, copromotor
Dr. I. E. Bal	Hanze University of Applied Sciences, external advisor

Independent members:

Prof. dr. G. Magenes	University of Pavia
Prof. ir. S.N.M. Wijte	Eindhoven University of Technology
Prof. dr. ir. E. Schlangen	Delft University of Technology
Prof. dr. M. Overend	Delft University of Technology
Prof. dr. H.L.M. Bakker	Delft University of Technology, reserve member

This research was funded by Hanze University of Applied Sciences.

Keywords: Unreinforced masonry, Cavity walls, Cavity wall ties, Timber joist-masonry connections, Cyclic tests, Parametric analysis, Mechanical model

Printed by: Ipskamp Printing, the Netherlands
Cover design: Merve Coruh Kavak

ISBN 978-94-6473-302-0

An electronic version of this dissertation is available at
http://repository.tudelft.nl/

The journey is its own reward.

Homer

Dedicated to the memory of my grandmother, Elife Arslan, who always believed in my abilities and supported me in every step I took. You were with me on this journey.

Summary

Post-earthquake structural damage shows that out-of-plane wall collapse is one of the most prevalent failure mechanisms in unreinforced masonry (URM) buildings. This issue is particularly critical in Groningen, a province located in the northern part of the Netherlands, where low-intensity ground shaking has occurred since 1991 due to gas extraction. The majority of buildings in this area are constructed using URM and were not designed to withstand earthquakes, as the area had never been affected by tectonic seismic activity before. Hence, the assessment of URM buildings in the Groningen province has become of high relevance.

Out-of-plane failure mechanisms in brick masonry structures often stem from poor wall-to-wall, wall-to-floor or wall-to-roof connections that provide insufficient restraint and boundary conditions. Therefore, studying the mechanical behaviour of such connections is of prime importance for understanding and preventing damages and collapses in URM structures. Specifically, buildings with double-leaf cavity walls constitute a large portion of the building stock in the Groningen area. The connections of the leaves in cavity walls, which consist of metallic ties, are expected to play an important role. Regarding the wall-to-floor connections, the traditional way for URM structures in Dutch construction practice is either a simple masonry pocket connection or a hook anchor as-built connection, which are expected to be vulnerable to out-of-plane excitation. However, until now, little research has been carried out to characterise the seismic behaviour of connections between structural elements in traditional Dutch construction practice.

This thesis investigates the seismic behaviour of two types of connections: wall-to-wall connections between cavity wall leaves and wall-to-floor connections between the masonry cavity wall and timber diaphragm, commonly found in traditional houses in the Groningen area. The research is divided into three phases: (1) inventory of existing buildings and connections in the Groningen area, (2) performance of experimental tests, and (3) proposal and validation of numerical and mechanical models. The thesis explores the three phases as follows:

(i) *An inventory of connections within URM buildings in the Groningen area is established.* The inventory includes URM buildings of Groningen based on construction material, lateral load-resisting system, floor system, number of storeys, and connection details. Specific focus is given to the wall-to-wall and wall-to-floor connections in each URM building. The thickness of cavity wall leaves, the air gap between the leaves and the size and spacing of timber joists are key aspects of the inventory.

(ii) *Experimental tests are performed on the most common connection typologies identified in the inventory*. This phase consists of two distinct experimental campaigns:

- The first experimental campaign took place at the laboratory of the Delft University of Technology to provide a comprehensive characterisation of the axial behaviour of traditional metal tie connections in cavity walls. The campaign included a wide range of variations, such as two embedment lengths, four pre-compression levels, two different tie geometries, and five different testing protocols, including both monotonic and cyclic loading. The experimental results showed that the capacity of the wall tie connection is strongly influenced by the embedment length and the tie geometry, whereas the applied pre-compression and the loading rate do not have a significant influence.
- The second experimental campaign has been carried out at the laboratory of the Hanze University of Applied Sciences to characterise the seismic behaviour of timber joist-masonry cavity wall connections, reproducing both as-built and strengthened conditions. Twenty-two unreinforced masonry wallets were tested, with different configurations, including two tie distributions, two pre-compression levels, two different as-built connections, and two different strengthening solutions. The experimental results highlighted the importance of cohesion and friction between joist and masonry since the type of failure mechanism (sliding of the joist or rocking failure of the masonry wallet) depends on the value of these two parameters. Additionally, the interaction between the joist and the wallet and the uplift of the latter activated due to rocking led to an arching effect that increased friction at the interface between the joist and the masonry. Consequently, the arching effect enhanced the force capacity of the connection.

(iii)*Mechanical and numerical models are proposed and validated against the performed experiments or other benchmarks*. Mechanical and numerical models for the cavity wall tie and mechanical models for the timber joist-masonry connections were developed and verified by the experimental results to predict the failure mode and the strength capacity of the examined connections in URM buildings.

- The mechanical model for the cavity wall tie connections considers six possible failures, namely tie failure, cone break-out failure, pull-out failure, buckling failure, piercing failure and punching failure. The mechanical model is able to capture the mean peak force and the failure mode obtained from the tests. After being calibrated against the available experiments, the proposed mechanical model is used to predict the performance of untested configurations by means of parametric analyses, including higher strength of mortar for calcium silicate brick masonry, different cavity depth, different tie embedment depth, and the use of solid bricks in place of perforated clay bricks.
- The results of the experimental campaign on cavity wall ties were also utilised to calibrate a hysteretic numerical model representing the cyclic axial response of cavity wall tie connections. The proposed model uses zero-length elements implemented in OpenSees with the Pinching4 constitutive model to account for the compression-tension cyclic behaviour of the ties. The numerical model is able to capture important aspects of the tie response, such as strength degradation, unloading stiffness degradation, and pinching behaviour. The mechanical and numerical modelling approach can be easily adopted by practitioner engineers seeking to model the wall ties more accurately when assessing URM structures against earthquakes.
- The mechanical model of timber-masonry connections examines two different failure modes: joist-sliding failure mode, including joist-to-wall interaction and rocking failure mode due to joist movement. Both mechanical models have been validated against the outcomes of the experimental campaigns conducted on the corresponding connections. The mechanical model is able to estimate each contribution of the studied mechanism. Structural engineers can use the mechanical model to predict the capacity of the connection for the studied failure modes.

This research study can contribute to a better understanding of typical Groningen houses in terms of identifying the most common connections used at wall-to-wall and wall-to-floor connections in cavity walls, characterising the identified connections and proposing mechanical models for the studied connections.

Samenvatting

Constructieve schade na aardbevingen laat zien dat uit-het-vlak bezwijken van muren één van de meest voorkomende faalmechanismen is in gebouwen van ongewapend metselwerk. Dit is ook een urgente uitdaging in Groningen, een provincie in het noorden van Nederland, waar sinds 1991 aardschokken van lage intensiteit voorkomen als gevolg van gaswinning. Aangezien het gebied in het verleden nooit door tektonische aardbevingen werd getroffen bestaat het merendeel van de gebouwen hier uit ongewapend metselwerk dat niet is ontworpen om aardbevingen te weerstaan. Daarom is de beoordeling van bestaande metselwerkgebouwen in de provincie Groningen van groot belang geworden.

Uit-het-vlak faalmechanismen in bakstenen metselwerkconstructies zijn vaak het gevolg van slechte wand-wand, wand-vloer of wand-dak verbindingen waardoor met name slanke wanden onvoldoende steun ervaren als gevolg van de zwakke randcondities. Daarom is onderzoek naar het mechanische gedrag van dergelijke verbindingen van groot belang om schade en instortingen in metselwerkconstructies te begrijpen en te voorkomen. In de regio Groningen komen vooral gebouwen met spouwmuren voor. De wand-wand verbindingen tussen binnen- en buitenblad van de spouwmuren, die bestaan uit metalen spouwankers, zullen daarom naar verwachting een belangrijke rol spelen. Wat betreft de verbinding tussen wand en houten vloeren is de traditionele manier ofwel een schuifverbinding waarbij de balk ingemetseld is in de muur, of een verbinding waarbij een haakanker wordt toegevoegd, beiden naar verwachting kwetsbaar zodra de wand uit-het-vlak geëxciteerd wordt. Tot nu toe is er echter weinig onderzoek gedaan naar het seismisch gedrag van dergelijke wand-wand en wand-vloer verbindingen.

Deze dissertatie onderzoekt het seismisch gedrag van twee typen verbindingen: wand-wand verbindingen in spouwmuren en van verbindingen tussen spouwmuren en houten vloeren zoals die in de traditionele Groningse huizen worden toegepast. Het onderzoek is onderverdeeld in drie fasen: (1) inventarisatie van bestaande gebouwen en verbindingen in de omgeving van Groningen, (2) uitvoering van laboratoriumproeven op de verbindingen, en (3) voorstel en validatie van numerieke en mechanische modellen voor de verbindingen. Het proefschrift onderzoekt deze drie fasen als volgt:

(i) *Er wordt een inventarisatie gemaakt van ongewapende metselwerkgebouwen en hun verbindingen in de regio Groningen.* De inventarisatie van de gebouwen is op basis van bouwmateriaal, weerstand tegen zijdelingse belasting, vloersysteem, aantal verdiepingen en verbindingsdetails. Voor elk metselwerkgebouw worden de details van de wand-tot-wand en wand-tot-vloer verbindingen beschreven en gecategoriseerd. Speciale aandacht wordt besteed aan de dikte van de spouwmuurbladen, de luchtspleet tussen de bladen en de grootte en afstand van de houten balken.

(ii) *Er worden experimentele proeven uitgevoerd op de meest voorkomende verbindingstypologieën die in de inventarisatie zijn geïdentificeerd*. Er zijn twee verschillende reeksen van experimenten uitgevoerd om de prestaties van respectievelijk de verbindingen tussen de beide metselwerkbladen en de verbindingen tussen houten balken en metselwerkbladen te onderzoeken.

- De eerste reeks experimenten is uitgevoerd in het laboratorium van de Technische Universiteit Delft om het axiale gedrag van traditionele metalen spouwankers in spouwmuren te karakteriseren. In deze reeks experimenten is een groot aantal variaties onderzocht: twee inbeddingslengtes, vier voordrukniveaus, twee verschillende geometrieën en vijf verschillende testprotocollen, waaronder monotone en cyclische belasting. Uit de resultaten van deze experimenten blijkt dat de capaciteit van de spouwmuurverbinding sterk wordt beïnvloed door de inbeddingslengte en de geometrie van de spouwankers, terwijl de toegepaste voordruk en de belasting snelheid geen significante invloed hebben.
- De tweede reeks experimenten is uitgevoerd in het laboratorium van de Hanze Hogeschool om het seismische gedrag van verbindingen tussen houten balken en gemetselde spouwmuren te karakteriseren, waarbij zowel de oorspronkelijke omstandigheden zoals ze zijn gebouwd als de omstandigheden na versterking werden gereproduceerd. In totaal werden tweeëntwintig ongewapende metselwerkwanden getest, met verschillende configuraties zoals twee verschillende verdelingen van de verbindingen, twee voordrukniveaus, twee verschillende as-built verbindingen en twee verschillende versterkingsoplossingen. De resultaten van deze experimenten toonden aan dat cohesie en wrijving tussen balk en metselwerk belangrijke parameters zijn omdat ze het bezwijkmechanisme bepalen, hetzij afschuiving tussen balk en

metselwerk, hetzij uit-het-vlak falen (rocking) van het metselwerk. Daarbij bleek de interactie tussen balk en muur, en de door rocking geactiveerde uplift van de muur tot een boogwerkingseffect te leiden. Dit resulteerde in additionele wrijving langs de hout-metselwerk interface en een toename van de krachtcapaciteit van de verbinding.

(iii) *Mechanische en numerieke modellen worden voorgesteld en gevalideerd aan de hand van de uitgevoerde experimenten of andere benchmarks.* Mechanische en numerieke modellen voor de spouwmuurverbinding en mechanische modellen voor de houtbalk-metselwerkverbindingen werden ontwikkeld en geverifieerd aan de hand van de resultaten van de experimenten om de faalwijze en de sterktecapaciteit van de onderzochte verbindingen in metselwerkgebouwen te voorspellen.

- Het mechanische model voor de spouwmuurverbindingen houdt rekening met zes mogelijke faalmechanismes, namelijk bezwijken van de verbinding, uitbreken van een kegel, uitrukken, knikken, doorboren en ponsen. Het mechanische model is in staat de gemiddelde piekkracht en het uit de proeven verkregen faalmechanisme vast te leggen. Na kalibratie aan beschikbare experimenten wordt het voorgestelde mechanische model gebruikt om de prestaties van niet-geteste configuraties te voorspellen door middel van parametrische analyses, waaronder een hogere sterkte van de mortel van het kalkzandsteenmetselwerk voor het binnenblad, een andere spouwdiepte, een andere verankeringslengte van de spouwankers en het gebruik van massieve in plaats van geperforeerde bakstenen voor het buitenblad.
- De resultaten van de reeks experimenten op spouwmuurverbindingen werden ook gebruikt om de hysterese en energie-dissipatie voor de cyclische axiale respons van spouwmuurverbindingen in het numerieke model te kalibreren. Het voorgestelde model maakt gebruik van nul-lengte-elementen in OpenSees met het constitutieve model Pinching4 voor het cyclische druk-trek gedrag van de spouwmuurverbindingen. Het numerieke model is in staat om belangrijke aspecten van de respons van de spouwankers te beschrijven, zoals de degradatie van de sterkte, de degradatie van de ontlastingsstijfheid en het knijpgedrag. Het mechanische model en de numerieke modelbenadering kunnen gemakkelijk worden overgenomen door ingenieurs uit de praktijk, die de spouwankers

nauwkeuriger willen meenemen bij de beoordeling van constructies tegen aardbevingen.

- Het mechanische model van hout-metselwerkverbindingen onderzoekt twee verschillende faalmechanismes: het faalmechanisme "schuivende balk" waarbij de balk uit de muur schuift, met inbegrip van de toegenomen wrijving door boogwerking en interactie tussen balk en muur, en het faalmechanisme "rocking" waarbij de muurdelen heen en weer bewegen met de balk. Beide mechanische modellen zijn gevalideerd aan de hand van de resultaten van de reeks experimenten op de overeenkomstige verbindingen. Het mechanische model is in staat om elke bijdrage van het bestudeerde mechanisme in te schatten. Constructeurs kunnen het mechanische model gebruiken om de capaciteit van de verbinding voor de bestudeerde faalwijzen te voorspellen.

Dit onderzoek kan bijdragen tot een beter begrip van kenmerkende Groningse huizen door het identificeren van de meest gebruikte wand-wand en wand-vloer verbindingen bij spouwmuren, het mechanisch karakteriseren van de geïdentificeerde verbindingen en het voorstellen van mechanische modellen voor de bestudeerde verbindingen.

Symbols and abbreviations

The frequently used notations and abbreviations in this dissertation are listed below.

Roman Symbols

A_1	area of loaded end which is under either the hooked end or zigzag end
A_2	piercing area of mortar under loaded end
a_b	factor varying from 0 to 1 to define the degree of moment restraint associated with the related bottom extremity
A_j	contact area of joist
A_{pt}	projected break-out area of mortar
A_s	area of cross-section of cavity wall tie connection
A_w	effective area of cone of mortar
C	thrust force per unit width of joist
c	cohesion along the embedded part of joist in masonry wall
d_t	diameter of cavity wall tie
e	eccentricity
E_{3t}	elastic modulus of tie evaluated between 1/10 and 1/3 of the maximum tensile stress
E_j	elastic modulus of joist
f_{bm}	flexural strength of mortar
f_c	compressive stress at the contact area between the joist and masonry
F_c	coupling force contribution of embedded wall ties
F_{cr}	cracking force
f_{ct}	tie strength at Euler's critical load
f_d	compressive stress at wall's middle height due to the vertical load applied at its` top plus the weight of the upper half of the wall
f_m	compressive strength of mortar
$F_{o,iw}$	rigid body mechanism force of inner leaf

$F_{o,ow}$ rigid body mechanism force of outer leaf

fp Selected pre-compression level

f_t tensile strength of mortar

f_{tt} tie tensile strength

f_{ut} ultimate tensile strength of cavity wall tie connection

f_{v0} initial shear strength of mortar

f_w bond strength between masonry unit and mortar

f_w bond strength between masonry unit and mortar

f_w masonry flexural strength

f_{yt} tie yield strength

h wall height

h_1 panel height below where the maximum tensile stress equals the masonry flexural strength

h_2 panel height above where the maximum tensile stress equals the masonry flexural strength

H_A contribution of arching force at peak force

h_b height of the applied force

H_C contribution of cohesion force at peak force

H_E peak force from the experiment

H_J contribution of joist deflection force at peak force

H_M peak force obtained by mechanical model

$H_{M,push}$ peak force in pushing obtained by mechanical model

$H_{M,pull}$ peak force in pulling obtained by mechanical model

H_S contribution of arching force at peak force

H_V contribution of initial normal force at peak force

I_j moment of inertia of joist along the cross-section

I_t moment of inertia of tie

I_w moment of inertia of wallet

K column effective length factor

l_b embedment length of cavity wall tie either in CB or CS masonry

l_c cavity length between two leaves

l_d edge distance from the end of tie to the surface of mortar

l_h cavity wall tie depth of a zigzag end or L-shaped hooked end

L_j total length of joist

l_t total length of cavity wall tie

l_w total thickness of cavity wall

M_b bottom cracking moment

M_L Richter Magnitude

M_t top cracking moment

N_A additional vertical force due to the arching effect

N_{buck} Compressive buckling capacity of cavity wall tie connection

N_{cone} Tensile break-out capacity of cavity wall tie connection

N_J additional vertical force due to the deflection of joist

N_{pier} Compressive piercing capacity of cavity wall tie connection

$N_{pull,CB}$ Tensile pull-out capacity of cavity wall tie connection embedded in CB masonry

$N_{pull,CS}$ Tensile pull-out capacity of cavity wall tie connection embedded in CS masonry

N_{punc} Compressive punching capacity of cavity wall tie connection

N_S additional vertical force acting on the contact area due to arching

N_{tie} Tie rupture capacity

N_V initial force acting on the contact area between joist and masonry

Q overburden load

t_j width of joist

t_m mortar joint thickness

t_w wall thickness

u idealised control perimeter for punching failure

u_{cr} cracking displacement

W weight of wall

W_C weight of the masonry above the joist

W_J dead load of joist

y dimensionless distance from the extreme compression fibre at the top and bottom sections of the wall to the line of action of the load

Z_d section modulus of the bedded area of masonry wall

Greek Symbols

α modification factor

α_t factor varying from 0 to 1 to define the degree of moment restraint associated with the related top extremity

γ parameter for the internal lever arm

γ_m density of wall

δ_j vertical displacement of the joist at peak force

Δ horizontal displacement of the inner leaf due to the joist

Δ_m monotonic ultimate lateral displacement

ε_{ct} tie strain at Euler's critical load

ε_{rt} tie elongation at rupture

ε_{tt} tie strain at tensile strength

ε_{yt} tie yield strain

$\emptyset$ angle of the tie with respect to the axis, in radians, in the case of a bent tie

μ friction coefficient

σ_N normal stress on joist

σ_S stress on joist due to arching

σ_{v0} applied pre-compression stress on wallet

τ shear strength of joist connection

ψ ratio of the applied vertical load to the weight of the upper half of the wall

Abbreviations

CB clay brick masonry

CS calcium silicate brick masonry

CoV coefficient of variation

EDB exposure database

LVDT linear variable displacement transducer

NCG Nationaal Coördinator Groningen

PGA peak ground acceleration

URM unreinforced masonry

TABLE OF CONTENTS

List of Figures

List of Tables

Chapter 1: Introduction

1.1 Background

A large gas field in the north of the Netherlands was discovered in 1959 in the province of Groningen, and gas extraction started in 1963 [1]. In order to stimulate the extraction of natural gas, a hydraulic fracturing process has been conducted from deep geological formations [2]. This process has led to reservoir depletion. Hence, low-intensity ground shaking has occurred since 1991 due to gas extraction. The first recorded induced seismicity was on December 5th, 1991, with a local magnitude, M_L, of 2.4. In the subsequent years, the number of human-induced earthquakes in the province of Groningen has considerably increased (Figure 1.1). The largest event was recorded on August 16th, 2012, near Huizinge, with a local magnitude, M_L, of 3.6 and horizontal peak ground acceleration (PGA) of 0.084g. A tremendous amount of research has been initiated related to induced seismicity since the area was hit by many induced earthquakes [1,3–8].

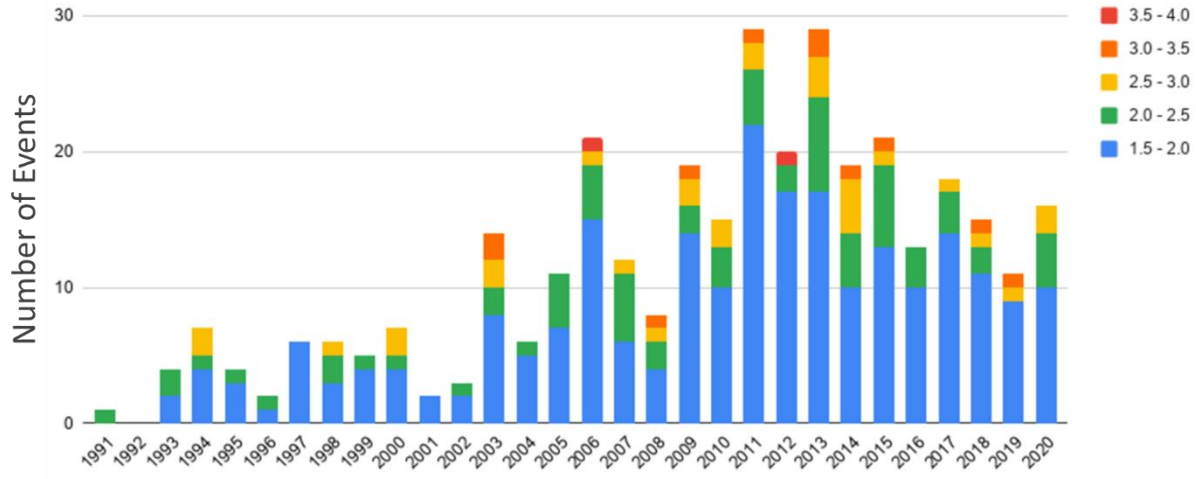

Figure 1.1 Registered induced earthquakes in Groningen between 1991 and 2020, with a lower limit of M_L=1.5 and subdivided into five groups: 4.0> M_L ≥3.5 (red), 3.5> M_L ≥3.0 (orange), 3.0> M_L ≥2.5 (yellow), 2.5> M_L ≥2.0 (green), and 2.0> M_L ≥1.5 from KNMI [9].

The earthquakes have a significant impact on the existing buildings. The majority of the existing buildings in the Groningen area are composed of unreinforced masonry (URM), representing 77% of the building stock [10]. URM buildings are typically low-rise in the Netherlands, which generally embody vulnerable structural elements such as large openings,

slender and cavity walls, or non-structural elements such as gable-end walls, chimneys, and parapets. Since tectonic earthquakes had never affected the area, the current building stock was not designed to withstand earthquakes.

Detached and terraced houses are the two most dominant housing types. A typical detached house in Groningen is characterised by either single-wythe or double-wythe clay-brick URM walls, timber floor and lack of any specific seismic detailing such as connections between structural elements [11,12]. A typical Groningen terraced house usually consists of 5 to 10 housing units. Terraced houses, namely low-rise residential URM buildings, are characterised by slender walls, large openings and the use of cavity walls [13,14]. Generally, the ground or first floor is made of rigid diaphragms (reinforced concrete floors), while the attic floor and the roof have flexible diaphragms (made of timber).

Detached house typology can be found in many countries all over the world. For example, a detached house is the most common typology in New Zealand, representing almost 80% of residential buildings [15], and 89% of the building stock is a detached house in Finland [16]. Similarly, in Australia, the detached houses cover 76% of the building stock [17]. As far as detached houses are concerned in the province of Groningen, the Netherlands, they are generally one- or two-storey buildings with irregular plan configurations and wide openings. URM Dutch detached houses are generally characterised by steep pitch roofs, e.g. gambrel, mansard or Dutch Gable etc. [18].

The other dominant type of residential structure in the area, the terraced houses, represents more than 50% of the URM building stock of the region [19]. The terraced house typology in the Netherlands often consists of URM cavity walls. Cavity walls are widely used for URM structures in many countries all over the world, especially for residential constructions.

The use of a cavity in masonry construction started in England in the early decades of the 19th century. The cavity wall, which was indicated as a hollow wall by Nicholson, is defined as “a wall built in two thicknesses, having a cavity between, either for the purpose of saving materials, or to preserve a uniform temperature in the apartments.” [20]. In the study by Hamilton [21], the cavity walls consisted of two walls with a thickness of 230 mm, separated by a 76 mm gap, interconnected by means of either solid clay brick headers or iron ties. However, using solid clay brick headers as a connection between the leaves, moisture can penetrate into buildings via the headers. Hence, the use of iron ties became more common. After World War I, cavity-wall construction started widely used in many countries all over the world [22–25].

In the Netherlands, a cavity wall usually consists of an inner load-bearing wall made of calcium silicate brick masonry and an outer veneer of clay brick masonry separated by a cavity. Metal ties are used for connecting the inner load-bearing leaf to the outer veneer. Cavity walls are commonly found in the other most diffuse house typology, called terraced houses. Although URM buildings represent almost 77% of the building stock in the Groningen area, where terraced houses are one of the most common typologies characterised by cavity walls, very limited research has focused on cavity wall tie connections at the component level.

The seismic behaviour of URM structures depends on several factors, including lack of homogeneity in masonry, material properties, geometry, the stiffness of the horizontal diaphragms and the connections between structural elements such as wall-to-wall, wall-to-floor or wall-to-roof connections. In addition, the in-plane stiffness of a masonry wall is significantly higher than its out-of-plane (OOP) stiffness. Hence, the seismic behaviour of masonry structures also depends on the capability to redistribute the horizontal loads between the structural elements. In order to explore the maximum in-plane strength of the wall and prevent the OOP mechanisms, the connection between the wall and floor plays an important role in the structures for the capability to redistribute the seismic loads [26].

Lessons from past earthquakes showed that satisfactory seismic performance is achieved when the building vibrates like a monolithic box. To this end, building components need to be well connected. Without box behaviour, the walls of a URM building behave independently, which can be followed by an OOP failure mechanism. Conversely, in the case of box behaviour, walls are connected to horizontal diaphragms such as floor and roof, which usually lead to a good building performance when subjected to earthquakes. Hence, to improve the seismic safety of masonry buildings, “box-type” behaviour which can be characterised by enhancing the structural integrity of the entire building, must be ensured.

The role of connections is essential during an earthquake excitation, which has been reported well in the literature [27]. The monolithic behaviour of masonry buildings could be enhanced by fully utilising the potential resistance and energy dissipation capacity using a connection between the floor and masonry wall [27]. In order to visualise the influence of box-type behaviour, Tomazevic [28] illustrated a total of 3 possible failure modes of a masonry building during an earthquake depending on how the walls are interconnected at the floor and roof levels and the stiffness of the floor (Figure 1.2). The uncoupled wall where timber joists are not connected, representing masonry buildings without box behaviour, is illustrated in Figure 1.2a. As seen, vertical cracks develop, and transverse walls can collapse, leading to an

out-of-plane local mechanism. On the other side, if the walls are connected with the floor tie beams, the masonry vibrates as a monolithic box, as seen in Figure 1.2b and c. The energy dissipation capacity of a masonry building which is one of the key parameters of seismic resistance can be significantly improved by providing a good connection of walls [27].

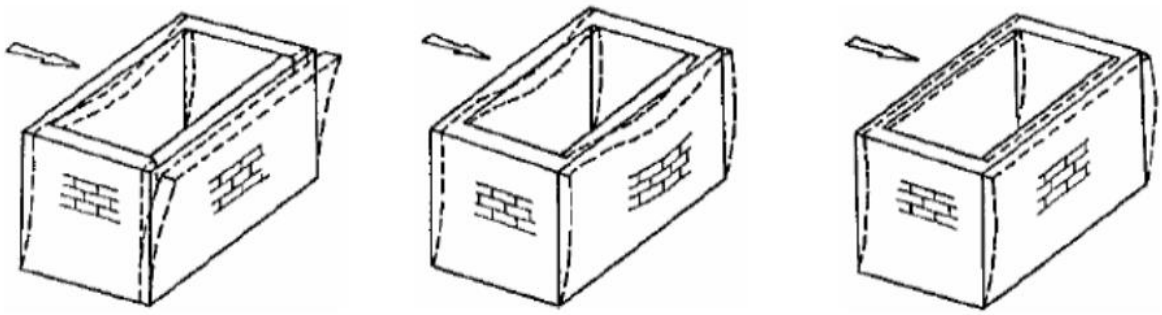

(a) (b) (c)

Figure 1.2 Vibration of masonry buildings during earthquake. Building with wooden floors without ties (a), building with wooden floors and tied walls (b) and building with rigid floors and tie-beams (c) from Tomazevic [28].

Post-earthquake structural damage such as that observed after the 1997 Umbria-Marche earthquake in Italy [29], the 2009 L'Aquila earthquake in Italy [30], the 2011 Canterbury earthquake in New Zealand [31] or the 2015 Gorkha earthquakes in Nepal [32] show that OOP wall collapse is one of the most common failure mechanisms in URM structures. It is also expected to be a critical issue in Groningen, as the building stock is constituted by slender walls and the use of cavity walls, which are generally connected by weak and corroded wall ties. OOP failure mechanisms in brick masonry structures primarily originated from insufficient connections at wall-to-wall and wall-to-floor levels. Therefore, the study of the mechanical behaviour of such connections is of prime importance to understand and prevent damage and collapse in URM structures. Until now, little research has been carried out to characterise the seismic behaviour of connections between structural elements in typical Groningen houses.

Cavity walls are particularly vulnerable to OOP mechanisms due to the slender geometry of the two leaves, and, in fact, the OOP behaviour of cavity walls represents a major concern during a strong shock [13,14,33]. In a study where full-scale brick veneer wall panel specimens were tested [34], it was found that OOP wall damage occurred when the veneer moved away from the interior wood backup, placing a high demand on the tensile force and displacement capacities of the ties, underlining the prominent role of the ties in the composite response of the two leaves. Giaretton et al. [23] showed that when a sufficient number of connections are

used, the OOP failure of cavity walls can be prevented. According to BSI PD 6697 [35], a minimum number of wall ties per unit can be calculated, which is not less than 2.5 ties per square metre and should be used for walls with both leaves having a size of 90 mm or thicker, whereas the spacing, embedment length in the mortar and inadequate number of ties will influence the overall capacity of the cavity wall.

An extensive multiscale testing program has been performed at Delft University of Technology since 2014 to characterise the seismic behaviour of URM buildings at the material, connection, component and assemblage level [36,37]. Whenever possible, experimental campaigns investigate first the structural behaviour at the material and component level and then on full-scale structures for both as-built/replicated and retrofitting conditions. First, the axial and shear capacity of connections between the leaves of cavity walls and between concrete slabs and masonry veneers was studied for both as-built (at the component level [38,39] and on full-scale structures [33]) and retrofitting ties [40,41]. As for the replicated as-built connections, the masonry piers and the concrete floor were connected by means of steel threaded rods, and a tailored system was tested to assess the OOP failure of retrofitted wall-to-floor connections. In addition, connections between timber floor joists and masonry walls were also tested [42]. Joist-masonry connections for both single-leaf and solid walls were studied; three configurations were investigated: the joist in a masonry pocket (i) without any anchors, (ii) with an anchor, and (iii) with a folded steel plate. The former two setups represent the as-built conditions, and the latter represents the retrofitted conditions.

Although valuable information can be found in the earlier studies, there is still a lack of essential knowledge regarding connection details specific to the Groningen case. Therefore, it is necessary to conduct both experimental and mechanical characterisations of the connection typologies mentioned above (wall-to-wall connections between cavity wall leaves and wall-to-floor connections between the masonry cavity wall and timber diaphragm). Experimental tests should be performed on connection details to develop and validate mechanical models to predict the failure mode and strength capacity of the examined connections in URM buildings.

1.2 Research questions, methodology and contributions

The main objective of this study is to investigate the seismic behaviour of wall-to-wall and wall-to-floor connections in typical Groningen houses. To this end, the research is structured into three phases: (i) an inventory of existing buildings and connections in the Groningen area

is established; (ii) experimental tests are performed on the identified connection typologies; (iii) numerical and mechanical models of the identified connections are developed and validated against the performed experiments or other benchmarks. The research will address several sub-questions, as outlined in Table 1.1, in order to provide a comprehensive understanding of the seismic behaviour of the connections in typical Groningen houses.

Table 1.1 Research questions associated with the primary objective.

Phases	Chapters	Research questions
The inventory of existing buildings in the Groningen area	Chapter 2: Inventory of existing as-built connections in Groningen masonry buildings	How can the most common connection types at wall-to-wall and wall-to-floor levels in the Groningen region be statistically described and interpreted?
Performing experimental tests on the connection typologies identified in the inventory	Chapter 3: Experimental characterisation of cavity wall tie connections	How can the axial behaviour of traditional masonry wall metal tie connections in cavity walls be experimentally characterised?
	Chapter 4: Experimental characterisation of timber joist-masonry connections	How can the timber joist-masonry connections be experimentally characterised?
Validating numerical and mechanical models against the performed experiments or other benchmarks	Chapter 5: Mechanical and numerical modelling of wall tie connections	How can the experimental results of cavity wall tie connections be interpreted to propose a mechanical model? How can the experimental investigation be studied to develop a numerical constitutive law for engineers and researchers?
	Chapter 6: Mechanical modelling of timber joist-masonry connections	How can the experimental results of timber joist-cavity wall connections be interpreted to propose a mechanical model?

The first phase, the inventory, allows defining the most common connection typologies used in the Groningen area. These typologies will be listed and statistically categorised depending on their prevalence in the Groningen region in terms of building typologies, structural systems, and connection details between structural elements, including the median properties of a typical Dutch cavity wall and timber joist. In the second phase, a significant number of variations were investigated for the cavity wall tie connections at the laboratory of Delft University of Technology. This included two different embedment lengths, four pre-compression levels, two tie geometries, and five testing protocols, which encompassed both monotonic and cyclic loading. In addition, a total of twenty-two wallets were tested at the laboratory of Hanze University of Applied Science to characterise the seismic behaviour of

timber joist-masonry connections. For the final phase, mechanical models were developed and validated using the experimental results to predict the failure mode and strength capacity of the examined connections in URM buildings.

The main contributions of this thesis are as follows:

- It provides a comprehensive database of connection details between structural elements for typical Groningen URM buildings. The thesis presents a statistical distribution for the most common connections and introduces additional information on the tie distribution, cavity depth, timber joist cross-sections, masonry wall thickness, and other relevant parameters.
- It provides a complete characterisation of the axial behaviour of traditional connections in cavity walls in terms of failure mechanism, average force-displacement curve, peak force, and displacement at the peak force and failure. This in-depth understanding improves the knowledge of the connection between the leaves in cavity walls which can be helpful in identifying and validating assessment methods and retrofit interventions. It also contributes to the improvement of testing, standardisation, and design of wall-to-wall metal ties, benefiting the construction industry in the long run.
- It investigates the behaviour of timber joist-masonry connections in cavity walls, representing the Dutch construction practice, in both as-built and strengthened conditions. It provides valuable insights into the behaviour of the failure mechanisms, ranging from unstrengthened connections to the strengthened ones.
- It introduces a mechanical model that can predict the failure mode and the strength capacity of metal tie connections in masonry cavity walls. This model can be adopted by structural engineers to estimate the peak force capacity of wall tie connections in masonry cavity walls and to assess their performance during seismic events.
- It conducts numerical exploration of the quasi-static cyclic response of tie tests. The developed numerical model enables structural engineers to accurately simulate the response of wall-to-wall connections.
- It identifies and predicts the failure mode and strength capacity of timber-joist connections in masonry cavity walls. The proposed mechanical model allows structural engineers to estimate the capacity of these connections.

1.3 Thesis outline

The research presented in this thesis consists of three phases divided into seven chapters, as schematised in Figure 1.3. The synopsis of each chapter is as follows:

As regards the first phase, Chapter 2 presents an inventory of URM structures in the Groningen region to document the most common connection types at wall-to-wall and wall-to-floor levels.

In the second phase, Chapter 3 and Chapter 4 cover the experimental campaign on the wall metal tie and the joist-masonry connections, respectively. Chapter 3 aims to provide a complete characterisation of the cyclic axial behaviour of cavity wall ties. It also helps to provide a better understanding of the behaviour of the tested metal wall ties for the industry to find suitable methods for developing their products and improving the seismic response of existing URM structures. The chapter is adapted from Arslan et al. [43]. Chapter 4 aims to investigate the behaviour of the timber joist-masonry cavity wall connections under cyclic axial loading with special attention to the developed failure mechanism and the definition of force-displacement curves for each group of tests performed. It describes the specimen geometry, the test setup, the adopted testing protocol, the tests carried out to characterise the used materials, the characteristics of the groups of specimens tested, geometry and loading protocols. Finally, it presents and discusses the test results, focusing on the developed failure mechanism and the definition of average force-displacement curves for each group of tests performed.

Regarding the final phase, Chapter 5 focuses on a mechanical model defined to predict the failure mode and the strength capacity of metal ties in masonry cavity walls. The mechanical model for the wall ties was published by Arslan et al. [44]. In addition, the chapter utilises the results of the experimental campaign described in Chapter 3 to calibrate a hysteretic model that presents the cyclic axial response of cavity wall tie connections. The numerical model was published by Arslan et al. [45]. Chapter 6 discusses an analytical model of timber-masonry connections, which examines two different failure modes. Chapter 7 discusses conclusions and gives recommendations for future research.

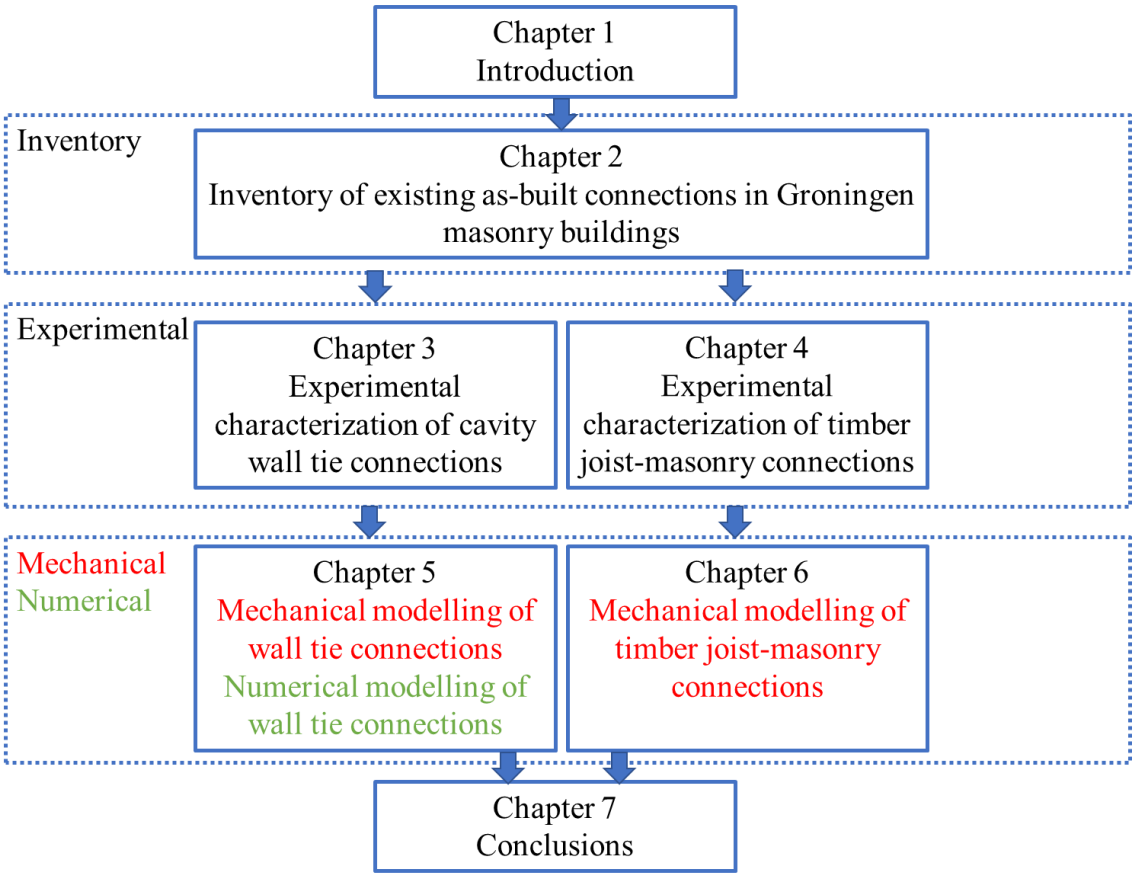

Figure 1.3 Thesis outline.

Chapter 2: Inventory of existing as-built connections in Groningen masonry buildings

Structural details must be adequately identified in order to assess the seismic response of a structure. To achieve this scope and obtain adequate understanding of the characteristics of a large number of buildings, typology classification is required. Hence, this chapter reports an inventory of unreinforced masonry buildings in the Groningen area, defined in terms of building typologies, structural systems, and connection details between structural elements. To prepare the inventory, a total of 267 addresses and 59 inspection reports received from Nationaal Coördinator Groningen (NCG) for seismic assessment of structures were compiled as a dataset. The inventory aims at defining the most common connection typologies used in the Groningen area. A classification system based on the V6 fragility and consequence model [46] is used to determine the building typologies. In addition, structural details from the compiled dataset were gathered in terms of cavity wall size and timber joist. Finally, the most common connection details were defined.

Section 2.1 presents a review of past typology research on unreinforced masonry (URM) buildings and the term “traditional Groningen houses”. Section 2.2 presents the inventory collection procedure with the studied building typologies and provides the distribution of building and connection typologies. It classifies the buildings based on the thickness of cavity walls and the dimension of timber joists. Section 2.3 compares the contents of the dataset presented with the building database elaborated by Arup [47].

2.1 Review of past typology studies of URM buildings

A review of previous studies that aimed to classify URM buildings into typologies is hereinafter presented. Structural characteristics, including construction details, geometry and materials, are essential to characterise and identify the vulnerability of URM buildings. Therefore, typological studies have been performed to better understand the characteristics of buildings [48–50] and, consequently, assess the vulnerability of buildings and protect them from future earthquakes.

In order to identify the vulnerability of structures to earthquakes, an interview-based CARTIS form (*Caratterizzazione TIpologica Strutturale*) was implemented in Italy [51]. In this study, the data was collected according to residential buildings' geometric and structural features via an interview-based survey. The aforementioned method was provided to define the representative buildings which were more vulnerable. Giaretton [52] conducted an inventory of historic stone load-bearing URM buildings in New Zealand, including general building information, architectural configuration and masonry type. It was found that most of the studied structures were located in high seismic hazard zones, and the use of construction stone types was usually related to the geology of the region.

Walsh [53] conducted a survey of the geometric characteristics of 206 URM buildings in Auckland, New Zealand. The included data was classified according to building geometric characteristics, depending on whether the walls were solid or cavity walls, the number of leaves and the wall construction material. In addition, the author evaluated the walls from the examined database for different restraint conditions in order to assess the influence of different retrofit solutions. He proposed a total of 4 cases, as follows (Figure 2.1):

- Case 1: No connection between diaphragm and masonry walls – the wall was restrained only at the base; hence, the wall can be considered a cantilever. It should be noted that the outer leaf of cavity walls was assumed to be restrained not only at the base but also at the top section due to either roof framing or the presence of solid parapets.
- Case 2: Only connection between diaphragm and masonry walls at roof level – the wall was restrained at the base and top section, and the parapet was free to move at its top. The critical element was the parapet due to its boundary condition. Regarding the cavity wall, Case 2 was treated as Case 1 since both have the same boundary condition.
- Case 3: Connection between the diaphragm and masonry walls at roof level and parapet restraint – the considered case was similar to Case 2 except for the parapet restraint. Due to the presence of parapet restraint, the critical element was the wall below the parapet since, in general, the parapet was smaller in height.
- Case 4: Connection between diaphragm and masonry walls at each level and parapet restraint – this condition can be characterised as all the diaphragms were connected to the wall.

It should be noted that the author, in addition to the cases mentioned above, described two different sub-cases, “A” and “B”, to take into account the connection type between cavity wall leaves. The sub-case “A” grouped buildings lacking existing cavity wall tie connections between the leaves, while the sub-case “B” included buildings in which the leaves were connected. By analysing the portfolio of 206 URM buildings, all the examined buildings were classified as Case 1A, because: (i) Cavity wall tie connections were assumed to be corroded, which led to considering the cavity wall as one leaf since there was no contribution from the outer leaf, and (ii) Although existing diaphragm connections at roof levels were found, lacking connection at any level above the ground due to uncertainties in condition was assumed.

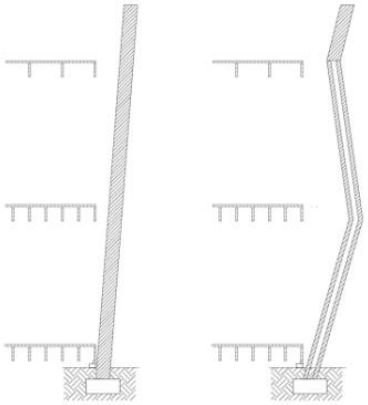

(a) Case 1: No above-ground diaphragm restraints

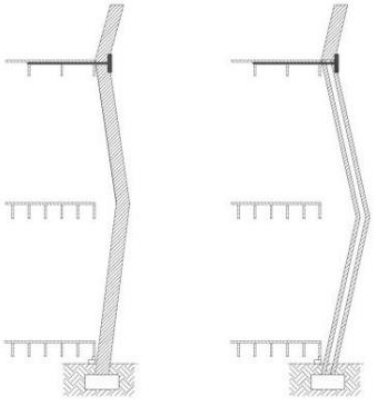

(b) Case 2: Diaphragm restraint at roof level only

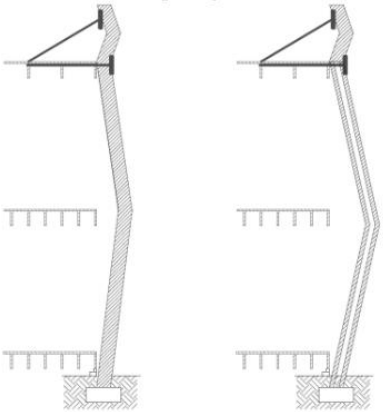

(c) Case 3: Diaphragm restraint at roof level and parapet restraint

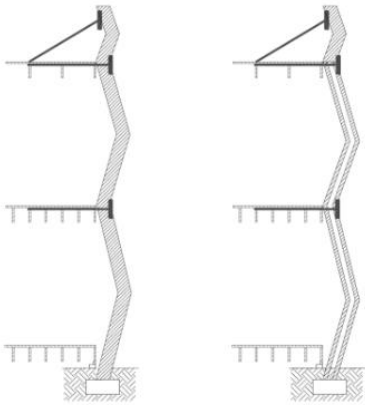

(d) Case 4: Diaphragm restraint at roof level and intermediate floor levels and parapet restraint

Figure 2.1 URM wall out-of-plane collapse mechanisms for different lateral restraint conditions (solid walls are shown on the left and cavity walls on the right of the figures) from Walsh [53]*. Note that the cavity walls were considered simply supported due to the roof framing and solid parapets on the outer leaves; Therefore, both Case 1 and Case 2 were treated identically.*

As regards the province of Groningen in the Netherlands (Figure 2.2), a need has arisen for a detailed regional inventory as a result of the induced seismicity in the area. A combination of datasets, surveys and GIS tools was used to identify the building typologies in Groningen [47]. The Groningen area contains 250,000 buildings with a total population of approximately 500,000 people. Approximately 200,000 buildings in the area are above the Groningen gas field.

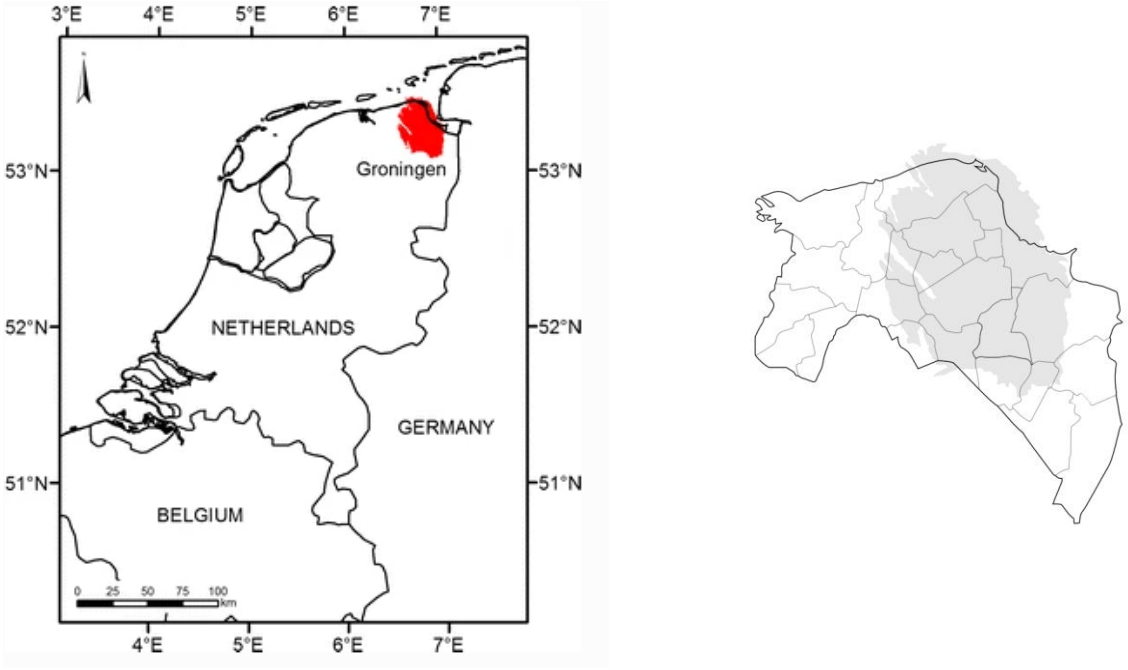

(a) (b)

Figure 2.2 Location of the Groningen gas field (highlighted in red) in the northern part of the Netherlands from Kruiver et al. [54] *(a) and close-up view of the region of Groningen and the gas field (in grey) from van Wijnbergen* [55] *(b).*

ARUP carried out a first inventory study that classified the buildings into typologies. Based on the results of such a study, unreinforced masonry is the primary building type in the region, estimated to consist of 90% of the building stock of the gas field and 75% of the region. The second common building type is reinforced concrete, with around 5% of the building stock is in the gas field area and 4% in the whole province. Wood and steel frame buildings represent less than 0.5% of the building stock [47]. A summary of the building type in the province of Groningen is reported in Figure 2.3.

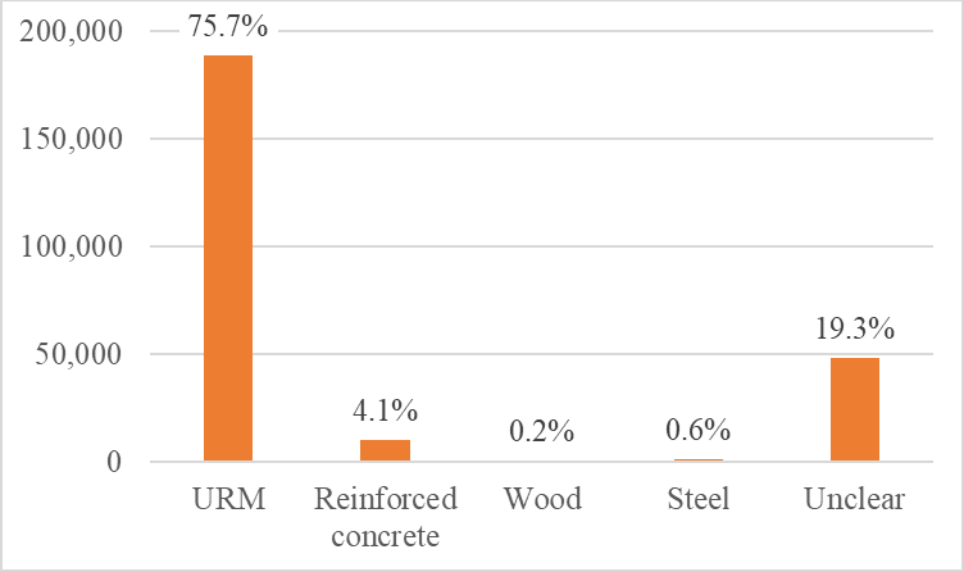

Figure 2.3 Percentage of URM buildings in Groningen adopted from Arup [47].

Analytical models were developed for masonry buildings in the Groningen region to capture all key modes using modal response spectrum analysis. The analytical results presented in the Arup Structural Upgrading [56] and terraced and semi-detached houses exhibited higher vulnerability to damage than other regional building typologies, such as labourer's cottages, mansions or villas.

ARUP assigned most unreinforced masonry buildings in the province of Groningen to the four following main typologies: detached/semi-detached houses with (i) flexible and (ii) rigid diaphragms and terraced houses with (iii) flexible and (iv) rigid diaphragms [47]. These are all low-rise buildings. In the study of Arup, the structures were further categorised into more building types under the main building typologies depending on attributes of the buildings such as geometric layout, material and type of lateral load-resisting system in each direction of the building, presence of external walls, floor system, number of floors and irregularities. Based on the results of the classification performed by ARUP, the building typologies *detached/semi-detached* and *terraced houses*, which represent the large majority of the building stock, can be defined as traditional Groningen houses. The work presented in this thesis is concerned only with "traditional Groningen houses" as they are the dominant building typologies in the region.

As seen in literature, geometric details of buildings, cavity vs solid walls, wall construction material, construction year, or the number of stories are essential characteristics to define a typology (among others [22,52,57–59]). However, in most cases, the connection details between structural elements are overlooked, particularly for the building inventory within the Groningen area.

2.2 Inventory of the buildings in Groningen

The inventory conducted in this study investigates traditional URM structures in Groningen, with special attention to the connection details between structural elements. A total of 267 addresses and 59 inspection reports were received from Nationaal Coördinator Groningen (NCG) for seismic assessment of structures. The dataset was compiled in order to prepare an inventory of URM buildings in the Groningen area concerning the material and type of lateral load-resisting system of the building, presence of external walls, floor systems and connection types at wall-to-wall, and wall-to-floor level. Besides, an overview of the characteristics of the studied buildings is provided in terms of the thickness of cavity wall leaves and air gap in between the leaves and the size and spacing of timber joists. The dataset was compiled aiming to guide the design of laboratory testing of prototypical buildings from the Groningen area. The inventory was checked and elaborated according to the v6 report of the Hazard and Risk study produced by EUCENTRE [46].

The v6 report uses the v6 exposure database (EDB v6) [60], which is an extract of a project database and consists of the location, structural characteristics and exposed population inside and within 5 km of the Groningen gas field. The URM buildings were assessed according to the GEM Building Taxonomy [61], namely, material and type of lateral load-resisting system, external walls, floor system, number of floors and irregularities. The examined building typologies are listed in Table 2.1 and illustrated in Figure 2.4.

Table 2.1 Building typologies in the v6 Model from Crowley et al. [46].

Code	Description
URM2L	URM aggregate unit with solid walls and timber floor
URM3L	URM 1-2 storey terraced unit with cavity walls and concrete floor (<90% openings)
URM4L	URM 1-2 storey terraced unit with cavity walls and concrete floor (≥90% openings)
URM5L	URM terraced unit with cavity walls and timber floor
URM6L	URM detached unit with solid walls and timber floor
URM7L	URM detached unit with cavity walls and concrete floor
URM8L	URM detached unit with cavity walls and timber floor
URM9L	URM aggregate unit with cavity walls and concrete floor and strengthened ground floor

The terraced unit is characterised by a homogeneous block, while the detached house refers to distinctly separate units. Differently from the terraced or detached unit, the aggregate unit is characterised by an inhomogeneous block made up of separate units/buildings that are closely spaced. The difference between URM3L and URM4L is due to the façade opening on the

ground floor. URM4L represents buildings with greater than or equal to 90% openings ratios on the ground floor, which can be calculated as the maximum ratio of the length of openings (due to windows and doors) to the total length of the façade wall, considering all ground floor façades of the building.

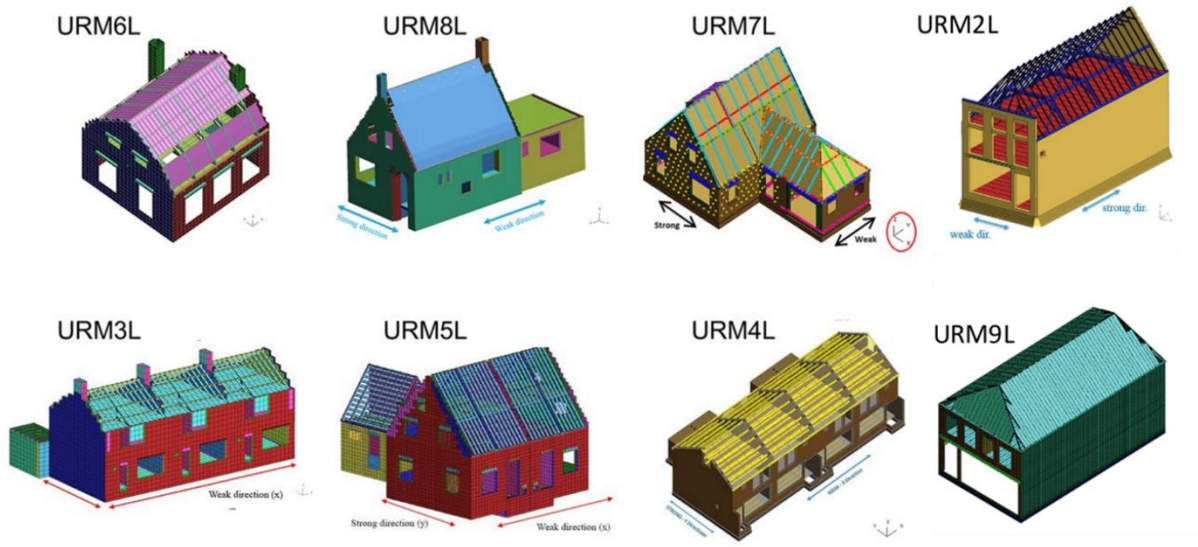

Figure 2.4 Screenshots of LS-Dyna numerical structural models from [46] *used in this work.*

For the purpose of understanding the main typologies of low-rise masonry buildings in the Groningen area, the distribution of the examined building into the typologies, as defined above in Table 2.1, is shown in Figure 2.5.

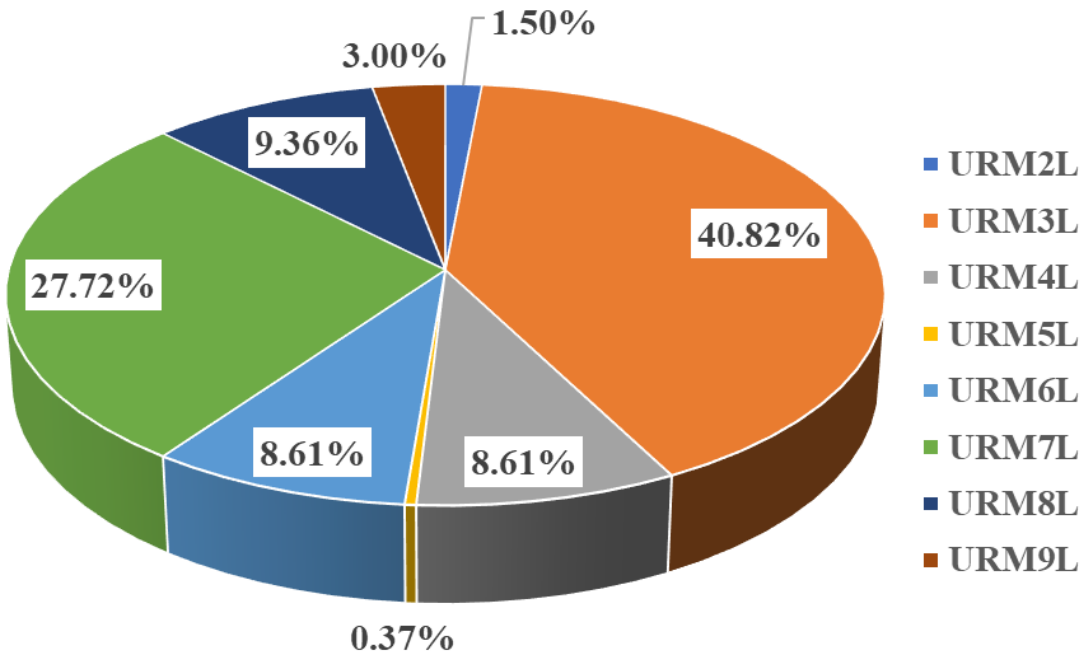

Figure 2.5 Distribution of building typologies in the Groningen area.

The most common typology is URM3L which equals almost 41% of the inventoried stock. The sum of the percentage of URM3L and URM4L representing typical terraced houses in the Netherlands is found as almost 50% of the inventory in this study, similar to what was reported in Esposito et al. [19]. Hence, the dataset used in the present study is considered representative in terms of the distribution of the buildings into different building typologies.

In the current study, the second more common building type is URM7L, detached houses with cavity walls and concrete floor; while in the study of Arup, it is detached houses with double-wythe clay brick and flexible diaphragm. However, it should be noted that the difference in distribution between detached houses with cavity walls and concrete floors and detached houses with double-wythe clay brick and the flexible diaphragm is not significant in the study of Arup. The corresponding double-wythe clay brick and flexible diaphragm structural systems in the v6 model is URM6L, representing almost 9% of the inventory in the current study. A similar distribution, 9%, is found for URM8L typology, detached houses with cavity walls and timber floors.

In terms of the construction period, traditional Groningen houses are divided into two groups based on the time threshold that resulted in a change in the production methodologies, namely the pre-World War II period (until 1945) and the post-war period [37,62]. Detached houses in the Netherlands represented the most common typology for the pre-war period. In contrast, terraced houses existed more commonly in the post-war period [56]. Figure 2.6a and b show the proportion of the building typologies depending on the two construction periods: pre-1945 and post-1945, respectively. As seen in Figure 2.6a and b, the dominant typologies for the pre-war and post-war periods are in line with the ones observed in the literature [37,56,62].

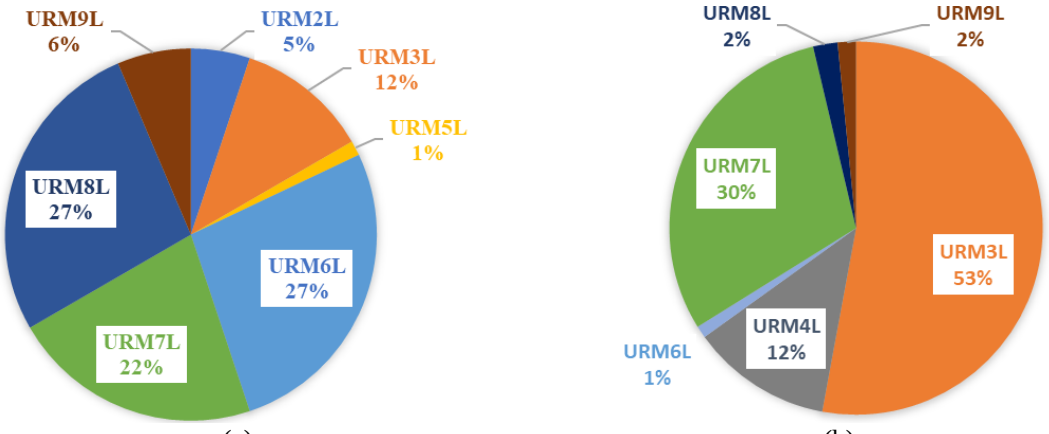

Figure 2.6 Building typologies based on construction period: pre-war period (a) and post-war period (b).

Regarding the types of walls that compose the lateral load-resisting system, cavity walls are a widely used wall system in the Groningen area, as presented in Figure 2.7.

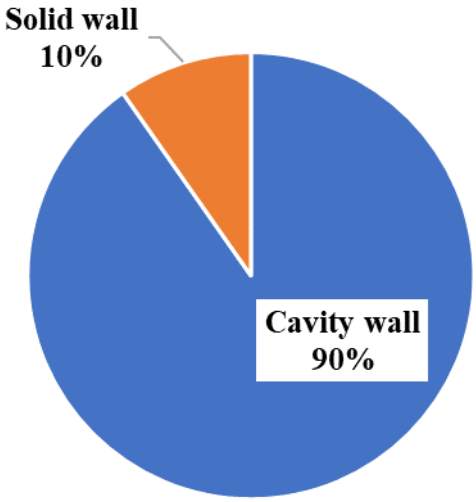

Figure 2.7 Distribution of wall systems.

According to the compiled dataset, the concrete floor (rigid diaphragm) is largely prevalent in the Groningen area (almost 80%, Figure 2.8). The second most common floor system is timber floor (flexible diaphragm), with more than 20% of the inventory. In addition, hollow-core RC and Nehobo floor systems can be found in a very limited percentage. It should be noted that URM structures with flexible diaphragms may not be able to provide box behaviour and, hence, may exhibit poor performance against earthquakes [26]. Thus, the floor type has an important influence on the seismic behaviour of URM structures.

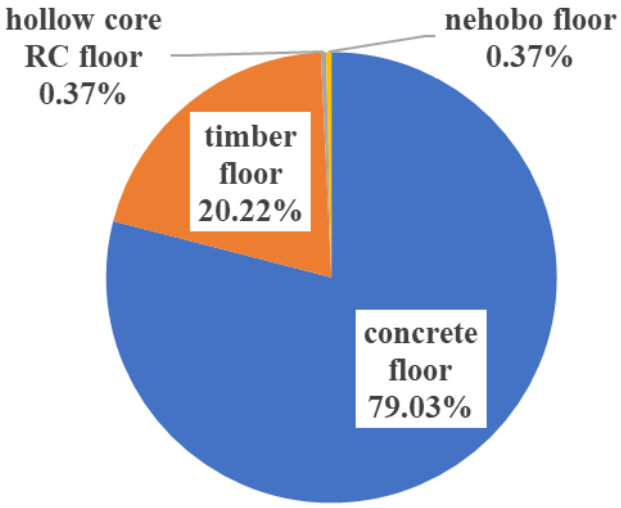

Figure 2.8 Distribution of floor systems.

The typologies of connections between structural elements, such as wall-to-wall or wall-to-floor connections, and their distribution are also studied and presented in the next sub-sections.

2.2.1 Classification of wall-to-wall connections

A cavity wall is a construction practice usually adopted for thermal and weather resistance and provides drainage [63,64]. In the Netherlands, a cavity wall usually consists of an inner leaf load-bearing wall made of calcium silicate brick masonry and an outer veneer of clay brick masonry separated by a cavity. The benefits of using calcium silicate bricks (CS) are the following: (i) low cost, (ii) good geometric shape and colour, (iii) relatively high strength quality, (iv) eco-friendly and (v) good fire resistance. Conversely, CS is not durable in terms of hardness, resistance to abrasion and watering. On the other hand, clay brick exhibits relatively better durability and aesthetics. Hence, calcium silicate brick is used as an inner leaf of a cavity wall, whilst the clay is used for the veneer of a cavity wall in the Netherlands.

Different construction practices occur in the way a cavity wall is constructed around the world. The first example of the use of a cavity wall originated in the United Kingdom, in which the cavity wall consists of two thick masonry leaves made of clay bricks [24]. URM cavity walls in New Zealand can be characterised as two leaves of clay brick masonry with a continuous air cavity [23]. In the United States, it can be found that a cavity wall consists of an outer leaf of split-face concrete brick and an inner load-bearing wall made of paper-faced gypsum sheathing [65]. Another example from Belgium, a cavity wall is composed of an inner load-bearing leaf made of fired-clay masonry units and an outer veneer leaf made of solid-clay bricks [38] or according to van der Pluijm and Vermeersch [66], the inner leaf was made with perforated clay blocs, while the outer leaf was made with solid soft mud clay bricks. Besides different materials, even the opposite of the usual structural practice in the Netherlands can be found elsewhere in the world, i.e., cavity walls in Australia that consist of an outer load-bearing leaf and an inner non-load-bearing leaf [67].

Typical Dutch cavity walls have 100 mm thick inner leaf and outer veneer, with an air gap in between equal to 80 mm [19,68]. However, the geometry of the cavity wall may vary from building to building in the region. A schematic representation of a cavity wall is illustrated in Figure 2.9. Table 2.2 lists all the reported variations for cavity walls from the dataset in terms of the thickness of inner and outer leaves and cavity width.

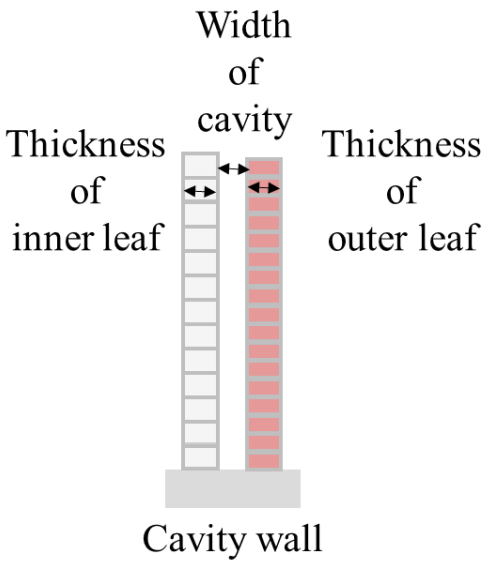

Figure 2.9 Schematic of a cavity wall.

Table 2.2 Documented cavity wall details in terms of thickness of leaves and gap width.

Cavity wall		**URM buildings**												
	1	**2**	**3**	**4**	**5**	**6**	**7**	**8**	**9**	**10**	**11**	**12**	**13**	**14**
Thickness of inner leaf (mm)	100	100	100	210	100	100	100	100	100	100	100	100	100	100
Width of cavity (mm)	10	20	40	40	50	60	70	80	80	90	100	120	150	190
Thickness of outer leaf (mm)	100	70	100	100	100	100	100	100	140	100	100	70	100	100

A statistical analysis of the cavity walls from the dataset is conducted to compute the median thickness of the inner leaf, cavity gap and outer leaf. The median values of 100 mm, 70 mm and 100 mm are computed for inner leaf, cavity, and outer leaf, respectively. In order to better understand the distribution of cavity gaps, the statistical distribution of the studied cavity wall details in terms of the width of the gap is shown in Figure 2.10.

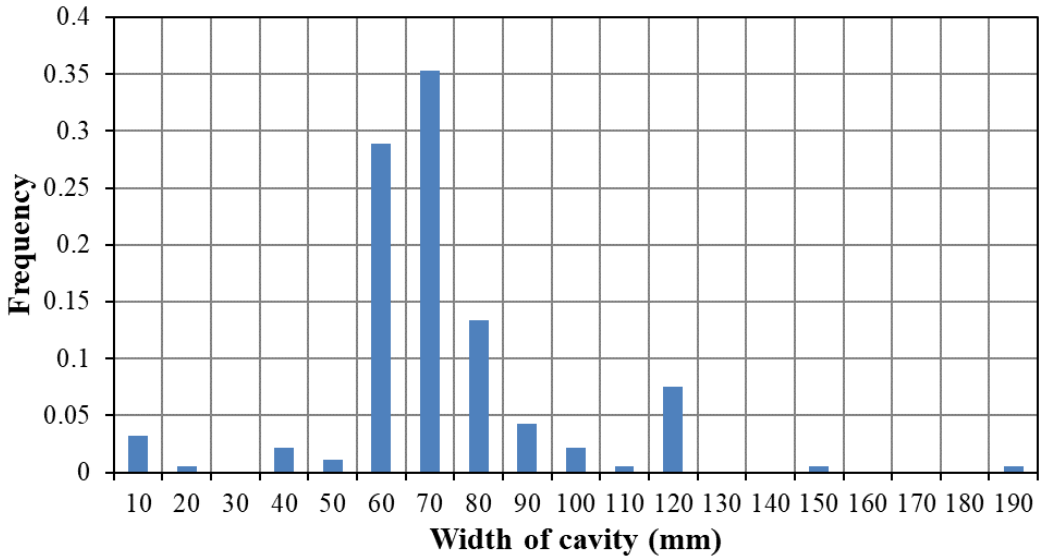

Figure 2.10 Distribution of cavity widths.

The cavity wall appears in 241 out of 267 addresses. Although the cavity wall is dominant based on the compiled dataset, the number of ties embedded in the masonry wall is reported for only 30% of the cavity walls in the inventory. Conversely, the majority, 63% of the cavity wall inventory, is characterised as a lack of information on the number of ties. Interestingly, a total of 7% of the cavity walls are defined as anchorless cavity walls. The anchorless cavity wall is a type of cavity wall which is designed and built without any connection between the leaves.

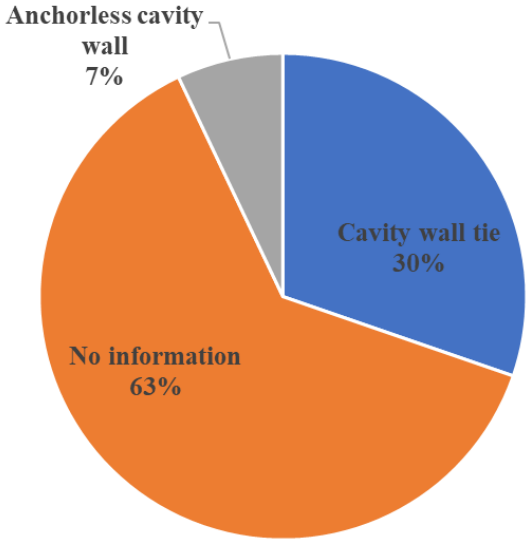

Figure 2.11 Distribution of wall-to-wall connections.

2.2.2 Classification of wall-to-floor connections

The two most common timber floor diaphragm-to-wall seating arrangements for URM structures in Dutch construction practice are the following: (i) over the entire width of a single leaf and (ii) over half the width of double-wythe URM walls. The former can be found particularly for cavity walls in which the joist is inserted on the thickness of the inner leaf of a cavity wall. The latter is mainly used for double-wythe URM clay masonry walls in which the joist beam is placed upon half of the thickness of the solid wall. Some examples of timber joist details from the dataset in terms of joist sizes and spacing are listed in Table 2.3, together with a schematic of a joist, as seen in Figure 2.12.

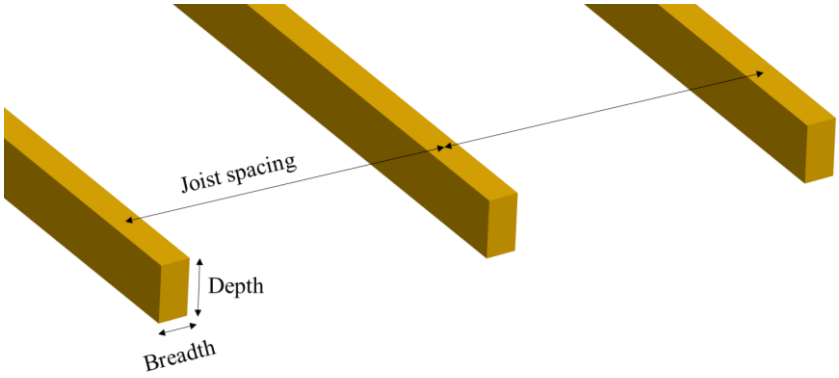

Figure 2.12 Schematic of timber joists with spacing.

Table 2.3 Documented timber joist details in terms of size and spacing.

Timber joist		**URM buildings**																
		1	**2**	**3**	**4**	**5**	**6**	**7**	**8**	**9**	**10**	**11**	**12**	**13**	**14**	**15**	**16**	**17**
Size of joist	**Breadth (mm)**	50	60	40	62	63	65	65	65	80	65	65	85	38	63	71	59	75
	Depth (mm)	185	110	75	168	160	145	140	130	220	175	170	230	120	160	221	196	200
Joist spacing (mm)		740	800	680	700	600	900	800	670	1150	585	620	820	600	770	770	610	1000

A statistical analysis of the timber joist details from the dataset is performed to compute the median of the breadth, depth and joist spacing. The median values of 65 mm, 160 mm and 755 mm are achieved for breadth, depth and joist spacing, respectively. Besides that, the statistical distribution of the examined details of the joist using a 2D scatter plot with a colour map is presented in Figure 2.13. The y-axis denotes the depth of the joist, while the x-axis is the breadth of the joist, and the colour map represents the joist spacing in which darker dots show shorter distances and vice versa.

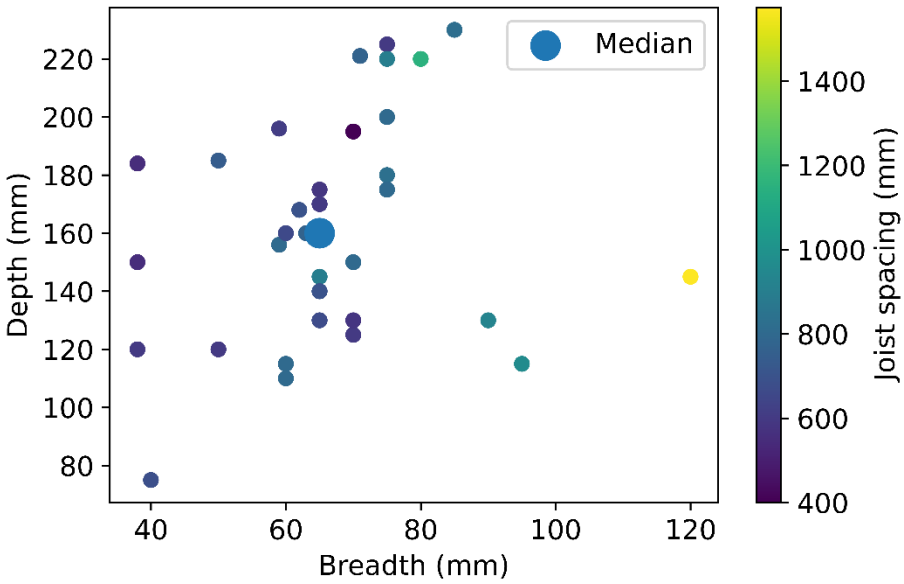

Figure 2.13 Overview of the observed timber joist details in terms of depth and breadth of the joist, and of joist spacing.

Regarding the wall-to-floor connections, the dataset is categorised into three types: (i) *connected*, indicating it is mentioned in the report that there is a connection between wall and floor, but it is not known what kind of connection itself, (ii) *no information*, denoting it is not known whether any connection was used and (iii) *anchor*, indicating floors are connected to walls via anchors, as seen in Figure 2.14. The x-axis denotes information about the connection levels from left to right: concrete floor-to-cavity wall, timber floor-to-cavity wall, concrete floor-to-solid wall, and timber floor-to-solid wall connections. Interestingly, 'no information' was retrieved in the case of timber floor-to-cavity wall and timber floor-to-solid wall connections, interpreting that they can be characterised without any specific detailing, which implies the use of masonry pocket connections. Regarding the concrete floor-to-cavity wall connections, the percentage of "No information" covers almost 68% of the inventory. When information was available, the use of an anchor between the inner leaf and the concrete floor was five times more probable than the use of other connections. It should be noted that regarding the use of the aforementioned anchor, the concrete slab did not bear on the inner leaf of the cavity wall (as it was supported in the transversal direction). Hence, it is only anchored to the inner leaf with small anchors that aim to prevent the out-of-plane collapse of the walls, as shown in Figure 2.15.

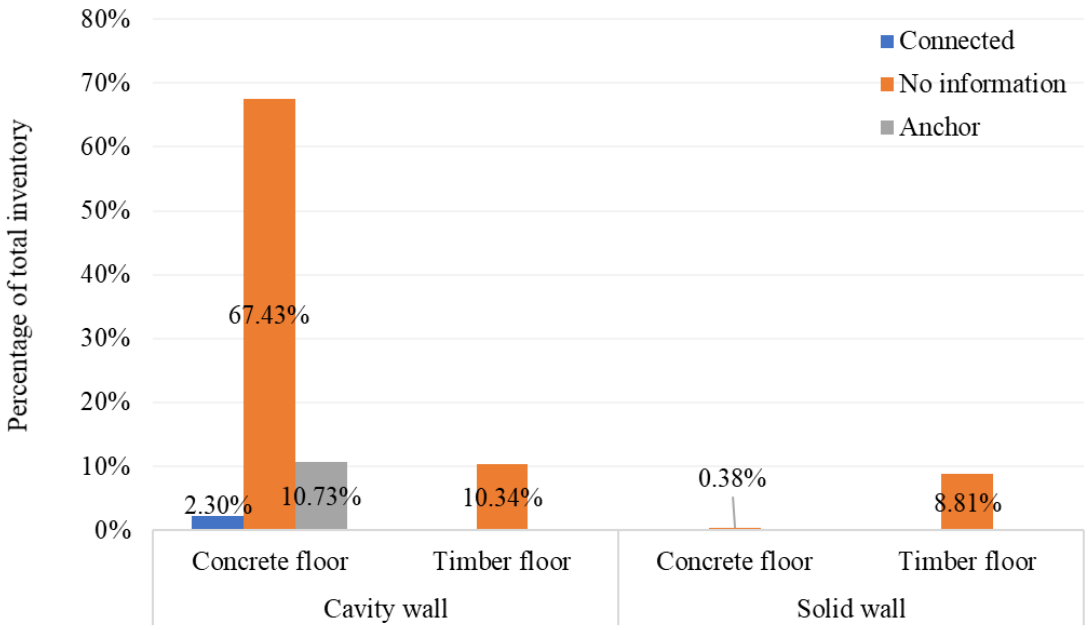

Figure 2.14 Wall-to-floor connections per type of wall system.

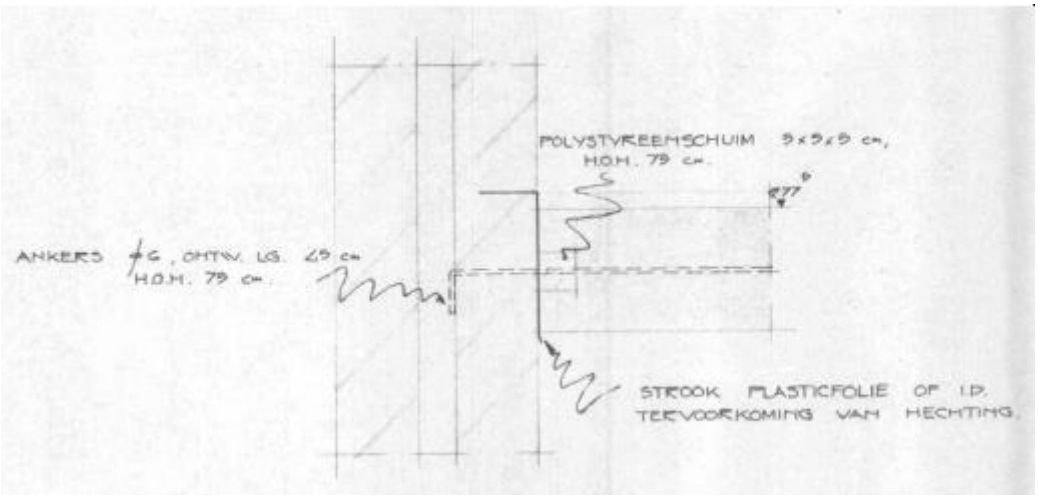

Figure 2.15 Example of wall-to-floor connection from the received dataset from NCG.

A detail common in traditional Dutch houses with the timber joist simply pocketed in the inner leaf of a cavity wall is shown in Figure 2.16a. In this case, the connection between the floor and the masonry wall relies on friction. Another common as-built connection for typical Dutch houses is the use of a hook anchor [13,69]. The hook anchor is an L-shaped steel anchor, as shown in Figure 2.16b.

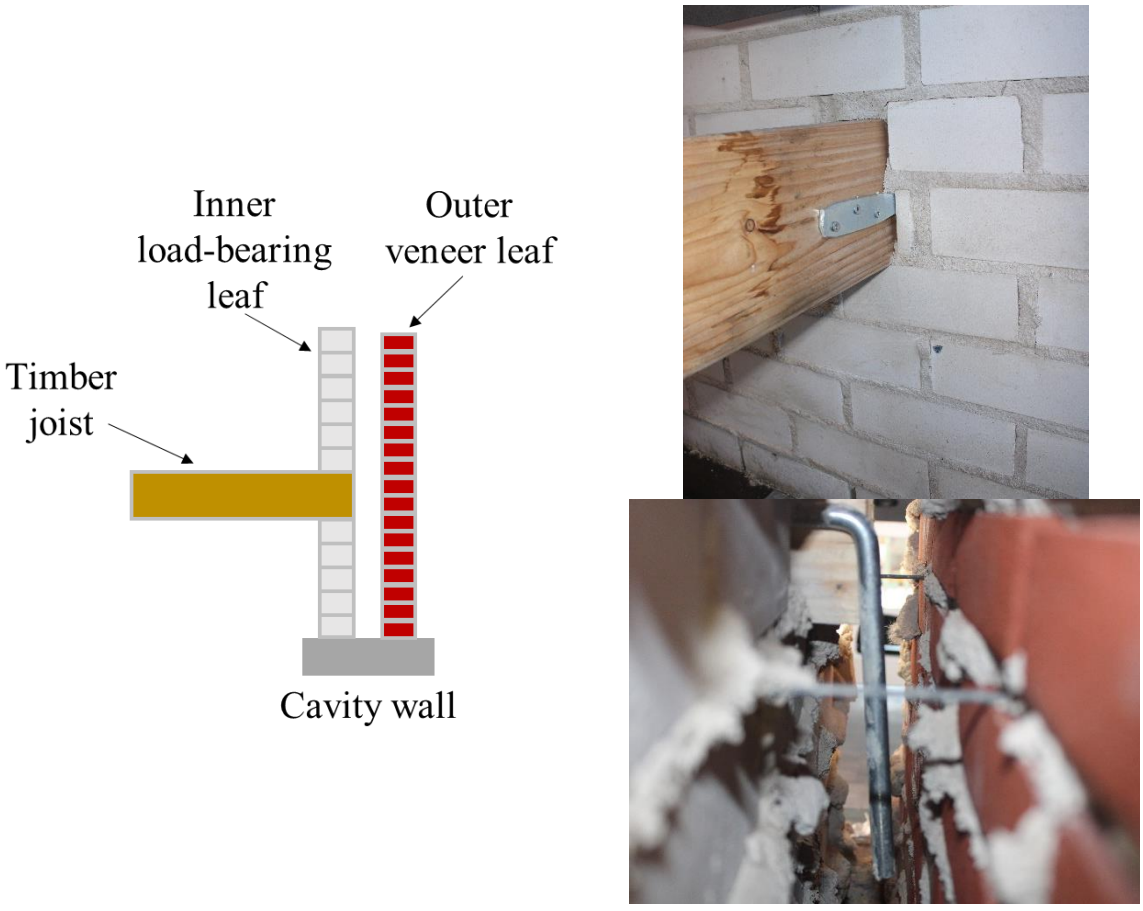

(a) (b)

Figure 2.16 As-built connections between a timber floor and a masonry wall: schematic of a masonry pocket connection (a), and detail of a timber joist with hook anchor (b).

2.3 Comparison of the classification based on the studied dataset with a previous categorisation

A comparison is conducted between the studied data described in the previous section and the database of Arup [47], which was introduced in section 2.1. The comparison focuses on building typologies and the prevalence of flexible floors and cavity walls in the region. It should be noted that the database considered by Arup covered a larger portion of the building stock in the gas field area. Initially, their research focused on a study area with approximately a 15 km radius centred at the epicentre of the Huizinge earthquake (the epicentre at 53.353 N 6.665 E). The research was then further extended to cover the whole gas field area due to the availability of more data in the gas field area.

In the research conducted by Arup, the typology code used was different from the one studied in this thesis. However, despite the difference in typology codes, it is possible to compare them based on the description of the building typology. The building typologies of

Arup for the initial study area and the extended study area are shown in Figure 2.17, with the initial database represented in blue and the extended database in red. The actual numbers are labelled on each bar of the histogram, providing further information about the distribution of building typologies in the two datasets.

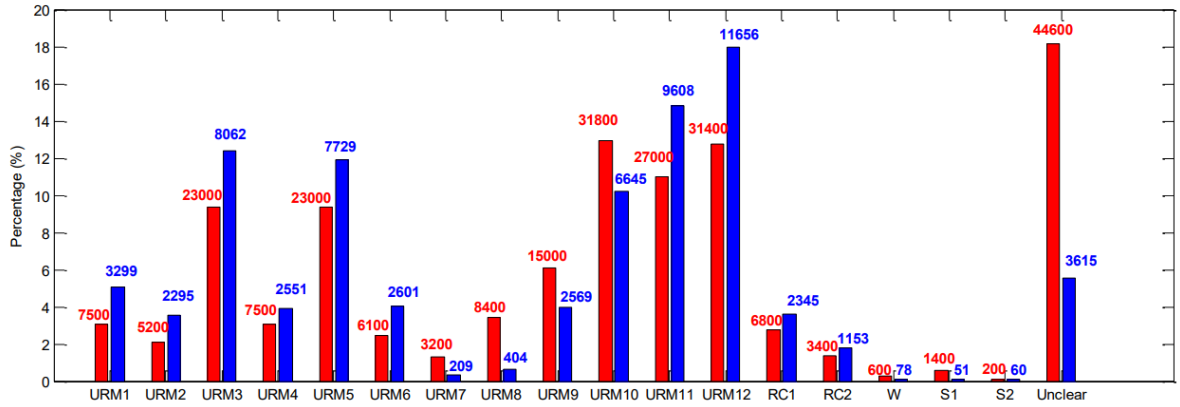

Figure 2.17 Building typology distribution in the study area from Arup [47] *(The initial building database is shown in blue, while the extended database is in red).*

As mentioned above, to compare the two datasets, the files are categorised according to the building typology: detached house with a flexible diaphragm, detached house with a rigid diaphragm, terraced house with a flexible diaphragm, and terraced house with a rigid diaphragm. It should be noted that the data of Arup included more building materials such as concrete, steel and wood, etc. Only the data related to URM buildings were taken into account. To better understand the distribution of the building typologies, Figure 2.18 shows the comparison among the studied dataset in this thesis, the initial building database from Arup and the extended building database from Arup. As seen in the figure, the distribution of the building typology of the terraced house does not represent the actual case in Groningen since the studied dataset was limited to a number of 267 addresses. The considered dataset underestimates the number of houses with flexible floors, especially in the case of terraced houses. This should be taken into account when the results related to the distribution of the connections are presented.

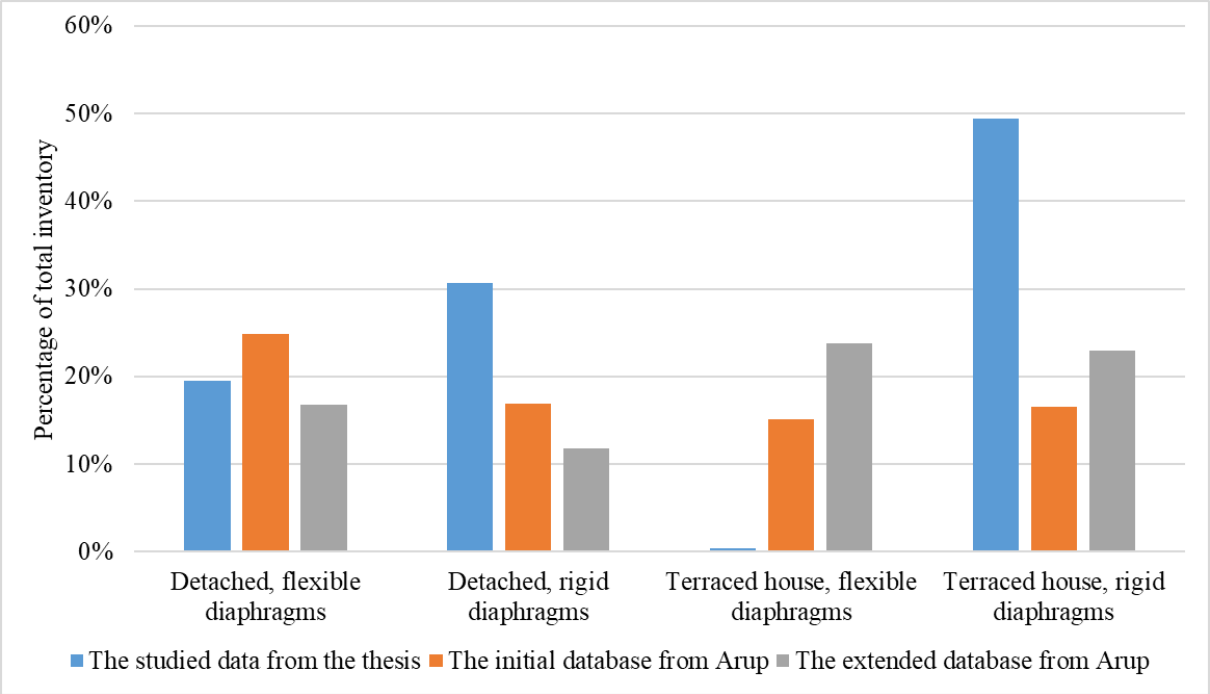

Figure 2.18 Comparison among the studied dataset in this thesis, the initial database from Arup and the extended database from Arup for four building typologies.

It is worth discussing that the studied dataset from NCG is geographically distributed in the Groningen Gas Field. Besides, investigators have prioritised buildings that needed strengthening according to NEN-NPR 9998 [70] (the current version is NEN NPR 9998:2020 [71]). Hence, a bias exists in the compiled dataset from NCG. On the other hand, NEN-NPR 9998 [70] had such high seismic demands that almost all the houses assessed by NCG required strengthening. For this reason, the bias is expected not to be significant, but it is hard to quantify. The reason why the typology of cavity walls with flexible diaphragms is estimated as very low according to the NCG data, although it is as vulnerable as terraced houses with concrete floors, may be related to bias. However, it should be noted that terraced houses with cavity walls and flexible diaphragms are found as 23.8% of the inventory in the study of Arup. Hence, the data received from NCG should be extended so that all the vulnerable elements from the area will be represented with a more accurate percentage based on the construction practice.

2.4 Conclusions

This chapter aims to identify and categorise unreinforced masonry buildings in the Groningen area in terms of materials used and the type of lateral load-resisting system, characteristics of

the external walls, floor system, number of floors and presence of irregularities. Special attention is paid to the documentation of connection details. Specifically, the focus is on traditional wall-to-wall and wall-to-floor connections in the studied dataset. Additionally, an overview of the characteristics of the studied buildings is provided in terms of the thickness of the cavity wall leaves, the size of the air gap between them, and dimensions and spacing of timber joists.

The findings of the inventory are as follows:

- The preferred construction type during the pre-war period was detached houses, while terraced houses became increasingly popular after World War II.
- Detached houses were expected to have double-wythe clay brick solid walls with timber floors up until approximately World War II. After that, URM buildings with single-wythe or cavity walls become more common. This finding aligns with the compiled file and the inventory conducted by ARUP [47]. The proportion of detached houses with solid walls and timber floors is similar to that of detached houses with cavity walls and timber floors.
- The cavity wall is commonly used for perimeter walls. The dimension of the cavity wall may vary from building to building, but median values of 100 mm, 70 mm and 100 mm are reported for the inner leaf, cavity, and outer leaf, respectively.
- Almost 20% of the URM buildings have timber floors, and the timber floor covers approximately 26% of the inventory regarding the attic floor.
- Hook anchors are the most common documented connection in the region between timber floors and masonry walls.
- Regarding the connections lacking detailed information, defined as "no information" in this chapter, it can be considered a connection that relies on friction.

World War II was a milestone in terms of construction techniques; hence after the war, not only the cavity-wall terraced house typology became predominant in the region, but also the cavity-wall construction technique was applied to the newly built detached houses.

Based on the findings from the above characterisation of the building stock and connection types, for this thesis, it has been decided to select the following characteristics and dimensions for the experimental campaigns presented in Chapter 3 and Chapter 4:

- The cavity wall consists of an inner 102-mm-thick load-bearing leaf made of calcium silicate units and an outer 100-mm-thick external veneer made of clay bricks separated by a cavity of 80 mm.

- The floor is flexible and consists of timber joist with a size of 55x155 mm.
- Regarding wall-to-wall connections, L-shaped ties with a diameter of 3.6 mm and a total length of 200 mm are embedded in the mortar joint of CS and CB leaves.
- Two different connections are considered between timber floors and masonry cavity walls: masonry pocket and hook anchor as-built connections.

Chapter 3: Experimental characterisation of cavity wall tie connections

As discussed in the previous chapter, the cavity wall tie was identified as the most common connection between cavity wall leaves in the traditional masonry structures in Groningen. Hence, an experimental campaign has been carried out at Delft University of Technology to provide a complete characterisation of the axial behaviour of traditional connections in cavity walls. This chapter exhibits findings on the behaviour of the metal tie connections between the masonry leaves often used in Dutch construction practice.

Section 3.1 presents a review of past experimental research. Due to the lack of knowledge of the connection between the leaves in cavity walls, the aforementioned experimental campaign was conducted to address the knowledge gap. Section 3.2 of the chapter describes the specimen geometry, the test setup and the adopted testing protocol. Section 3.3 describes the tests carried out to characterise the used materials. It also describes the characteristics of the groups of specimens tested, obtained by a combination of different materials, geometry and loading protocols. Section 3.4 presents and discusses the test results, with special attention on the developed failure mode and the definition of average force-displacement curves for each group of tests performed. This chapter is adapted from Arslan et al. [43].

3.1 Review of Past Experimental Research

With the aim of characterising the seismic behaviour of typical unreinforced masonry (URM) Dutch houses, an extensive multiscale testing program was performed at TU Delft in 2015, the results of which are presented in Messali et al. [37]. Part of the research focused on terraced houses built in the Netherlands during the period 1960-1980 [19,36] and characterised by the use of cavity walls. The double-leaf masonry construction also exists in other regions of the world, such as Australia, New Zealand, and North America, as well as in various parts of northern Europe. In the framework of the same multiscale testing campaign, an integrated testing program was carried out at EUCENTRE laboratories in Pavia in 2015, where, among others [72], two full-scale shake table tests were conducted on terraced houses [13,14]. Furthermore, recent shake table experiments [68,73] on single-leaf and double-leaf cavity walls

clearly underline the dominance of out-of-plane (OOP) failure mechanisms in these slender URM walls.

The out-of-plane behaviour is a common failure mechanism of slender masonry walls during an earthquake, which often stems from poor wall-to-wall, wall-to-floor or wall-to-roof connections that provide insufficient restraint to overturning. Cavity walls are particularly vulnerable to out-of-plane mechanisms due to the slender geometry of the two leaves, and, in fact, the out-of-plane behaviour of cavity walls represents a major concern during a strong shock [13,14,33]. The experimental findings of cavity wall tie connections are reviewed hereinafter based on the tests on the full-scale walls and the connection only.

In a study where full-scale brick veneer wall panel specimens were tested [74], it was found that out-of-plane wall damage occurred when the veneer moved away from the interior wood backup, placing a high demand on the tensile force and displacement capacities of the ties, underlining the prominent role of the ties in the composite response of the two leaves. Giaretton et al. [23] showed that when a sufficient number of connections are used, the out-of-plane failure of cavity walls can be prevented. According to BSI PD 6697 [35], a minimum number of wall ties per unit can be calculated, which is no less than 2.5 ties per square metre and should be used for walls with both leaves having a size of 90 mm or thicker, whereas the spacing, embedment length in the mortar and inadequate number of ties will influence the overall capacity of the cavity wall.

In the study by Walsh et al. [33], in-situ tests were carried out on full-scale masonry cavity walls for both existing and retrofitted metal ties, concluding that the retrofitting of cavity walls with adequate spacing, as well as adequate compressive and shear stiffness, can greatly improve the OOP capacity of URM walls. Also, some laboratory tests were conducted to investigate the behaviour of URM cavity walls on both existing ties [67,68,73] and retrofitted ties [40,75], where various tie failures have occurred.

Regarding the tests on the connection only, Choi and LaFave [76] and Reneckis and LaFave [77] performed experiments at the component level on brick-tie-wood, representing current U.S. construction practice. The monotonic tests (tension, compression, and shear) and the cyclic tests were carried out to capture the local performance of overall wall systems in order to assess the influence of tie thickness, initial offset displacement, attaching method of ties to wood studs, type of loading, eccentricity and embedment length. The details of the construction of specimens are illustrated in Figure 3.1a.

Regarding the screw-connected tests, the primary failure mode was a pull-out tie from the mortar joint in tension, while the governing failure mode was buckling of the tie in compression [76]. As far as the force-displacement curve of the specimens under cyclic axial loading is regarded, an unsymmetrical behaviour with a pinching effect was observed, as shown in Figure 3.1b. The pinched hysteresis shape exhibited strength and stiffness degradation. They found that the quality of brick veneer, particularly concerning the installation of the ties, plays an essential role in the overall wall system performance.

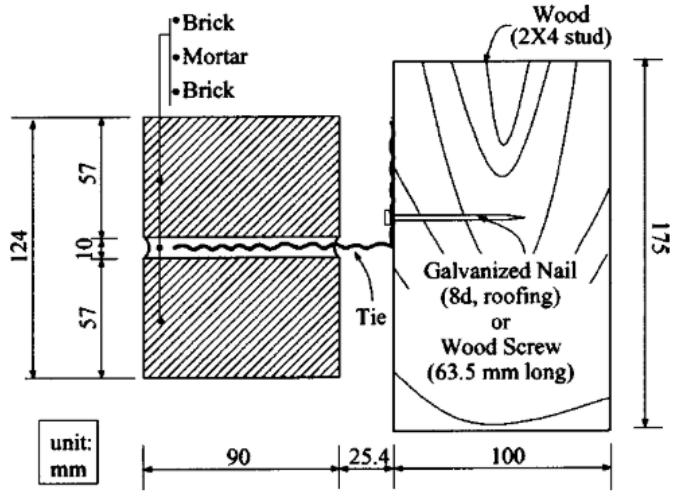

(a)

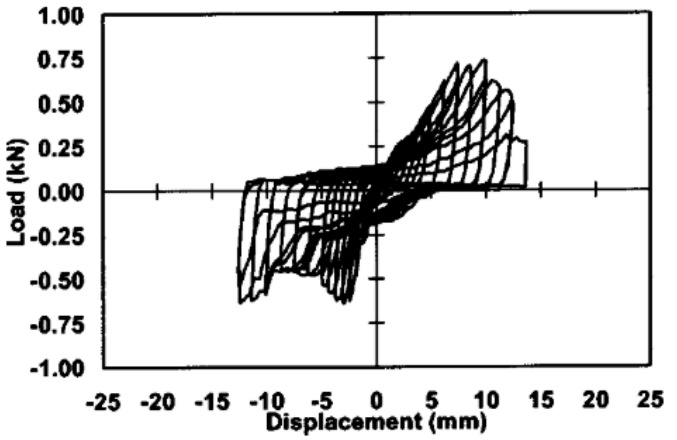

(b)

Figure 3.1 Geometry of specimen tested by Choi and LaFave [76] *(a) and corresponding force-displacement curve (b).*

An experimental investigation was performed on different brick-tie-brick assemblages on the connections in cavity walls based on construction practices from Portugal and other South European countries [78], evaluating the response at the component level under cyclic loading

in terms of stiffness, strength, dissipation of energy and failure modes. In the experiment, the total displacement of the tie was measured by LVDT 1, which was attached to the actuator, while the relative displacement of the tie from the masonry prism by means of LVDT 2, which was attached to the masonry prism and the tie, as seen in Figure 3.2a.

A total of 4 different failure modes were observed during the experiment conducted by Martins et al. [78], including tie buckling, tie pull-out, tie fracture at the middle length and tie fracture at the interface of the mortar joint of the prism. The dominant failure mode was the pull-out of the tie in tension and buckling of the tie in compression. The tie fracture failure mode was associated with the fatigue of the tie promoted by the cyclic loading, which occurred at the end of the test Figure 3.2b. They concluded that the primary role of the cavity wall ties on masonry outer leaves is the transfer of out-of-plane lateral loads from the outer leaf to the inner leaf through the connection between both elements. For this reason, Martins et al. [78] stated that the ties should have adequate resistance and stiffness both in tension and compression. They also concluded that the tie shape and geometry were the most important factors influencing the strength of the tie connections.

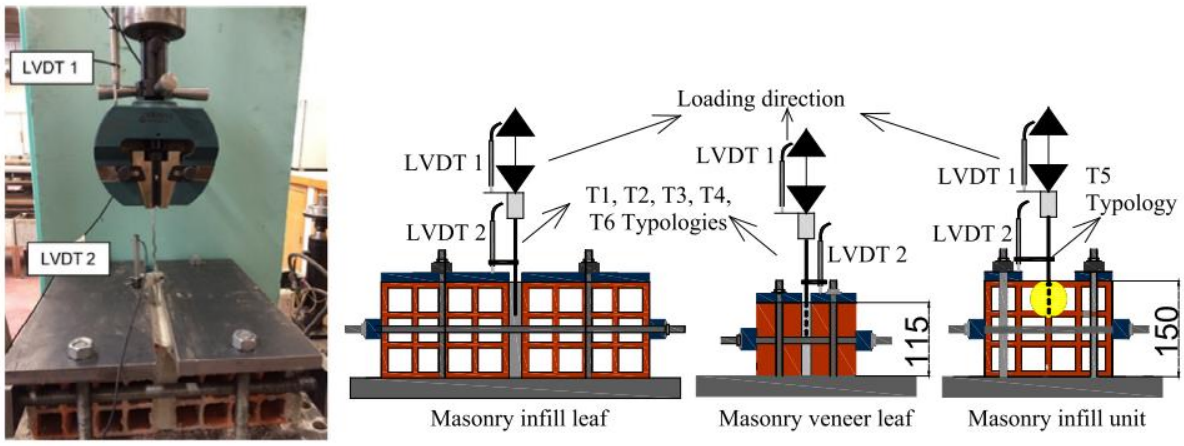

(a)

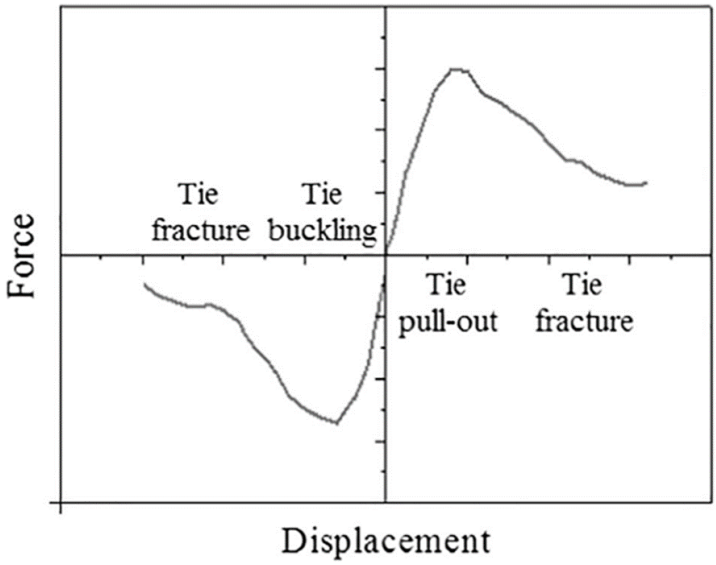

(b)

Figure 3.2 Details of test setup (a) and scheme of phenomena of failure modes observed during the experiment from Martins et al. [78].

An experimental campaign on cavity wall ties was carried out at TU Delft to characterise the behaviour of the connections in terms of resistance, envelope curve and dissipated energy [39]. The specimens were typical wall ties used in Dutch terraced houses, embedded either in calcium silicate or in perforated clay brick couplets. Different loading conditions (axial and shear, monotonic and cyclic loading) and different confining compressive loads on the couplets were considered. It was found that the wall ties tested were able to connect the two leaves for relatively small seismic out-of-plane displacement demands but might fail in larger wall out-of-plane displacements, even before the wall reaches its collapse capacity.

The following sections present the outcome of an experimental campaign on cavity wall ties carried out at the Macrolab/Stevin laboratory of TU Delft. The experiments aim to provide a complete characterisation of the cyclic axial behaviour of cavity wall ties. This research can also provide a better understanding of the behaviour of the tested metal wall ties for the industry to find suitable methods for developing their products and improving the seismic response of existing URM structures.

3.2 Experimental test programme

The experiments presented here aim to characterise the cyclic axial behaviour of metal cavity wall ties. Each specimen consisted of two bricks connected by means of mortar (couplets) and included an embedded metal wall tie that was designed to represent a portion of as-built URM cavity walls (Figure 3.3). Two hundred two couplets were tested in total, consisting of two types of masonry units: solid calcium silicate (CS) and perforated clay brick masonry (CB).

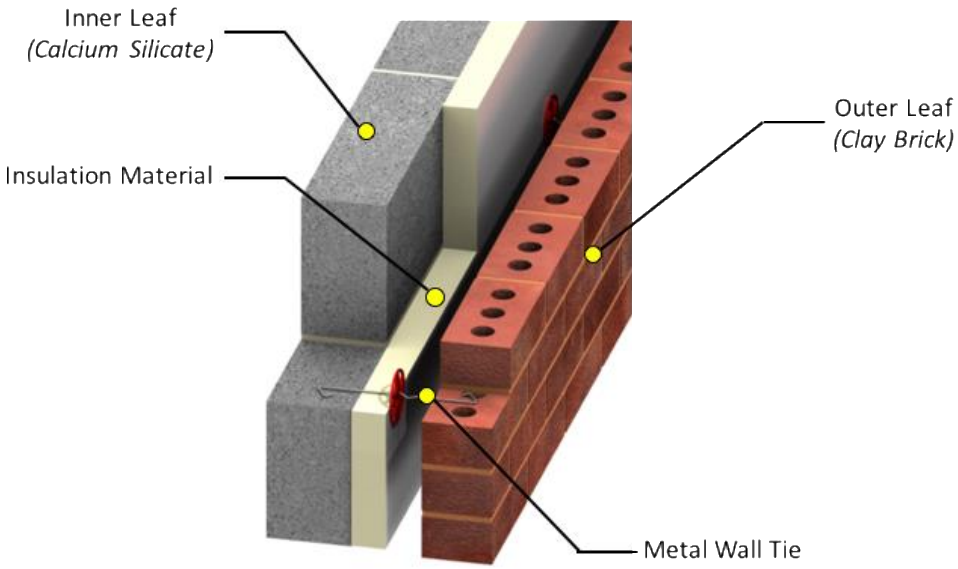

Figure 3.3 Schematic of a typical cavity wall.

3.2.1 Test Specimens

The test specimens were constructed by an experienced mason to ensure the best possible quality control and were cured for a minimum of 28 days (Figure 3.4). The ties were placed inside the mortar bed joint, replicating real-world applications (Figure 3.5).

The flow of the mortar was determined in agreement with NEN-EN 1015-3 [79]. During the construction phase, no free movement of the ties was allowed inside the fresh mortar, and

the specimens were built in agreement with NEN-EN 845-1+A1 [80]. In practice, the zigzag end of the tie is embedded in the CB masonry, while the L-shaped hooked end is embedded in the inner CS walls, as shown in Figure 3.5.

Figure 3.4 Construction details of the tested specimens: construction of CS specimen (a), example of a CB specimen (b) and of a CS specimen (c).

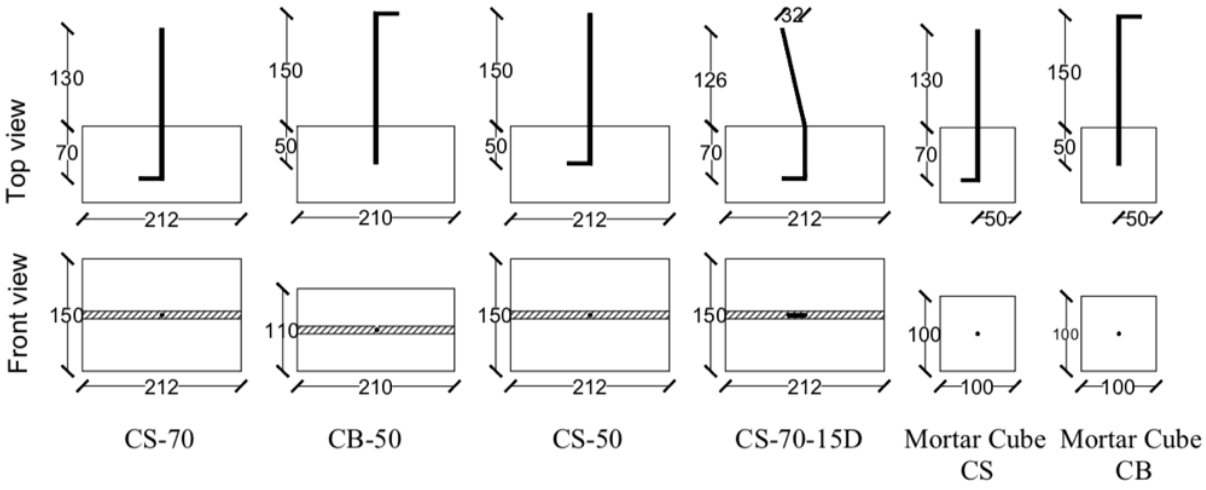

Figure 3.5 Geometry of tested specimens.

L-shaped ties with a diameter of 3.6 mm and a total length of 200 mm were embedded between two bricks in the mortar joint. The embedment length was different at each end of the tie: the zigzag end was embedded for a length of 50 mm (CB-50), whereas the hooked ends were embedded for two different lengths of the straight portions, 70 mm (CS-70) and 50 mm (CS-50), representing possible variations in practice. For a number of specimens, the tie was

bent 15° from the axis perpendicular to the vertical (CS-70-15D), meaning imperfect applications are often observed in practice. From the previous campaign [39], the bent tie was embedded in the CS masonry because the test results highlighted that the tie connections in the inner leaf play a critical role in overall wall performance. Although only the configuration of the tie was bent parallel to the bed joints (horizontally), similar behaviour of the tie was expected in case of deformations imposed perpendicularly to the bed joint (vertically) due to the isotropic behaviour of the tie itself.

In addition to the masonry couplets, 32 mortar cube samples were constructed to investigate the embedment of the tie in the mortar alone. A number of specimens tested in the current experiment campaign were chosen to establish a force-displacement curve accurately and indicate the variability of the material. Specimens which reached their full capacity are presented in this chapter. As in practice in Dutch construction, the mortar used for CS and CB layers is different [37,68]. In mortar cube tests with ties, both mortar types were tested. For each of these specimens, the tie was embedded into the mortar cube with an anchoring length of 70 mm for mortar used with CS or 50 mm for mortar used in CB bricks.

To provide a complete characterisation of the connection typology, six types of specimens were eventually tested, as shown in Table 3.1 and Figure 3.5:

- CS-70: the hooked part of the tie is embedded in a CS couplet, with a 70 mm anchoring length.
- CS-70-15D: the hooked part of the tie is embedded in a CS couplet, with 70mm, and the zigzag end of the tie is bent 15°.
- CS-50: the hooked part of the tie is embedded in a CS couplet with a reduced embedment length of 50 mm.
- CB-50: the zigzag end part of the tie is embedded in a CB couplet with an anchoring length of 50 mm.
- Mortar Cubes of CS Mortar: the hooked part of the tie is embedded in a mortar cube made of the same mortar used for the CS couplets, with an anchoring length of 70 mm.
- Mortar Cubes of CB Mortar: the zigzag end part of the tie is embedded in a mortar cube made of the same mortar used for the CB couplets, with an anchoring length of 50 mm.

Table 3.1 Specimens tested per each loading protocol.

Specimen Type	Loading Protocol	Lateral Pre-compression (MPa)	Embedment Length (mm)	Bending (deg)	Number of specimens
CS-70	MT	0.1	70	0	11
	MT	0.3	70	0	10
	MT	0	70	0	3
	MT	0.6	70	0	3
	MT-HS	0.1	70	0	6
	MC	0.1	70	0	12
	MC	0.3	70	0	9
	MC	0	70	0	1
	MC	0.6	70	0	1
	MC-HS	0.1	70	0	3
	Cyclic	0.1	70	0	9
	Cyclic	0.3	70	0	11
CS-70-15D	MT	0.1	70	15	6
	MC	0.1	70	15	6
	Cyclic	0.1	70	15	8
	Cyclic	0.3	70	15	8
CS-50	MT	0.1	50	0	3
	MC	0.1	50	0	2
	Cyclic	0.1	50	0	9
CB-50	MT	0.1	50	0	12
	MT	0.3	50	0	11
	MT	0	50	0	3
	MT	0.6	50	0	3
	MT-HS	0.1	50	0	6
	MC	0.1	50	0	10
	MC	0.3	50	0	10
	MC	0	50	0	1
	MC	0.6	50	0	1
	MC-HS	0.1	50	0	3
	Cyclic	0.1	50	0	10
	Cyclic	0.3	50	0	11
Mortar Cubes for CS	MT	0	70	0	3
	MC	0	70	0	3
	Cyclic	0	70	0	10
Mortar Cubes for CB	MT	0	50	0	3
	MC	0	50	0	3
	Cyclic	0	50	0	10

Note: MT = Monotonic Tensile; MT-HS = Monotonic Tensile High Speed; MC = Monotonic Compressive; MC-HS = Monotonic Compressive High Speed.

3.2.2 Test Setup

The test setup was assembled based on the recommendations reported in NEN-EN 846-5 [81] and is shown in Figure 3.6. The testing machine was connected to a contrast steel frame and integrated with a data acquisition system (Figure 3.6a). The specimen was placed in the test machine so that the tie lay aligned vertically along the centreline axis of the test machine, and the tie was clamped to have a free distance from the couplet equal to 80 mm (Figure 3.6b), a gap representative of the Dutch construction practice. An image of the setup with the names of the different components is shown in Figure 3.6c.

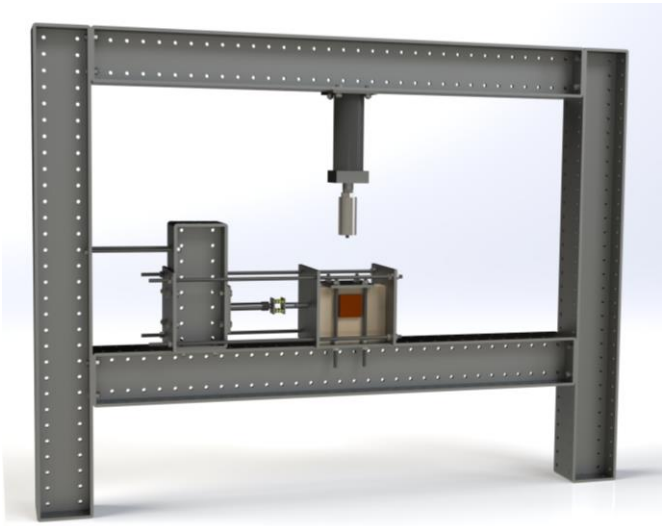

(a)

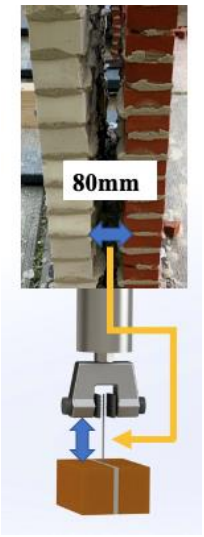

(b)

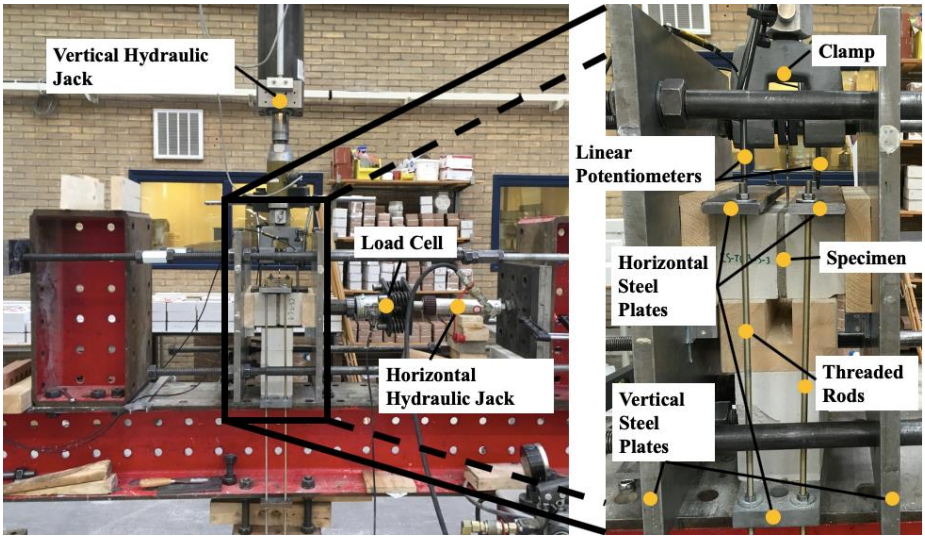

(c)

Figure 3.6 Testing setup: schematic of the general [39] *(a) and axial setup (b); detail of the actual setup (c).*

During the test, a horizontal compressive force was applied to the couplet and maintained constant by a manually operated hydraulic jack. Two lateral steel plates ensured the diffusion

of the compressive load on the entire lateral surfaces of the couplets. Different levels of pre-compression were applied to the specimens: 0 MPa, 0.1 MPa, 0.3 MPa, and 0.6 MPa. The applied pre-compression levels were considered to be representative of a cavity wall at different levels of a typical URM residential building, regardless of the boundary conditions. The axial load is applied vertically to the wall tie using a displacement-controlled apparatus equipped with a jack. The machine was provided with a clamp for gripping the free end of the tie efficiently. The vertical displacements of the bricks of the couplets were prevented by two horizontal steel plates connected by steel threaded rods. Two linear potentiometers were installed symmetrically on the two opposite sides of the clamp, pointing against the steel plate on top of the couplet. Their measuring range was 10 mm (Figure 3.6).

3.2.3 Loading protocol

The specimens were subjected to two different loading protocols, which are quasi-static monotonic and cyclic loading. Monotonic tests were conducted to obtain the maximum strength capacity of the connection under tension and compression. In addition, the obtained result is useful to highlight the initial curve without any degradation in strength or stiffness. In order to capture any strength and stiffness degradation, the repetition of same amplitude cycles and small displacement cycles should be included for cyclic loading.

Two loading speeds were conducted for the monotonic tests: (1) quasi-static loading rate, which is considered to be conservative due to a low loading rate and (2) high-speed rate investigating the effect of speed rates closer to those that occur during earthquakes. The nominal displacement corresponding to the peak force was determined by the monotonic tests. From monotonic tests, it was possible to define the cyclic group amplitude with increments of three cycles each time in the first phase, and then is followed by two degradation cycles that were repeated at higher amplitudes in the second phase with the purpose of capturing the cyclic degradation on the tie-mortar bond. Five different loading schemes were applied:

- MT (Monotonic Tensile): the pull-out displacements (introducing tensile loading in the connection) is increased monotonically with a rate of 0.1 mm/s up to failure.
- MT-HS (Monotonic Tensile High Speed): the pull-out displacements (introducing tensile loading in the connection) are increased monotonically with a higher rate of 1 mm/s up to failure.

- MC (Monotonic Compressive): the displacements of the clamp towards the couplet (introducing compressive loading in the connection) are increased monotonically with a rate of 0.1 mm/s up to failure.
- MC-HS (Monotonic Compressive High Speed): the displacements of the clamp towards the couplet (introducing compressive loading in the connection) are increased monotonically with a higher rate of 1 mm/s up to failure.
- C (Cyclic): the displacements imposed on the clamp are cyclically varied to apply both tensile and compressive loads to the connection. The loading history for this test is divided into two phases. In phase 1, three groups of three cycles of amplitude equal to 0.1 mm, 0.25 mm, and 0.5 mm are performed. In phase 2, each cycle comprises two runs of increased amplitude with respect to the previous cycle and two runs of reduced displacement, calculated as 40% of the displacements of the two previous runs (Figure 3.7). The loading rate is chosen to maintain a constant duration of every cycle until reaching 1 mm/s. Afterwards, it is kept constant.

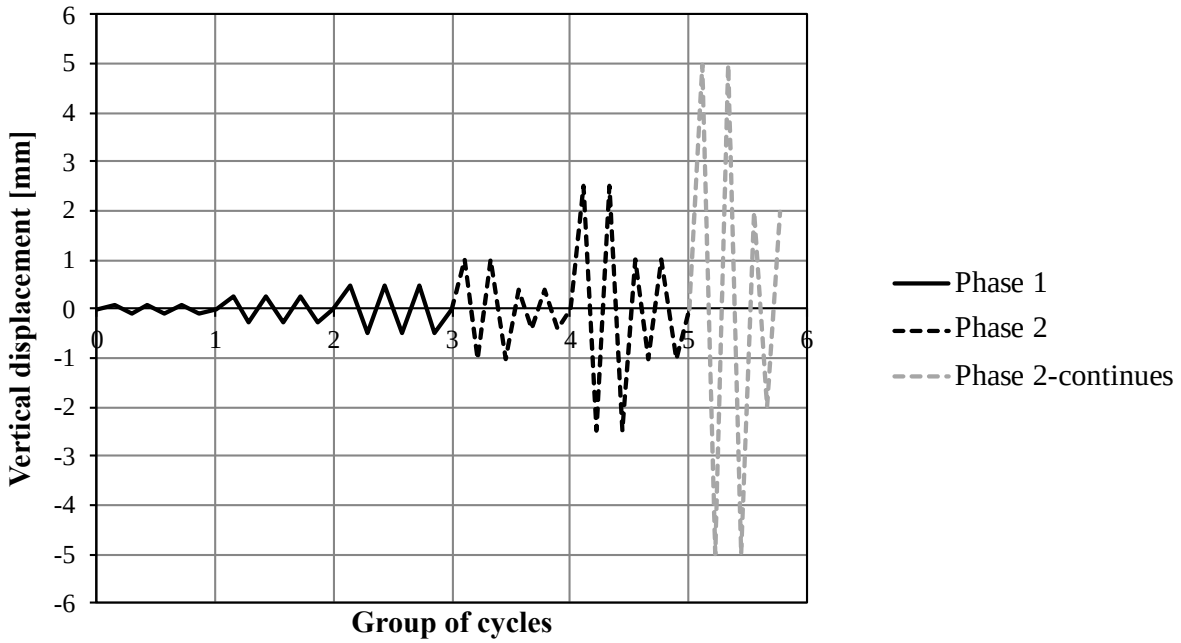

Figure 3.7 Cyclic loading protocol.

3.3 Mechanical characterisation of materials

A series of companion tests were performed to characterise the mechanical properties of the materials used in the testing campaign. The flexural and compressive strength of the mortar,

the tensile and compressive capacity of the tie, and the bond strength between the masonry unit and mortar were investigated.

3.3.1 Flexural and compressive strength of mortar

The mechanical characterisation of the mortars both for CS and CB were defined in terms of mean compressive strength, f_m, and flexural strength of mortar, f_{bm}, in agreement with NEN-EN 1015-11 [82]. The flexural strength, f_{bm}, of the mortar was calculated as follows:

$$f_{bm} = \frac{3}{2}\frac{F_{max,b}\, d_1}{t_s h_s^2} \quad 3\text{-}1$$

where $F_{max,b}$ is the maximum bending load, d_1 is the distance between the supports (100 mm ± 0.5 mm), h_s is the height of the mortar specimen (40 mm), and t_s is the thickness of the mortar specimen (40mm). The compressive strength of the mortar, f_m, was determined as follows:

$$f_m = \frac{F_{max,c}}{t_s l_p} \quad 3\text{-}2$$

where $F_{max,c}$ is the maximum compressive load, and l_p is the length of the loading plate (40 mm).

Remix BM2 M5 was used in the specimens of CB, while Remix Brickfix BFM was used in the CS specimens. The results of the flexural and compressive strength tests are reported in Table 3.2. For CS specimens, the flexural tests were performed on 24 specimens and compressive tests on 48 specimens. The compressive strength is equal to 5.65 MPa with a coefficient of variation of 0.15, whereas the flexural strength is determined as 2.43 MPa with a coefficient of variation of 0.13. For CB specimens, the flexural strength test was performed on 15 specimens and the compressive strength test on 30 specimens. The compressive strength is equal to 6.47 MPa with a coefficient of variation of 0.11. The flexural strength is equal to 2.29 MPa with a coefficient of variation of 0.24.

Table 3.2 Flexural and compressive strength of CS and CB.

Material property	Symbol	UM	CS		CB	
			Average	C.oV.	Average	C.oV.
Compressive strength of mortar	F_m	MPa	5.65	0.15	6.47	0.11
Flexural strength of mortar	F_{bm}	MPa	2.43	0.13	2.29	0.24

Figure 3.8 shows the statistical distribution of flexural and compressive strength of both types of mortar. The majority of the masonry buildings in the Netherlands were mainly of low-quality mortar [83], and as mentioned, two different mortar types were used [37,68].

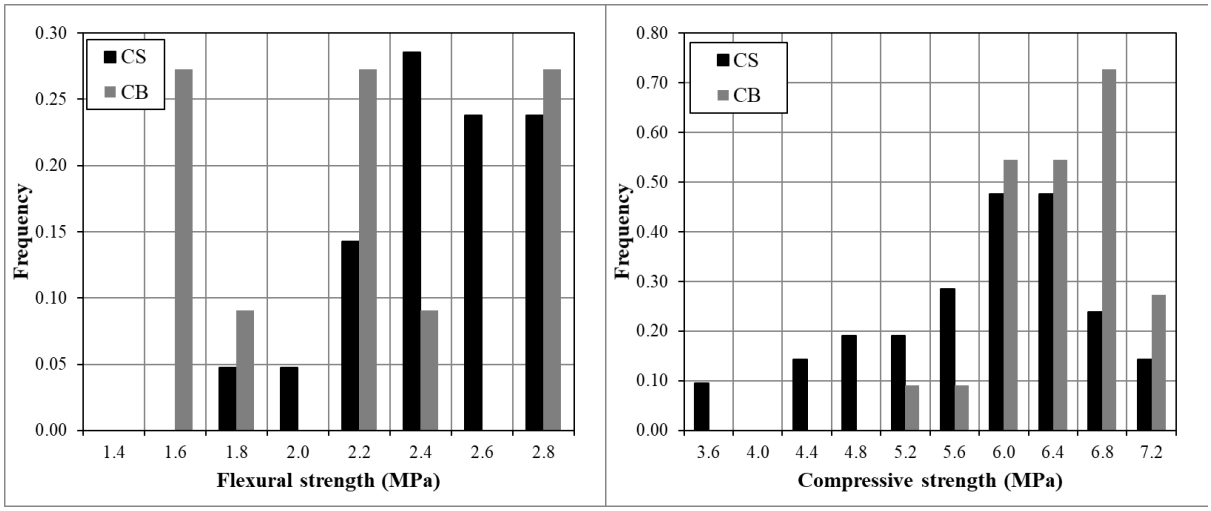

(a) (b)

Figure 3.8 Statistical distribution of flexural strength (a) and compressive strength (b) of the mortar adopted for CS and CB specimens.

3.3.2 Bond strength of masonry

The bond strength between the masonry unit and mortar was determined in agreement with the bond wrench test proposed by EN 1052-5 [84]. The computer-controlled test set-up was used. The specimen was rigidly held by a support frame that holds the specimen in accordance with EN 1052-5 [84]. A clamp, with a lever attached, was applied to the masonry unit. The lever was used to apply a bending moment to the brick-mortar interface. The load was applied by a jack operated automatically, and a load cell attached to the jack measured the applied force. The bond wrench strength, f_w, is calculated on the assumption that the stress distribution is linear over the width of the top masonry unit as follows:

$$f_w = \frac{F_1 e_1 + F_2 e_2 - \frac{2}{3} t_u \left(F_1 + F_2 + \frac{F_3}{4}\right)}{\frac{l_j w_j^2}{6}} \tag{3-3}$$

where F_1 is the failure load, measured and applied by the jack. F_2 is the normal force as a result of the weight of the bond wrench apparatus. F_3 is the weight of the masonry unit pulled off the specimen, including the weight of adherent mortar. Furthermore, e_1 is the distance from the applied load to the tension face of the specimen, e_2 is the distance from the centre of gravity of the clamp to the tension face of the specimen, l_j is the mean length of the bed joint, and w_j is the mean width of the bed joint. Figure 3.9 reports the classification of the type of failures.

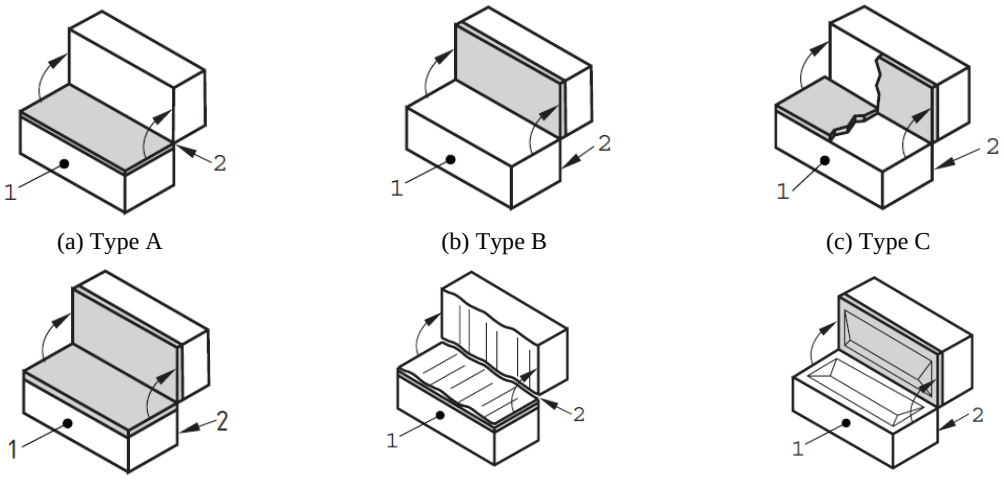

(a) Type A (b) Type B (c) Type C

(d) Type D (e) Type E (f) Type F

Figure 3.9 Classification of failure modes in agreement with EN-1052-5 [84] *(1 tension face, 2 compression face).*

In total, 27 CS and 17 CB couplets were tested for material characterisation. These tests were carried out on the couplets after the testing when the bond between the mortar and the brick was not damaged. The mean bond strength was equal to 0.34 MPa (St. Dev. of 0.09 MPa) and 0.52 MPa (St. Dev. of 0.14 MPa) for the CS and CB specimens, respectively. A stronger bond was obtained for the CB masonry than CS brick masonry, possibly due to the differences in the mortar used. The values of the bond strength and the corresponding bond failure types of the couplets are shown in Table 3.3.

Table 3.3 Bond strength for each group of tested couplets.

CS									CB					
No.	f_w (MPa)	Bond failure type	No.	f_w (MPa)	Bond failure type	No.	f_w (MPa)	Bond failure type	No.	f_w (MPa)	Bond failure type	No.	f_w (MPa)	Bond failure type
1	0.28	Type A	10	0.35	Type A	19	0.26	Type A	1	0.64	Type A	10	0.25	Type A
2	0.29	Type D	11	0.38	Type A	20	0.40	Type A	2	0.57	Type C	11	0.39	Type A
3	0.33	Type A	12	0.38	Type A	21	0.45	Type A	3	0.52	Type A	12	0.54	Type A
4	0.24	Type D	13	0.35	Type A	22	0.46	Type D	4	0.41	Type D	13	0.48	Type A
5	0.13	Type A	14	0.34	Type C	23	0.27	Type D	5	0.64	Type A	14	0.66	Type D
6	0.32	Type A	15	0.26	Type A	24	0.30	Type D	6	0.64	Type A	15	0.66	Type A
7	0.30	Type C	16	0.25	Type A	25	0.54	Type C	7	0.64	Type A	16	0.49	Type A
8	0.39	Type A	17	0.30	Type A	26	0.45	Type A	8	0.41	Type C	17	0.26	Type A
9	0.38	Type D	18	0.41	Type D	27	0.28	Type A	9	0.64	Type A	-	-	-
Avg.	0.34								0.52					
SD	0.09								0.14					
CoV	0.25								0.26					

3.3.3 Tensile and compressive strength of tie

In addition to the mortar tests, tie tests were performed as well. A stainless-steel bar was used with a diameter of 3.6 mm and 316 Grade. The tension properties of the tie were defined in terms of average values of elastic modulus, E_{3t}, yield strength, f_{yt}, yield strain, ε_{yt}, tensile strength, f_{tt}, strain at tensile strength, ε_{tt}, and elongation at rupture, ε_{rt}, according to ASTM E8/E8M-21 [85]. A summary of the connection mechanical properties resulting from material characterisation tests is reported in Table 3.4. Young's modulus was derived as the chord elastic modulus evaluated between 1/10 and 1/3 of the tensile strength. The yielding of the tie occurred at a stress level of approximately 1/3 of the tensile strength. For the sake of simplicity, it is defined as Young's modulus; in fact, it refers to the stiffness of the cavity wall tie, including the effect of the geometry of the tie. Hence, the geometry of the tie caused not only a lower yield strength but also the failure occurred in the zigzag end.

The behaviour of the connection under compressive loading was interpreted in terms of Euler's buckling. The compression properties of the tie were defined in terms of strength at Euler's critical load, f_{ct}, and strain at critical load, ε_{ct}, according to ASTM E9-19 [86]. Additionally, the column effective length factor, K, computed via the experimental results, is also reported.

Table 3.4 Summary of the outcomes of the material characterisation tests on cavity wall ties.

Loading Protocol	Material property	Symbol	UM	Tie	
				Average	CoV
Tensile loading	Elastic modulus of tie evaluated between 1/10 and 1/3 of the maximum tensile stress	E_{3t}	MPa	32920	0.03
	Tie yield strength	f_{yt}	MPa	135	0.01
	Tie yield strain	ε_{yt}	-	0.0045	0.04
	Tie tensile strength	f_{tt}	MPa	411	0.01
	Tie strain at tensile strength	ε_{tt}	-	0.13	0.08
	Tie elongation at rupture	ε_{rt}	-	0.14	0.07
Compressive loading	Tie strength at Euler's critical load	f_{ct}	MPa	198	0.05
	Tie strain at critical load	ε_{ct}	-	0.011	0.18
	The column effective length factor	K	-	0.45	-

3.4 Experimental results

This section presents the results obtained in terms of failure mode, average force-displacement curve, peak force, and displacement at the peak force and failure, identified as the point of

reduction by 20% of the peak force as conventionally assumed in several studies available in the literature (among other [87–89]). After reaching a 20% reduction of their peak force, the specimens continued to their collapse state to observe full capacity on the connections. The tensile and compressive force-displacement curves obtained for the monotonic protocols are shown together in the same diagram for the sake of simplicity. The envelope curve regarding the cyclic loading was derived according to the recommendations provided in ASTM E2126-19 [90]. Table 3.5 lists the mean peak force/displacement, along with the standard deviation and reduction by 20% of peak force. The force-deformation response of all the experiments conducted is accessible in open-source data storage [91]. It should be noted that all curves obtained during the experimental campaign are provided in Annex A.

Table 3.5 Mean results of the axial tests on cavity wall tie connections (standard deviations between brackets).

Specimen type	Loading protocol	Pre-C Level (MPa)	Axial strength		Displacement at peak		Displacement at failure	
			Tensile (kN)	Comp (kN)	Tensile (mm)	Comp (mm)	Tensile (mm)	Comp (mm)
CS-70	MT, MC	0.1	2.28 (0.22)	-1.72 (0.25)	11.27 (1.98)	-3.25 (0.50)	17.1 (1.86)	-3.75 (0.55)
		0.3	2.33 (0.23)	-1.84 (0.16)	10.38 (1.49)	-3.05 (0.56)	17.9 (4.08)	-3.64 (0.78)
		0	2.54 (0.08)	-1.83	9.72 (2.81)	-3.44	11.6 (4.64)	-2.03
		0.6	2.60 (0.23)	-1.65	12.33 (0.11)	-2.85	18.1 (1.25)	-1.30
	MT-HS, MC-HS	0.1	2.30 (0.12)	-1.83 (0.19)	9.48 (0.98)	-2.90 (0.72)	16.1 (0.84)	-3.55 (0.83)
	Cyclic	0.1	1.76 (0.15)	-1.66 (0.22)	6.70 (2.28)	-2.85 (0.83)	10.6 (2.36)	-3.70 (0.75)
		0.3	1.97 (0.43)	-1.78 (0.11)	7.03 (2.88)	-2.72 (0.58)	11.0 (3.33)	-3.36 (0.31)
CS-70-15D	MT, MC	0.1	2.51 (0.13)	-1.35 (0.06)	13.07 (1.20)	-4.48 (0.82)	19.23 (3.87)	-5.04 (0.76)
	Cyclic	0.1	2.07 (0.18)	-1.45 (0.10)	9.74 (0.10)	-3.82 (0.65)	14.5 (1.27)	-4.49 (0.31)
		0.3	2.07 (0.28)	-1.44 (0.11)	9.61 (0.35)	-4.12 (0.83)	14.8 (1.54)	-4.66 (0.55)
CS-50	MT, MC	0.1	1.87 (0.14)	-1.80 (0.23)	8.25 (0.60)	-2.52 (0.13)	14.4 (0.81)	-2.92 (0.04)
	Cyclic	0.1	1.63 (0.12)	-1.96 (0.22)	4.58 (0.80)	-3.38 (1.77)	10.6 (1.19)	-4.54 (2.37)
CB-50	MT, MC	0.1	3.59 (0.56)	-1.85 (0.18)	7.16 (3.15)	-2.12 (0.31)	8.60 (3.48)	-2.45 (0.36)
		0.3	3.65 (0.35)	-1.82 (0.15)	7.90 (1.64)	-2.15 (0.22)	10.3 (2.68)	-2.51 (0.31)
		0	3.09 (0.40)	-1.94	4.27 (1.84)	-2.22	5.10 (2.19)	-1.55
		0.6	3.99 (0.34)	-1.99	8.98 (2.12)	-1.92	9.34 (1.40)	-1.59
	MT-HS, MC-HS	0.1	3.24 (0.56)	-1.69 (0.40)	5.50 (2.59)	-2.15 (0.20)	7.12 (3.52)	-3.07 (0.21)
	Cyclic	0.1	3.37 (0.42)	-1.58 (0.07)	6.19 (2.24)	-0.44 (0.18)	9.24 (2.54)	-1.18 (0.14)
		0.3	3.79 (0.35)	-1.62 (0.06)	8.97 (1.14)	-0.35 (0.17)	11.6 (2.10)	-1.16 (0.15)
Mortar Cubes for CS	MT, MC	0	1.95 (0.10)	-1.90 (0.02)	11.64 (1.94)	-2.02 (0.18)	19.0 (1.30)	-2.72 (0.23)
	Cyclic	0	2.08 (0.23)	-1.78 (0.13)	1.83 (2.75)	-2.66 (0.60)	12.47 (5.23)	-3.57 (0.51)
Mortar Cubes for CB	MT, MC	0	1.54 (0.04)	-1.82 (0.06)	2.43 (0.59)	-3.10 (0.32)	5.38 (2.06)	-3.85 (0.33)
	Cyclic	0	1.49 (0.15)	-1.91 (0.07)	2.14 (0.43)	-3.62 (0.59)	3.98 (0.99)	-4.25 (0.42)

Note: Pre-C Level = Pre-compression Level; Comp = Compressive

3.4.1 Failure modes

During the experimental campaign, four different failure modes were observed: sliding failure, tie failure, buckling failure and expulsion failure, as similarly reported in the literature [76,92,93]. The obtained failure modes are illustrated in Figure 3.10.

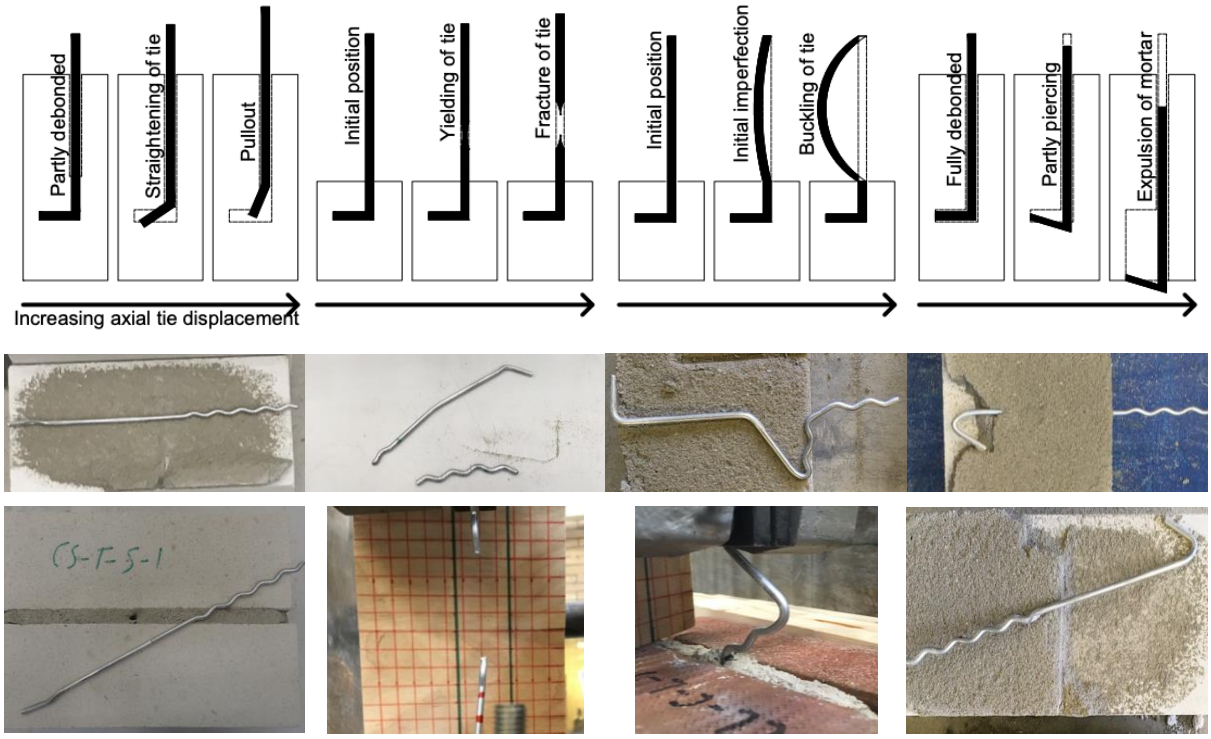

Figure 3.10 Failure mode sequence for cavity wall tie connections: Sliding failure (a), Tie failure (b), Buckling failure (c) and Expulsion failure (d).

When the specimens were subjected to monotonic tensile loading, the couplets exhibited either of the following two failure modes:

- Sliding failure (Type A): the tie slides along the tie-mortar interface (Figure 3.10a);
- Tie failure (Type B): the tie yielding is followed by a fracture of the tie (Figure 3.10b).

The sliding failure mode, which was governed by the straightening of the tie and crushing of the surrounding mortar, is the most common failure mode in tension, and only a few connections failed due to the tie failure. 92% of the specimens failed in the sliding failure (Type A). In the former case, failure occurs due to poor bonding between the tie and the mortar and due to the low strength of the mortar. Hence, as expected, the primary failure mode is sliding failure in tension. In the latter case, the mortar and the couplet remain intact; thus, neither cracks in the mortar joints nor detachment at the brick-mortar interface are observed.

Regarding the compressive loading, the couplets showed either of the two failure modes:

- Buckling failure (Type C): the failure is caused by the buckling of the tie (Figure 3.10c);
- Expulsion failure (Type D): the failure is achieved by piercing and expulsion of the cone of mortar around the tie (Figure 3.10d).

The large majority of the couplets loaded in compression were characterised exhibiting buckling failure. Only in 8% of the tested couplets was expulsion failure observed. Buckling of the tie is expected as a dominant failure mode in compression. Hence it can be concluded that the cavity wall tie connection behaviour is more dependent on the tie buckling capacity than on the bond strength capacity between tie and mortar.

It should be noted that the description of the evolution of the failure modes, as presented in Figure 3.10, was obtained by stopping a number of additional tests apart from the main specimens at different values of the imposed displacement and, when needed, the test was stopped for opening the specimens by performing bond wrench tests to observe the condition of the tie embedded in the mortar. The results of the additional tests were used to investigate the evolution of the failure mode and to define the flexural strength of the couplets via the bond wrench tests.

3.4.2 Load-Displacement curves

Based on the recorded test data, force-displacement curves were generated for each specimen. The relative displacement between the couplet and cavity wall tie is indicated on the horizontal axis of the load-displacement curves. It is important to note that the positive displacement and force in these graphs correspond to the tie pull-out (henceforth called tension) direction of loading. Hence, the direction of pushing the tie towards the couplet (henceforth called compression) indicates the negative displacement. In the following, the experimental findings of the groups of specimens tested are discussed, including CS-70, CS-70-15D, CS-50, CB-50, Mortar cubes for CS and Mortar cubes for CB.

CS-70 Specimens

Figure 3.11 shows the force-displacement curves for CS-70 couplets for monotonic loading. It should be noted that the whole curves are reported beyond the point of failure, which was identified as the point of reduction by 20% of the peak force. The figure also shows the average curve obtained by averaging the data from eleven specimens as an example.

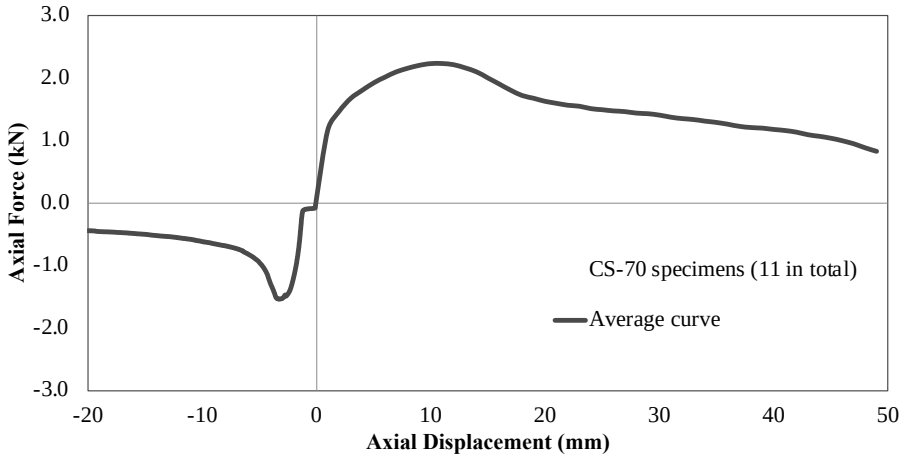

Figure 3.11 Experimental results of CS specimens with 70 mm anchored length for a pre-compression level of 0.1 MPa.

Regarding the monotonic loading for CS-70, the average curves of each testing group are presented in Figure 3.12. In CS-70 specimens, three different failure modes were observed: Type A (100%) for monotonic tensile loading and Type C (82%) or Type D (18%) for compressive loading. Regarding the monotonic tensile loading, the peak strength was reached when the hooked part of the tie started straightening, followed by the sliding between the mortar and the tie. An initial linear elastic behaviour of the connection up to about half of the peak load was followed by hardening up to the peak. The post-peak phase was characterised by gradual softening up to large displacements (50mm). Qualitatively similar behaviour was obtained irrespectively on the applied pre-compression level and loading rate.

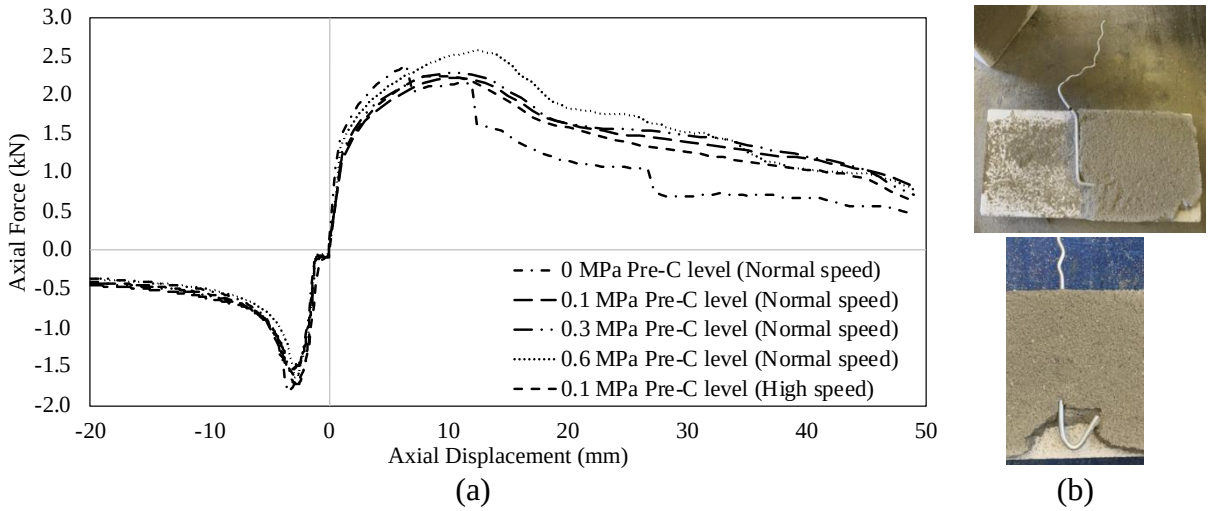

Figure 3.12 Average results for monotonic loading for CS specimens with 70 mm anchored length (a) and observed failure modes (b).

In compression, the linear-elastic behaviour of the connection was observed up to the peak load, which was achieved due to either buckling of the tie or expulsion of the cone of mortar.

A drastic reduction of resistance was observed in the post-peak phase. The behaviour of the specimens was consistent for every test regardless of the failure modes. As regards the cyclic tests on CS-70 specimens, an example full cyclic curve, which is characterised by the pinching effect as well as its envelope curve, is presented in Figure 3.13.

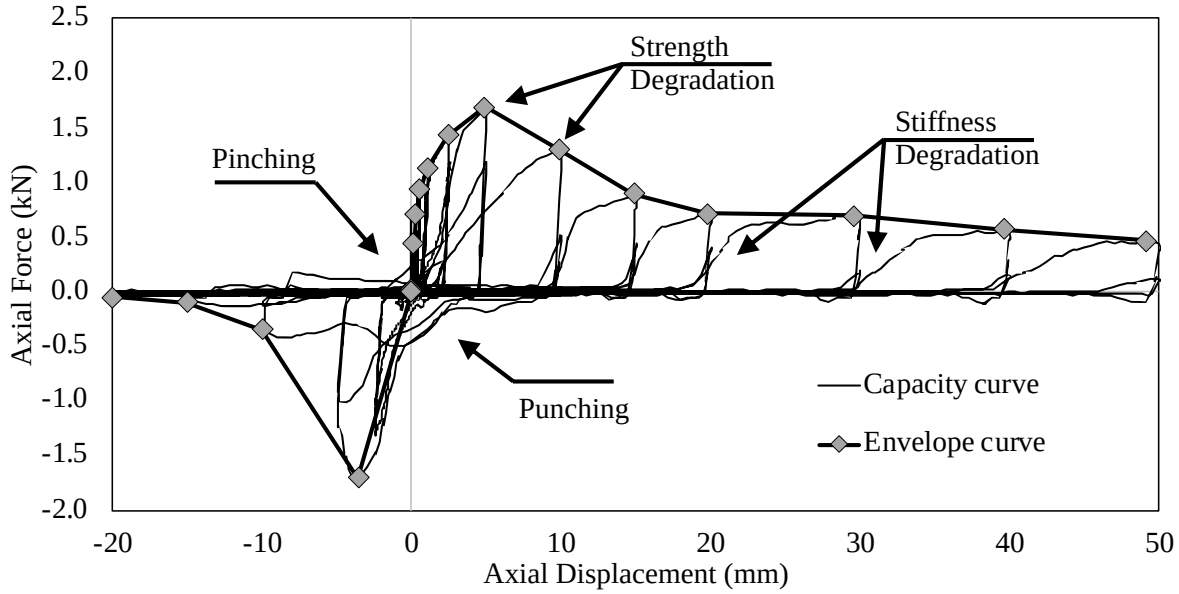

Figure 3.13 Force-displacement envelope curve for CS specimens with 70 mm anchored length.

The results of the cyclic tests are given in terms of envelope curves in Figure 3.14. As shown in Figure 3.14, a nonlinear force-deformation response was detected even in the initial loading stages. After the peak load was reached, a pronounced pinching effect was observed. This behaviour primarily occurred due to the loss of bond strength around the tie-mortar interface and the crushing of the mortar around the hook. The backbone curves were similar to those obtained for the monotonic tests, and the failure mode of the specimens was a combination of the mechanisms described for the monotonic tests. When the failure mode was a combination of Type A and Type C, at the end of the test, the tie failed with rupture due to deterioration of the mortar. The peak load in tension obtained for cyclic loading was lower than that obtained during the corresponding monotonic tests, and the post-peak behaviour was more brittle.

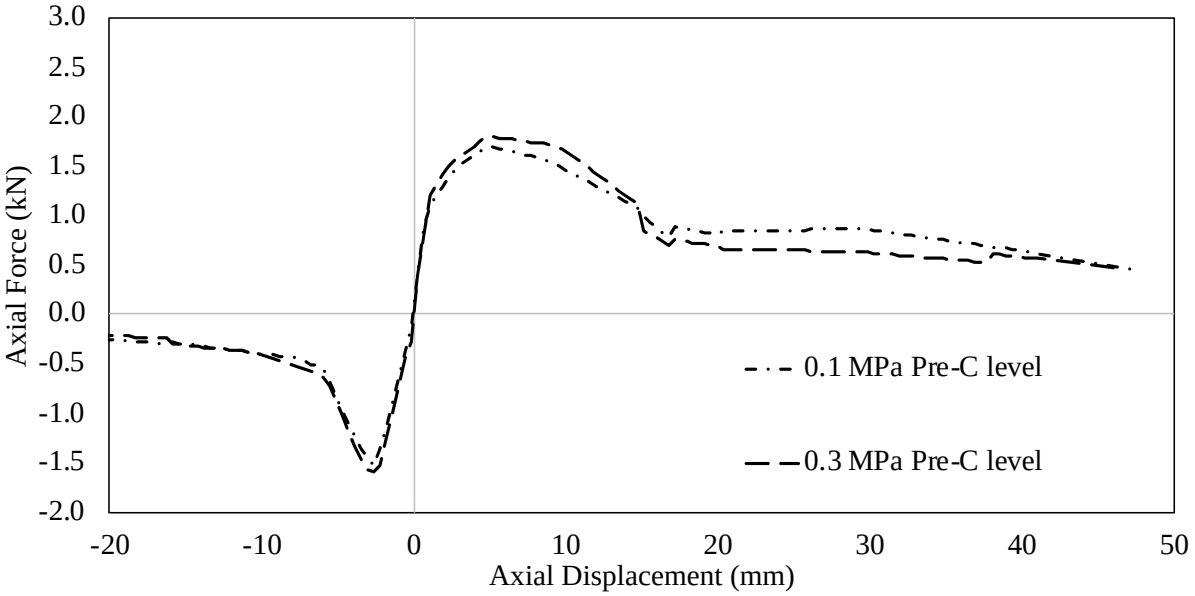

Figure 3.14 Summary of results for cyclic loading for CS specimens with 70 mm anchored length.

To have a detailed understanding of the obtained results, the average force-displacement curves defined for every testing variation of the CS specimen are shown in Figure 3.15. The test has been performed with different types of variations: two embedment lengths, four pre-compression levels, two different tie geometries, and five different testing protocols for CS specimens. It was observed that the levels of pre-compression had negligible influence on the behaviour of connections (Figure 3.15a). Similarly, the loading rate also had no influence on the behaviour (Figure 3.15b). On the contrary, the loading repetition led to a significant decrease in the strength of specimens, even though stiffness and ductility did not change (Figure 3.15c). When bent ties were considered (Figure 3.15d), an increase of capacity in tension was observed and vice versa in compression.

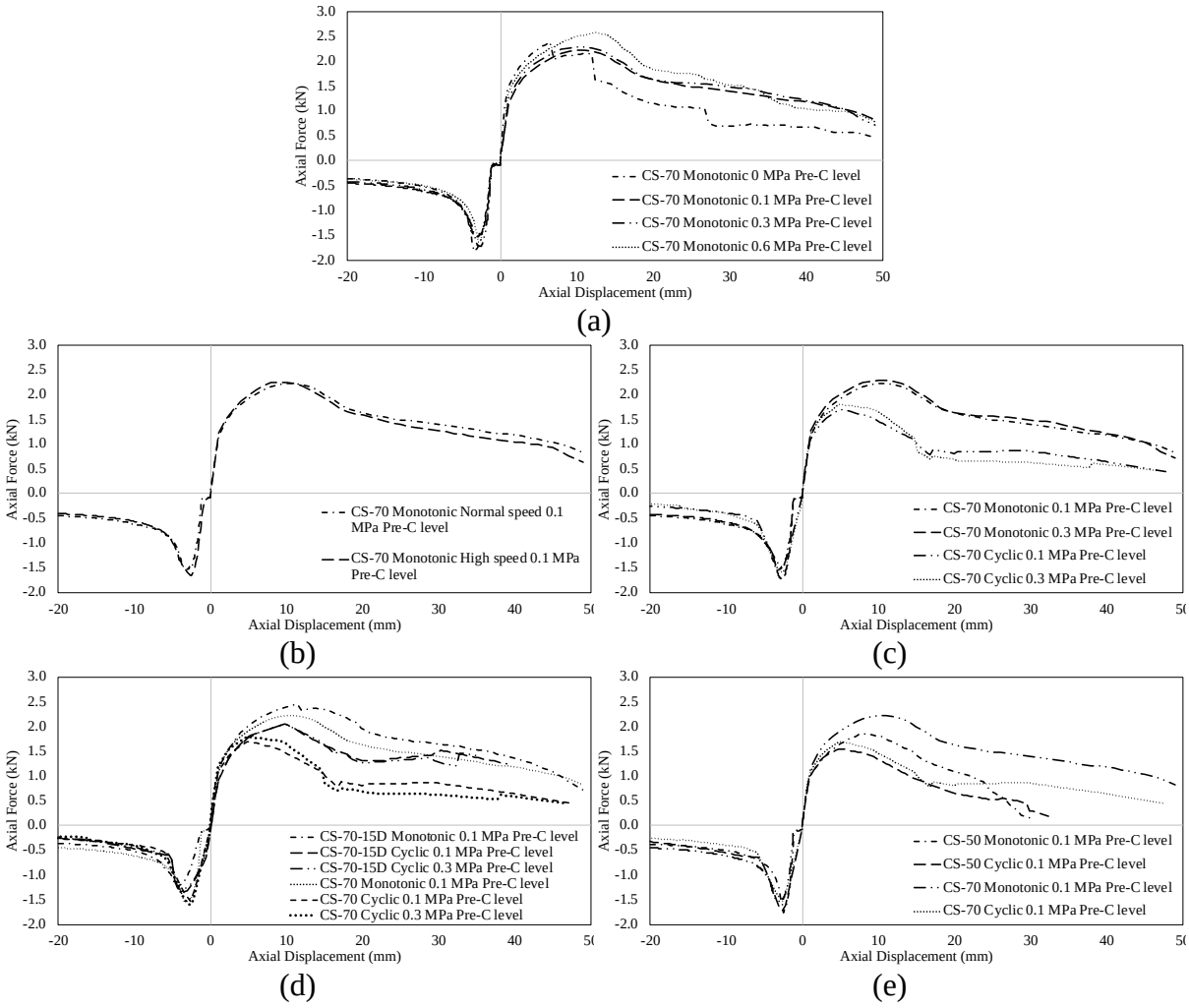

Figure 3.15 Force-displacement curve comparison of variations for CS specimens.

CS-70-15D Specimens

CS-70-15D specimens are characterised by the embedment of the hooked end of the tie in CS couplets with an embedment length of 70 mm and a 15-degree bent tie. Bent ties were studied to represent the real case installation situation from the field, as seen in common construction practice. Figure 3.16 illustrates the force-displacement curves obtained for monotonic loading by averaging the single force-displacement data at a pre-compression level of 0.1 MPa and the average envelope curves for cyclic loading for different lateral pre-compression levels. The observed failure modes were Type A (100%) and Type C (100%) for monotonic tensile and compressive loading, respectively, and a combination of these two mechanisms for the cyclic tests. The curves for monotonic and cyclic loading were very close to each other in the initial loading and diverged when the displacement increased; however, the curves for cyclic loading at pre-compression levels of 0.1 MPa and 0.3 MPa were very close to one another during all loading. In tension, the force-displacement curve is linear up to about

one-third of the peak load and then characterised by a hardening branch. In compression, nonlinear behaviour was observed even in the initial loading stage. The envelope curves for cyclic loading were characterised by smaller force values for tensile displacements, while the peak compressive force was slightly larger for cyclic tests.

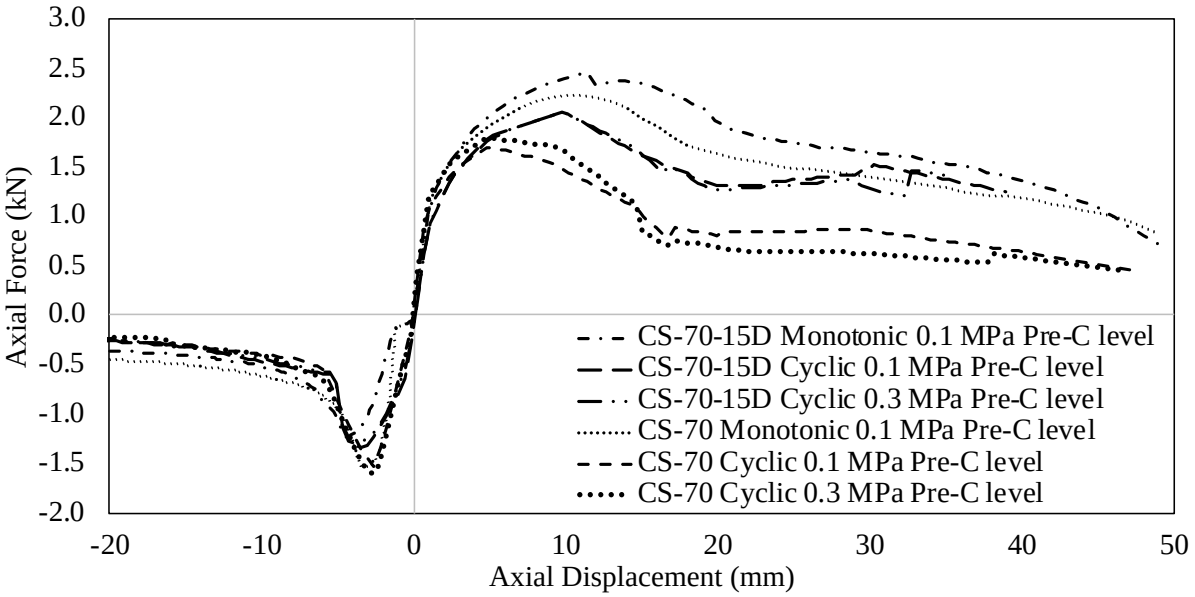

Figure 3.16 Summary of results for monotonic and cyclic loading for bent and non-bent tie for CS specimens with 70 mm anchored length.

CS-50 Specimens

CS-50 specimens are characterised by an embedment length of the hooked end of the tie in CS couplets equal to 50 mm. Figure 3.17 shows the average force-displacement curves obtained for monotonic loading, as well as the average envelope curves for cyclic loading, both monotonic and cyclic tests performed at a pre-compression level of 0.1 MPa. The failure behaviour of the corresponding specimens under tensile loading was defined by Type A, while under compressive loading, it was defined by Type C. The characteristic behaviour of the connection was similar with CS specimens with 70 mm anchored length: straightening of the tie under tension and buckling under compressive loading. The force-displacement curve in the tension stage was found to be linear up to about one-half of the peak load, after which the behaviour was detected as nonlinear, while regarding the compressive stage, it was found that a straight portion of the force-displacement curve was up to the peak load. The failure mode of the specimens regarding the cyclic tests was a combination of the mechanisms described for the monotonic tests.

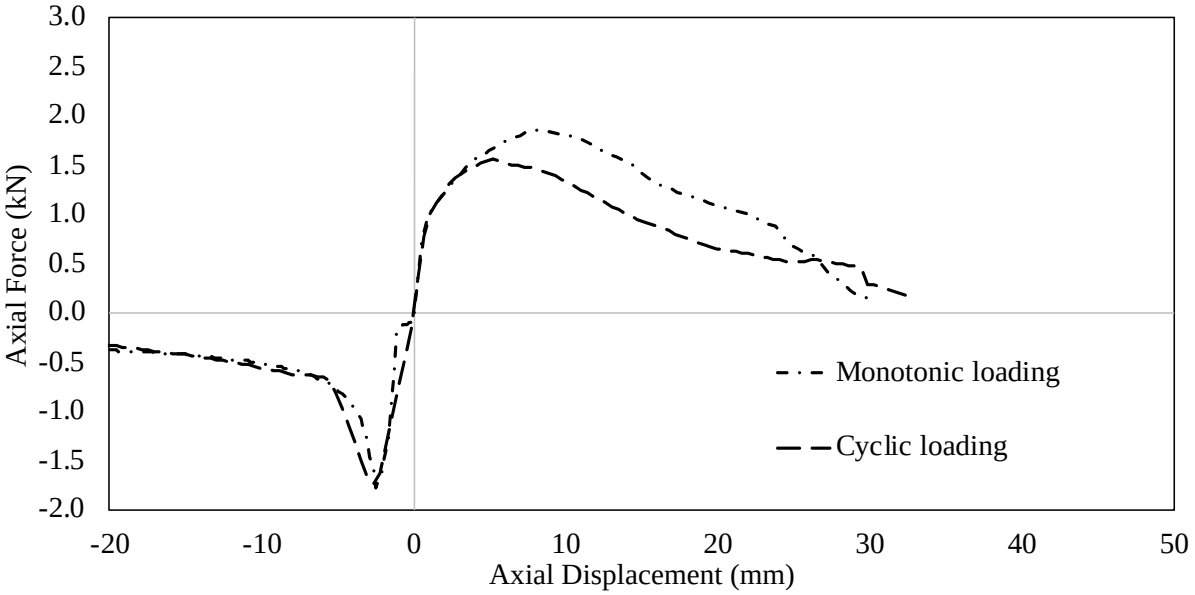

Figure 3.17 Summary of results for monotonic and cyclic loading for CS specimens with 50 mm anchored length.

CB-50 Specimens

CB-50 specimens are characterised by the embedment of the zigzag end of the tie in CB couplets with an embedment length of 50 mm. The following variations were performed for CB-50 specimens for the monotonic tests: four different pre-compression levels and two different rates of load application. Figure 3.18 shows the force-displacement average curves obtained for each corresponding variation.

Two types of failure modes were observed regarding the monotonic tensile loading: Type A and Type B; while for the monotonic compressive loading, the failure mode was Type C. Regarding the monotonic tensile loading, the peak of resistance of the specimens was achieved either when the tie reached the ultimate capacity of the tensile strength of 4.1 kN or when the mortar crushing in the bed joint started around the tie. The position of fracture was observed next to the embedment of the tie due to the geometry of the tie, and at the end of the test, the tie failed with a brittle rupture. The force-displacement curve started with a linear part up to about one-half of the peak load. After that point, hardening took place up to the peak load. Both failure modes showed a rather brittle post-peak behaviour.

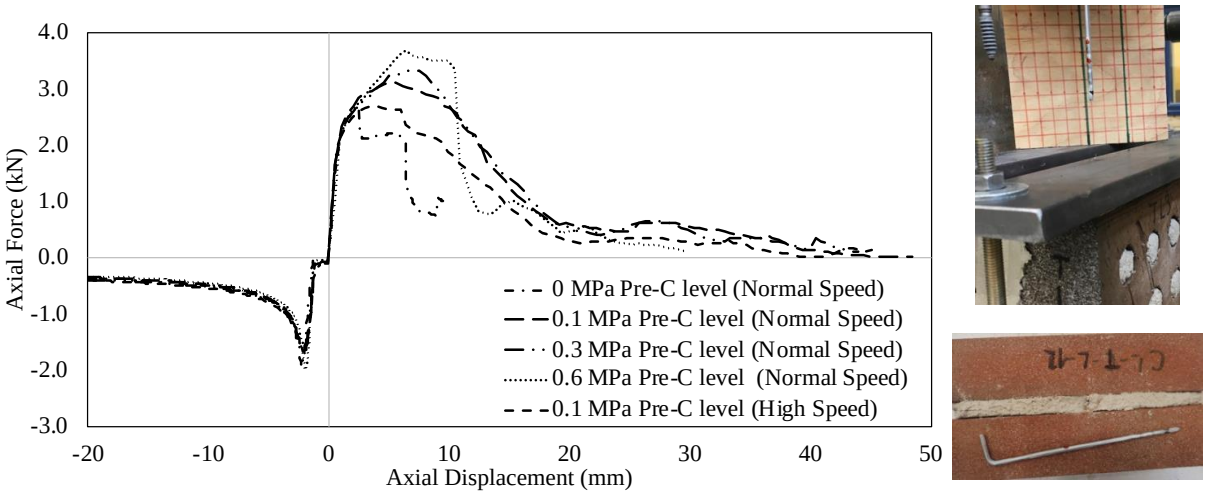

(a) (b)

Figure 3.18 Summary of results for monotonic loading for CB specimens (a) and observed failure modes (b).

For the monotonic compressive loading, the peak of resistance of the specimens, independently of the applied pre-compression level and speed rate, was achieved when the tie buckled. Compressive behaviour started with a linear portion up until the compressive strength was reached. A hyperbolic reduction of resistance was detected in the post-peak phase. The behaviour of the specimens was consistent for every test.

Figure 3.19 shows the average envelope curves of the CB-50 specimens for the cyclic loading. For these specimens, only two pre-compression levels (0.1 MPa and 0.3 MPa) were investigated. The behaviour and the failure mode of the specimens under cyclic loading was a combination of those observed for the monotonic tensile and compressive loading. Additionally, it was observed that the cyclic behaviour was nonlinear and asymmetry since the early loading stage, and after the peak load was reached, the force-displacement curves were characterised by the pinching effect for increasing displacements.

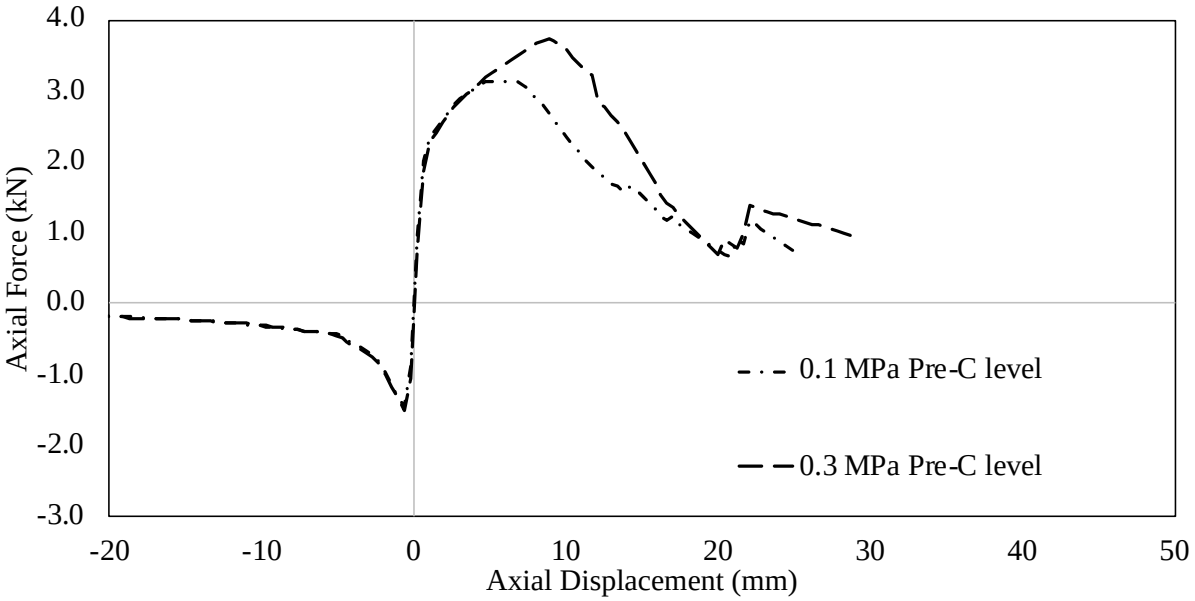

Figure 3.19 Summary of results for cyclic loading for CB specimens in terms of envelope curve.

To have a detailed understanding of the obtained results, the average force-displacement curves defined for every testing variation of the CB specimen are shown in Figure 3.20. The CB specimens were tested under different conditions: four different pre-compression levels and five different testing protocols. For CB specimens, it can be observed that the peak strength increases with the lateral pre-compression (Figure 3.20a), highlighting the presence of a dowel effect on the specimen behaviour. On the other hand, neither the loading repetition (Figure 3.20b) nor the loading rate (Figure 3.20c) significantly affects the results.

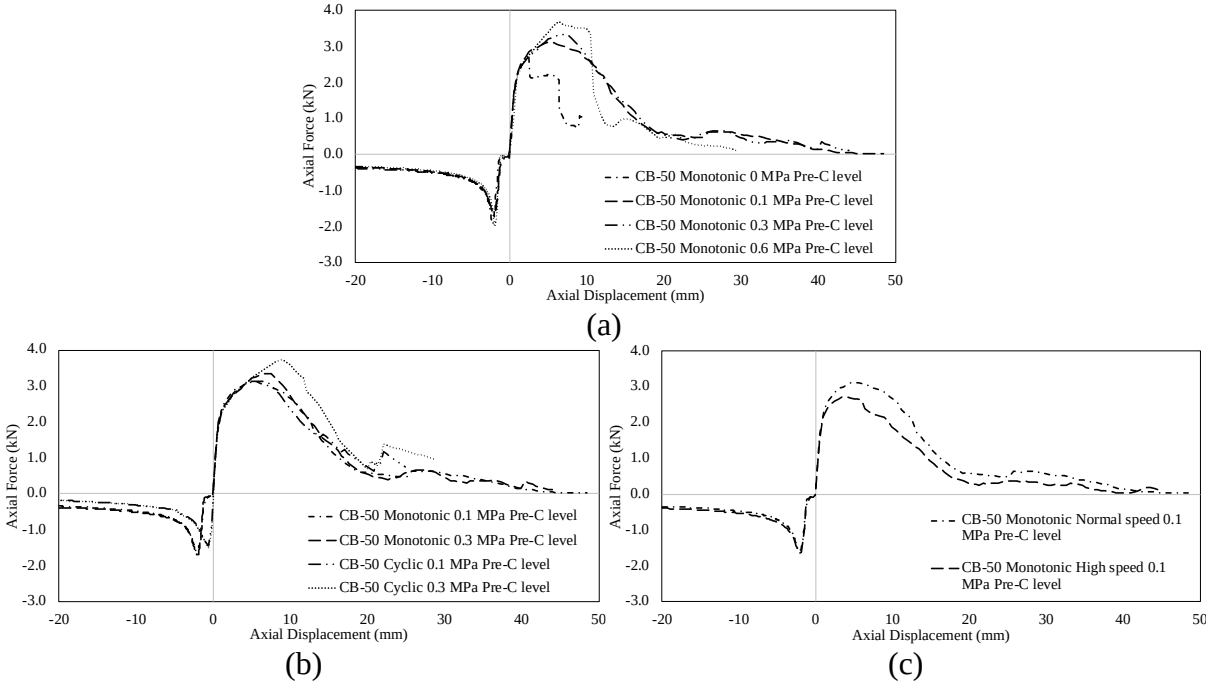

Figure 3.20 Force-displacement curve comparison of variations for CB specimens.

Mortar cubes for CS and CB

The ties embedded inside CS and CB mortar cubes were tested under monotonic and cyclic loading in order to decouple the mortar-tie interaction from other possible influencing parameters. Figure 3.21 shows the average force-displacement curves for both monotonic and cyclic loading (in the latter case, the envelope curves) of ties embedded in CS and CB mortar cubes. When the cubes were subjected to monotonic tensile loading, the failure mode was the same observed for the ties embedded in couplets: crushing of the mortar and straightening of the tie (Type A). A first peak was achieved during the loading history when the bond strength capacity was reached between the tie and mortar. The peak of resistance of the specimens was then attained after straightening the tie. After the peak, the observed reduction of capacity was rather ductile for the CS mortar cubes and more brittle for the CB mortar cubes. In compression, only buckling of the tie (Type C failure) was observed for both CS and CB mortar cubes. Qualitatively similar behaviour was obtained for each specimen, with a hyperbolic reduction of the resistance in the post-peak phase. The observed failure mode of cubes for the cyclic loading was a combined failure mode of monotonic loading.

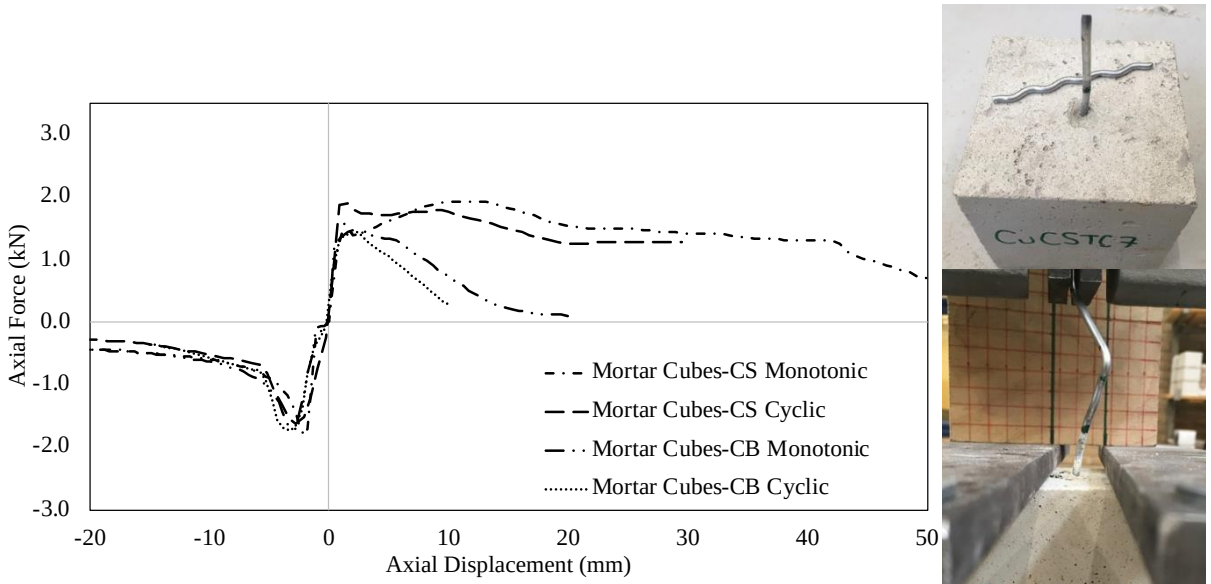

(a) (b)

Figure 3.21 Summary of results for CS and CB mortar cubes (a) and observed failure mode (b).

Regarding the tests of specimens with mortar cubes, the behaviour of the ties embedded in CS mortar is similar to that observed when the ties are embedded in the couplets (Figure 3.22a), while the force capacity of the ties with CB mortar is halved when they are embedded in the

mortar cubes (Figure 3.22b) due to absence of dowel effect. Note that the numerous small hollows present in the perforated CB specimens provide extra resistance due to a dowel effect.

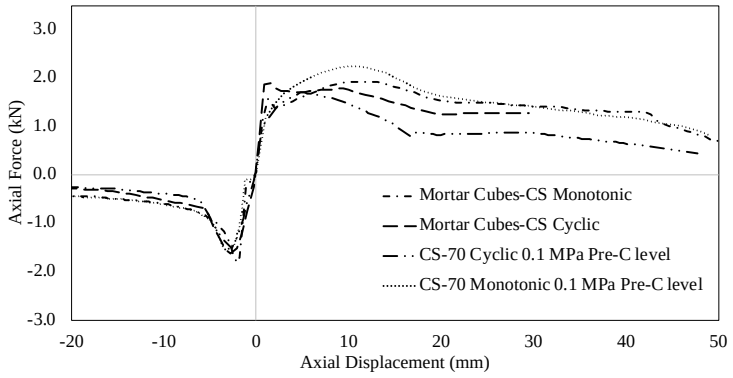

(a)

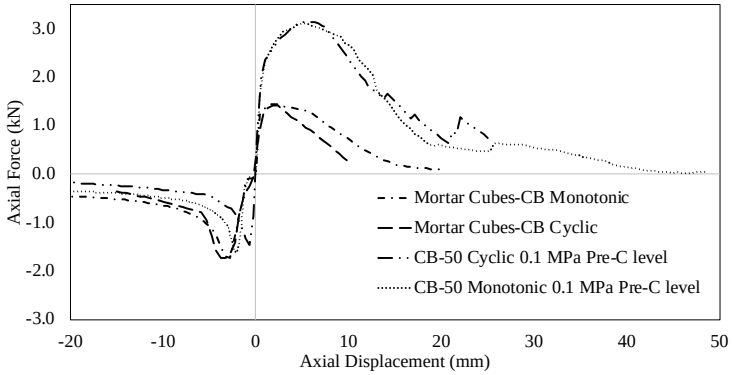

(b)

Figure 3.22 Force-displacement curve comparison of variations for CS (a) and CB (b) mortar cubes.

Comparing the results obtained during a previous campaign also performed at the laboratory of TU Delft [39] and those presented in this chapter, the significantly higher resistance observed in the current campaign is probably caused by an improved quality of the specimens and better workmanship. Namely, thanks to higher precision and consistency during the construction phase, the specimens have developed higher mechanical properties. Considering the current campaign, very consistent results were obtained, while during previous experimental campaigns, the bond between the tie and the mortar of a number of specimens failed in a very early loading stage due to poor mechanical properties.

3.5 Conclusions

This chapter aims to assess the seismic response of the wall metal tie connections in typical Dutch masonry double-leaf cavity walls, which are composed of an inner load-bearing leaf made of calcium silicate brick masonry and an outer leaf made of clay brick masonry. The tie

was pulled from either a calcium silicate (CS) couplet or a clay brick (CB) couplet. This section discusses and compares the experimental results obtained under monotonic tensile and compressive loading, as well as cyclic loading, and for different connection geometry and loading protocols.

The following results are reported:

- Comparing the experimental results of the monotonic and cyclic tests in terms of the peak load, on average, a 19% larger peak load is observed for monotonic tests for the CS specimens, and a similar increase in peak load is also observed for the CB specimens.
- Larger values of the bond strength are obtained for the CB couplets thanks to the dowel action of the mortar in the brick holes. For the same reason, a significant reduction of pull-out strength is obtained when the ties are embedded in the mortar cubes compared to the couplets.
- Overall, it can be concluded that the behaviour of the studied wall-tie connection is mainly governed by the behaviour of tie embedment in the CS leaf.

The studies carried out in this experimental campaign may improve the knowledge of the connection between the leaves in cavity walls, which can be helpful in identifying and validating suitable assessment methods and retrofit interventions. The findings of this study can help improve the testing, standardisation and, eventually, design of wall-to-wall metal ties, which the construction industry benefits from in the long run. As a finding of such, it can be suggested that the bonding between the tie and the mortar and the tie stiffness can be improved for the companies for new products.

Chapter 4: Experimental characterisation of timber joist-cavity wall connections

The unreinforced masonry (URM) building stock in Groningen is characterised by flexible diaphragms, cavity walls, single- or double-wythe walls and lack of effective wall-to-diaphragm connections, as identified in Chapter 2. As clearly stated in the literature [26,94], the out-of-plane (OOP) failure mechanism is related to insufficient or absent wall-to-floor connections. Since little research on timber joist-cavity wall connections for typical URM Dutch houses can be found in the literature, an experimental campaign was conducted in the laboratory of the Hanze University of Applied Sciences. The campaign aimed to provide a complete structural characterisation of connections of timber joists to URM cavity walls in as-built and strengthened conditions under cyclic axial loading. A total of twenty-two cyclic tests on timber joists connected to URM wallets, both in as-built and strengthened conditions, were performed with the following configurations: two different cavity wall tie distributions, two pre-compression levels, two different as-built connections, and two different strengthening solutions.

Section 4.1 describes a review of past experimental research to identify the knowledge gap. Section 4.2 describes sample geometry, test setup, and adopted testing protocol. Section 4.3 presents the tests carried out at the material level to characterise the used materials. Sections 4.4, 4.5 and 4.6 present and discuss the test results for unstrengthened connections, connections with strengthened timber joists, and connections with strengthened cavity walls and timber joists, respectively. Special attention is devoted to the failure modes and the hysteretic behaviour for each group of tests performed.

4.1 Review of Past Experimental Research

A review of as-built and strengthened connections on URM structures is presented in this section. Wall-to-floor connections are important players in ensuring the global stability of URM structures against seismic and other dynamic actions. If these connections are inadequate or absent, an earthquake-resistant box-type behaviour cannot be guaranteed, and local mechanisms such as bending, sliding, and out-of-plane failure of URM walls can be observed.

It is important to underline that the prevailing weak links for typical URM buildings are as follows: (i) connections between floors and masonry walls and (ii) the OOP bending behaviour of masonry walls [95]. These two links can be associated in such a way that collapse in the OOP direction can be due to the activation of the local mechanism, i.e., the failure of the connection may trigger a progressive collapse with the consequent cantilever behaviour of the walls. If the connection is inadequate, the wall can generate a cantilever-type behaviour, and the overturning mechanism can be activated easily. On the other side, even when the connection is proper, the wall can fail under rocking behaviour. Therefore, understanding the behaviour of connections is of prime importance to understanding and preventing damage to URM structures.

Traditional wall-to-floor connections in URM structures can be categorised as friction-based (hereinafter referred to as *mortar pocket connections*) and anchor-based, such as iron straps, metal tie-bars or hooked anchors. The masonry pocket connection can be characterised as the simplest and oldest construction practice in which the joist is inserted over the width of a masonry wall or half the width of a masonry wall for thin or thick walls, respectively. The latter, anchor-based connections, are a relatively modern solution in which the timber joist is connected to the masonry using iron straps. The experimental findings of these two types of joist-masonry connections are reviewed hereinafter based on tests on full-scale buildings and the connection only.

As stated in the literature, the out-of-plane behaviour is a common failure mode of unreinforced masonry structures during a seismic excitation, governed mainly by the absence of adequate connections between the structural elements such as wall-to-wall, wall-to-floor or wall-to-roof. In case of poor wall-to-floor connection, frictional resistance may play an important role in seismic assessment of out-of-plane mechanisms. Bothara et al. [96] conducted an experimental campaign on a half-scale two-storey URM building constructed using a conventional timber floor and roof and single wythe clay brick masonry, in which timber joists were connected to wooden wall plates laid on the longitudinal walls. Since the seismic performance of the URM building as a whole without focusing solely on connection, was aimed, it was only reported that limited relative displacement between the floor and the wall was observed due to the high frictional strength.

In order to understand the dynamic behaviour of historic stone masonry with timber floor and roof and evaluate possible strengthening solutions, an experimental campaign on three full-scale two-storey buildings was carried out at the EUCENTRE laboratory in Pavia [97]. The

structures consisted of timber floors and roofs. The first structure was representative of a vulnerable building lacking anchors between walls and floor [98], and with the timber joists simply placed on half the width of the external walls. The specimen showed a local out-of-plane failure due to the poor connections. In Building 2, the floor diaphragm-to-wall connections were improved by the inclusions of anchors, which allowed to prevent premature OOP failures. As a consequence, the building exhibited a global response, and presented higher lateral strength and stiffness.

An experimental investigation was performed on a full-scale two-story URM building subjected to a quasi-static test by Yi [99]. Metal ties were used to connect the timber floor to the masonry wall at every three joists (Figure 4.1a). The rest of the joists were simply supported at their ends (Figure 4.1b). At the conclusion of the cyclic test, a large amount of sliding was observed between the joist and masonry wall in the case of the masonry pocket connections. On the other hand, the joists connected with ties to the wall underwent smaller sliding. It was also reported that the ties were able to provide sufficient connection to redistribute the seismic demand from the OOP-loaded walls to the diaphragm.

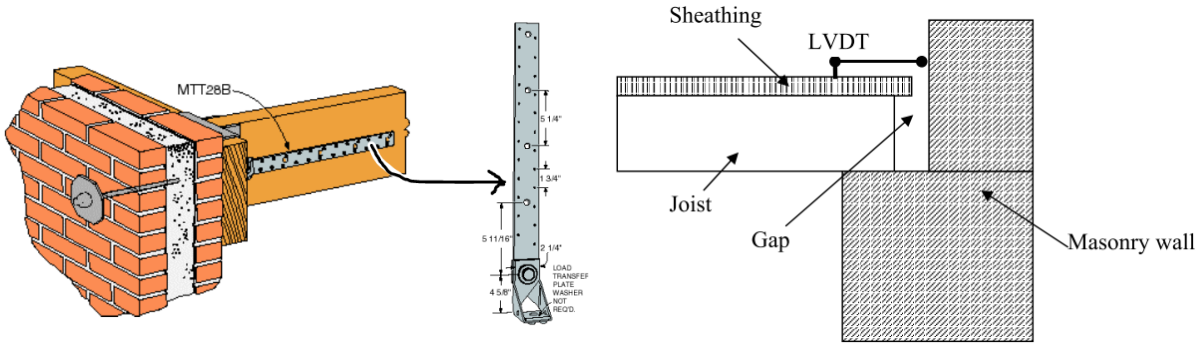

(a) (b)

Figure 4.1 Joist masonry wall connections details, from Yi [99]*: metal tie connections (a) and masonry pocket connections (b).*

With the aim of characterising the seismic behaviour of typical Dutch houses, an extensive multiscale testing program was performed at EUCENTRE laboratories [72]. Specifically, this campaign aimed at investigating the seismic behaviour of structural components, assemblies, and complete buildings. Among others, full-scale shaking table tests of a cavity wall terraced house [100] and a double-wythe clay-brick detached house [11] with flexible timber diaphragms were conducted. Two different connections, mortar pocket connections and connections with hook anchors, were used between timber joists and masonry walls for both the terraced and detached houses to represent the actual as-built condition. The hook anchors

were placed on the pocket of the inner leaf for the cavity wall terraced house, while they were inserted into the masonry between the two wythes for the detached house (Figure 4.2). It was reported that no sliding or significant differential displacements between joists and masonry was recorded, although the connections were damaged. For this reason, the connections were in general assessed to perform adequately. However, since the research focused on the global dynamic behaviour of the buildings, the performance of the single connections was not further investigated.

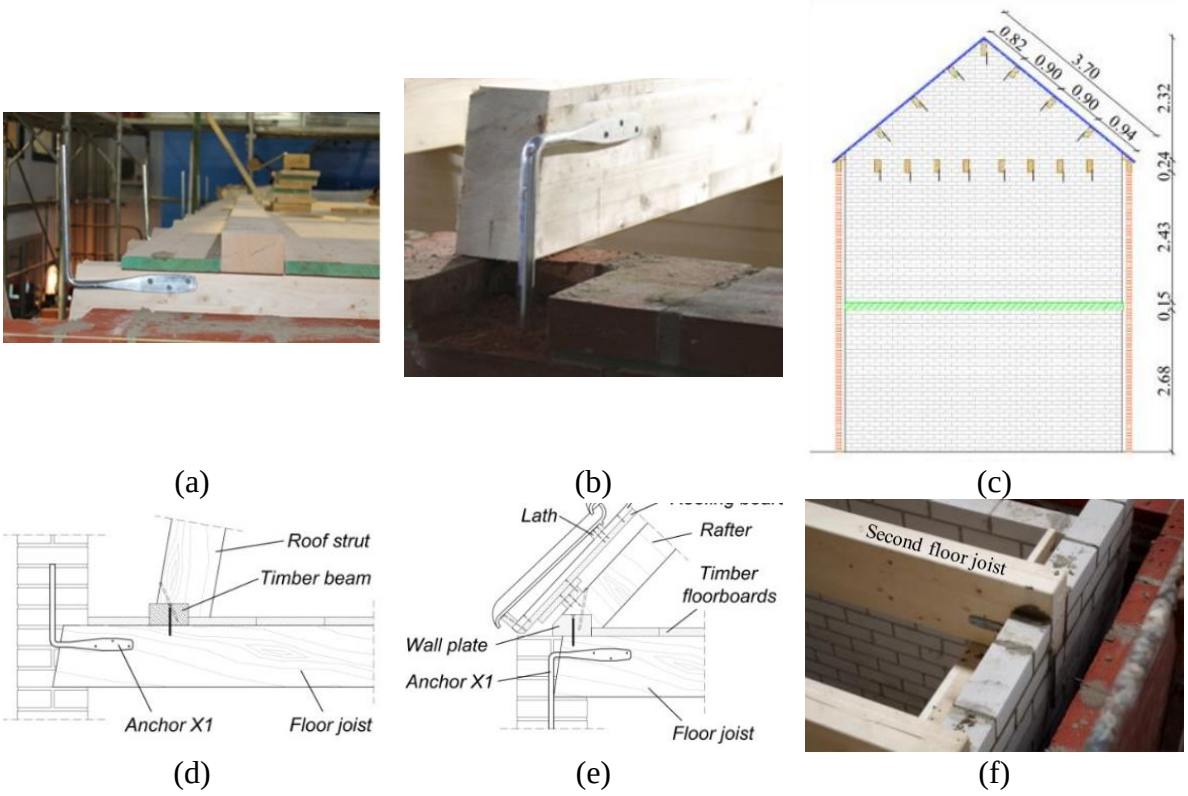

Figure 4.2 Wall-to-floor connections: hook anchor embedded in the double-wythe clay wall (a,b,d and e) [11]*, and detail of the anchor placed on the inner leaf of a cavity wall (c and f)* [100].

With regard to tests conducted at component level, and specifically on mortar pocket connections, Almeida et al. [101] performed an experimental study to characterise the frictional resisting mechanism between a timber floor and masonry. In this experimental program, triplet tests were conducted to investigate the cyclic friction of timber-timber and mortar-timber connections. The wall-to-floor connection was designed to be representative of unstrengthened conditions, in which the timber joist is supported by a masonry wall. Two different mortar types were considered: antique mortar and modern mortar. The antique mortar represented a weak-quality mortar used in historic buildings consisting of hydraulic lime and sand, while the

modern one is a high-quality mortar without aggregates. They found that the surface roughness of the timber can be a governing factor in increasing friction resistance, while the loading rate had no influence on the friction behaviour. The authors also mentioned that the specimens with antique mortar did not exhibit a frictional type of behaviour and were hence excluded from the experiment, since the mortar was grinding, breaking up and degrading into powder.

Lin and Lafave [94] conducted a testing campaign on two different types of typical wall-to-floor connections, with and without nailed strap anchors. The specimens were subjected to three different loading methods, namely: static monotonic, static cyclic loading and dynamic cyclic loading. The specimens represented a common typology for joist-wall connections in URM buildings. The as-built mortar pocket connections provided a lower strength capacity compared to the specimens with nailed strap anchors. An average friction coefficient of 0.5 was defined for the former specimens, in good agreement with the values found in previous literature, e.g. those given in the American Civil Engineer's Handbook [102].

Ravenshorst and Mirra [103] conducted an experimental investigation on different timber joist-masonry wall connections in single-wythe calcium silicate masonry walls and double-wythe clay brick masonry walls based on construction practices from the Netherlands, particularly Groningen. The specimens aimed to simulate the connections at the roof level in which the specimens did not have an overburden load at the top. The study aimed at evaluating the response of wallets under quasi-static and dynamic loading in terms of stiffness, strength and failure modes. A total of seven configurations were studied, of which two configurations represented as-built timber-masonry connections, namely mortar pocket and hook anchor, while the remaining five configurations were strengthened as follows to understand the influence of the strengthening strategy:

(i) Steel angle anchored to the masonry and screwed to the joist,
(ii) Additional steel bracket placed below the current joist,
(iii) Hook anchor glued to the wall,
(iv) Screws through timber and masonry with an angle of 45 degrees,
(v) Timber blocks with mechanical anchors between the joist and wall.

It was reported that the as-built specimens with mortar pockets exhibited purely frictional behaviour; on the other hand, the as-built specimens with hook anchors exhibited frictional behaviour when pushing the joist towards the wall, while a resisting process was involved due to the hook anchor when the joist was pulled from the wall. The main outcomes from the experimental campaign can be summarised as follows:

(i) The specimens strengthened with steel angles anchored to the masonry showed increased strength, stiffness, and ductility. The failure mode was the yielding of the screws.

(ii) The specimens strengthened with the additional steel bracket exhibited better strength and stiffness than the as-built specimens with hook anchors. The failure mode was yielding and bending of screws and steel brackets.

(iii) The specimens strengthened with the glue exhibited brittle behaviour, and the failure mode was a detachment of the glued surface.

(iv) The specimens strengthened with the screws showed brittle behaviour too. The failure mode was characterised by a large and distributed crack pattern in the masonry.

(v) The specimens strengthened with the timber blocks exhibited highly dissipative behaviour as well as high strength. The failure mode was yielding and bending of screws and nails.

Previous studies have provided insight into the seismic behaviour of wall-to-diaphragm connections, and most importantly, the finding of these have shown that connections between masonry wall and diaphragm are critical to ensure "box-type" behaviour. However, the experimental campaign at EUCENTRE [72] considers only timber joist-cavity wall connections on full-scale buildings, while Ravenshorst and Mirra [103] focus on as-built timber-masonry connections in a single-leaf wall. Hence, there is a lack of experimental results that consider cavity walls with timber joists in as-built and strengthened conditions representing timber joist-masonry cavity wall connections in typical Dutch masonry structures. In order to fill the gaps in the knowledge, an experimental campaign has been carried out at Hanze University of Applied Sciences to provide a complete characterisation of the axial behaviour of timber-joist connections in cavity walls, as reported below.

4.2 Experimental testing programme

The experiments presented in this paper aim at providing a comprehensive characterisation of the cyclic axial behaviour of timber joist-cavity wall connections in as-built conditions and to assess the performance of possible strengthening solutions. As discussed in Chapter 2, terraced houses with cavity walls and flexible diaphragms are found as 23.8% of the inventory in the study of Arup. Additionally, it is expected to have an even higher ratio since terraced houses

with cavity walls and rigid diaphragms may also have timber attic floors. Therefore, two vulnerable elements of the Dutch construction practice, cavity wall and flexible timber diaphragm, are studied together in order to provide a complete characterisation of the cyclic axial behaviour of timber joist-masonry connections and effective strengthening solutions.

The timber floor or roof is one of the most common horizontal diaphragms in URM buildings [104]. The common way to connect timber floor joists to masonry walls is by inserting the joists in pockets in the masonry, which is based on a friction mechanism. Besides, in some countries, such as the Netherlands, hook anchors are used between timber joists and masonry walls in as-built condition (Figure 4.3).

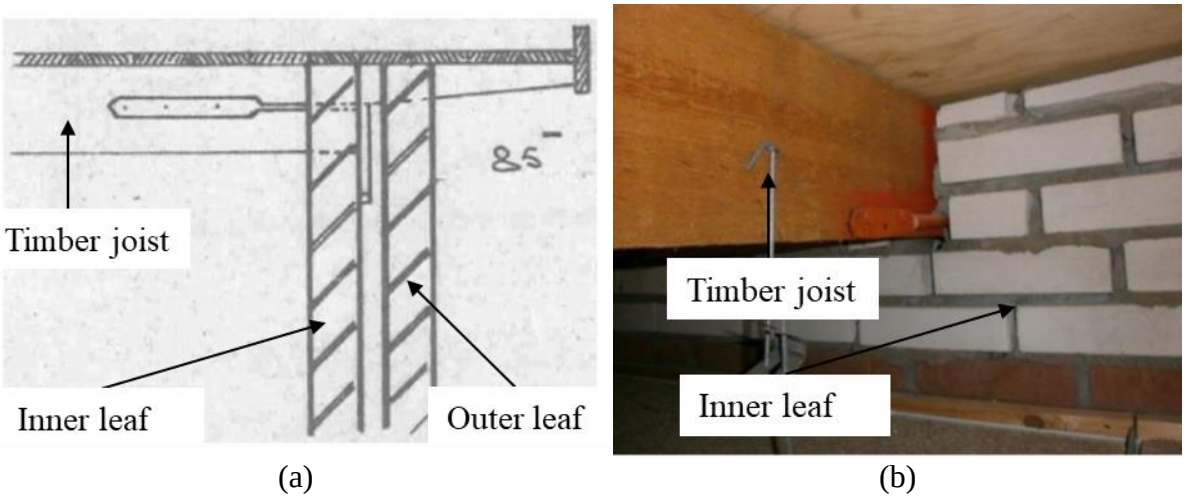

(a) (b)

Figure 4.3 Connection example in a typical Dutch house: Elevation view of a cavity wall with a timber joist (a) and timber joist seated in a pocket located in the inner leaf of a cavity wall (b) [69].

4.2.1 Overview of Test Specimens

This study aims to characterise the cyclic axial behaviour of timber joist-masonry connections, reproducing cavity walls with timber joists in as-built and strengthened conditions. Placing a timber joist in a pocket in the inner leaf of a cavity wall is a common construction technique observed in the traditional Dutch construction practice and in other parts of the world. All wallets tested in this study were constructed on a steel beam by an experienced mason to ensure the best possible quality control. The specimens were built at the BuildinG laboratory. Each specimen consisted of a cavity wall with metal ties and a timber joist laid in a pocket in the inner leaf of the wall. The specimens were left to cure for at least 28 days prior to testing (as-built conditions) or strengthening (strengthened conditions).

The cavity wall was composed of an inner load-bearing leaf made of calcium silicate brick masonry (CS) and an outer non-load-bearing leaf made of clay brick masonry (CB) with an 80mm cavity (Figure 4.4). The inner leaf was nominally 1030 mm high, 930 mm wide, and 102 mm thick, while the outer leaf was approximately 950 mm high, 930 mm wide and 100 mm thick in order to provide the simplest, nevertheless realistic simulation of a cavity wall. The timber joist, with a size of 55 x 155 mm and a total length of 1600 mm long, was inserted on a 10-mm-thick mortar bed joint below and above the timber sections into the CS leaf. Embedding the timber joist in the mortar bed joint is a common practice not only in the Netherlands [100,105] but also elsewhere in the world [106]. The geometrical dimensions of the joist were adopted based on the study conducted in Chapter 2, achieving a realistic representation of boundary conditions and inertial mass.

(a) (b)

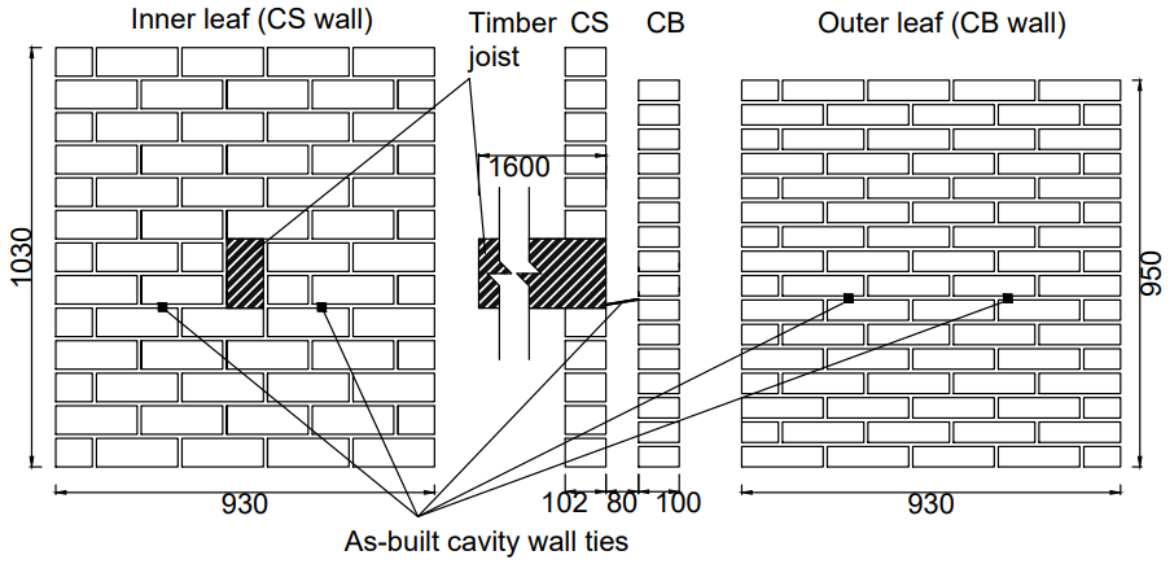

(c)

Figure 4.4 The wallets during construction (a and b), and geometry of a specimen with two as-built cavity-wall ties (dimensions are in mm).

Regarding the as-built wall-to-wall connections, similarly to Chapter 3, L-shaped ties with a diameter of 3.6 mm and a total length of 200 mm were embedded between two bricks in the mortar joint. The embedment length differed at each end of the tie: the zigzag end was embedded for a length of 50 mm, whereas the hooked ends were embedded for a length of 70 mm. Regarding the as-built wall-diaphragm connections, the timber end was either simply placed into the width of the inner leaf or reinforced by a 14-mm-diameter L-shaped steel anchor (hook anchor). The details of the cavity wall tie and hook anchor can be seen in Figure 4.5.

Two different levels of pre-compression were applied only to the inner leaf, which are 0.1 MPa and 0.3 MPa. The applied pre-compression levels were considered representative of a cavity wall at the first and second levels of a typical URM residential building, as similarly done by Graziotti [68].

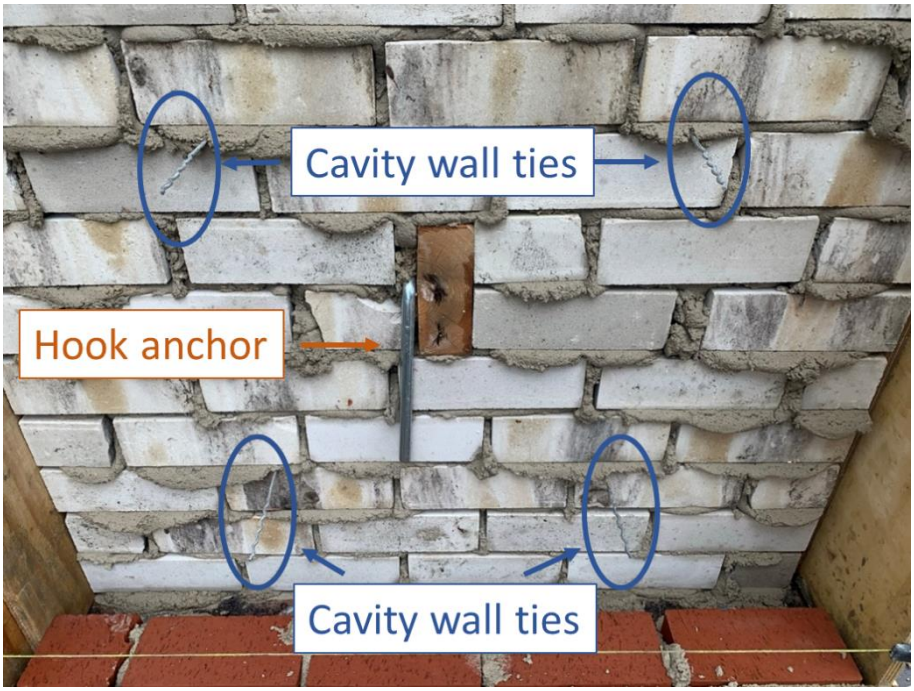

(a)

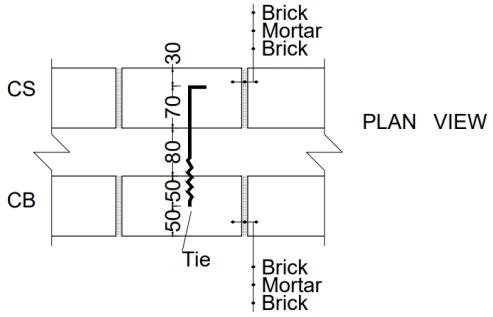

(b)

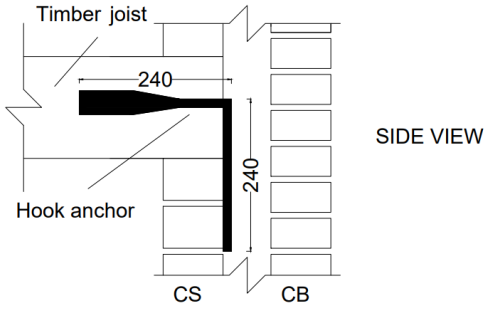

(c)

Figure 4.5 Connection details: view of the external side of the inner leaf of a cavity wall (a), cavity wall tie connection (b), and hook anchor connection (c) (dimensions are in mm).

Twenty-two tests were performed on timber joist-masonry connections, with multiple conditions and configurations: (i) six wallets in as-built condition, each one with different configurations (ii) the first six walls already tested were retrofitted using helical bars and retested, (iii) ten wallets strengthened using mechanical anchors applied in four different configurations. Regarding the strengthened condition, the four configurations were: (a) four walls were tested unstrengthened as control specimens since a different veneer unit type and a different mortar quality were used for the inner leaf, (b) two walls were retrofitted using timber blocks, (c) two walls lacking as-built wall ties were retrofitted using the timber blocks and post-installed cavity wall tie anchors, (d) two walls with as-built cavity-wall ties were retrofitted using the timber blocks and post-installed cavity wall tie anchors. Table 4.1 summarises the characteristics of the tested walls. It should be noted that the inner leaf was vertically loaded to the desired initial pre-compression level; however, variations in vertical pre-compression may occur since the vertical pre-compression stress was not measure during the experiment; hence in Table 4.1, it is called "initial pre-compression level". A detailed description of the boundary conditions is provided in sub-section 4.2.2.

Table 4.1 Overview of the specimens in terms of applied pre-compression level and connections details in unstrengthened and strengthened conditions.

Specimen Type	Specimen Name	Initial pre-comp. level	As-built condition		Strengthened condition	
			Timber joist-wall connection	Number of As-built wall ties	Timber joist-wall connection	Number of post-installed ties
Unstrengthened connections	J1	0.1 MPa	Pocket connection	2 ties	-	-
	J2	0.1 MPa	Hook anchor	2 ties	-	-
	J3	0.1 MPa	Pocket connection	4 ties	-	-
	J4	0.1 MPa	Hook anchor	4 ties	-	-
	J5	0.3 MPa	Pocket connection	4 ties	-	-
	J6	0.3 MPa	Hook anchor	4 ties	-	-
	J3-C	0.1 MPa	Pocket connection	4 ties	-	-
	J4-C	0.1 MPa	Hook anchor	4 ties	-	-
	F1	0.1 MPa	Pocket connection	2 ties	-	-
	F2	0.1 MPa	Pocket connection	2 ties	-	-
Connections with strengthened timber joists	TJ1*	0.1 MPa	Pocket connection	2 ties	Helical bar	-
	TJ2*	0.1 MPa	Hook anchor	2 ties	Helical bar	-
	TJ3*	0.1 MPa	Pocket connection	4 ties	Helical bar	-
	TJ4*	0.1 MPa	Hook anchor	4 ties	Helical bar	-
	TJ5*	0.3 MPa	Pocket connection	4 ties	Helical bar	-
	TJ6*	0.3 MPa	Hook anchor	4 ties	Helical bar	-
Connections with strengthened cavity walls and timber joists	F3	0.1 MPa	Pocket connection	2 ties	Timber blocks	-
	F4	0.1 MPa	Pocket connection	2 ties	Timber blocks	-
	F5	0.1 MPa	Pocket connection	-	Timber blocks	4 cavity anchors
	F6	0.1 MPa	Pocket connection	-	Timber blocks	4 cavity anchors
	F7	0.1 MPa	Pocket connection	2 ties	Timber blocks	2 cavity anchors
	F8	0.1 MPa	Pocket connection	2 ties	Timber blocks	2 cavity anchors

* After testing in the as-built condition, the specimens were strengthened and retested.

4.2.1.1 Specimens for unstrengthened timber joist-masonry connections

Ten wallets were tested in unstrengthened connections, reproducing cavity walls with timber joists in as-built condition. In common Dutch practice, the timber joist end is either simply placed on a pocket located in the inner leaf of a cavity wall, as-built masonry pocket connection, or a 14-mm-diameter hook anchor is added to improve the connection. For the latter solution, the connection is provided by the hook anchor, fastened to the timber joist with three screws. In the experimental campaign, the hook anchor was passed through the CS leaf, bearing against the exterior surface of the CS leaf. The details of the cavity wall tie and hook anchor can be seen in Figure 4.5b and c, respectively.

A total of 6 specimens were tested under the configuration of masonry pocket connection, as shown in Table 4.2. Solid clay brick masonry was used for the veneer of 4 specimens as follows: (i) 2 ties/m2 for a pre-compression level of 0.1 MPa (J1), (ii) 4 ties/m2 for a pre-

compression level of 0.1 MPa (J3, J3-C) and (iii) 4 ties/m2 for a pre-compression level of 0.3 MPa (J5). Additionally, perforated clay brick masonry was used for the veneer of 2 specimens, both with 2 ties/m2 and a pre-compression level of 0.1 MPa (F1, F2) and a higher mortar strength quality was used for the inner leaf of 3 specimens (J3-C, F1 and F2). It should be noted that the tests were carried out in phases so that the specimens were built at different construction times. For this reason, a different veneer unit type and mortar quality were used during the second construction phase when compared to the materials used during the first phase. However, the use of these materials is justified in the case of traditional Groningen houses since they can all be found in Dutch construction practice.

Table 4.2 Test wallets in as-built conditions with masonry pocket connections.

		Specimen ID					
		J1	J3	J5	J3-C	F1	F2
Timber-joist connection		-	-	-	-	-	-
Ties/m^2		2	4	4	4	2	2
Initial pre-compression level (MPa)		0.1	0.1	0.3	0.1	0.1	0.1
Type of Mortar	CS	Remix BM2 M5	Remix BM2 M5	Remix BM2 M5	Remix/Sakrete mortar	Remix/Sakrete mortar	Remix/Sakrete mortar
	CB	Remix BM2 M5	Remix BM2 M5	Remix BM2 M5	Remix BM2 M5	Remix BM2 M5	Remix BM2 M5
Type of clay brick		Solid clay brick	Solid clay brick	Solid clay brick	Solid clay brick	Perforated brick	Perforated brick

A total of 4 specimens were tested under the timber joist with hook anchor configuration as shown in Table 4.3 as follows: (i) 2 ties/m2 for a pre-compression level of 0.1 MPa (J2), (ii) 4 ties/m2 for a pre-compression level of 0.1 MPa (J4, J4-C) and (iii) 4 ties/m2 for a pre-compression level of 0.3 MPa (J6).

Table 4.3 Test wallets in as-built condition with masoned-in anchor.

		Specimen ID			
		J2	J4	J6	J4-C
Timber-joist connection		Hook anchor	Hook anchor	Hook anchor	Hook anchor
Ties/m^2		2	4	4	4
Initial pre-compression level (MPa)		0.1	0.1	0.3	0.1
Type of Mortar	CS	Remix BM2 M5	Remix BM2 M5	Remix BM2 M5	Remix/Sakrete mortar
	CB	Remix BM2 M5	Remix BM2 M5	Remix BM2 M5	Remix BM2 M5
Type of clay brick		Solid clay brick	Solid clay brick	Solid clay brick	Solid clay brick

A summary of geometrical details and boundary conditions of the as-built specimens is presented in Table 4.4. It should be noted that a detailed description of the boundary conditions is provided in the following sub-section.

Table 4.4 Test wall configurations for the unstrengthened specimens.

Wallet dimensions [mm] and support arrangement	Wallet	Hook anchor	σ_{VO} [MPa]
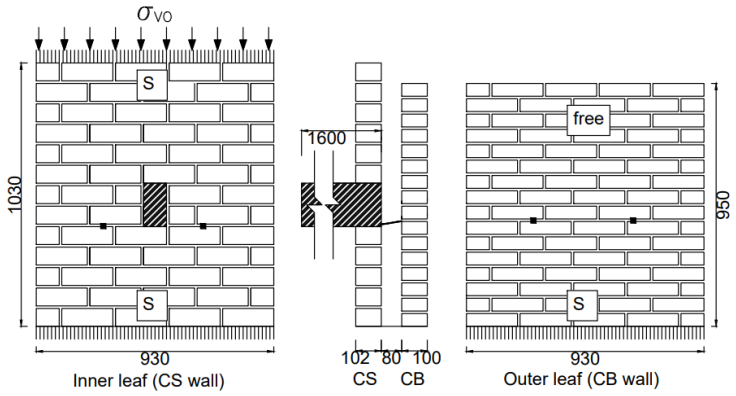	J1	no	0.1
	J2	yes	0.1
	F1	no	0.1
	F2	no	0.1
	J3	no	0.1
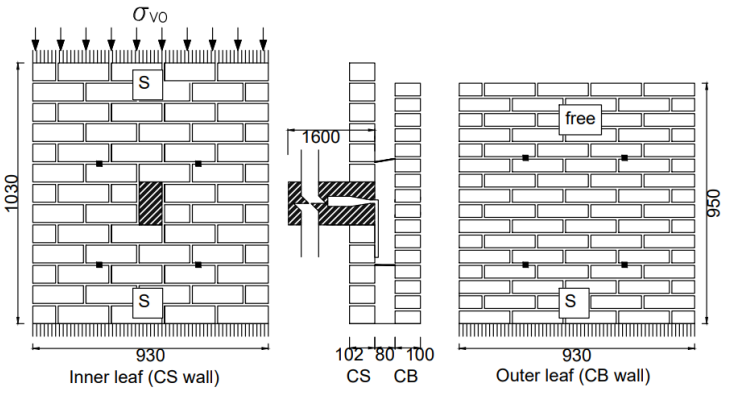	J4	yes	0.1
	J5	no	0.3
	J6	yes	0.3
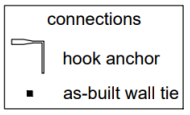	J3-C	no	0.1
	J4-C	yes	0.1

Note: S = simply-supported edge and Free = free edge

4.2.1.2 Test specimens with strengthened timber joist-masonry connection by means of helical bars

After completing the testing of timber joist-cavity wall specimens in as-built condition, the six walls whose veneer was made of solid clay brick masonry (J1, J2, J3, J4, J5 and J6) were retrofitted by connecting the outer leaf and the timber joist with helical bars and retested. The helical bar is a twisted stainless steel reinforcing bar under the brand name “HeliBar” [107]. Two helical bars with a diameter of 6 mm and a total length of 335 mm were used. The retested

specimens were named by adding “T” onto the front of the names of the corresponding as-built specimens, i.e., TJ1 to TJ6.

To simulate the real installation of helibars, two holes perpendicular to the wall and in the orientation of the joist were drilled through the whole thickness of the outer leaf and 80 mm through the joist. Then the clay mortar bed was cut with a minimum length of 120 mm for each helical bar. Firstly, the post-installed spiral bars were installed through the holes to tie the outer veneer to the joist. After installing helical bars in the uniaxial direction of the joist, the spiral bars were bent 90 degrees in the bed joint of the outer veneer with approximately a length of 120 mm. Therefore, out of a total length of 335 mm, a length of 80 mm was embedded in the joist, 80 mm of the bar was in the cavity gap, a length of 50 mm of the bar was embedded in the outer leaf and the rest of the tie which was around 120 mm was bent in the clay leaf. Finally, the slots were filled with high-strength epoxy materials. Installation and schematic overview of the helical bars are shown in Figure 4.6a and b, respectively. Regarding the boundary condition, the inner leaf was simply supported, while the outer leaf was considered a cantilever system, as seen in Figure 4.6c.

(a)

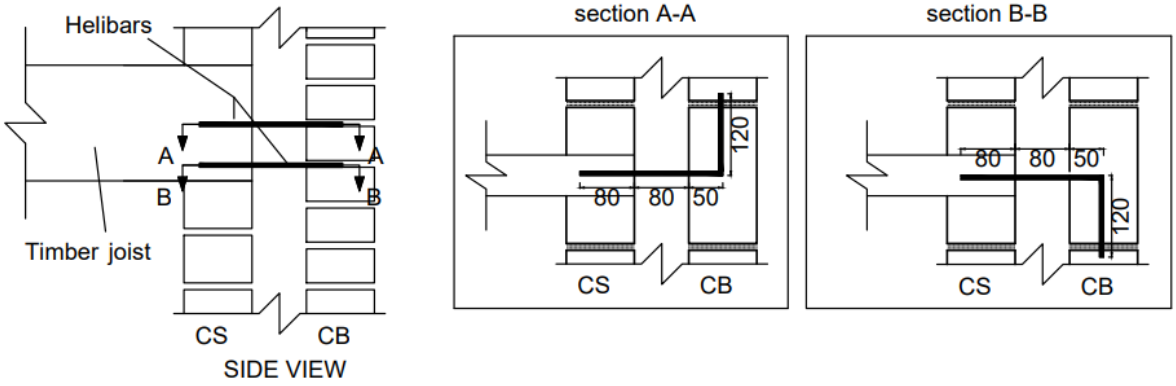

(b)

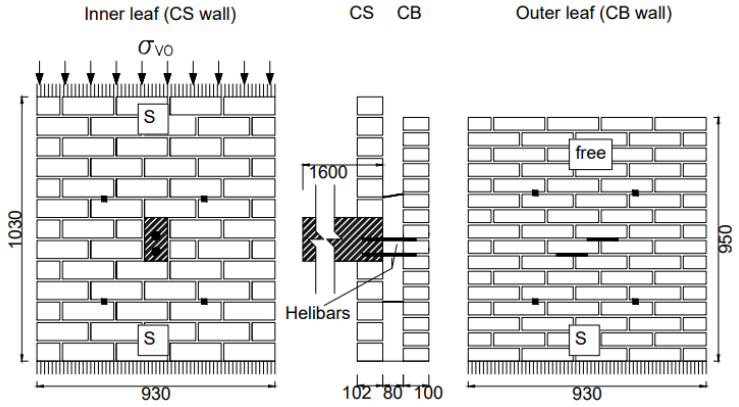

(c)

Figure 4.6 Details of the strengthened connections with helical bars: installing procedure for helical bars (a), schematic overview of helical bars (b), and test wall configuration for the strengthened connection (c) (dimensions are in mm).

4.2.1.3 Specimens with strengthened cavity wall anchors and timber joist-masonry connections by means of timber blocks

A third set of specimens was strengthened by means of the addition of timber blocks and retrofitting anchors. A total of six walls were constructed of the same configuration as specimen J2, except for a different veneer unit type, namely perforated clay brick and a different mortar quality used for the inner leaf.

In order to measure the influence of the strengthening solution for a clear characterisation of the behaviour of connections, the specimens were divided into four groups: (i) control specimens, (ii) two walls were retrofitted using timber blocks, (iii) two walls without as-built wall ties were retrofitted using the timber blocks and post-installed cavity wall tie anchors, (iv) two walls with as-built cavity-wall ties were retrofitted using the timber blocks and post-installed cavity wall tie anchors. The specimens were designed to be representative of different levels of strengthening solutions for the improvement of the behaviour of the wall-to-wall and wall-to-floor connections on the same wallet configuration.

The installation overview of the timber blocks and post-installed mechanical anchors is shown in Figure 4.7. Timber blocks with mechanical anchors were used to strengthen the connection between the timber joist and the inner leaf of the cavity wall. The timber blocks were placed on both sides of the joist and fastened to the inner leaf by means of anchors with a total length of 120 mm and a diameter of 10 mm and then screwed to the joist with steel angles, as shown in Figure 4.7a, b and c.

The post-installed cavity wall tie anchors were used to strengthen the connection between two leaves of the cavity wall. 225 mm long cavity anchors with 8 mm diameter were inserted through bricks. The first step consisted of pre-drilling through the brick face of the inner leaf until almost the middle of the outer leaf. Then, the tie anchor and its plug were placed into the pre-drilled hole, as shown in Figure 4.7d and e.

For Specimen F5 and F6, which lack as-built ties, a total of four post-installed cavity anchors were placed at the 5^{th} and 10^{th} courses from the bottom of the inner leaf. Regarding Specimen F7 and F8, only two post-installed cavity anchors were located at the 10^{th} course from the bottom of the inner leaf. A summary of geometrical details and boundary conditions of the strengthened specimens with the timber blocks is presented in Table 4.5.

(a)

(b)

(c)

(d)

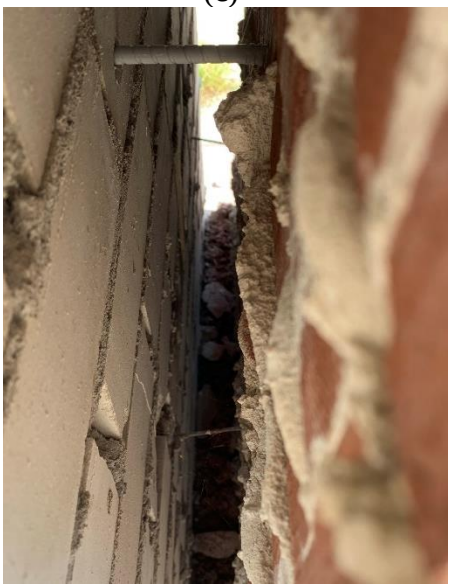

(e)

(f)

Figure 4.7 Details of the strengthened connection with timber blocks: installing procedure for anchors used in timber blocks (a and b), steel angle between timber joist and block (c), post-installed cavity wall anchors (d and e), and final view of the strengthened specimen (f).

Table 4.5 Test wall configurations for the strengthened condition.

Wallet dimensions [mm] and support arrangement	***Wallet***	***σ_{VO} [MPa]***
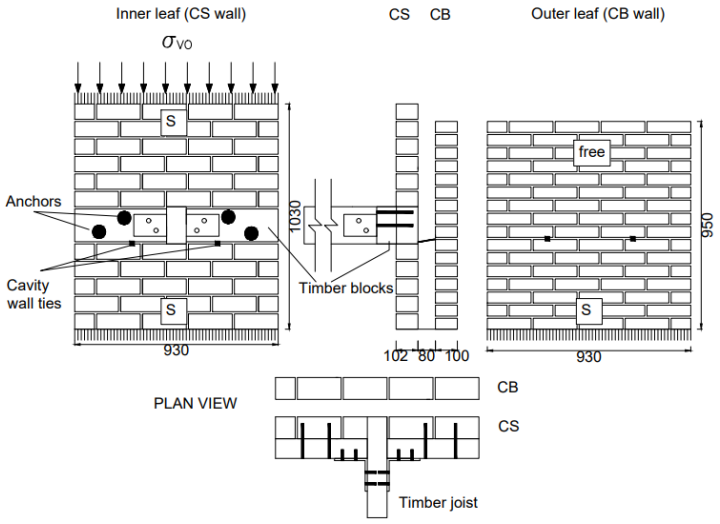	*F3*	*0.1*
	F4	*0.1*
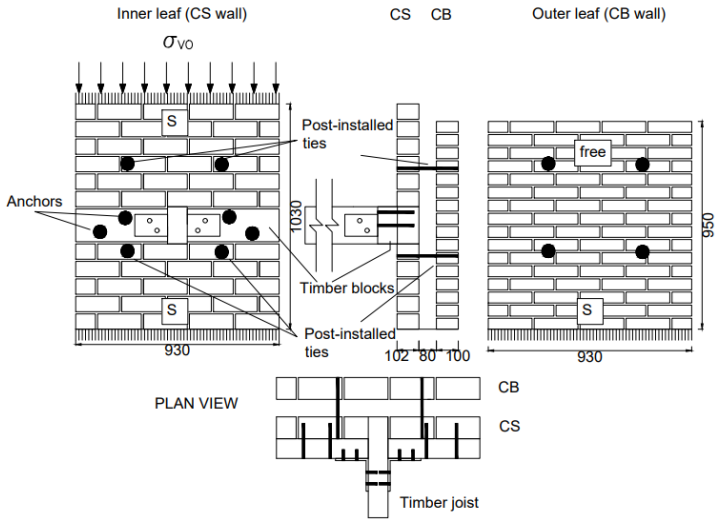	*F5*	*0.1*
	F6	*0.1*

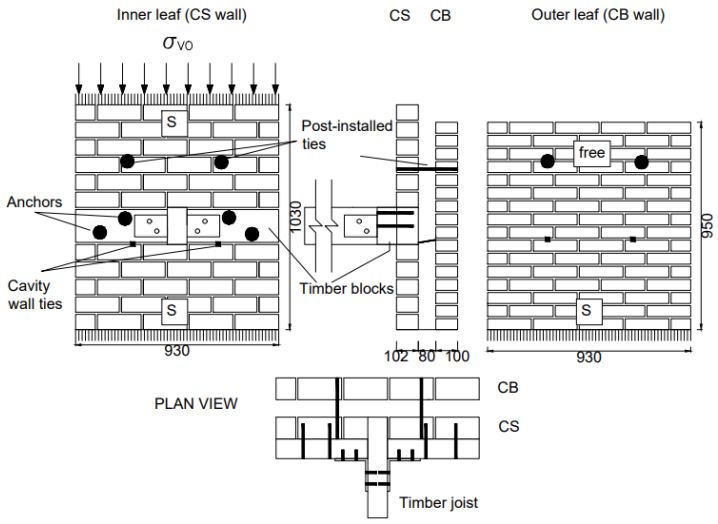

F7	*0.1*
F8	*0.1*

Note: S = Simple support

4.2.2 Test Setup and Boundary Conditions

The wallet specimens were tested on an out-of-plane test setup at the BuildinG laboratory. The test setup was composed of a stiff reaction frame, two air bellows and an actuator. The reaction frame consisted of steel HEB-profile members with a width of 2250 mm, a depth of 2250 mm, and a height of 1900 mm (Figure 4.8).

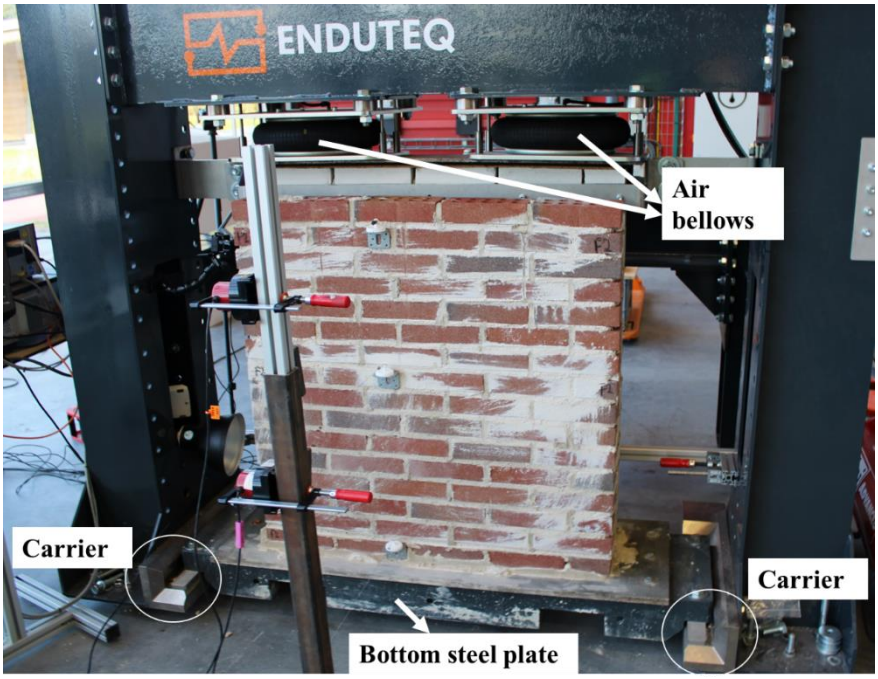

Figure 4.8 Overview of the testing setup.

In order to restrain the specimen to the frame, a bottom steel plate was used. A timber plywood plate was attached to the bottom steel beam to provide a proper surface for the specimens. The specimens were built on the steel beam in which high-adjustable steel support was connected during the construction period to support the timber joist, as seen in Figure 4.9. The support was removed when the specimen was placed in the test setup. After that, the bottom steel plate was bolted to the two carriers on the legs of the frame.

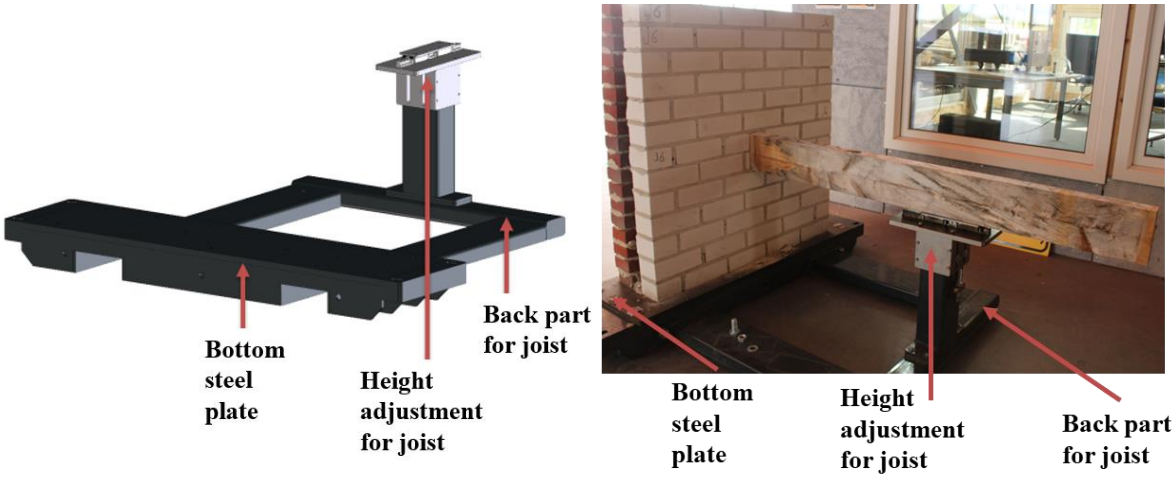

(a) (b)

Figure 4.9 Detail of the bottom steel plate: schematic view (a) and photograph (b).

The specimens were loaded via the joist with the electric actuator, which has a capacity of 30 kN for both positive (pulling) and negative (pushing) directions, integrated with a data acquisition system. The actuator was positioned over the joist and was aligned horizontally along the centreline axis of the joist. The free end of the joist was connected to the actuator, allowing for the transfer of the applied load in the uniaxial direction of the joist through the pressure apparat (Figure 4.10). It should be noted that due to the way the free end of the joist was connected to the actuator, rotation of the joist was prevented.

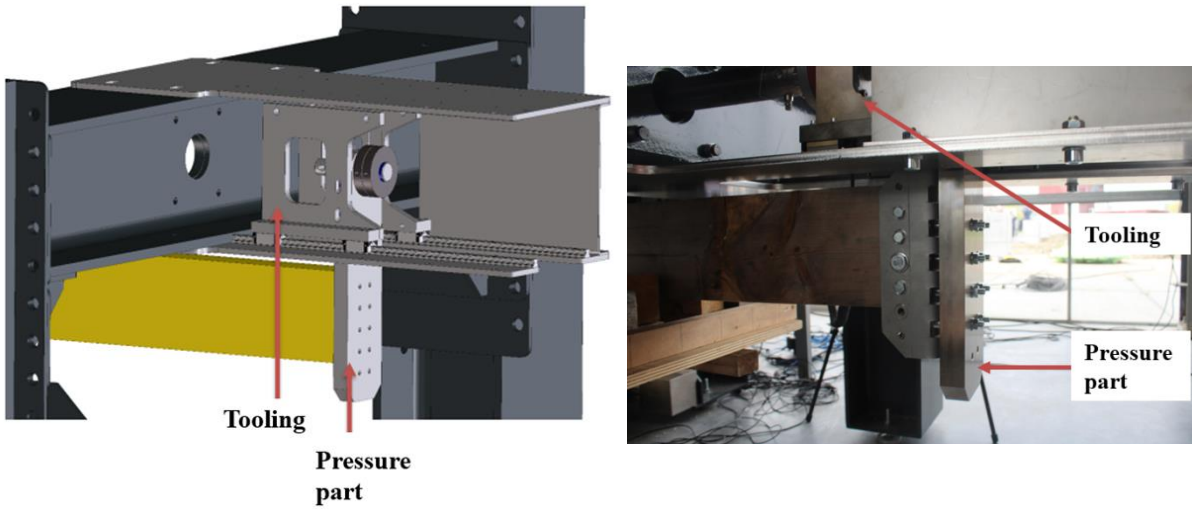

(a) (b)

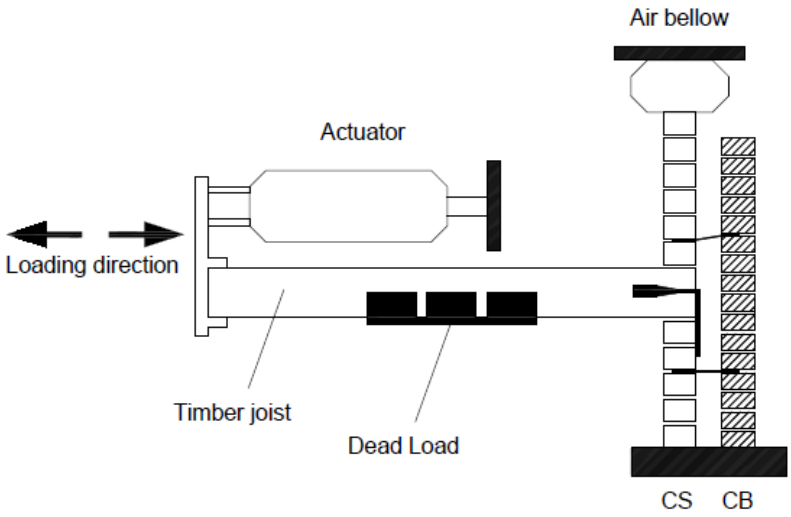

(c)

Figure 4.10 Tooling configuration for connecting the actuator to the joist with the test setup: schematic view of the tooling configuration (a) and photograph (b), and schematic view of the test setup (c).

The specimens were subjected to vertical pre-compression via two air bellows to simulate the effect of load-bearing walls acting on the inner leaf of the masonry structure. A steel plate was placed on the top of the load-bearing inner leaf in order to distribute the pre-compression stress uniformly at every point. In order to prevent OOP movement of the inner leaf of the cavity wall, a pair of steel braces was introduced to the test setup. The braces were fixed to the test setup and the top of the inner leaf. The details of applying pre-compression level and steel braces can be seen in Figure 4.11. A vertical dead load of 100 kg was applied to the middle of the joist to simulate the self-weight of the portion of the floor supported by the joist.

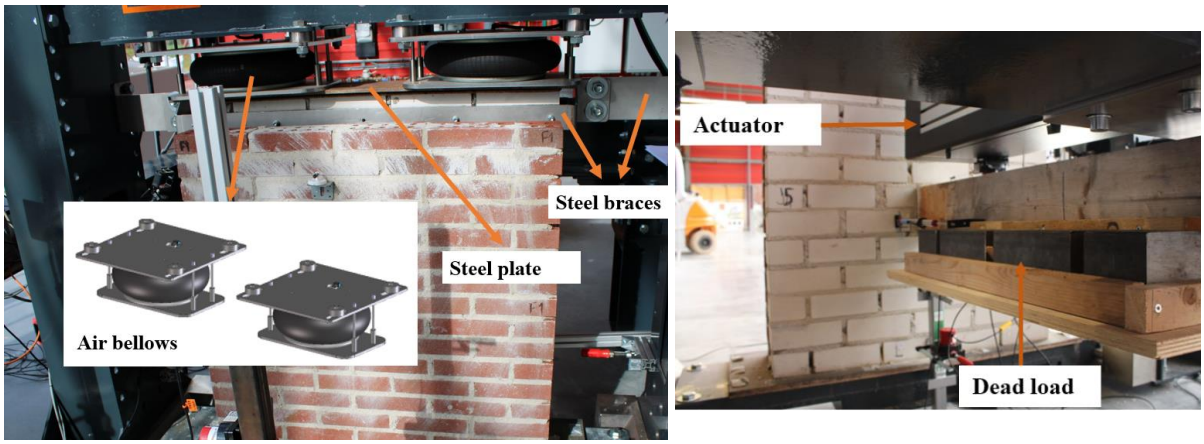

(a) (b)

Figure 4.11 Test setup: Air bellows, steel plate and braces details (a); detail of actuator and dead load (b).

The top horizontal edge of the inner leaf was restrained against the vertical translation due to the presence of the air bellows to apply the overburden. Because of that, in the case of overturning and subsequent vertical displacements of the top block of the inner leaf, variations in the vertical pre-compression may occur. Hence, the initially applied overburden is called the initial pre-compression level, as in Table 4.1. The bottom horizontal edge of the inner leaf was bonded to the timber plywood, which may cause some degree of timber bearer boundary condition. Hence, it can be expected that the vertical load will be in between the wall face and the wall centreline. The first assumption considers a free rotation along the centreline, while the second considers an end fixity at the bottom of the inner leaf. Morandi [108] reported that assuming the ends of a wall as a simply-supported boundary condition will lead to considering a conservative solution. Hence, the out-of-plane boundary condition of the inner leaf was treated as a simply-supported system in which the rotations at both the top and bottom of the wall were free. While the boundary condition of the outer veneer was treated as a cantilever system, in which the top edge of the wall was free to rotate and translate. The boundary condition of the specimens is schematically shown in Figure 4.12.

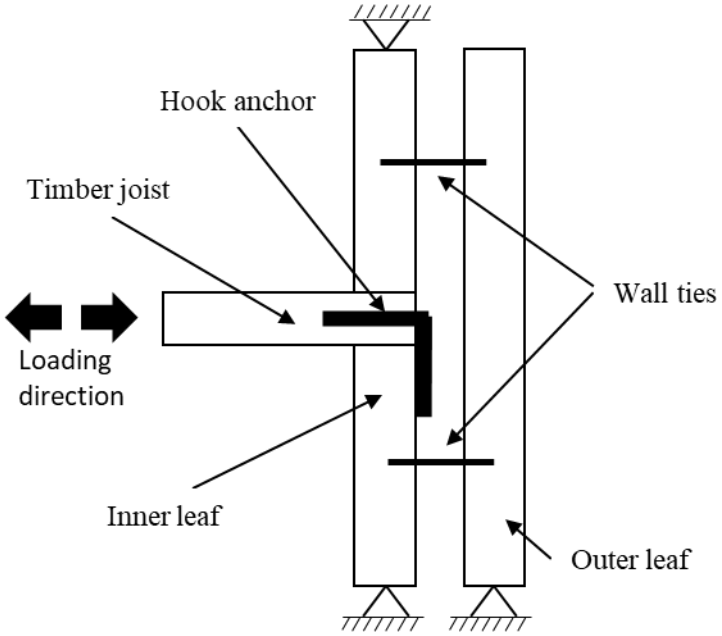

Figure 4.12 Schematic of the boundary conditions.

The vertically fixed restraint condition may induce arching effect in the case of OOP rocking of the inner leaf. This highlights the importance of considering potential scenarios where the arching effect becomes relevant in real buildings. Such situations can take place when load redistribution occurs above the connection as a result of the OOP rocking mechanism of the wall. This redistribution may develop in case of stiff portions of masonry above the connections so that local uplifting is prevented.

The location of the sensors is shown in Figure 4.13. A total of three potentiometers were placed on both surfaces of the inner and outer leaves in symmetric to measure the absolute displacement. Hence, the three potentiometers of each leaf were positioned at the bottom, mid-height and at the top of the wallet. The relative displacement of the leaves was obtained between the symmetric sensors such as Potentiometer 1 and 4, Potentiometer 2 and 5 and Potentiometer 3 and 6. The relative displacement between the CS leaf and joist was measured using LVDT 7 and 8. The absolute displacement of the timber joist was measured by the sensor in the actuator. LVDT 9 is placed to measure the relative displacement between the joist and timber block regarding the strengthened specimens.

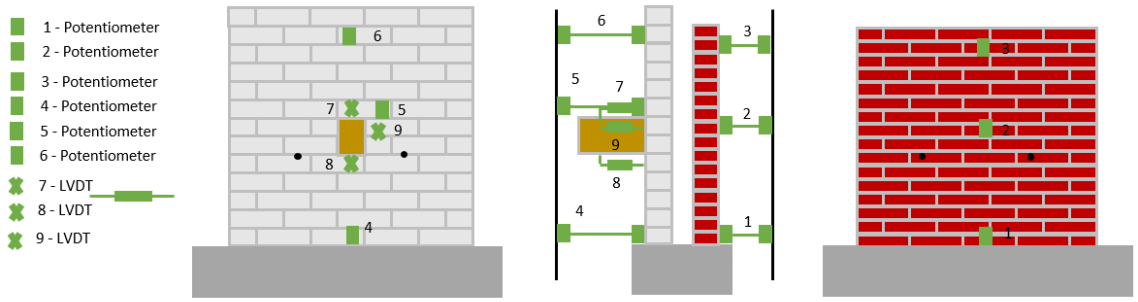

Figure 4.13 Location of the sensors during the conducted tests.

4.2.3 Loading protocol

The specimens were subjected to a quasi-static reversed-cyclic according to Method B of the ASTM standard [90], originally developed for ISO 16670 [109]. With the aim of evaluating the strength and stiffness degradation of the specimens, a cyclic loading protocol was involved.

A displacement-controlled procedure was applied. A monotonic test needs to be conducted to determine the ultimate displacement, which will be used as a reference deformation to obtain the amplitudes of the cycles. Ravenshorst & Mirra [103] conducted a monotonic test on a single-wythe masonry wall with a timber joist to study its ultimate capacity. Hence, the reference deformation of the cyclic test in this study was derived from the monotonic test conducted by Ravenshorst & Mirra [103], as it is very similar. As Method B – ASTM E2126 [90] suggests, the reference deformation, Δ_m, from the Monotonic tests was chosen as a value of 20 mm. The loading protocol consists of three fully reserved cycles at the displacement of 1.25%, 2.5%, 5%, 7.5%,10%, 20%, 40%, 60%,80%, 100%, 120%, 140%, 160%, 180%, 200%, 220%, 240% and 280% of the reference deformation. The loading rate was set at 0.3 mm/s. The cyclic loading protocol is given in Table 4.6 and Figure 4.14.

The tests were concluded based on the visual observation of the damage in the specimens and mostly for a displacement approximately half the width of the inner leaf, similar to that of the study of Ravenshorst & Mirra [103], which was also greater than the ultimate displacement derived from the monotonic test, corresponding a limit to its potential out-of-plane deformation of a masonry wall subjected to an earthquake.

Table 4.6 Cyclic loading scheme for masonry-timber joist experiment (adopted from Method B – ASTM E2126 [90]*).*

Step	Number of cycles	Amplitude, % Δ_m	Target displacement (mm)
1	3	1.25	0.25
2	3	2.5	0.5
3	3	5	1
4	3	7.5	1.5
5	3	10	2
6	3	20	4
7	3	40	8
8	3	60	12
9	3	80	16
10	3	100	20
11	3	120	24
12	3	140	28
13	3	160	32
14	3	180	36
15	3	200	40
16	3	220	44
17	3	240	48
18	3	280	52

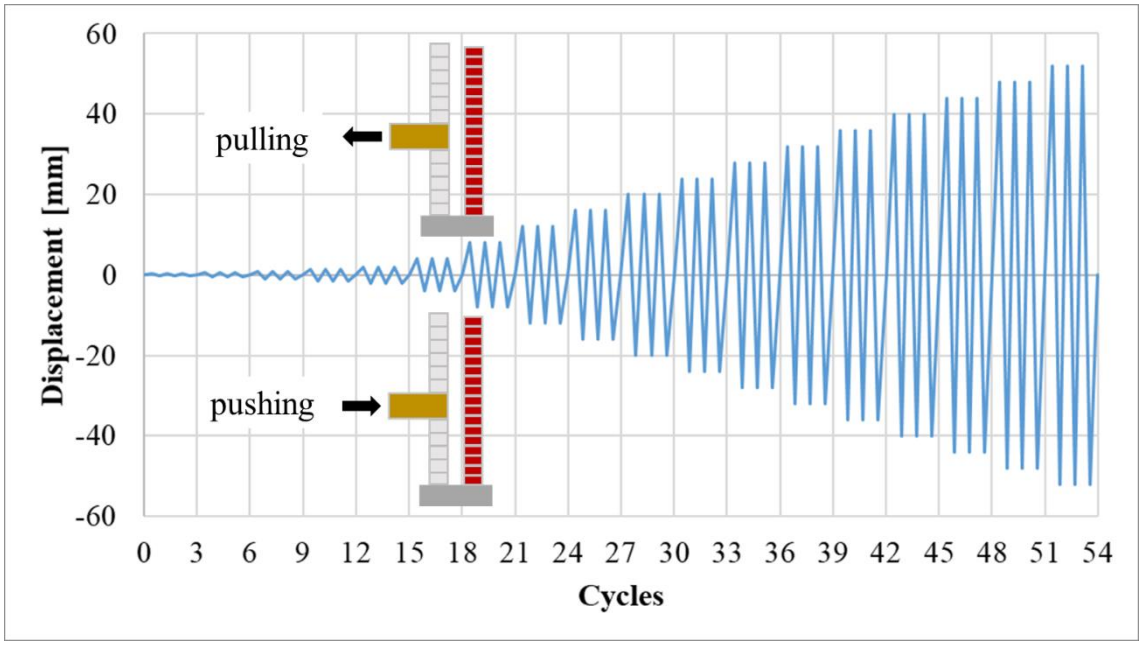

Figure 4.14 Cyclic loading protocol.

4.3 Mechanical characterisation of materials

A series of companion tests were performed to characterise the mechanical properties of the materials used in the testing campaign. The flexural and compressive strength of the mortar, the bond strength between the masonry unit and mortar, and the tensile and compressive capacity of the tie were investigated.

4.3.1 Flexural and compressive strength of mortar

The mechanical characterisation of the mortars for inner and outer leaves was defined in terms of mean compressive strength, f_m, and flexural strength of mortar, f_{bm}, in agreement with NEN-EN 1015-11 [82].

The majority of the masonry buildings in the Netherlands were mainly of low-quality mortar [83]. However, as discussed in Chapter 3, a parametric study was conducted with a high-strength quality mortar to predict the potential failure mode. Hence, two different mortar qualities were used in this study for validation purposes. Regarding the specimens of J1, J2, J3, J4, J5 and J6, a low-strength mortar (Remix BM2 M5) was used for the inner and outer leaves. Differently, for the specimens of J3-C, J4-C, F1, F2, F3, F4, F5, F6, F7 and F8, the Remix BM2 M5 was used in the outer leaf, while a high-strength mortar (Remix/Sakrete M10) was used in the inner leaf, as listed in Table 4.7.

Table 4.7 Used mortar for each specimen.

		Specimen ID															
		J1	J2	J3	J4	J5	J6	J3-C	J4-C	F1	F2	F3	F4	F5	F6	F7	F8
Type of Mortar	Inner leaf	M5	M5	M5	M5	M5	M5	M10	M10	M10	M10	M10	M10	M10	M10	M10	M10
	Outer leaf	M5	M5	M5	M5	M5	M5	M5	M5	M5	M5	M5	M5	M5	M5	M5	M5

Note: M5 = Remix BM2 and M10 = Remix/Sakrete mortar

The results of the flexural and compressive strength tests are reported in Table 4.8. The tests were performed on randomly selected specimens. For the mortar quality of 5M, the flexural tests were performed on 60 specimens and compressive tests on 120 specimens. The compressive strength equals 4.25 MPa, whereas the flexural strength is determined as 1.53 MPa. The specimens built with Remix BM2 M5 showed a coefficient of variation approximately equal to 30%. For the mortar quality of 10M, the flexural strength test was performed on 12 specimens and the compressive strength test on 24 specimens. The compressive strength is equal to 10.78 MPa. The flexural strength is equal to 3.04 MPa. In both cases, for the specimens built with Remix/Sakrete M10, the coefficient of variation is limited

to less than 10%. Figure 4.15 shows the statistical distribution of flexural and compressive strength of both types of mortar.

Table 4.8 Flexural and compressive strength of the mortar used for the CS and CB wallets.

Material property	Symbol	UM	Remix BM2 (5M)		Remix/Sakrete (10M)	
			Average	C.oV.	Average	C.oV.
Compressive strength of mortar	F_m	MPa	4.25	0.29	10.78	0.09
Flexural strength of mortar	F_{bm}	MPa	1.53	0.30	3.04	0.07

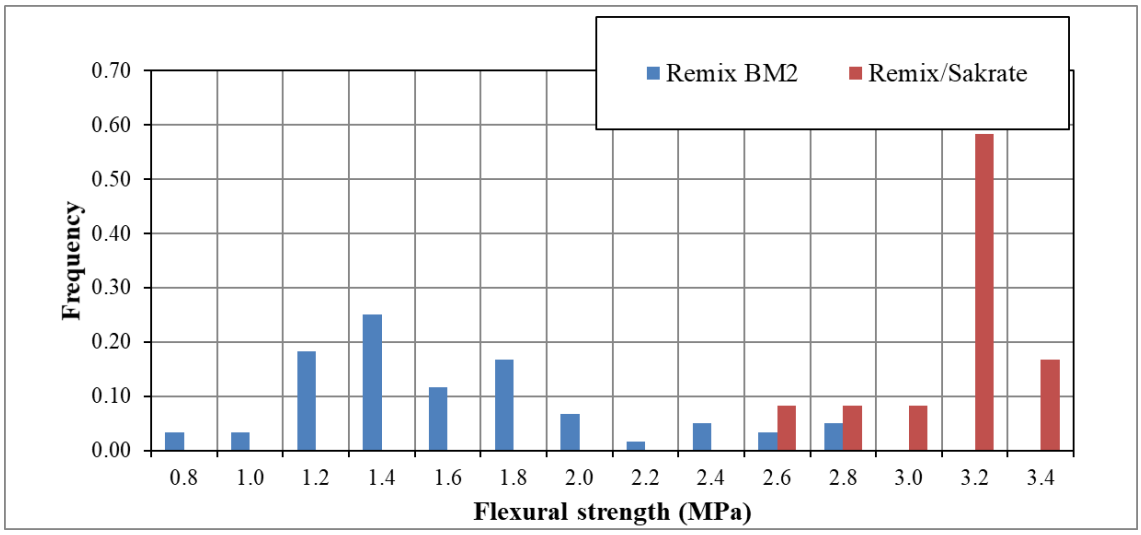

(a)

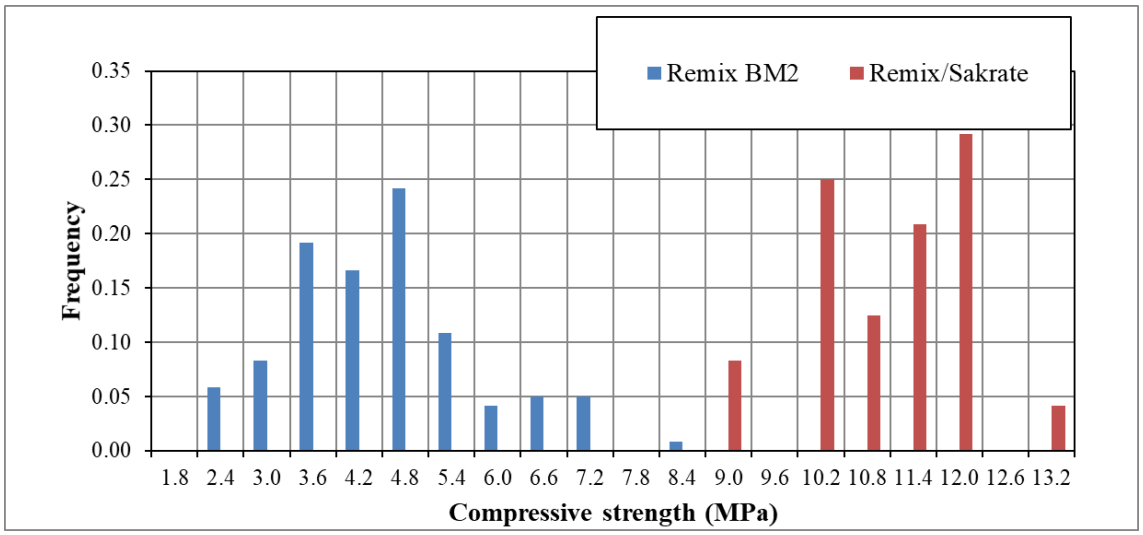

(b)

Figure 4.15 Statistical distribution of flexural strength (a) and compressive strength (b) of the used mortar types.

4.3.2 Bond strength of masonry

The bond strength between the masonry unit and mortar, f_w, was determined in agreement with the bond wrench test proposed by EN 1052-5 [84]. Solid clay bricks were used for the outer leaf regarding the specimens of J1, J2, J3, J4, J5, J6, J3-C and J4-C. Differently, for the specimens of F1, F2, F3, F4, F5, F6, F7 and F8, perforated clay bricks were used in the outer leaf. The units adopted in the whole experimental campaign for the inner leaf were CS bricks, as listed in Table 4.9.

Table 4.9 Brick details for the inner and outer leaves.

		Specimen ID															
		J1	J2	J3	J4	J5	J6	J3-C	J4-C	F1	F2	F3	F4	F5	F6	F7	F8
Type of brick	Inner leaf	CS	CS	CS	CS	CS	CS	CS	CS	CS	CS	CS	CS	CS	CS	CS	CS
	Outer leaf	S-CB	S-CB	S-CB	S-CB	S-CB	S-CB	S-CB	S-CB	P-CB	P-CB	P-CB	P-CB	P-CB	P-CB	P-CB	P-CB

Note: CS = calcium silicate brick, S-CB = solid clay brick and P-CB = perforated clay brick

Four types of couplets were tested, representative of the tested specimen in the experimental campaign, namely, the inner leaf with a low-strength mortar (CS-5M), the inner leaf with a high-strength mortar (CS-10M), the outer leaf built with solid clay brick and a low-strength mortar (S-CB–5M), and the outer leaf built with perforated clay brick and a low-strength mortar (P-CB–5M). For each type, a total of 10 couplets were tested for material characterisation. The values of the bond strength and the corresponding bond failure types of the couplets are shown in Table 4.10.

Table 4.10 Bond strength for each type of masonry adopted during the tests.

Sample No.	CS - 5M		CS - 10M		S-CB - 5M		P-CB - 5M	
	f_w (MPa)	Bond failure type	f_w (MPa)	Bond failure type	f_w (MPa)	Bond failure type	f_w (MPa)	Bond failure type
1	0.08	Type A	0.44	Type A	0.53	Type D	0.37	Type B
2	0.09	Type A	0.60	Type B	0.49	Type D	0.27	Type B
3	0.09	Type A	0.59	Type A	0.49	Type D	0.44	Type A
4	0.10	Type A	0.34	Type A	0.34	Type D	0.59	Type B
5	0.10	Type A	0.40	Type A	0.47	Type C	0.53	Type C
6	0.08	Type A	0.50	Type A	0.37	Type D	0.48	Type C
7	0.08	Type A	0.49	Type A	0.36	Type D	0.42	Type D
8	0.09	Type A	0.48	Type A	0.34	Type D	0.50	Type C
9	0.11	Type A	0.25	Type A	0.32	Type D	0.26	Type B
10	0.12	Type C	0.52	Type A	0.40	Type C	0.35	Type A
Average	0.09		0.46		0.41		0.42	
Standard deviation	0.01		0.11		0.08		0.11	
CoV	0.15		0.24		0.19		0.26	

4.3.3 Tensile and compressive strength of helical bars

Regarding the specimens first tested in the as-built condition and then retrofitted and retested, helical bars were used as a strengthening solution in order to connect the timber joist and outer leaf. A helical bar is a helical stainless steel reinforcing bar used for masonry repair and strengthening. In this experimental campaign, two helical bars with a diameter of 6 mm and 304 Grade stainless steel spiral shape were used per each strengthened specimen. It should be noted that a particular material characterisation test for the helical bars used in this experimental campaign was not conducted. However, the properties of helical bars were taken from the product sheet of Helifix HeliBar in terms of tensile and compressive strength capacity, as seen in Table 4.11.

Table 4.11 Summary of the material properties of the 6 mm stainless steel spiral Helical bar with 304 Grade.

Loading	**Material property**	**UM**	**Results from** [107]
Tensile loading	0.2% Proof stress	N/mm^2	995
	Ultimate tensile strength	kN	9.8
	Shear strength	kN	5.5
Compressive loading	Compressive strength (gap=75mm)	kN	2.20
	Compressive strength (gap=100mm)	kN	1.59
	Compressive strength (gap=125mm)	kN	1.15

4.4 Experimental results of unstrengthened connections

The following sections describe the experimental outcomes for each of the two categories, namely masonry pocket connections and hook anchor as-built connections. To this end, the results obtained are reported in terms of failure mode, hysteretic behaviour, and peak strength capacity by applying the cyclic loading protocol under displacement control up to large displacements (around 40mm). It is important to note that the positive displacement and force in these graphs correspond to the joist pull (henceforth called pulling) direction of loading. Hence, the direction of pushing the joist towards the wall (henceforth called pushing) indicates the negative displacement.

4.4.1 Failure modes

The damage progression was quite complex and recorded with all observed cracks at the conclusion of the cyclic test. The specimens with masonry pocket connection exhibited a joist-sliding failure mode, which included partial joist-to-wall interaction, while the specimens with hook anchor exhibited a rocking failure mode. The former failure mode was characterised by the joist sliding, causing diagonal cracks propagating from the joist. The rocking failure mode occurred depending on the loading direction due to the hook action of the anchor. As the joist moved together with the inner leaf, an OOP rocking mechanism was activated in the pulling direction. Conversely, in the pushing direction, when the joist moved toward the wall, there was only resistance due to the friction between timber and mortar. Hence, for the specimens with hook anchors, the damage pattern resulted in more extensive cracks with the cracking of bricks due to the hook anchor. The crack pattern of each specimen in as-built condition can be seen in Figure 4.16. The position of the embedded ties and the joist is also presented for ease of comparison of the position of the cracks with respect to the timber joist and cavity wall ties.

For the specimens with masonry pocket connections, a local failure mechanism with sliding of the joist was expected to occur. The out-of-plane failure mechanism was characterised by the diagonal cracks propagating from the joist due to the applied overburden pressure and good initial bond between the joist and the inner leaf. The diagonal cracks would not be expected to be observed in the inner leaf when pure sliding occurs, as obtained in the study by Ravenshorst & Mirra [103]. Regarding the outer leaf, it was observed that the veneer rotated as a rigid body on the base thanks to the cavity wall ties, effectively transferring the deformation to the outer veneer. The inner leaf was characterised by one or two large horizontal cracks at the joist level and the base of the wallet, while the veneer was characterised by a horizontal crack only at the base.

The considered variations, namely two different tie distributions, two different pre-compression levels, two different as-built connections and two different mortar types, were compared as follows:

- Two ties (J1) vs four ties (J3) – a higher number of embedded ties in the cavity wall leads to an increase in the damage observed in the inner leaf due to the fact that cracks are concentrated around the ties. The capacity of the wall tie connection depends on the embedment of the extremity of a tie. For example, the pull-out capacity of the zigzag end of the tie embedded in clay brick is higher than the pull-out capacity of the hooked end of the tie embedded in calcium silicate, as

highlighted in Chapter 3. Hence, the damage around the tie can be observed only in the inner leaf.

- 0.1 MPa (J1, J2, J3, J3-C, J4 and J4-C) vs 0.3 MPa (J5 and J6) – the inner leaf exhibits fewer cracks under the higher pre-compression stress condition. The stiffness of the wall increases with higher overburden.
- Masonry pocket connection (J1, F1 and F2) vs joist with hook anchor (J2) – the specimens with the hook anchor underwent more damage in the inner leaf.
- Low-quality mortar (J1) vs high-quality mortar (F1 and F2) – the specimens with low-quality mortar exhibit very extensive damage. As expected, an increase in the mortar strength can lead to an increased bonding performance of mortar as well as strength of connection, allowing more damage localisation around the ties.

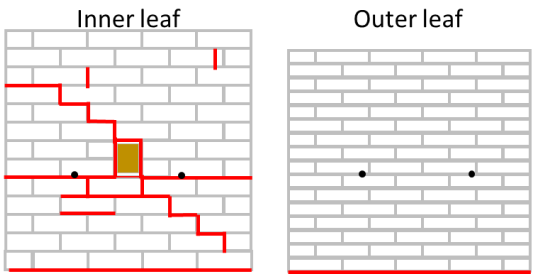

(a) J1 (σ_{VO} =0.1 MPa, masonry pocket connection)

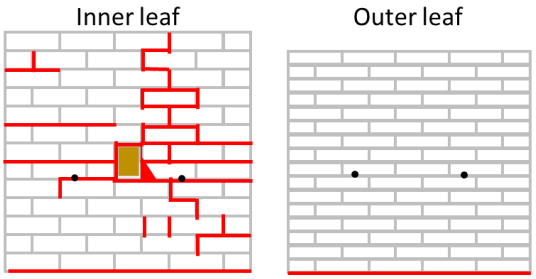

(b) J2 (σ_{VO} =0.1 MPa, joist with hook anchor)

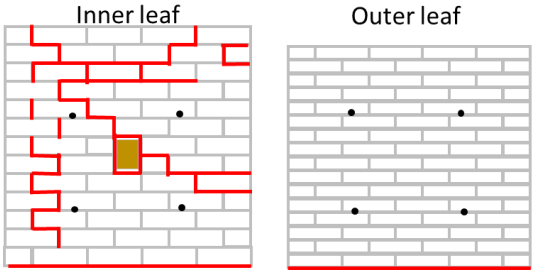

(c) J3 (σ_{VO} =0.1 MPa, masonry pocket connection)

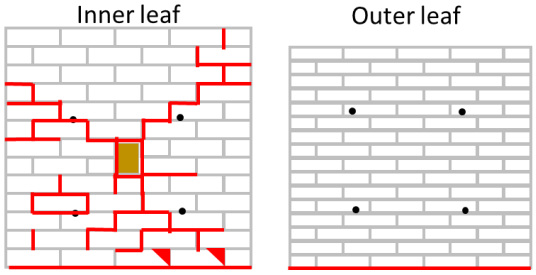

(d) J4 (σ_{VO} =0.1 MPa, joist with hook anchor)

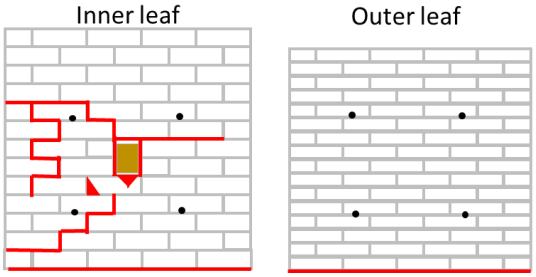

(e) J5 (σ_{VO} =0.3 MPa, masonry pocket connection)

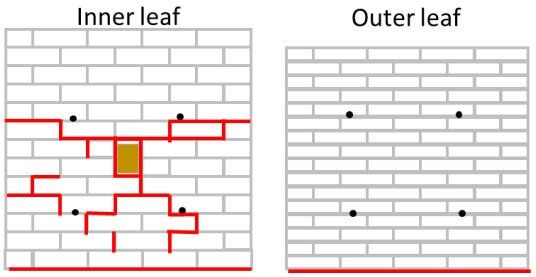

(f) J6 (σ_{VO} =0.3 MPa, joist with hook anchor)

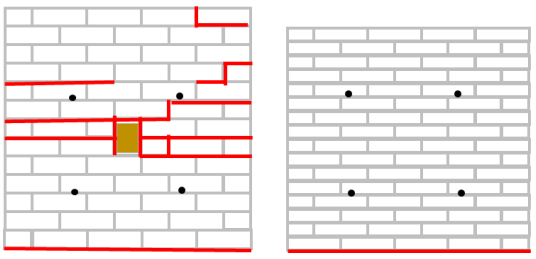

(g) J3-C (σ_{VO} =0.1 MPa, masonry pocket connection)

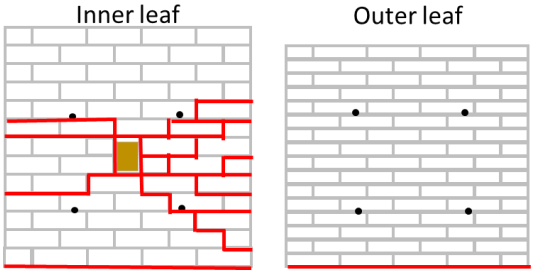

(h) J4-C (σ_{VO} =0.1 MPa, joist with hook anchor)

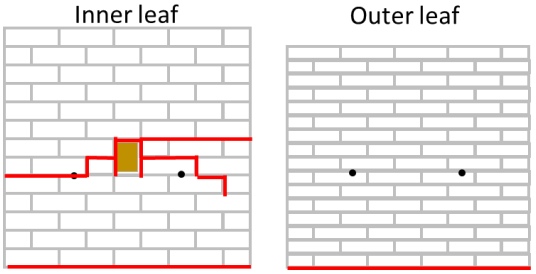

(i) F1 (σ_{VO} =0.1 MPa, masonry pocket connection)

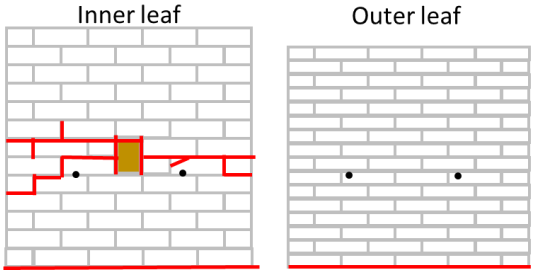

(j) F2 (σ_{VO} =0.1 MPa, masonry pocket connection)

Figure 4.16 Crack patterns of the unstrengthened specimens at the conclusion of the tests.

Both out-of-plane displacements in pulling and pushing for inner leaf (CS) and outer veneer (CB) at the middle and top levels can be seen in Table 4.12. Figure 4.17 presents an exaggerated image of the deformed shapes of specimens with maximum displacement in positive and negative directions to facilitate a better understanding of the failure mode of specimens. The deformations are amplified 10 times with respect to real deformations and the deformed shape represents the out-of-plane displacements of the inner and outer leaves measured by the peak displacement in each potentiometer. Regarding the envelope deformed shapes, the displacements of the measured points of the leaves were connected by linear branches. It should be noted that although lateral support was provided along the top of the inner leaf to prevent OOP movement, this proved to be quite flexible, which could not restrain the horizontal displacement completely.

The specimens with hook anchors showed higher displacement capacity than that of the specimens with masonry pocket connections. In the specimens with masonry pocket connection, the highest out-of-plane displacement at the middle of the inner leaf where the joist was inserted is 7.2 mm obtained in pulling for Specimen F2, while the rest are around 5 mm. On the other side, the highest out-of-plane displacement of the outer leaf was observed at the top of the wall, being free on top at a displacement of 15.8 mm. The deformed shapes were very similar in both pulling and pushing with a very limited displacement. It can be concluded that the OOP rocking mechanism was activated due to not only the connectivity between timber and masonry and the two leaves but also the test setup, causing additional vertical forces due to the arching effect. A more dedicated analysis of the aforementioned behaviour is provided in Chapter 6.

Table 4.12 Out-of-plane displacements recorded for both the pulling and pushing directions.

Connection	Wallet	CB leaf				CS leaf			
		Middle (mm)		Top (mm)		Middle (mm)		Top (mm)	
		Pulling	Pushing	Pulling	Pushing	Pulling	Pushing	Pulling	Pushing
Masonry pocket connection	J1	1.1	0.6	2.6	0.6	0.3	1.4	0	1.8
	J3	5.1	0.3	9.5	1	0.9	5.5	0.1	6.6
	J5	1.2	0	2.5	0	0.2	1.6	0	1.8
	J3C	4.1	3.9	6.6	6.2	2	7.1	1.3	8.4
	F1	3.4	3.3	5.6	4.9	2.9	3	1.8	2
	F2	7.7	9.6	12.8	15.8	7.2	6.7	3.8	3
Hook anchor	J2	6.1	0	11.6	0	0	7.1	0	7.1
	J4	11.2	0	19.5	0.1	0	11.3	0.1	8.8
	J6	2.8	0.2	4.4	0.2	0	2.8	0	2.8
	J4C	7.1	6.5	11.9	10.6	8.9	9.5	3.7	4.7

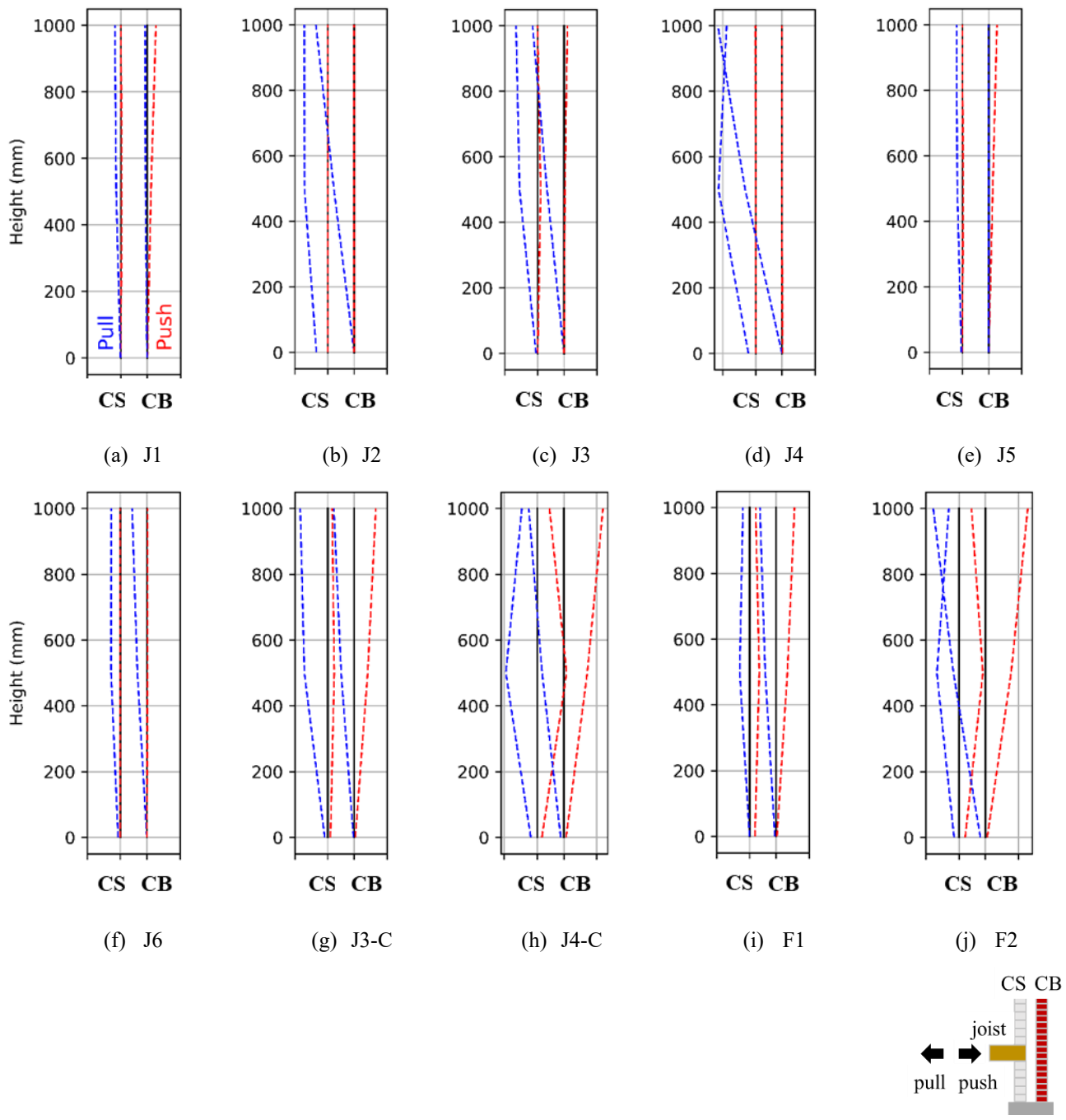

Figure 4.17 Deformed shapes of the unstrengthened specimens. The deformations are amplified 10 times with respect to real deformations. The dashed lines indicate the envelope of the deformed shapes in both the positive (pulling) and negative (pushing) directions.

4.4.2 Load-Displacement curves

Based on the recorded data, force-displacement curves were generated for the unstrengthened specimens, as presented in Figure 4.18. The relative displacement between the joist and wall is indicated on the horizontal axis of Figure 4.18.

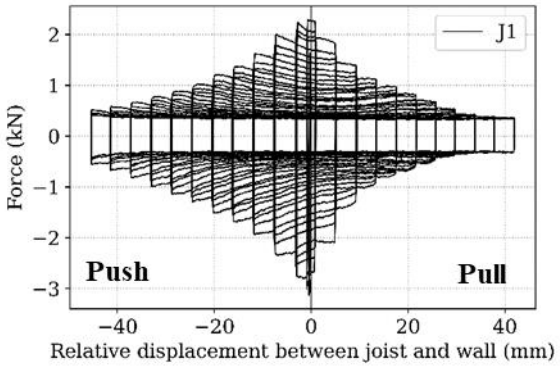

(a) J1 (σ_{VO} =0.1 MPa, masonry pocket connection)

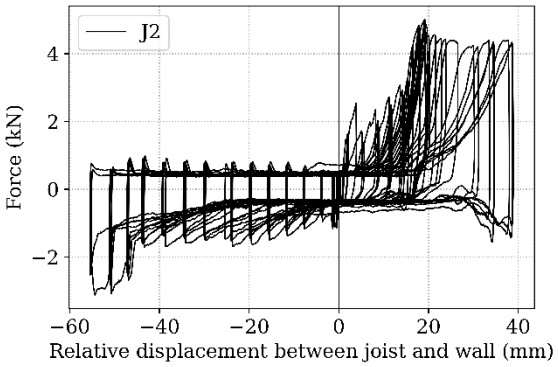

(b) J2 (σ_{VO} =0.1 MPa, joist with hook anchor)

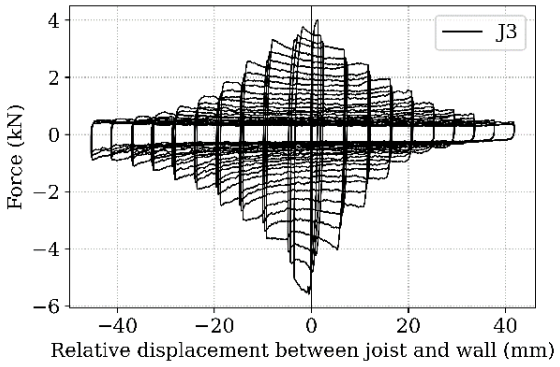

(c) J3 (σ_{VO} =0.1 MPa, masonry pocket connection)

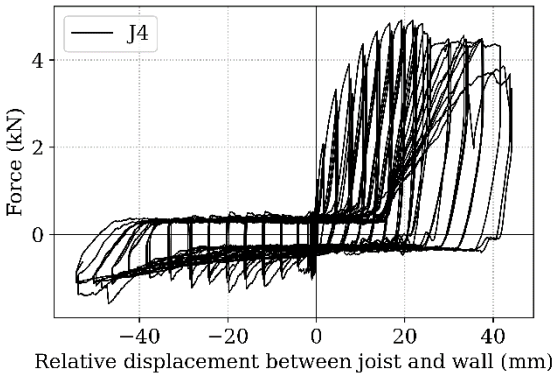

(d) J4 (σ_{VO} =0.1 MPa, joist with hook anchor)

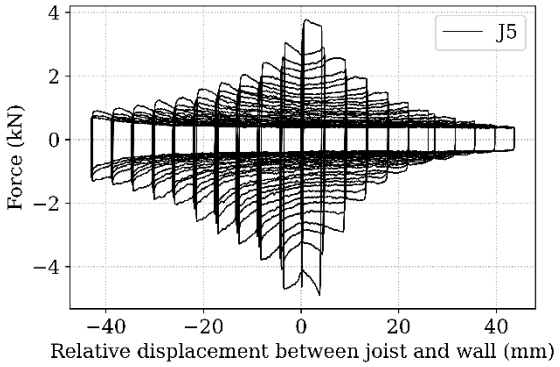

(e) J5 (σ_{VO} =0.3 MPa, masonry pocket connection)

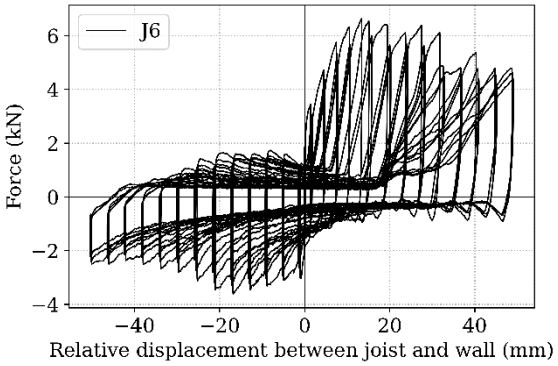

(f) J6 (σ_{VO} =0.3 MPa, joist with hook anchor)

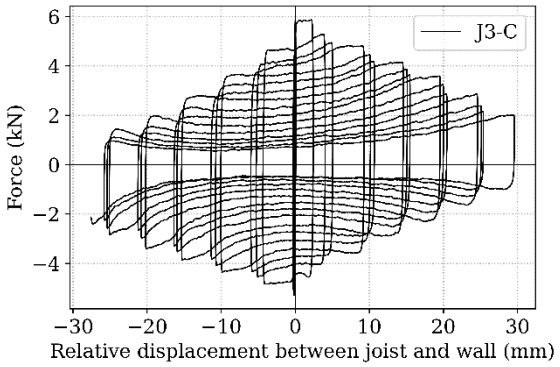

(g) J3-C (σ_{VO} =0.1 MPa, masonry pocket connection)

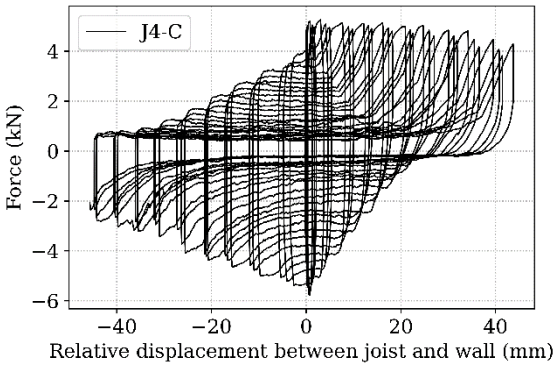

(h) J4-C (σ_{VO} =0.1 MPa, joist with hook anchor)

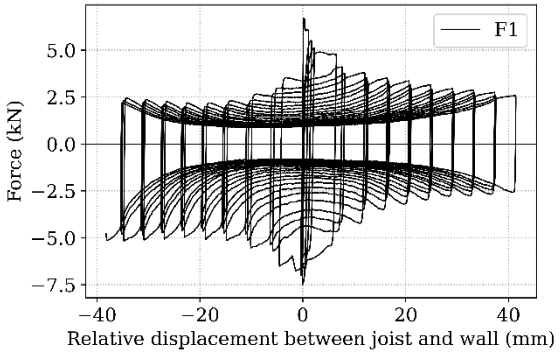

(i) F1 (σ_{VO} =0.1 MPa, masonry pocket connection)

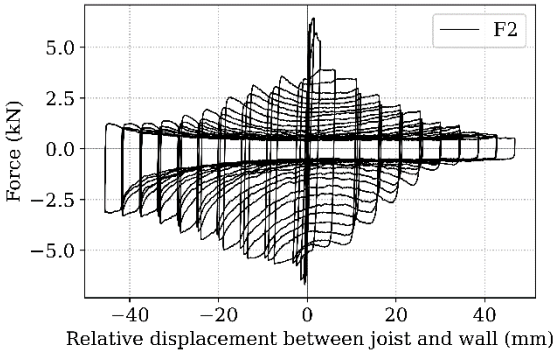

(j) F2 (σ_{VO} =0.1 MPa, masonry pocket connection)

Figure 4.18 Hysteresis curves of the unstrengthened specimens.

Neither the force-displacement curves obtained for the specimens with masonry pocket connections nor with hook anchors were symmetrical with respect to pulling and pushing. The hysteresis loops of the masonry pocket connections were mainly characterised by frictional behaviour, but additional contributions were observed, as explained in detail in sub-section 4.4.3. The hysteresis loops of the hook anchors exhibited unsymmetrical behaviour. Generally, material nonlinearity and the effect of the hook anchor were involved in the hysteresis behaviour. In addition, a pronounced pinching effect was observed due to how the hook anchor was located, bearing against the exterior surface of the CS leaf in pulling while providing only frictional behaviour in the pushing.

The unsymmetrical behaviour was expected for the timber joist with hook anchor due to the contribution of connection depending on the loading direction. In pulling, the joist may move together with the inner leaf due to the hook anchor as a stiff connection; conversely,

when the joist moved toward the wall, there was only resistance due to the friction between timber and mortar.

Regarding the specimens with masonry pocket connection, although frictional resistance governs the behaviour of the joist in both loading directions, an unsymmetrical behaviour may be observed. Unsymmetrical curves obtained in this experimental campaign, including the specimens with masonry pocket connection, were attributed to the nonlinearity of the cavity wall system with the test setup, causing additional vertical forces, particularly in initial loading stages, due to the arching action in the inner leaf and the deflection of the joist caused by the displacement of the point supported on. The additional vertical forces caused by the arching action and joist are discussed in the following sub-section.

Regarding the specimens with masonry pocket connection, the peak force was observed in the initial linear elastic stage, and the post-peak was characterised by softening. It is easy to recognise that a plastic plateau occurred towards the end of the loading cycle, which was relatively symmetric, relying on friction mechanisms associated with the joist inserted on the inner leaf pocket. These remarks show that the plastic state was characterised by the sliding of the joist, hence, without any additional shear force since there was no uplift or lowering of the contact point between the joist and the masonry. Therefore, the friction coefficient between masonry and timber is computed based on the last cycles of loading at the plastic plateau for both loading directions, and its result is equal to a value of 0.6.

The coefficient of friction of 0.6 is deemed appropriate for the contact surface, which is in between timber and mortar, as largely determined by several studies in the literature [94,101,103]. It should be noted that the coefficient of friction for the rest of the specimens was set to a friction coefficient equal to 0.6 since the specimens with masonry pocket connections were based on frictional capacity.

All the specimens with anchor hooks (J2, J4, J6 and J4-C) showed an asymmetrical behaviour of the hysteresis curve (Figure 4.18). Comparing the results obtained in pulling and pushing, the significantly higher resistance observed in pulling was due to the hook anchor, which acted only in pulling as a stiff connection. Hence, the masoned-in anchor increased the capacity in the pulling direction. It should be noted that regarding Specimen J4-C, the peak capacity was higher than the rest of the specimens with hook anchors. It can be seen that at the very beginning of the loading, the peak force was observed. Therefore, Specimen J4-C exhibits the peak force in the initial linear elastic stage, and the post-peak behaviour, similarly to the other specimens with hook anchors, was characterised by a plateau due to the yielding of the

hook anchor. Conversely, the cohesion contribution of J2, J4 and J6 was almost zero since the peak force was obtained at a loading stage of about 20mm.

The hysteresis loops of Specimen J2 and Specimen J4 (Figure 4.18b and d, respectively) were similar. However, the OOP capacity of J4 was slightly higher than Specimen J2 since Specimen J4 had a total number of four ties, increasing the rocking capacity. Since the overburden influences the friction force, Specimen J6 applied a pre-compression level of 0.3 MPa and had a higher force capacity than Specimen J2 and J4 (Figure 4.18f).

Regarding Specimen J2, in pushing, after an initial linear elastic behaviour, the capacity curve provided a plateau with a slight hardening up until the anchor touched. Then a drastic hardening curve, as highlighted in blue in Figure 4.19a, was entered since the masoned-in anchor touched the outer veneer, which then provided a hard restrain and prevented the joist movement. It should be noted that although the cavity gap was 80 mm, the hardening started when the relative displacement was around 50 mm due to the angle and thickness of the anchor. After the masoned-in anchor touched the outer veneer, a higher displacement can be seen at the middle and top levels of the outer leaf (Figure 4.19b).

An interesting observation not only in Specimen J2 but also in the rest of the load-displacement curves is that several force spikes were observed due to a stick-slip phenomenon highlighted in green in Figure 4.19c and d. Due to the rough interface between the joist and masonry, the stick-slip phenomenon occurred as a result of the sliding of the joist during intermediate reloading and unloading, which led to a change from dynamic to static friction. Another important observation from these figures is that the determined static friction coefficient from the specimens with masonry pocket connection was in line with the timber joist with hook anchor specimens, which can be seen from the plastic plateau in the pushing direction of Figure 4.19a and c (yellow dashed lines).

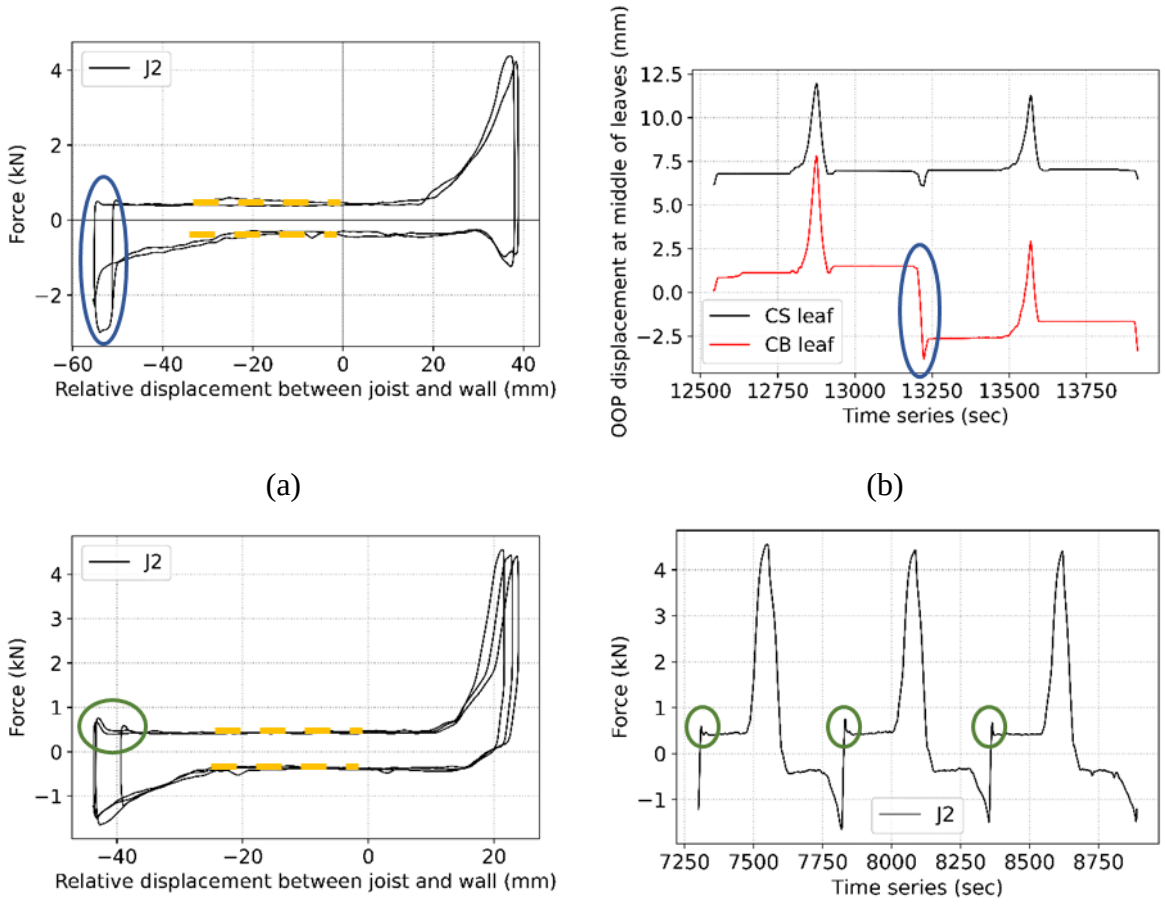

Figure 4.19 Hysteresis loop of force versus relative displacement between joist and inner leaf for Specimen J2 (a), OOP displacement at middle of inner and outer leaves for the corresponding cycles (b), and an example of the force spikes occurred during the testing (the spikes are highlighted in green) (c and d). The examined hysteresis loop of J2 is shown in (c) and the corresponding force responses in (d).

4.4.3 Mechanical contributions to the total connection resistance

Asymmetrical curves obtained in this experimental campaign can be attributed to the nonlinearity of system. Additional vertical forces were introduced on the joist-wallet interface due to the test setup since the vertical displacement at the top of the inner leaf was partially restrained by the air bellows.

It was noted that the joist was deforming during the experiment because one extreme of the joist was fixed in the testing machine and cannot displace vertically, but the other extreme moved due to the OOP rocking of the inner leaf and the sliding of the joist in the pocket, as shown in Figure 4.20. The OOP rocking determined either an uplift or a lowering of the contact point between the joist and the masonry due to the classical pivot interfaces at the wall top and

bottom. The pivot point at the bottom (B in Figure 4.20) was in the corner of the bottom brick, while the pivot point at the top (T in Figure 4.20) was in the middle, impacting a lower displacement compared to the rigid body below the joist. Additionally, the sliding can further modify the height of that point. The joist deformation introduced then an additional shear force due to the flexural and shear stiffness of the element.

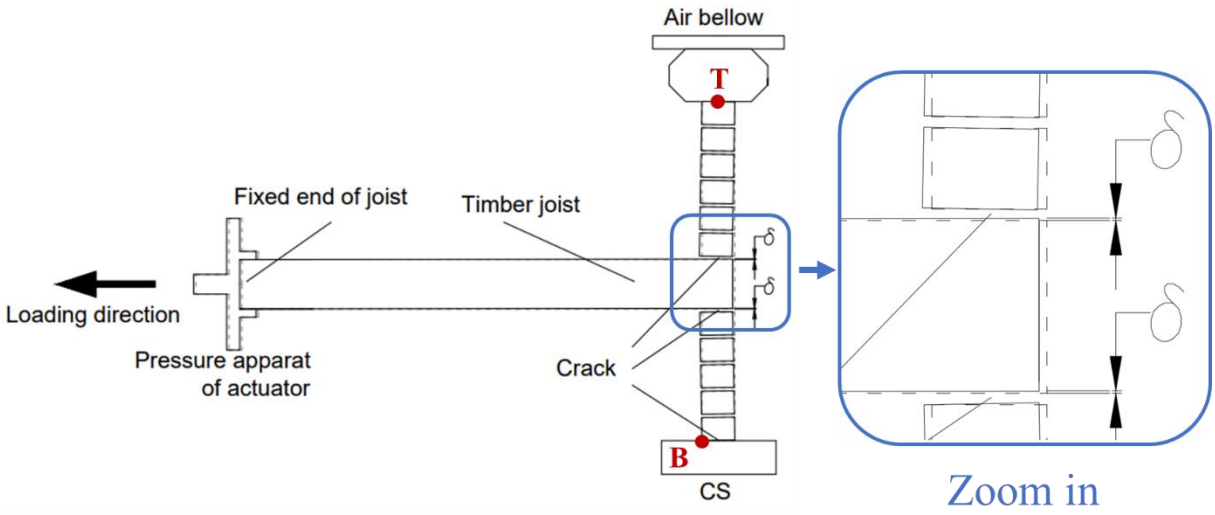

Figure 4.20 Vertical deformation of joist at embedded edge during testing.

Regarding the second additional vertical force, the way the vertical load was applied leads to vertically fixed restraint conditions (Figure 4.21), restraining the vertical motion of the wallets and activating an arching effect after the starting of the rocking failure mode. The arching effect determined an increase of the compressive stress on the contact area between the joist and the masonry with increasing horizontal displacement of the inner leaf. Therefore, the frictional resistance increased gradually at the increase of the OOP displacements of the inner leaf.

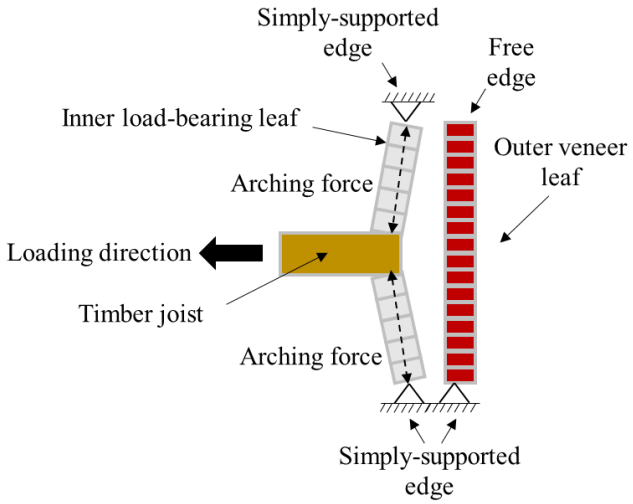

Figure 4.21 Schematic description of the arching effect mechanism.

Regarding Specimens J3-C, F1 and F2, the obtained peak force was higher, and the hysteresis curves had a different shape than that of J1, J3 and J5. These differences were attributed to bond strength. This can be explained by the fact that a stronger bond will cause not only a higher peak force but also a higher arching force due to the activation of the second-order effect thanks to the out-of-plane displacement in the inner leaf. In order to highlight the difference due to the higher bond capacity and arching effect, the obtained test results are compared in terms of the OOP displacement at the middle of the inner leaf for the specimens with masonry pocket connection, as seen in Figure 4.22. As expected, Specimen J3-C, F1 and F2 had a higher OOP displacement in the inner leaf.

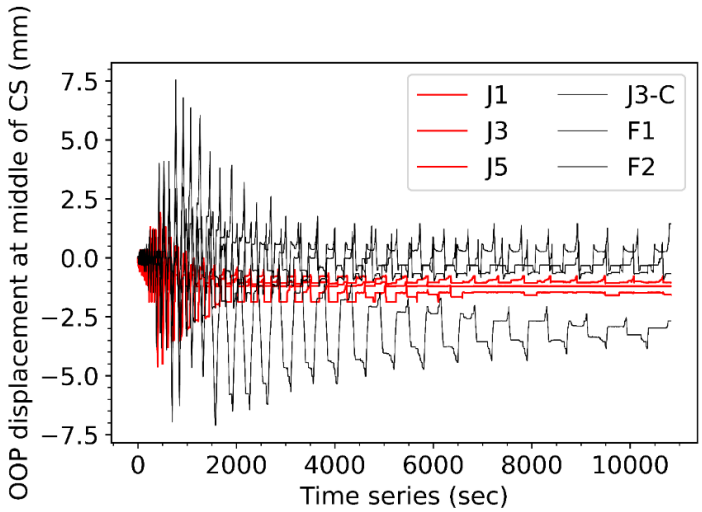

Figure 4.22 OOP displacement recorded at the middle of the inner leaf for the specimens with masonry pocket connection (red curves represent J1, J3 and J5, and black curves are J3-C, F1 and F2).

4.4.4 Hysteretic energy dissipation

Energy dissipation capacity for connections should be described as an ability to absorb energy input from earthquakes and reduce the amount of energy transmitted to other structural elements. This capacity is a crucial indicator of how well a connection performs under seismic loading. To determine the energy dissipation capacity of the specimens, the cumulative dissipated energy was calculated based on the area enclosed in the "Force-Displacement" loops. In this case, the force refers to the total reaction force of the joist, while the displacement is the horizontal displacement of the joist. The cumulative energy dissipated by the system for a specific displacement of the joist is calculated by adding up the energy dissipated per loop up to that reversed cyclic displacement.

A comparison of the accumulated hysteretic energy for the specimens with masonry pocket connection and the timber joist specimens with hook anchor is given in Figure 4.23a and b, respectively. The specimens with masonry pocket connections dissipated slightly more energy than hook anchors. This would be expected due to the frictional behaviour and displacement capacity of the masonry pocket connection. On the other side, the specimens with hook anchors led to damage to the surroundings of the joist due to the nature of the connection in the pulling direction, causing less energy dissipation. However, since the second-order effect is activated for both connections, the energy dissipation characteristics were similar.

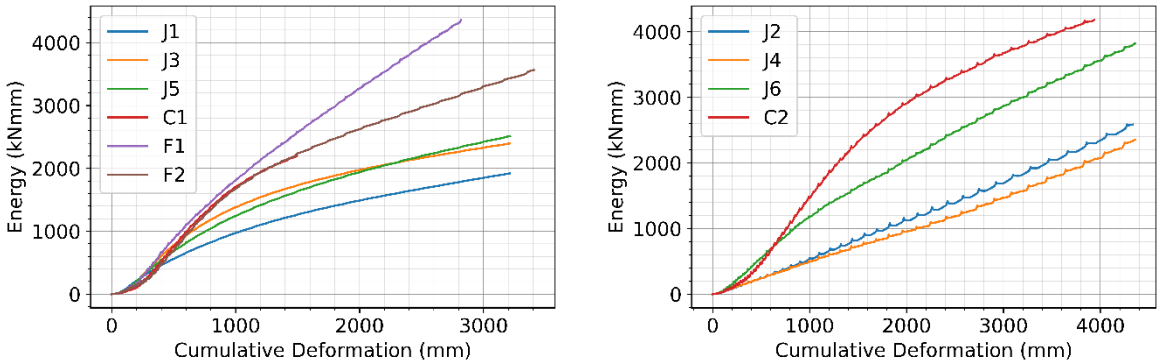

(a) (b)

Figure 4.23 Cumulative hysteretic energy for the specimens with a masonry pocket connection (a) and the specimens with a hook anchor (b).

4.5 Experimental results of the specimens with strengthened timber joist-masonry connection by means of helical bars

Specimens J1, J2, J3, J4, J5 and J6 were strengthened and retested, which are called henceforth TJ1, TJ2, TJ3, TJ4, TJ5 and TJ6, respectively. It was noticed that the specimens in the as-built

condition exhibited moderate damage and hence were strengthened in order to fully investigate the capacity of the specimen. The experimental findings will be described in the following sections.

4.5.1 Failure modes

Unlike the unstrengthened connections, the retested specimens exhibited a rocking failure mode as the governing mode. In this case, the rocking failure mode occurred when the outer leaf began to exhibit a rigid body rotating about its base. A more dedicated analysis of this failure mode is provided in Chapter 6. The crack pattern of each specimen noted at the conclusion of the cyclic test and the corresponding deformed shape with maximum displacement in positive and negative directions are provided in Annex B. The condition of the cavity wall ties and the helical bars in terms of buckling or rupture are also presented. After the strengthening, the veneer displaced more which can be explained by the formation of the horizontal cracks at the bottom and mid-height of the CB leaf during the experiment. Besides, the CB leaf was more vulnerable due to the boundary condition, as the top edge was free and with no overburden.

A comparison was performed between the unstrengthened and strengthened connections for the specimens with masonry pocket connections. Specimen TJ1 exhibited more cracks not only in the inner but also in the outer leaf compared to Specimen J1 (Figure 4.24). The specimen showed the rocking failure mode since the strengthened connection between the joist and wall activated the tilting of the outer leaf firstly around its base and then at the middle height of the wall. One of the helical bars, the strengthening anchor, failed due to buckling. It should be noted that the cavity wall consisted of two as-built wall ties, which were not sufficient to keep the wall stable in case of large deflections.

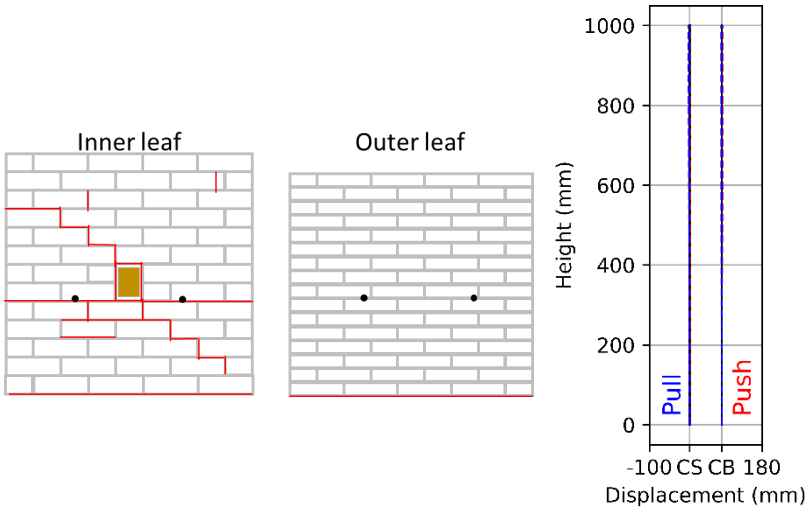

(a) J1 (σ_{VO} =0.1 MPa)

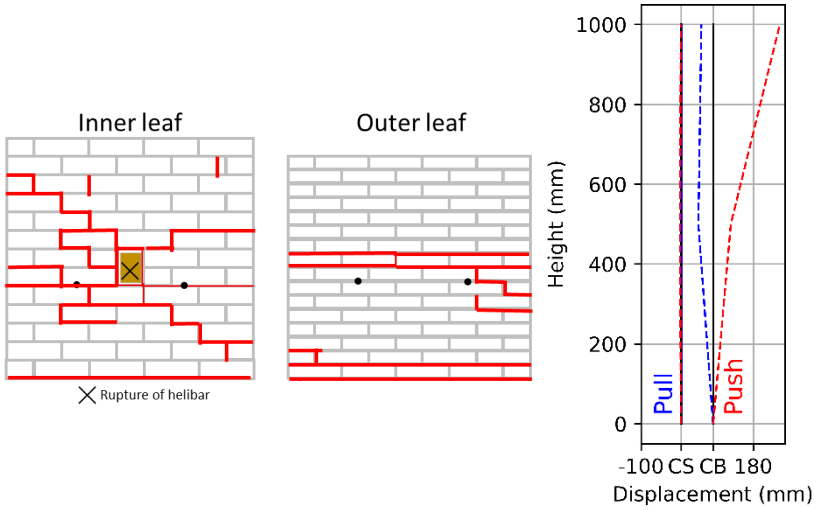

(b) TJ1 (σ_{VO} =0.1 MPa)

Figure 4.24 Comparison between the unstrengthened and strengthened connections in terms of crack pattern and out-of-plane deflections for specimens J1 (a) and TJ1 (b).

Regarding Specimen TJ2, which was constructed of the same configuration as TJ1 except for the hook anchor, similar progressive damage was accumulated by the inner and outer leaves. However, due to the presence of the hook anchor, the bricks below the joist were coming off the inner leaf. Specimen TJ3 had two more as-built cavity-wall ties compared to the two aforementioned specimens, which decreased the deformation of the outer veneer. However, again one of the embedded ties failed due to buckling. As-built wall ties of Specimen TJ4 exhibited more damage compared to Specimen TJ3, which was constructed of the same configuration except for the hook anchor. In this case, the hook anchor, particularly in pulling, contributed to higher strength capacity, determining higher load transfer via the cavity wall ties. The crack pattern of each specimen is presented in Annex B.

Unlike the other strengthened specimens with the helical bars, in the case of the applied pre-compression level of 0.3 MPa, Specimen TJ5 and TJ6 exhibited rupture of both helical bars at the beginning of the loading process (Figure 4.25). As seen in the literature [68,110], a higher applied overburden pressure can increase the initial stiffness of the wall. The OOP rocking mechanism could not be activated if the applied strengthening solution for the connection did not achieve to distribute the horizontal loads to the wall. Both specimens showed a similar deformation in terms of crack patterns and deformed shapes. Firstly, a horizontal crack appeared at the bottom of the CB leaf, followed by the rupture of both helical bars without any displacement, neither in the inner leaf nor in the outer veneer. Finally, after the rupture of the bars, a joist-sliding failure mode took place.

(a) (b)

Figure 4.25 Rupture of helical bars during testing of specimens TJ5 (a) and TJ6 (b).

A comparison is made between Specimen J6 and TJ6 to investigate the propagation of cracks and the deformed shape with maximum displacement in positive and negative directions, as shown in Figure 4.26. When comparing the inner leaf of both specimens, one can observe that the diagonal cracks, which met around the joist, were extended with new horizontal cracks in the 1st, 4th and 9th bed joints from the bottom. When comparing the inner leaf of both specimens, the outer leaf of Specimen J6 remained in the elastic range during the whole testing. Conversely, after the strengthening, the outer leaf of TJ6 exhibited a quite complex damage pattern. The first cracking consisted of a horizontal crack in the 1st bed joint from the bottom. Secondly, diagonal cracks appeared around each cavity wall tie connection. Since joist sliding is the governing failure mode for both specimens, a similar deformed shape was observed.

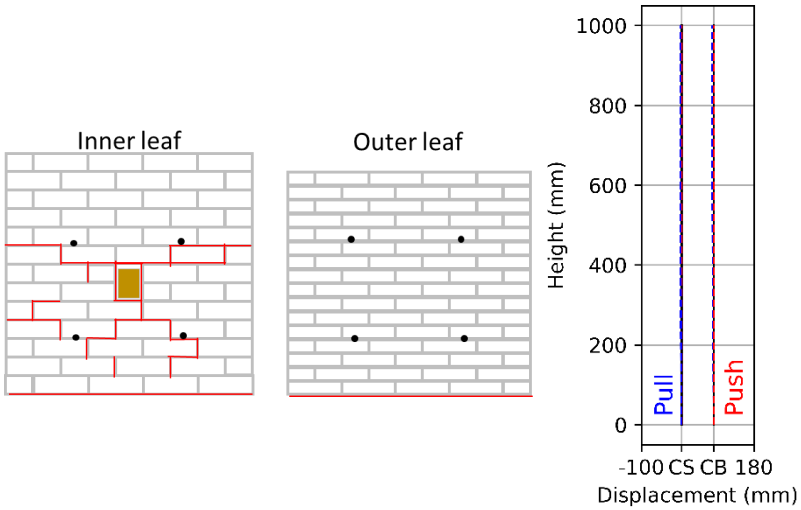

(a) J6 (σ_{VO} =0.3 MPa)

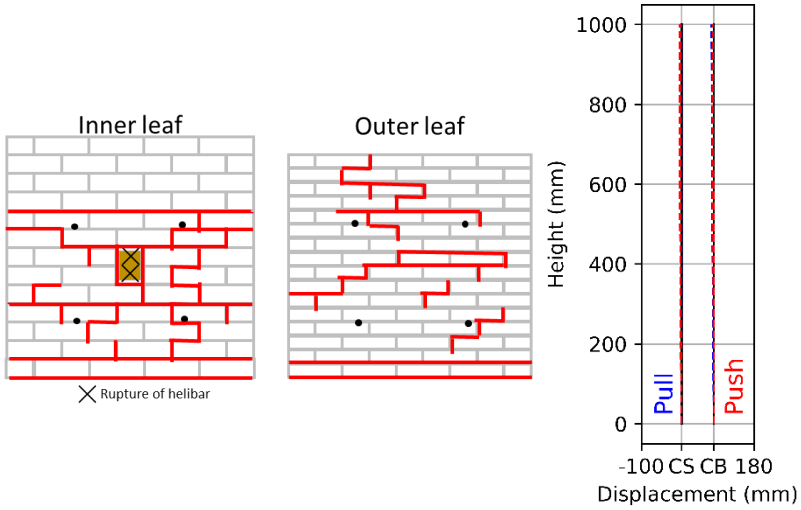

(b) TJ6 (σ_{VO} =0.3 MPa)

Figure 4.26 Comparison of the outcomes of the tests in terms of crack pattern and out-of-plane deflections for specimens J6 and TJ6.

4.5.2 Load-Displacement curves

Force-displacement curves were generated for the strengthened specimens with helical bars, as presented in Figure 4.27. The relative displacement between the joist and wall is indicated on the horizontal axis of Figure 4.27.

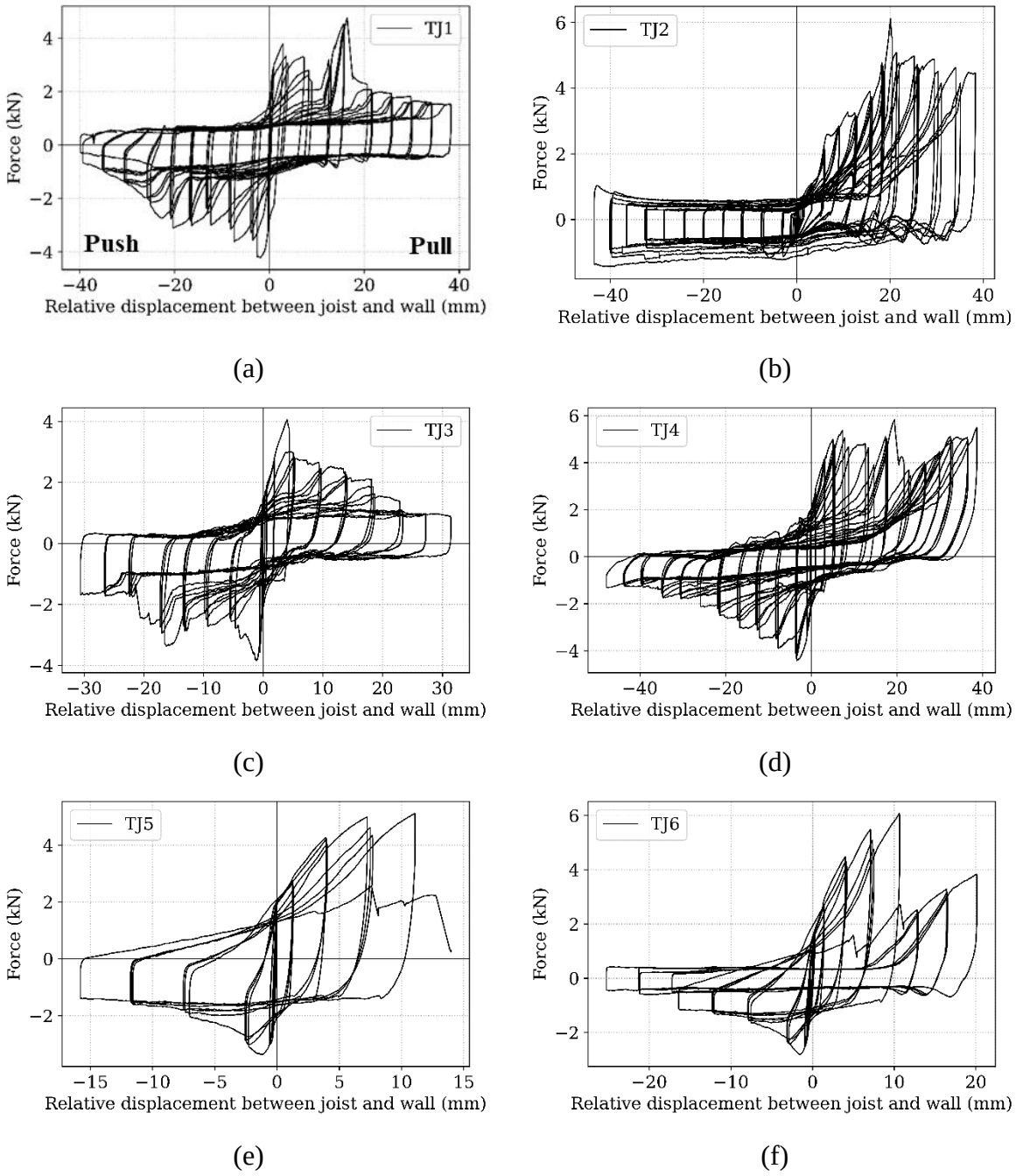

Figure 4.27 Hysteresis curves for the retrofitted and retested specimens.

The hysteresis curve of TJ1 was quite symmetrical in the initial loading stages, characterised by a hinge formation at the bottom of CS. After that point, a softening behaviour took place in pulling and pushing. A second drastic hardening, as seen in Figure 4.28a, began due to the high stresses that occurred in the cavity wall ties and the helical bars, causing the second hinge formation at the middle of CB. In order to further explore the second hardening curve, the focus is placed on the OOP displacement at the middle height of the inner leaf with a comparison between Specimen J1 and TJ1 (Figure 4.28b). When the second hinge took place

in the middle of CB, the OOP displacement at the middle height of the inner leaf was increased, highlighting the contribution of the ties. In addition to that, the inner leaf of TJ1 was displaced in the OOP direction more than two times compared to Specimen J1 thanks to the cavity wall ties effectively transferring the deformation from the outer veneer to the inner leaf, as seen in Figure 4.28b. After the formation of the second hinge in the veneer, the difference between the OOP displacement of the middle and top of the outer leaf becomes not symmetrical for pushing and pulling, as highlighted in red in Figure 4.28c; the corresponding deformed shape can be seen in Figure 4.28d.

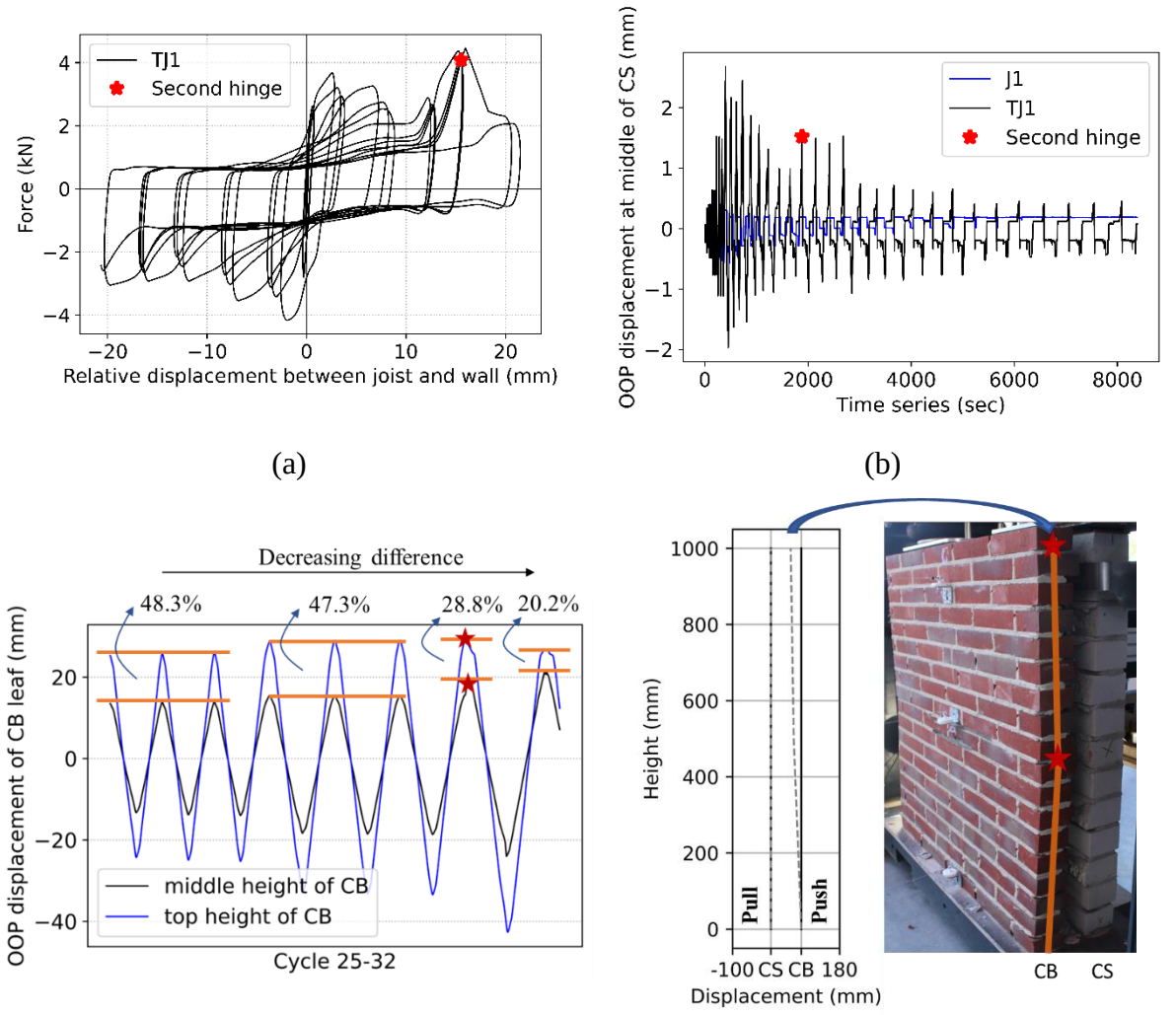

Figure 4.28 Experimental results of specimen TJ1: force transferred via the connection versus relative displacement between the joist and the inner leaf (a), comparison between J1 and TJ1 in terms of the OOP displacement at the middle of the inner leaf (b), OOP displacement at the middle height and at the top of the outer leaf (c), and the deformed shape at the end of the test with a photograph of the corresponding moment during the test (d).

A comparison between Specimen J1 and TJ1 is presented in Figure 4.29 in terms of the backbone envelope curve and accumulated hysteretic energy. The main difference between the two specimens is that the first peak for Specimen TJ1 was due to the capacity of the wall-to-floor connection, while the second peak differently from Specimen J1 was due to achieving the total capacity of the cavity wall system, causing mid-hinge in the outer leaf. Specimen TJ1 presented a higher capacity in both loading directions than one of its corresponding as-build conditions. As mentioned earlier, activating the OOP rocking mechanism by applying the helical bars led to an increase in the strength capacity of the connection. The strengthening solution exhibited a similar energy dissipation, as seen in Figure 4.29c. It is worth mentioning that TJ1 was retrofitted and retested and achieved almost the same amount of energy with a shorter cumulative deformation compared to J1.

It should be noted that the comparison between Specimen J1 and TJ1, J2 and TJ2, J3 and TJ3, J4 and TJ4, J5 and TJ5, and J6 and TJ6 is provided in Annex B in terms of the backbone envelope curve and accumulated hysteretic energy.

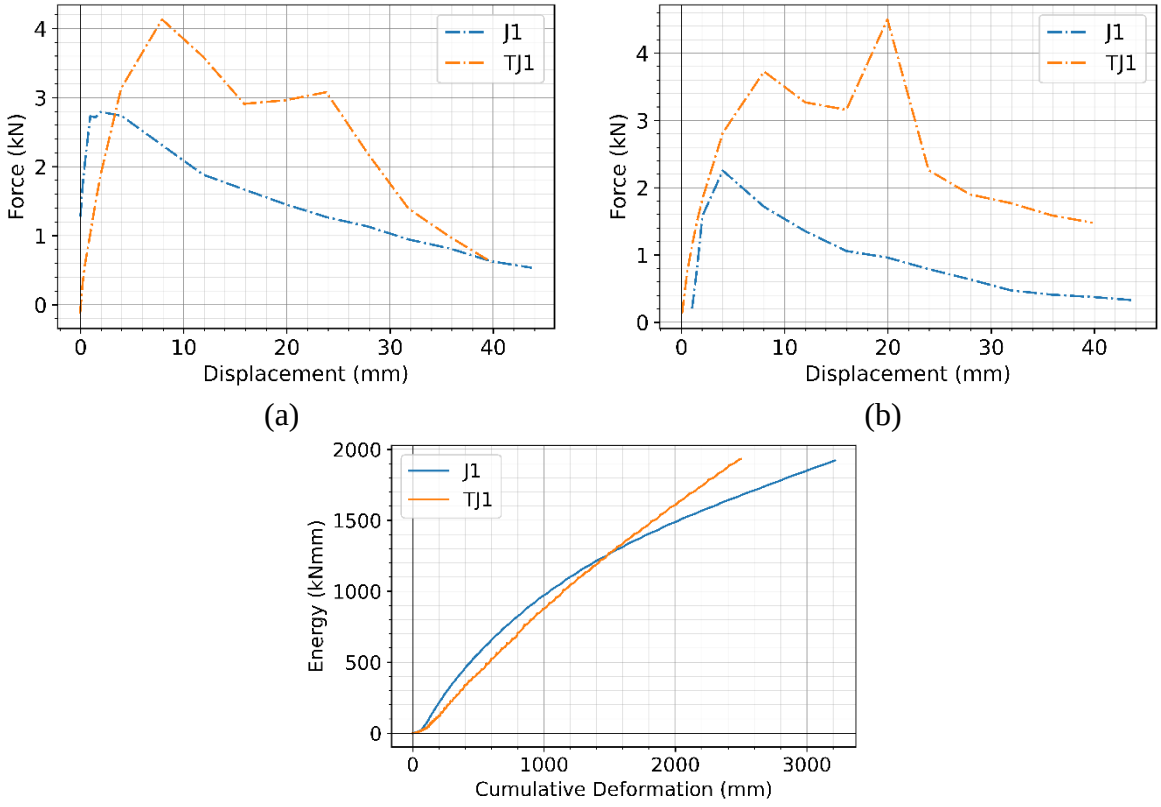

Figure 4.29 Comparison between J1 and TJ1 in terms of average envelope curves in the pulling (a) and pushing (b) directions, and of cumulative hysteretic energy (c).

Regarding Specimen TJ2, connecting the outer leaf and the timber joist with the helical bars led to a horizontal crack along the 1st bed joint from the bottom of the outer leaf, followed by the OOP rocking mechanism of the cavity wall. A second horizontal crack took place in the middle of CB and tended to instability. The strengthened connection provided a better connection for the wall, which can be detected from the deformation of the outer leaf. However, the strength capacity did not increase compared to that of the as-built condition since the total number of cavity wall ties is insufficient to adequately connect the leaves.

Specimen TJ3 exhibited a more brittle behaviour compared to Specimen TJ1 since the stiffness of TJ3 is higher due to a large number of as-built ties. Unlike the previous specimens, both hinges at the base and middle height of the outer leaf were detected in the initial loading stages since the flexural capacity of the wall wasn't enough to carry the load caused by the strengthened connection. The two leaves, up to an imposed displacement of 4 mm, were moving in parallel due to the contribution of the cavity wall ties transferring force and deformation, and the softening behaviour took place after this point (Figure 4.30a). Another interesting observation is that after this point, the sliding of the joist took place; thus, the OOP deformation only occurred in the outer veneer with the hinges, leading to a complete formation of the rocking mechanism of the outer veneer (Figure 4.30b). Followed by the hinges, the middle height of the outer leaf (highlighted with a red star) was moving in the opposite direction of the top part of the outer leaf creating a phase difference movement (highlighted with a yellow star), as seen in Figure 4.30c and d.

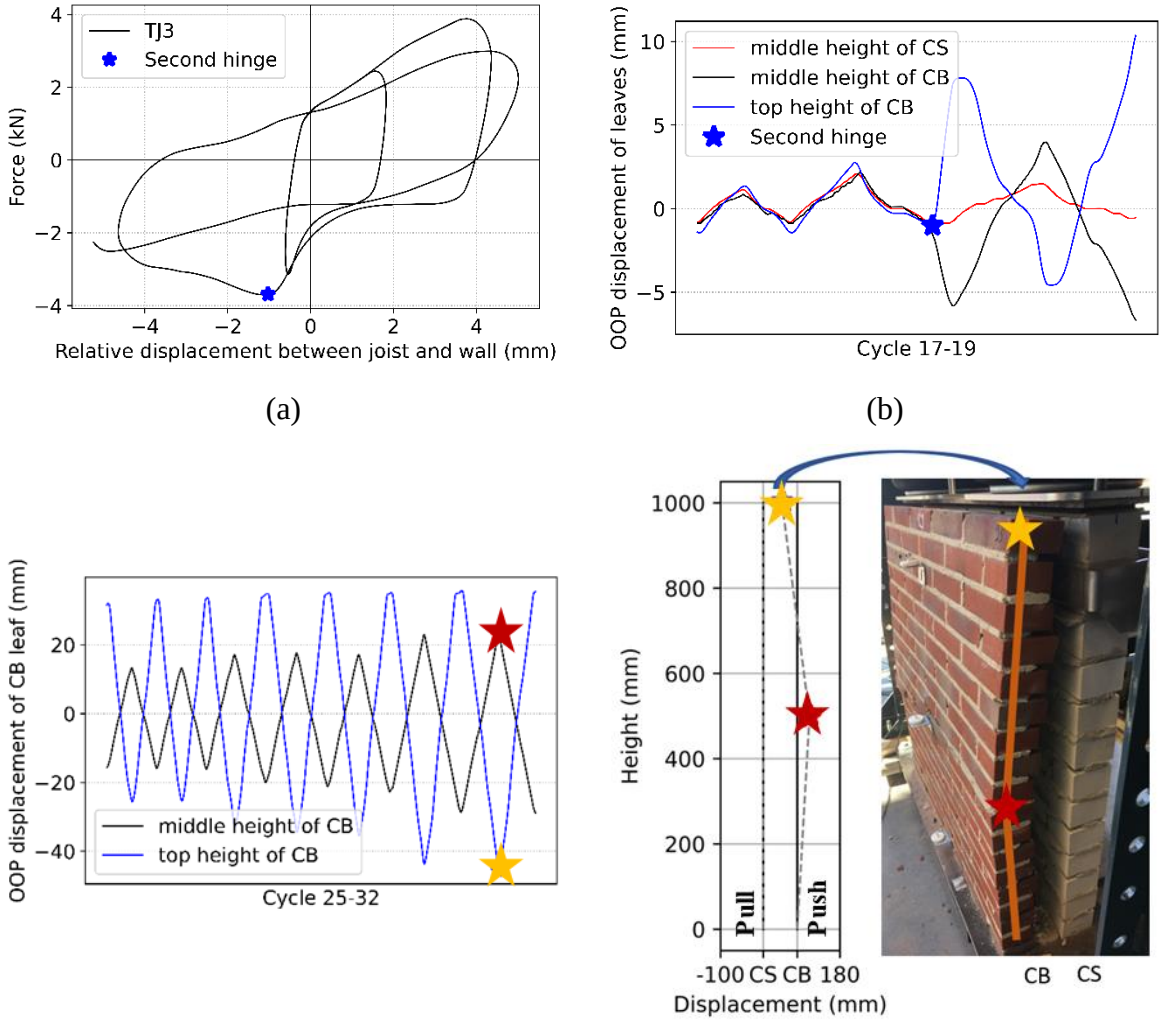

Figure 4.30 Detail of the experimental results of specimen TJ3. For cycles 17-19: Hysteresis loop of force versus relative displacement between the joist and inner leaf (a), and OOP displacement at middle height and of inner and outer leaves, and at the top of the outer leaf (b). For cycles 25-32: OOP displacement at the middle height and at the top of the outer leaf (c), and the deformed shape at the end of the test with a photograph of the corresponding moment (d).

Specimen TJ4 showed the rocking failure mode as the aforementioned specimens and as shown in Figure 4.31. In pulling, the post-peak phase was characterised by a plastic plateau up to large displacements (40mm). Although the failure mode was characterised by rocking behaviour, the global wallet behaviour in the pulling direction was affected by the local anchor behaviour, the yielded masoned-in anchor exhibiting a plastic plateau on the analogy with a plain steel bar. While in the pushing direction, the post-peak showed a softening behaviour due to the hinges at the bottom and middle of the outer leaf.

(a) (b)

Figure 4.31 Rocking behaviour of specimen TJ4 under pulling (a) and pushing (b) loading.

Unlike the aforementioned strengthened specimens, for Specimen TJ5 and TJ6, the capacity of the strengthened connection was not able to activate the OOP rocking mechanism behaviour as the helical bars ruptured due to the increased stiffness and lateral resistance of the wall caused by the higher pre-compression level and the larger number of embedded ties. The connection exhibited an initial linear elastic behaviour of the connection up to 2 mm displacement, followed by hardening in the pulling direction and softening in pushing until the failure of the helical bars. The hysteresis curve was asymmetric, which can be attributed to the behaviour of the helical bars in tension and compression. The helical bars buckled in compression while exhibiting a pull-out failure in tension. It should be noted that an increase in the applied overburden pressure results in an increase in the initial stiffness of the specimen. Therefore, the helical bars ruptured for both Specimen TJ5 and TJ6, which used the same strengthening solution (helical bars) and had a pre-compression level of 0.3 MPa.

Annex B (Figure B.2) presents a comparison between the as-built and strengthened conditions of each corresponding group in terms of the backbone envelope curve and accumulated hysteretic energy. The left, middle, and right diagrams display the envelope curves under tensile and compressive loading, as well as the accumulated energy, respectively.

4.6 Experimental results of the specimens with strengthened cavity wall anchors and timber joist-masonry connections by means of timber blocks

A total of six walls were constructed of the same configuration as specimen J2, except for a different veneer unit type, namely perforated clay brick and a different mortar quality used for the inner leaf. Specimen F4 was damaged during positioning on the test setup and hence excluded from the cyclic test. The experimental findings will be described in the following section.

4.6.1 Failure modes

The strengthened specimens, in general, exhibited a rocking failure mode. However, except for Specimen F3, a local failure mechanism at the anchors between the wallet and the timber blocks occurred in addition to the rocking failure mode. The specimens presented a failure of the connection between the timber blocks and the inner leaf due to the presence of post anchors sufficiently increased OOP capacity shifting than the weakest failure mechanism from rocking to the failure of the connection. On the other side, regarding Specimen 3 lacking post-installed cavity wall tie anchors, the inner leaf was not restrained to horizontal displacement via the cavity wall tie anchors; hence, the OOP capacity of the wallet was weaker than the capacity of the connections between the timber block and the wallet, exhibiting rocking behaviour.

It should be noted that after applying the strengthening solution, cracks were initiated on the specimen around the anchors of the timber blocks, which had fastened the timber blocks to the inner leaf. Hence, the crack pattern before testing is also marked. The crack pattern of each strengthened specimen can be seen in Figure 4.32 at the conclusion of strengthening and testing by the left and right diagrams, respectively. The position of the as-built ties, the post-installed cavity wall anchors, the anchors used for timber blocks and the joist is also presented to compare the position of the cracks with respect to the anchors.

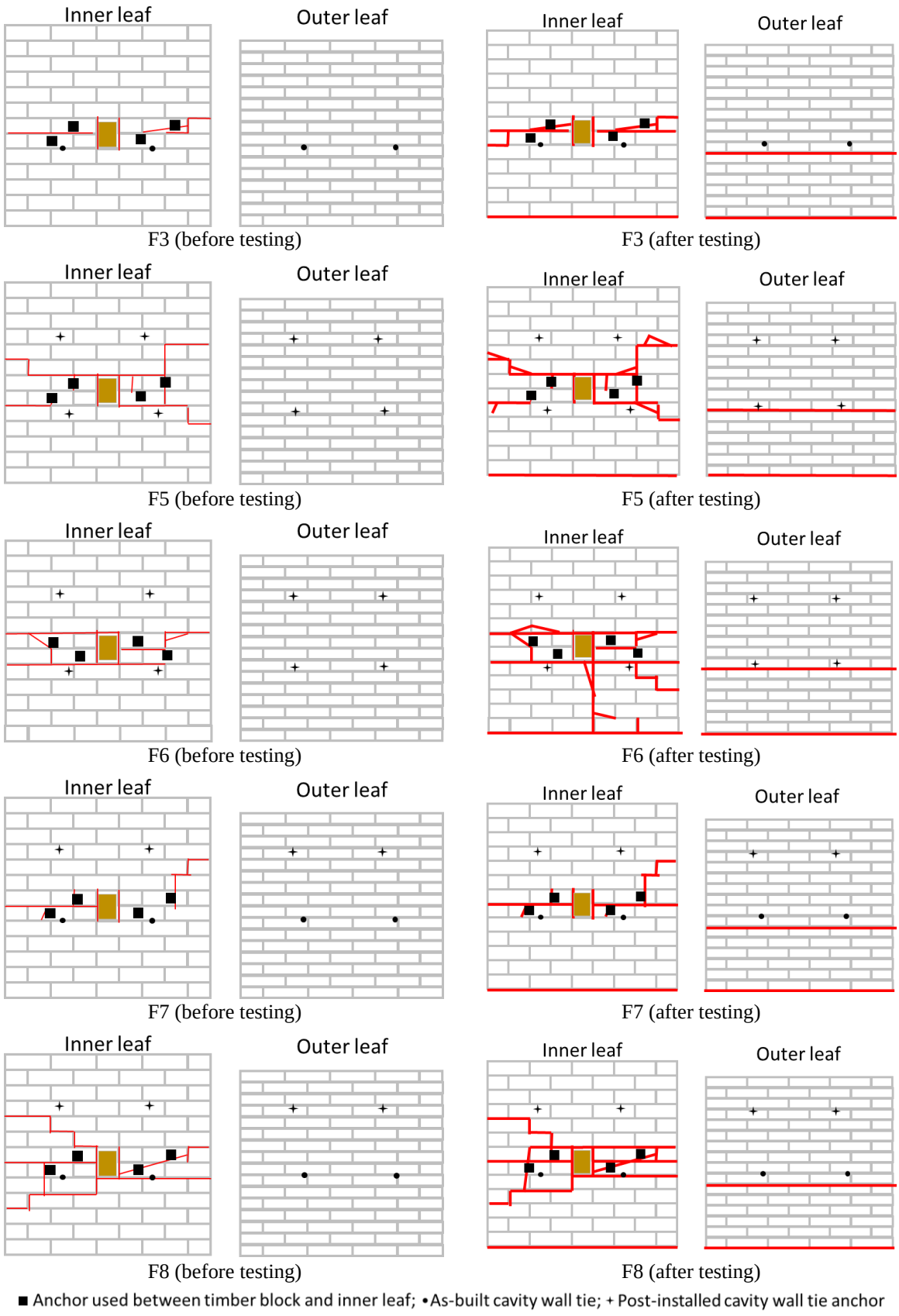

Figure 4.32 Crack patterns of the strengthened specimens after strengthening (left diagrams) and testing (right diagrams).

The deformed shape of strengthened specimens with maximum displacement in positive and negative directions can be seen in Figure 4.33. Unlike the previously presented strengthening solution, the inner leaf undergoes the rocking type behaviour as well, resulting in the formation of a hinge at the bottom and middle height of the CS leaf. Hence, the rocking behaviour was the governing failure mode.

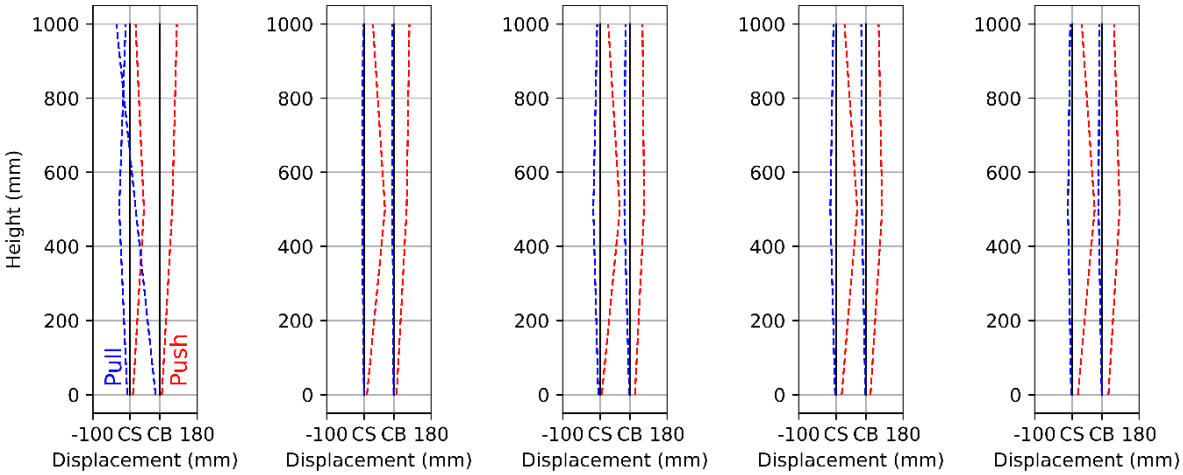

(a) F3 (b) F5 (c) F6 (d) F7 (e) F8

Figure 4.33 Deformed shapes of the strengthened specimens. The dashed lines indicate envelope deformed shapes in positive and negative directions.

4.6.2 Load-Displacement curves

Force-displacement curves were generated for the strengthened specimens with timber blocks and post-installed cavity wall ties, as presented in Figure 4.34. The relative displacement between the joist and wall is indicated on the horizontal axis of Figure 4.34. The strengthened specimens generally exhibited a higher strength capacity than those in the as-built condition. The main difference between the previous specimens, as mentioned earlier, and the current strengthening method was that during the experiment, there was a progressive shift towards only one side of loading, specifically the pulling (positive) direction, in which slippage developed due to the pull-out of the anchors from the wallet. On the other side, while pushing the joist towards the wallets, the slippage of the joist remained in the same position. It should be noted that despite being a strengthened specimen with timber blocks, Specimen F3 exhibited symmetrical behaviour for both loading directions due to retrofitting only using the timber blocks lacking post-installed cavity wall tie anchors, leading to lower OOP capacity of the wallet, which caused it to exhibit rocking behaviour.

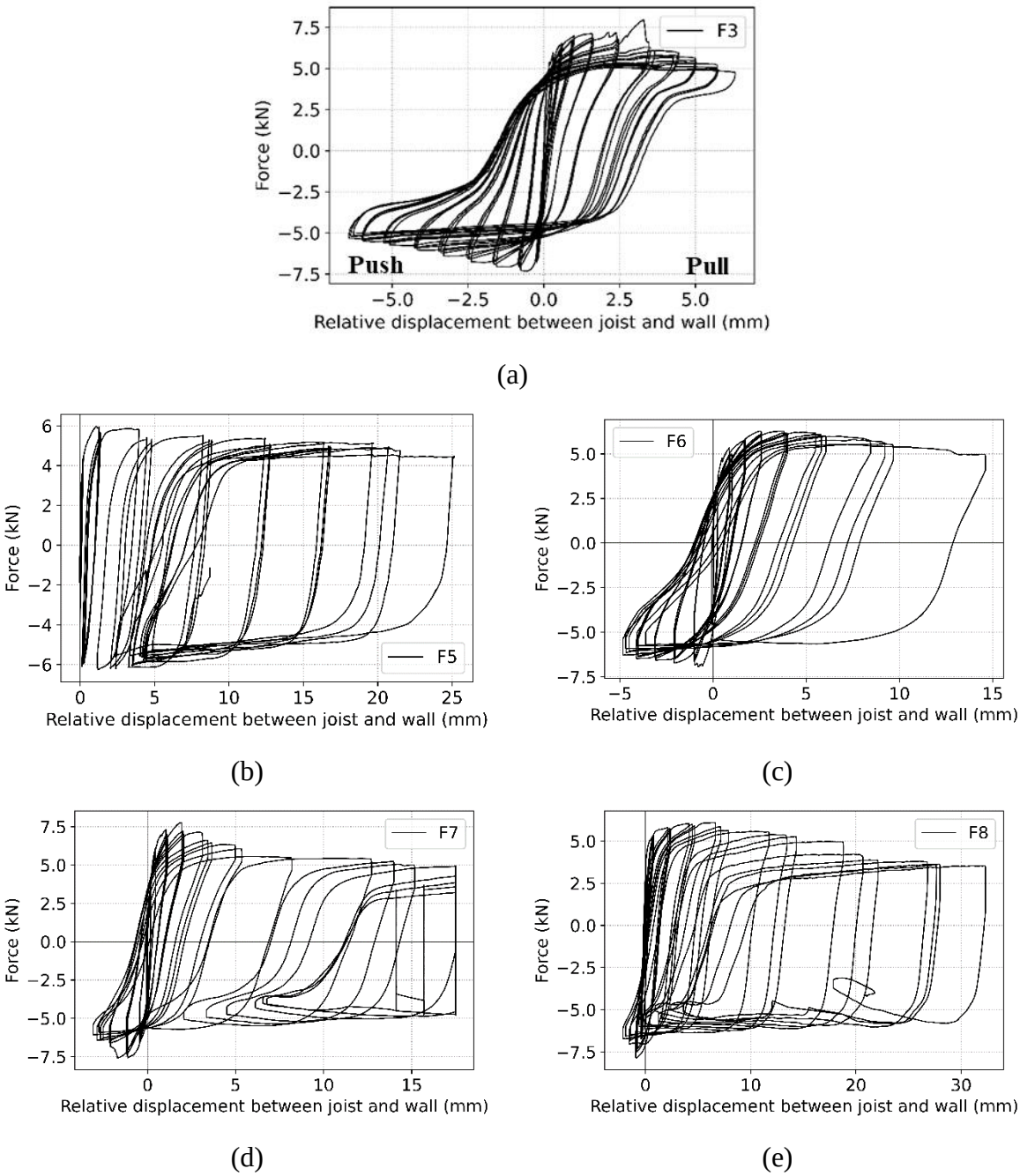

Figure 4.34 Hysteresis curves of the strengthened specimens.

Specimen F3 (the specimen retrofitted using timber blocks) exhibited the highest strength capacity in pulling. The hysteresis curve was quite symmetrical, indicating similar behaviour for both loading directions. In pulling, an initial linear elastic behaviour of the connection up to about half of the peak load was followed by hardening up to the peak. The post-peak phase was characterised by softening. An abrupt change of the force was observed in pulling due to the development of a second hinge at the middle height of the outer leaf (Figure 4.35a and b). The onset of cracking at the mid-height of the outer veneer was captured by a decreasing

difference between the middle and top of the outer leaf, highlighted in red in Figure 4.35c, and the corresponding deformation shape can be seen in Figure 4.35d. Up to the second hinge at the middle of the outer leaf, cracking occurred simultaneously at the bottom and mid-height of the inner leaf and the bottom of the outer veneer.

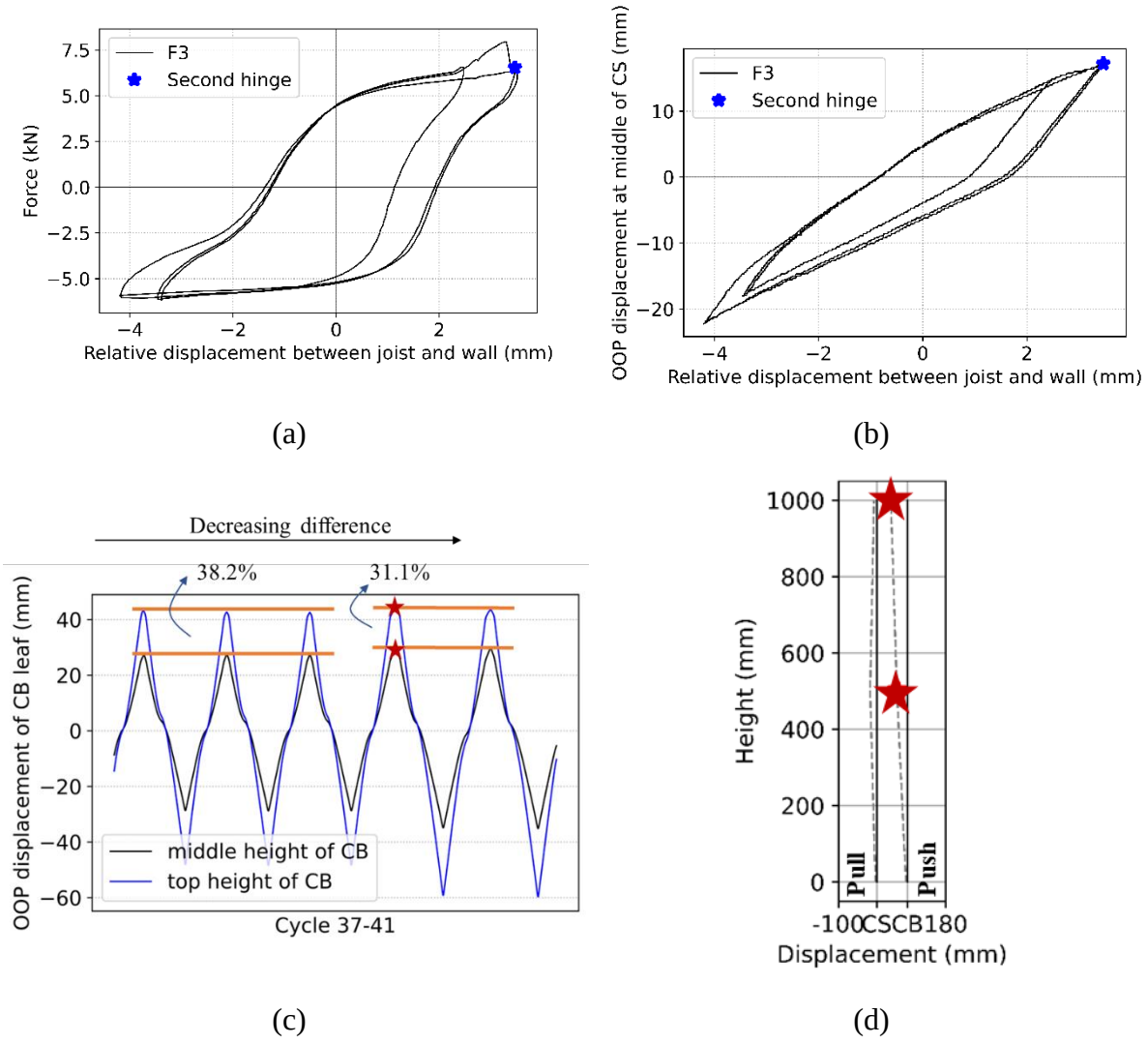

Figure 4.35 Detail of the behaviour of Specimen F3. Hysteresis curve corresponding to the development of a second hinge at the middle of the outer leaf (a), OOP displacement at the middle height of the inner leaf versus relative displacement between the joist and inner leaf (b), OOP displacement at middle height and top of the outer leaf (c) and the deformed shape corresponding to the moment of the development of the second hinge (d).

Specimens F5 and F6 have the same configuration. The hysteresis curves of F5 and F6 were unsymmetrical, presenting a similar behaviour. An initial linear elastic behaviour of the connection up to about one-sixth of the peak load was followed by hardening up to the peak. The post-peak phase was characterised by softening. Both specimens were characterised by the formation of hinges in the inner and outer leaf at the very beginning of the loading sequence

(Figure 4.36a). As seen in Figure 4.36b, both leaves were displaced simultaneously thanks to the post-installed ties. The as-built and post-ties provided a sufficient coupling of the horizontal displacement of the two leaves, as seen in Figure 4.36c. Besides, the timber blocks were accompanied by a high value of slip at the anchors of timber blocks in the joist pulling direction of loading; while the joist moved toward the wall, OOP displacement in the inner leaf took place in the loading direction.

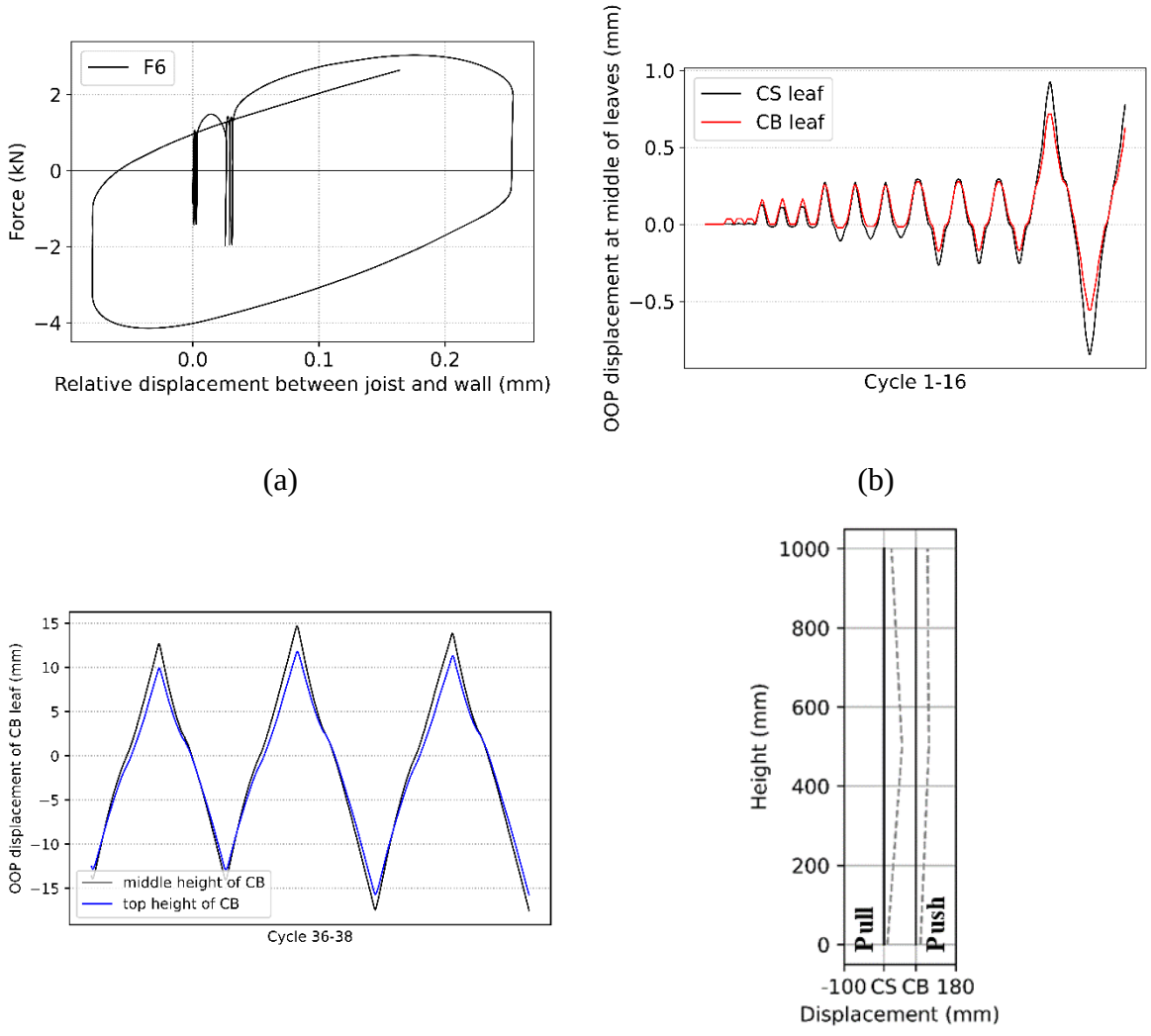

Figure 4.36 Detail of the experimental results of specimen F6. For cycles 1-16: Hysteresis loop of force versus relative displacement between the joist and inner leaf (a), and OOP displacement at middle height and of inner and outer leaves, and at the top of the outer leaf (b). For cycles 36-38: OOP displacement at the middle height and at the top of the outer leaf (c), and the deformed shape at the end of the test (d).

Although Specimens F7 and F8 with as-built cavity-wall ties were retrofitted using post-installed cavity wall tie anchors and Specimens F5 and F6 without as-built cavity-wall ties were

retrofitted using post-installed cavity wall tie anchors, the capacity of Specimens F7 and F8 were of a similar magnitude to the peak forces from Specimens F5 and F6. As the total number of ties was the same for all the specimens mentioned above, the specimens only with post-installed cavity wall tie anchors would exhibit a higher capacity since they have a higher strength capacity. However, in this case, bonding between the tie and masonry played an essential role; as reported in this study, the post-installed anchors caused damage during the installation; hence the pull-out capacity of the anchors was decreased. Overall, the failure mode was the rocking behaviour besides the failure of the connection between the timber blocks and the formation of a hinge at mid-height of the inner leaf and the veneer leaf.

4.6.3 Hysteretic energy dissipation

For ease of comparison, backbone envelope curves of the strengthened specimens are obtained from the peak points of each cycle. The envelope curves under tensile and compressive loading are shown in Figure 4.37a and b, respectively. The effect of the strengthening of the connection between the joist and inner leaf and the inner and outer leaves can be seen as follows:

- The specimens with as-built wall ties retrofitted using the timber blocks and post-installed cavity wall tie anchors had the highest capacity.
- The specimens with as-built wall ties retrofitted only using the timber blocks exhibited slightly less strength capacity than the aforementioned specimens.
- Interestingly, the specimens lacking as-built wall ties retrofitted using timber blocks and post-installed cavity wall ties produced the least strength capacity, which can be explained by the failure of the bond between the post-installed cavity wall anchors and masonry.

A comparison of the accumulated hysteretic energy for the specimens with strengthened cavity wall anchors and timber joist-masonry connections is given in Figure 4.37c. The cumulative dissipated energy was evaluated by calculating the area enclosed by the "Force-Displacement" loops. The total energy dissipated by the system is determined by adding up the energy dissipated per loop up to that reversed cyclic displacement. The strengthened specimens dissipated a similar amount of energy compared to that of the specimens with timber joist-masonry connections strengthened by means of helical bars and unstrengthened connections. It should be noted that although the energy was dissipated via more elements compared to the previous specimens, including bond strength between masonry and as-built connections, friction in the as-built connections, post-installed cavity wall anchors and the anchors used for

timber blocks, and residual deformation in the connections and anchors, the total dissipated energy was similar due to the brittle behaviour of post-installed cavity anchors and the damage propagated during the installation of the anchors. Hence, comparing the specimens within the same strengthening solution was similar in terms of energy dissipation due to the same reason mentioned above.

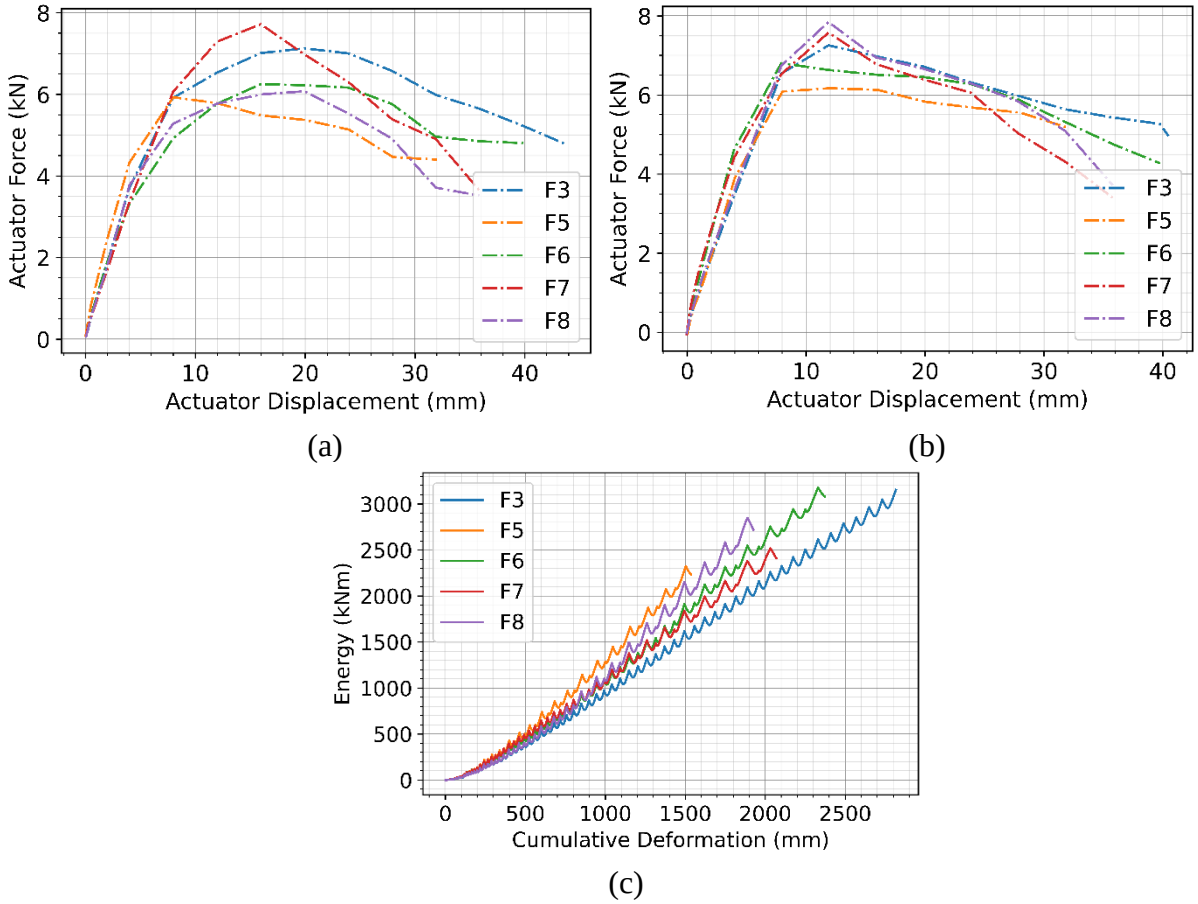

Figure 4.37 Average envelope curves for the strengthened specimens in both the pulling (a) and pushing (b) directions. Cumulative hysteretic energy (c).

4.7 Conclusions

This chapter presents the results of an experimental campaign that consists of quasi-static cyclic tests performed on as-built and strengthened timber joist-cavity wall specimens. The experimental campaign aimed at providing a complete characterisation of the behaviour of the timber joist-cavity wall connections under cyclic axial loading.

Regarding the as-built condition, two different failure modes were obtained: joist-sliding and rocking failure modes. Regarding the joist-sliding failure mode, the considered variations had an influence on the capacity. For example, an increase in the pre-compression level resulted

in a higher friction force, while a higher quality of mortar strength influenced the cohesion between timber and masonry. The failure mode was characterised by the cohesion and friction between the joist and masonry. Hence, the diagonal cracks propagating from the joist in the shape of punching shear were due to the bonding between the joist and the masonry wall. Additionally, the capacity of the connection was affected by an additional vertical force due to the arching effect. This force, resulting from the arching effect, increased with larger horizontal displacements, leading to a higher frictional force at the interface between the joist and masonry.

The obtained force-displacement curves of the as-built specimens were asymmetrical with respect to the pulling and pushing loading directions. Although the hysteresis loops of the masonry pocket connections, namely mortar pocket and hook anchor, were mainly characterised by frictional behaviour, additional vertical forces were observed due to the boundary conditions of the specimens. On the other hand, the asymmetrical hysteresis loops for the hook anchors were attributed to the effect of the hook anchor. In addition, the pinching effect was developed as the hook anchor was located on the pocket of the inner leaf, bearing against the exterior surface of the CS leaf in pulling while relying on frictional behaviour only in the pushing direction.

A large part of the current chapter on timber-joist connections has been dedicated to highlighting two significant factors: frictional behaviour and the arching effect. These factors are essential to consider as they are commonly encountered in real buildings, and their presence can impact the performance of timber-joist connections. The specific contributions discussed in this chapter include:

(i) Frictional behaviour: This refers to the resistance observed and expected at the interface between timber joists and the masonry wall.

(ii) Arching effect: Special attention should be given to assessing the out-of-plane behaviour of masonry walls at the lower floor level, where higher overburdens and stiffer parts of the wall above may activate the arching action.

In the case of both hook anchor as-built and strengthened connections, failure was attributed to the rocking of the wallet. Therefore, the capacity was primarily governed by the out-of-plane behaviour of the cavity wall system. This behaviour was influenced by the flexural strength of both the inner and outer leaves and the coupling force provided by the ties between the leaves. In general, only a slight increase in capacity compared to the as-built condition was observed for the strengthened specimens, as an OOP rocking mechanism was already activated

for the as-built condition: this limits the capacity of the wall system so that the improvement of the connection performance has little influence.

By comparing the experimental results of the strengthened connections to the as-built specimens in terms of peak load, an average increase of 5% in peak load for pulling and 9% for pushing was observed. It should also be mentioned that, particularly in the strengthened specimens with timber blocks, post-installed cavity wall anchors work as stress concentrators, leading to splitting cracks around the anchors. Hence, comparing the specimens with as-built wall ties retrofitted with timber blocks to the specimens lacking as-built wall ties and retrofitted via timber blocks and post-installed cavity wall ties, a lower strength capacity was observed.

In closing, the added value of strengthening is the increased displacement capacity of the joist, thus preventing sliding and unseating of the joist. The contribution of the strengthening of the timber joist is not an increase of strength but creating deformation compatibility between wall and joist, thus increasing overall deformation structural capacity and ductility.

Chapter 5: Mechanical and numerical modelling of wall tie connections

As part of the final phase of the thesis, following the completion of the experimental campaign on the cavity wall tie connections, which was explained in detail in Chapter 3, mechanical and numerical models are developed and verified by the experimental results of the cavity wall tie connections. The research presented in this chapter focuses on a mechanical model developed to predict the failure mode and the strength capacity of metal tie connections in masonry cavity walls and a numerical model adopted for the cyclic axial response of cavity wall tie connections. The proposed mechanical model considers six possible failures, namely tie failure, cone break-out failure, pull-out failure, buckling failure, piercing failure, and punching failure. The mechanical model has been validated against the outcomes of the aforementioned experimental campaign. Furthermore, the proposed mechanical model is used to extrapolate the experimental results to untested configurations by performing parametric analyses on key parameters, including a higher strength mortar of the calcium silicate brick masonry, a different cavity depth, a different tie embedment depth, and solid versus perforated clay bricks. Section 5.1, which describes the mechanical model for the wall ties, is adapted from Arslan et al. [44].

The proposed numerical model utilises the results of the experimental campaign on tie connections to calibrate a hysteretic model that represents the cyclic axial response of cavity wall tie connections. The proposed numerical model uses zero-length elements implemented in OpenSees with the Pinching4 constitutive model to account for the compression-tension cyclic behaviour of the ties. Section 5.2, which describes the numerical model for the wall ties, is already described in the study of Arslan et al. [45].

5.1 Mechanical modelling of cavity wall tie connections

As mentioned, despite the advantages of cavity walls in terms of durability and installation functions such as moisture control, observations from damaged buildings have shown that cavity walls are vulnerable to out-of-plane (OOP) failures when the connections between the two leaves are weak (Figure 5.1). The behaviour of the cavity wall tie needs to be adequately investigated and to be properly modelled. For this reason, the experimental campaign on the

wall tie connections explained in detail in Chapter 3 is used here for model validation. Briefly, the campaign was based on tests at the component level, including a large number of parameter variations, i.e., two embedment lengths, four pre-compression levels, two different tie geometries, and five different testing protocols — the experimental campaign aimed to define the capacity of the cavity wall ties. Different failure modes of the ties were observed during the experimental campaign: sliding, tie, buckling, and expulsion.

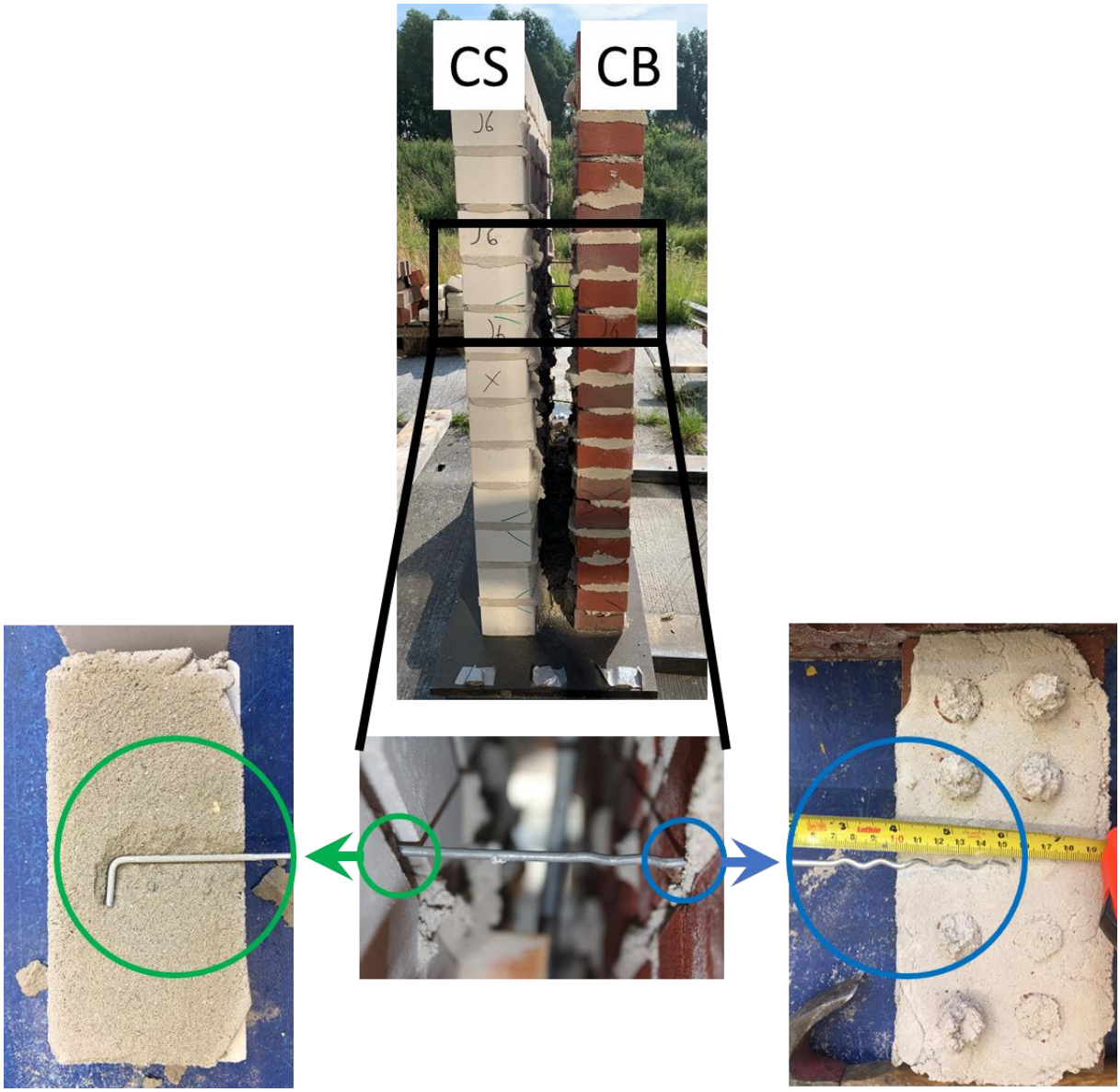

Figure 5.1 Cavity wall (inset – zoom on inner-to-outer leaf with cavity wall tie).

5.1.1 Review of Past Research on mechanical modelling

In literature, various failure modes were reported for cavity wall tie connections either through tests at the component level [38,76,111,112] or on full-scale structures [34,74,113–115]. In the

latter case, the primary cause of failure for most cavity walls was related to the failure of the wall tie connections [74,76,115], raising the need to provide better mechanical modelling for this structural component. Different types and geometries of the ties, errors in construction, insufficient embedment, and installation methods can affect the overall strength and failure modes of the tie connection. Nevertheless, little research (such as [116–119]) has been performed to define a mechanical model of cavity wall ties in masonry structures.

The possible failure modes of anchors embedded in masonry bed joints are similar to those observed for cast-in-place headed anchors embedded in concrete, which have been widely studied under various conditions, such as for a single anchor far from edges [120–123] or for an anchor near edges [124,125]. The existing failure modes of anchors embedded in concrete for tension both far from and near edges are shown in Figure 5.2, namely, rupture, concrete breakout cone, pull-out, splitting and blow-out failures [126]. The observed failure modes in concrete can be applied to anchors in masonry since the developed analogy between anchor and substrate is similar.

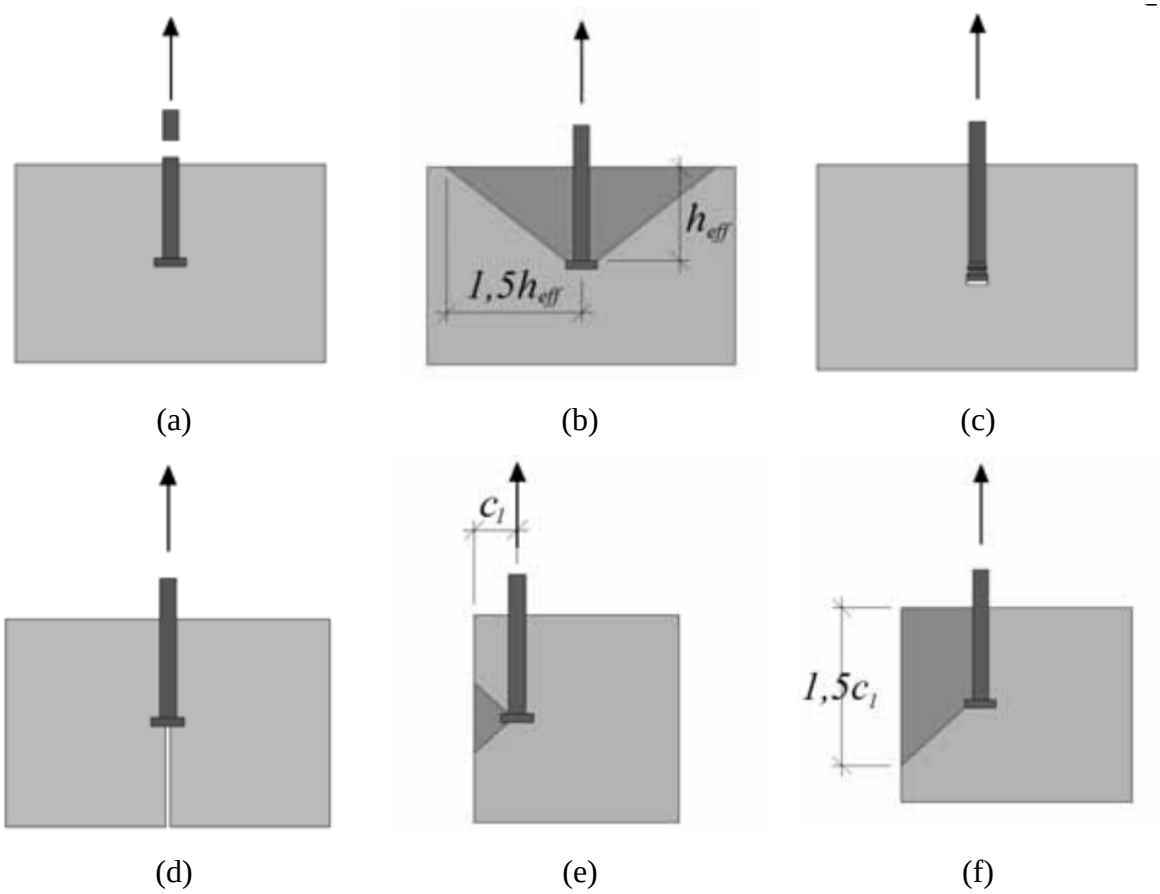

Figure 5.2 Failure modes observed for anchors for tension in concrete from Kuhlmann et al. [126]*: steel failure (a), concrete cone failure (b), pull-out failure (c), splitting failure (d), local blow-out failure (e), steel failure (f).*

Arifovic and Nielsen [127] too proposed an analytical model for anchors in masonry based on the theory of plasticity and calibrated after the experimental results conducted by Hansen et al. [128]. The proposed model was based on the distinction between local and global failure modes. The local failure modes regard the inner interface between the grout and the anchor, whereas the global failure modes regard the outer interface between masonry and grout. A total of five failure modes (combined brick-cone failure, splitting failure, sliding failure of an anchor in the joint and the brick, and punching failure) were defined to compute the load-carrying capacity of the anchors. The proposed model in masonry was developed by the analogy of the approach of the anchorage theory, and it is worth noticing that mortar can behave similarly to normal concrete [129].

Different failure modes of anchors in masonry walls are also identified by the Masonry Standards Joint Committee [130], such as rupture failure, pull-out failure and tensile cone break-out failure. A 45-degree cone model is used for predicting tensile cone break-out failure with constant tensile stress acting over the projected failure cone by MSJC. However, MSJC does not take into account the difference between the zigzag end of the tie embedded in clay brick and the hooked end of the tie embedded in calcium silicate, which is often present in constructions.

In compression, punching failure is a possible failure mode. Moe [131] proposed an empirical equation to compute the punching strength based on the experiments conducted by the author. In this proposed equation, the punching strength is proportional to the square root of the compressive strength of the concrete. The work of Moe served as a basis for punching shear design provisions of the ACI Building Code. The assessment of the punching failure is presented in the ACI 318-14 Building Code provisions [132].

Lintz and Toubia [133] proposed a simplified analytical method to determine the amount of load transferred via the ties to the brick in veneers and found that placing vertical reinforcement in the outer leaf may allow for an increase in the design strength.

The metal ties used in Dutch construction practice are not initially designed and built against seismic forces. This is because Groningen, a northern area within the Netherlands, was not a seismically prone area until recently when the gas extraction caused small shallow earthquakes. This is the reason why the metal ties studied may lack the necessary strength and ductility to resist seismic actions. If designed and constructed properly, however, metal ties can make a significant contribution to the seismic resistance of masonry cavity walls. In Australian practice, for example, several types of metal ties can be used in accordance with the Australian

Masonry Structures Code, AS 3700 [134]. Extensive research supports this; for example, Page et al. [135] developed an analytical model to predict loads in the wall ties under seismic actions. The study provides a valuable understanding of the behaviour of cavity walls in terms of the relative stiffness and the boundary conditions of each leaf and the stiffness of the ties. Another study was conducted on typical Australian cavity walls to determine individual tie forces subjected to lateral loads [136]. In this study, a steel strip tie was used between the outer and inner leaves. The strip ties are more flexible and thus may fail in buckling at a very low load, compared to the L-shaped ties used in the Netherlands. Page et al. [136] developed a simplified test method to monitor each individual tie force in the cavity wall so that tie force redistribution can be detected when cavity wall tie connections reach their capacity.

Considering the models already described in the literature and the outcomes of the experimental campaign carried out at Delft University of Technology, explained in detail in Chapter 3, a mechanical model which considers six different possible failure modes is proposed in this thesis to define the axial behaviour of metal tie connections in masonry cavity walls. The outcomes of this research are limited to masonry walls with the characteristics considered, whereas other construction techniques and/or materials would require specific studies. Namely, the mechanical model refers to connections in cavity walls made with calcium silicate bricks (CS) and solid or perforated clay bricks (CB). The model has been calibrated and validated against the experiments introduced in Chapter 3. Finally, the proposed mechanical model has been used to integrate the outcomes of the experimental campaign by performing parametric analyses to assess the influence of several key parameters.

5.1.2 Development of mechanical model

A mechanical model is proposed for each of the six basic failure modes, namely tie failure, cone break-out failure, pull-out failure, buckling failure, punching failure and piercing failure. Once the strength of each mechanism is known, the governing failure mode is the mode with the lowest strength that governs the capacity of the connection.

Metal ties are used in masonry buildings to connect the inner leaf made of CS brick masonry and the outer veneer of clay brick masonry in a cavity wall. Different types of cavity wall metal ties can be found. The current study focuses on cavity walls made of calcium silicate brick masonry (for the inner leaf), and perforated clay brick masonry (for the outer leaf), connected by metal ties with a zigzag end embedded in calcium silicate brick masonry (CS) and a hooked end were embedded in perforated clay brick masonry (CB), as explained in

Chapter 3. The geometry used to define the model is shown in Figure 5.3. L-shaped cavity wall ties with diameter, d_t, and the total length, l_t, are embedded between two bricks in the mortar joint with thickness, t_m. Embedment length, l_b, is different at each end of the tie in the leaves of cavity walls. The zigzag end with length, l_h, approximately two times of the diameter of the tie is embedded in the CB masonry, while the L-shaped hooked end with length, l_h, is embedded in the inner CS walls. The cross section of the wall is shown in Figure 5.3c, while Figure 5.3d shows the plan view.

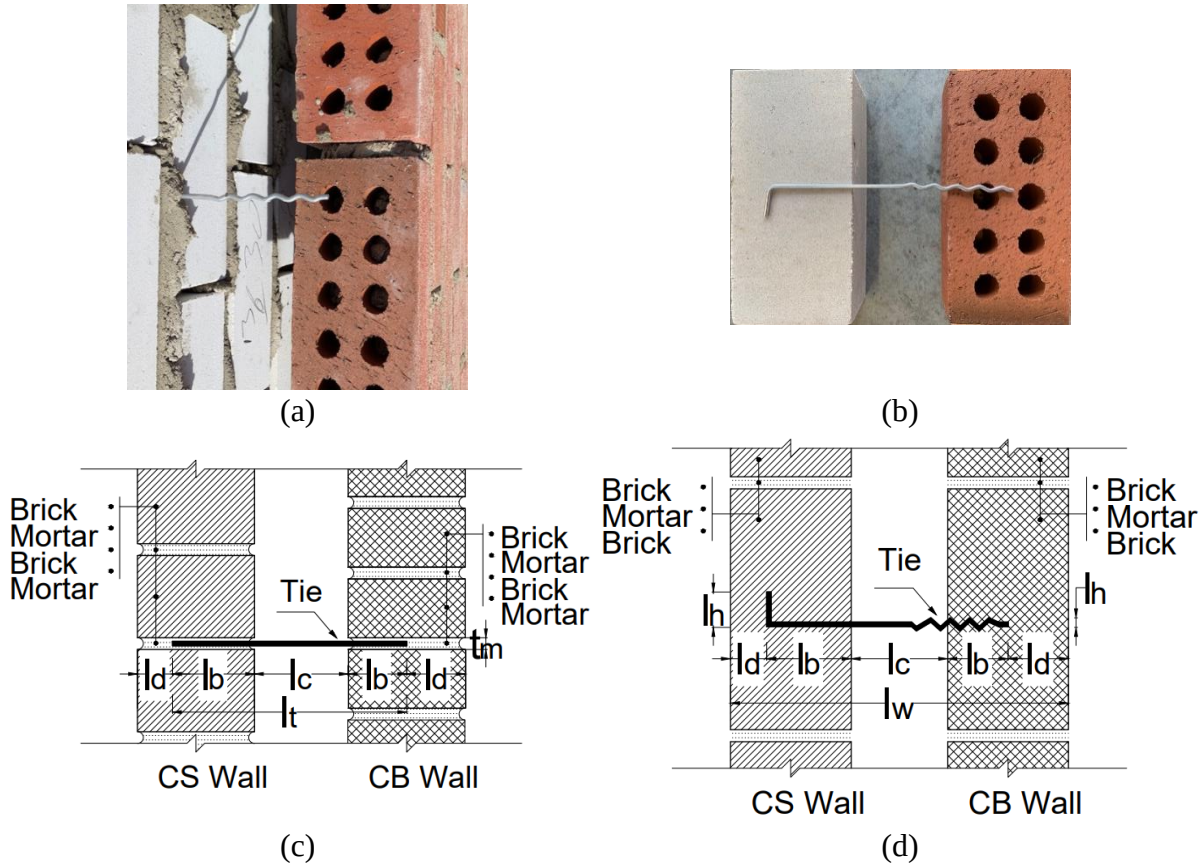

Figure 5.3 Connection details in cavity walls: tie embedded in CS (a), cavity wall tie(b), cavity wall side view (c), and cavity wall plan view (d).

It should be noted that the study presented here focuses on the axial behaviour of the cavity wall tie connections since the stiffness of the ties in shear is low and thus neglected. The behaviour of the connections under tensile and compressive axial loads is distinguished. In the literature, pull-out failure and buckling failure are the commonly observed failure modes [38,112,137].

5.1.3 Failure modes in Tension

Cavity wall ties can transfer the applied tensile load to the masonry in a variety of forms. Load-transfer mechanisms may be typically identified by bonding, friction, straightening of the hooked end or of the zigzag end (depending on the embedment of the tie). Three potential failure modes are identified: tie failure, cone break-out failure and pull-out failure. A sketch which depicts each proposed failure mode is shown in Figure 5.4.

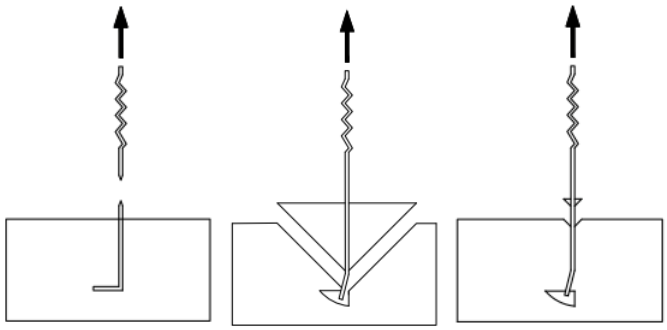

(a) (b) (c)

Figure 5.4 Failure modes in Tension of a cavity wall tie connection: Tie failure(a), Cone break-out failure (b) and pull-out failure (c).

5.1.3.1 Tie failure

Failure of the tie is defined as the attainment of the upper limit on the achievable load-carrying capacity of a metal tie. In order to detect this tie failure in cavity walls, the outer interface between the mortar of the bed joint and the bricks, as well as the inner interface between the tie and the mortar, must provide an adequate bond so that the tie will develop its yield strength.

Tie failure occurs when the fracture strength of the steel is reached while the mortar remains undamaged (Figure 5.4a). Hence, tie failure can occur when any failure of the interface between the tie and the mortar or of the mortar is prevented. Therefore, the embedment depth of the tie needs to be deep, and the bond strength of the mortar should be sufficiently large. The tensile strength of the tie determines then the strength of the connection. The nominal strength of the tie is calculated by using Eq. (5-1):

$$N_{tie} = A_s \cdot f_{ut} \tag{5-1}$$

where A_s is the area of the cross-section and f_{ut} is the ultimate tensile strength of the tie. The tie failure represents the upper limit of the achievable tensile load-carrying capacity of a cavity wall tie connection.

5.1.3.2 Cone break-out failure

Cone break-out failure in masonry is a cone-like failure which is assumed to occur similarly to the corresponding mechanism in concrete [138]. The failure mode can be described as composed of two contributions which are the cone break-out failure in the mortar and the shear failure along both the interfaces between the mortar and the bricks.

The cone break-out failure in the mortar is characterised by the formation of a prism of mortar radiating out from the embedded head of the tie. It is assumed that the prism has a failure angle of approximately 45-degrees and a constant tensile stress uniformly distributed over the projected area of the failure surface.

Using the approach in MSJC [139], the tensile break-out capacity of a single anchor can be calculated as follows:

$$B_{anb} = 0.332 \cdot \sqrt{f_m} \cdot A_{pt} \tag{5-2}$$

where $0.332 \cdot f_m$ represents the constant tensile stress, and A_{pt} is the projected break-out area (Figure 5.5). Development of the projected break-out area of a single cavity wall tie may be restricted by the thickness of the mortar joint, which is a limited space between the bricks. Therefore, this approach cannot be applied directly to the cavity wall ties, embedded in the mortar joint. The reduced projected tension area can be calculated by using Eq. (5-3):

$$A_{pt} = 2 \cdot l_b \cdot t_m \tag{5-3}$$

where t_m is the thickness of the mortar joint, l_b is the embedment length of the tie. In addition to the failure load predicted by Eq. (5-2), for the shear failure along both the interfaces between the mortar and the bricks, an additional contribution given by the friction at the interface between the mortar and the brick needs to be considered. Therefore, the contribution of the initial shear strength and the coefficient of friction of mortar needs to be taken into account on the interface of mortar and brick.

The revised equation is presented as Eq. (5-4), where the first term defines the tensile break out of the mortar, whereas the second and third terms are related to the friction coefficient and the initial shear strength of mortar, respectively.

$$N_{cone} = 0.332 \cdot A_{pt} \cdot \sqrt{f_m} + 2\left(\mu \cdot f_p + f_{v0}\right) \cdot A_w \tag{5-4}$$

$$A_w = {l_b}^2 \tag{5-5}$$

where in Eq. (5-1) to (5-5),

Tensile Strength of the tie	MPa	$\boldsymbol{f_u}$
Compressive strength of the mortar	MPa	f_m
Tie embedment length	mm	l_b
Friction coefficient of Mortar	-	μ
Initial shear strength of mortar	MPa	f_{v0}
Selected pre-compression level	MPa	f_p
Effective area of the cone of the mortar	mm^2	A_w

The initial shear strength and coefficient of friction vary for different masonry typologies. It should be noted that the initial strength of the perforated clay masonry can be much higher than CS or solid clay masonry due to the dowel effect [140].

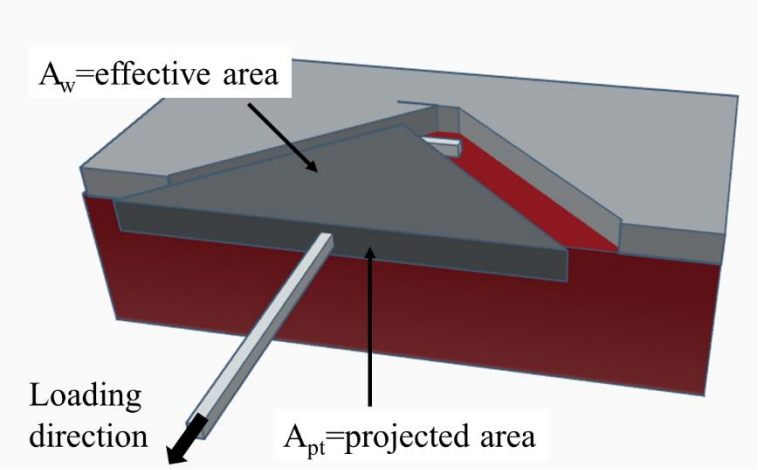

Figure 5.5 Effective area of the cone of the mortar joint used to compute the shear strength.

5.1.3.3 Pull-out failure

Pull-out failure occurs due to poor bonding along the inner interface between the tie and the mortar. Therefore, the pull-out failure is characterised by straightening the tie followed by extensive slip, whereby the surrounding mortar does not have a significant splitting or crushing. The pull-out failure may govern the failure when the mechanical interlock is inadequate, and thus it cannot develop sufficient frictional resistance in the inner interface.

Kuhn and Shaikh [138] proposed a method for determining the pull-out strength of hooked anchors embedded in concrete and masonry construction which was also defined in MSJC [139]. The equation is applicable to bent-bar anchors (J- or L-bolt), which can be seen in Figure 5.6. The axial tensile strength of bent-bar anchor bolts for straightening and pull-out of the anchor from masonry can be computed according to MSJC [139] as follows:

$$B_{anp} = 1.5 \cdot f_m \cdot e_b \cdot d_b + 2.07 \cdot \pi \cdot (l_b + e_b + d_b) \cdot d_b \quad (5\text{-}6)$$

where e_b is the projected leg extension of the bent-bar anchor, measured from the inside edge of the anchor at the bend to the farthest point of the anchor in the plane of the hook, d_b is the diameter of the anchor, and l_b is effective embedment length of the bent anchor. The pull-out strength was calculated as the sum of two components, namely bearing force and friction force. The former component was for straightening the hooked part of the anchor. The bearing strength was the product of the projected surface area of the hooked end in the direction of force multiplied by the compressive strength of the concrete. Additionally, an empirical constant, 1.5, was employed to calibrate the bearing strength by fitting various test data for pull-out strength available in the literature. The latter expression representing friction was characterised by multiplying the surface area of the anchor with an estimated bond strength of concrete (2.07 MPa).

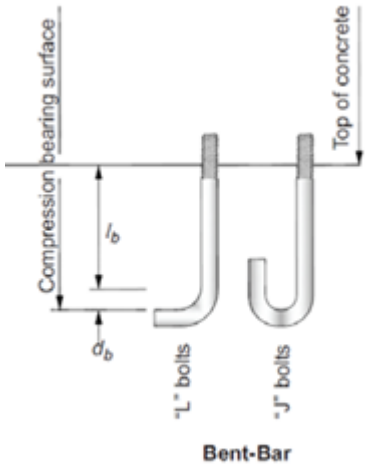

Figure 5.6 Bent-bar anchor bolts from MSJC [139].

In their study, the bond strength between the hooked anchor and masonry was assumed as a value of 2.07 which may not be the same with different mortar quality. Hence, in order to take into account different bond strength values, the equation by Kuhn and Shaikh [138] is revised with a modified empirical constant with an additional parameter, the square root of compressive strength, to be adopted for metal ties embedded in masonry, considering different tie geometries (hooked end, zigzag end, bent), mortar (mortar between CS bricks or CB bricks) and types of bricks. The pull-out force, N_{pull}, for the hooked part of the tie embedment in the CS, can be computed by using Eq. 6:

$$N_{pull,CS} = 1.5 \cdot f_m \cdot l_h \cdot d_t + \alpha \cdot \sqrt{f_m} \cdot \pi \cdot (l_h + l_b) \cdot d + \frac{12 \cdot E_{3t} \cdot I_t \cdot \phi}{l_c \cdot {d_t}^3} \quad (5\text{-}7)$$

where $\emptyset$ is the angle of the tie with respect to the axis, in radians, in the case of a bent tie (Figure 5.7). The model is based on the sum of three components: bearing forces of the embedded hook and the deflection of the anchor due to bending representing imperfect application in practice, and a friction force. The first part of the expression of the equation, the same as Eq. (5-6), refers to the bearing of the hooked anchor embedded in CS. The second term represents the frictional resistance and is computed by the surface area of the tie multiplied by the square root of mortar compressive strength, f_m, and a modification factor. The second term revised is due to the steel-concrete interface bond, proportional to the square root of compressive strength via a factor [141,142]. The modification factor, α, was calibrated against the experimental results leading to a semi-empirical relationship, whose value is chosen to equal to 0.5 for CS masonry. The last term represents the force needed to deflect the hooked end of the tie.

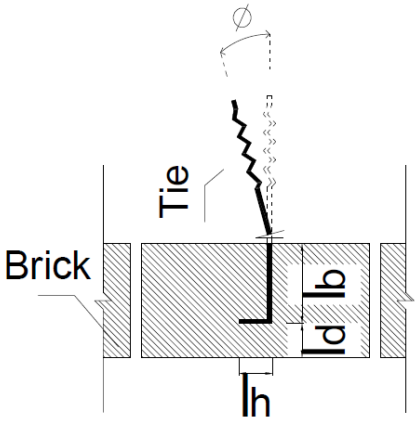

Figure 5.7 Schematic of a bent tie (φ in radians).

The pull-out strength N for CB brick can be computed using Eq. (5-8):

$$N_{pull,CB} = 1.5 \cdot f_m \cdot l_b \cdot d_t + \alpha \cdot \sqrt{f_m} \cdot \pi \cdot l_b \cdot d_t \quad (5\text{-}8)$$

where α is a modification factor calibrated against the experimental results, whose value is chosen equal to 1 for CB masonry. A conservative value has been chosen for the modification factor since the shape of tie where embedded in mortar is zigzag representing thus deformed bar condition.

Different equations for computing the pull-out strength of CS and CB, particularly for computing the friction force, are needed due to the differences in behaviour of the embedded

ends of the tie. The hooked part of the tie embedded in CS masonry is also taken into account for the friction force, while the zigzag end of the tie embedded in CB masonry is assumed to be rectilinear.

5.1.4 Failure modes in Compression

The failure modes of cavity wall ties in compression are classified into the following categories: buckling, punching, and piercing. The failure modes can be seen through the cross-section of mortar joint in Figure 5.8.

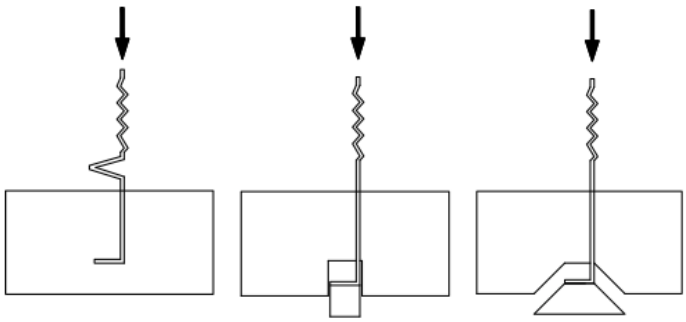

Figure 5.8 Failure modes in Compression of a cavity wall tie connection: Buckling (a), Piercing (b) and Punching (c).

5.1.4.1 Buckling Failure

The failure of a cavity wall tie may be initiated by the buckling of the tie due to its initial imperfections or a non-axial load. For example, buckling of the tie was found to be the most frequent failure mode in compression in the experimental campaign carried out on the wall tie connections, as already mentioned in Chapter 3. The buckling capacity of a metal tie can be simply computed via the Euler formula [143]. In order to determine the critical buckling load, the Euler formula was used as a starting point; the equation was then revised in the case of bent ties.

The compression strength is determined as the Euler's critical load as follows:

$$N_{buck} = \frac{\pi^2 \cdot E_{3t} \cdot I_t}{K^2 \cdot {l_c}^2} \tag{5-9}$$

where K is the column effective length factor, E_{3t} is the elastic modulus of the tie, I_t is the second moment of area of the tie and l_c is the cavity length between two leaves. For bent ties,

the compression strength can be computed as follows to take into account the initial deformation:

$$N_{buck} = \frac{\pi^2 \cdot E_{3t} \cdot I_t}{K^2 \cdot {l_c}^2} - \frac{12 \cdot E_{3t} \cdot I_t \cdot \phi}{l_c \cdot {d_t}^3} \quad (5\text{-}10)$$

The factor *K* is chosen as 0.5 for all the typologies due to the clamped-clamped boundary conditions of the tie provided by the embedment in the mortar joints, which prevent rotations and translations at the two ends of the tie (Figure 5.9). It should be noted that in an earlier experimental work by Derakhshan et al. [67], it was found that bent ties, which often are observed in practice due to the misalignment of the mortar joints, did not return significantly different performance compared to straight ties, and especially the buckling load was not affected.

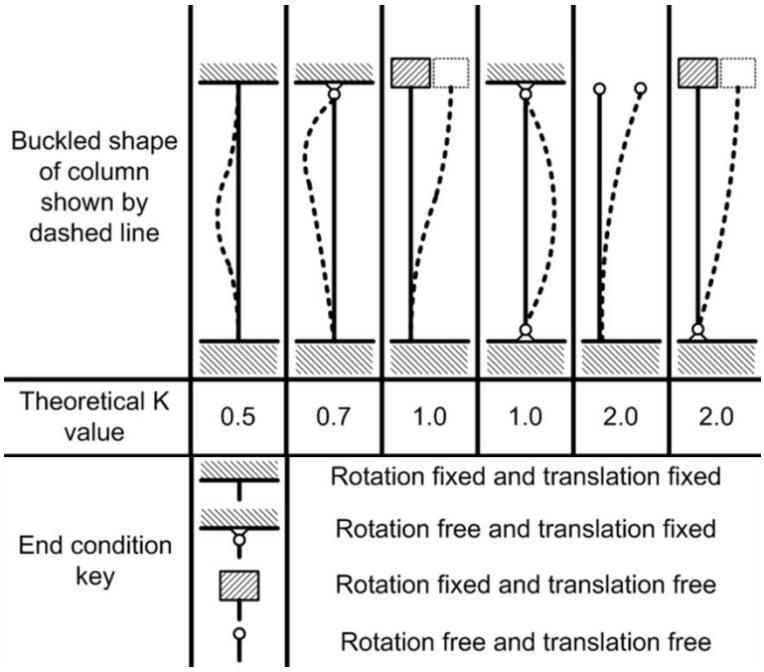

Figure 5.9 Column effective length factors for Euler's critical load from Column Research Council & Johnston [144].

5.1.4.2 Piercing Failure (Bearing Failure)

The piercing failure is characterised by a portion of mortar punched out from beneath the cavity wall tie. The width of the piece of mortar is limited by the width of the embedded head of the tie, whereas the length corresponds to the length of the bent part of the tie. No mechanical model has been proposed in the literature to determine the piercing strength of a wall tie connection in a masonry wall since a cavity wall tie is a tiny element, making it vulnerable and is mainly associated with buckling failure. However, the phenomenon of mechanical behaviour

of piercing in masonry is developed by the analogy of the bearing failure in concrete. Thus, the approach for computing the bearing strength in concrete can be used as starting point also for connections in masonry walls.

The piercing failure of the cavity wall tie closely resembles the bearing failure of rigid plates in unreinforced concrete, for which Hawkins [145] proposed a mechanical model. Hawkins [145] proposed a method for determining the bearing strength of concrete, which shows good agreement in predicting the failure modes and loads in tested specimens. His model is based on a wedge theory, where the wedge, which forms under the bearing plate, splits the surrounding concrete. Hawkins (1969) assumed that the movement of the wedge is restrained by frictional forces and normal forces along the wedge. Similarly, the piercing failure of cavity wall ties can be characterised by a cone of mortar radiating underneath from the base of the tie, and the slope of the piercing envelope with respect to the surface of the mortar joint is approximately 90-degrees. The piercing capacity of the cavity wall ties can be calculated according to an equation that is derived following the approach proposed by Hawkins (Eq.(5-11)):

$$N_{pier} = A_1 \cdot (f_m + 12.5 \cdot f_t \cdot \left(\sqrt{\frac{A_2}{A_1}} - 1\right)) \tag{5-11}$$

with:

$$f_t = 0.332 \cdot \sqrt{f_m} \tag{5-12}$$

$$A_1 = l_h \cdot d_t \tag{5-13}$$

$$A_2 = l_h \cdot l_d \tag{5-14}$$

where f_t is the tensile strength of the mortar, A_1 is the area of the loaded end which is under either the hooked end or zigzag end, and A_2 is the piercing area of mortar under the loaded end. It should be noted that cohesion between the brick and mortar is neglected due to the relatively small failure area. The details of A_1 and A_2 can be seen in the drawing in Figure 5.10. The expressions of l_h and d_t in Eq. (5-13) and Eq. (5-14) are chosen as the thickness of mortar for CB masonry due the zigzag shape of the tie.

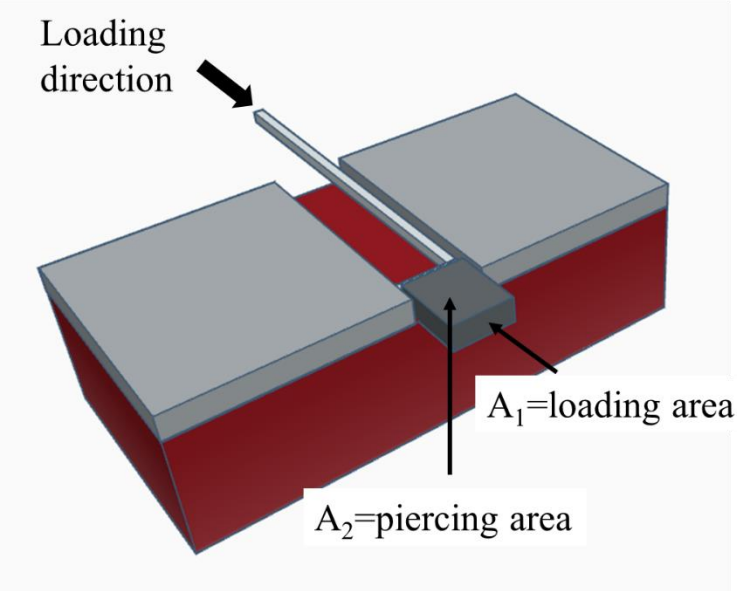

Figure 5.10 The areas of mortar joint used to compute the Piercing strength.

5.1.4.3 Punching Failure

One of the most common failures in concrete is the punching shear of slabs. The punching failure can be defined as a possible failure mode for cavity wall ties as well [127]. The punching failure of cavity wall ties can occur underneath the base of the embedded tie in the mortar joint, and it is characterised by the development of cracks from the end of the embedded tie and up to the face of the mortar joint, followed by the detachment of a conical body from the mortar joint. Thus, the approach suggested by ACI for concrete can also be applied for computing the punching capacity of metal ties in cavity walls; as a result, traditional analytical procedures to determine the punching shear strength of unreinforced concrete slabs can be followed.

The formulation proposed by the ACI code is based on an empirical relationship derived for punching in concrete [132]. Concrete is a material that is not directly comparable with mortar. It is, however, the closest material to mortar, from which an analogy of behaviour can be derived. An idealised control perimeter, u, at a distance, l_d, from the end of the tie to the surface of the mortar is considered in the ACI code. The idealised control perimeter for a cavity wall tie can be seen in Figure 5.11. Hence, the punching resistance of cavity wall ties can be determined as follows:

$$N_{punc} = 0.332 \cdot \sqrt{f_m} \cdot u \cdot l_d \quad (5\text{-}15)$$

It is assumed that punching failure occurs when the normal stress determined by the force applied in compression reaches a critical value equal to $0.332 \cdot f_m^{0.5}$ in MPa. Cohesion between the brick and mortar is neglected due to the relatively small failure area.

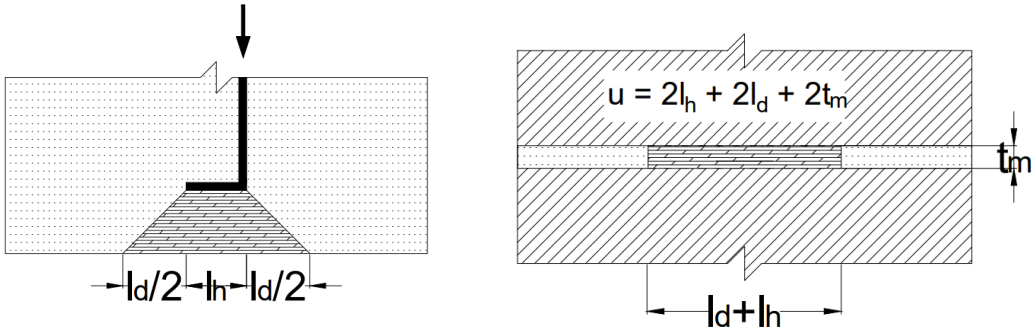

(a) (b)

Figure 5.11 Idealised control perimeter for cavity wall tie specimens for punching failure: mortar joint section (a), front view (b).

5.1.5 Calibration of the proposed model against the tests performed at TU Delft

The capacity of the connections derived from the experimental campaign on the cavity wall ties used for the calibration of the mechanical model is summarised in Table 5.1. As already mentioned in the experimental campaign on the wall tie connections, the embedment length and the geometry of the tie significantly affect the capacity of the connection, while the applied pre-compression does not have a significant impact. Since the outcomes of the experiment tests are not affected by the four levels of pre-compression applied (0 MPa, 0.1 MPa, 0.3 MPa, and 0.6 MPa), this variation is hereinafter not considered.

Table 5.1 Summary of cavity wall tie connection properties.

Material Characteristic	Unit	Symbol	Failure type	Typology	
				CS70	CB50
Diameter of the tie	mm	d	Piercing Failure	3.6	10
			All	3.6	3.6
Tensile Strength of the tie	MPa	f_{ut}	All	411	411
Compressive strength of the mortar	MPa	f_m	All	5.65	6.47
Tie embedment length	MPa	l_b	All	70	50
Mortar joint thickness	mm	t_m	All	10	10
Friction coefficient of Mortar	-	μ	All	0.81	0.66
Initial shear strength of mortar	MPa	f_{v0}	All	0.24	0.82
Selected pre-compression level	MPa	f_p	All	0.1	0.1
Based thickness of the tie	mm	l_h	Pull-out Failure	25	0
			Piercing Failure	25	10
			Punching Failure	25	7.2
Edge distance	mm	l_d	All	30	50
Modification factor	-	α	All	0.5	1
Elastic modulus of the tie	MPa	E_{3t}	All	32920	32920
Cavity length	mm	l_c	All	80	80

The values of the capacity predicted via the proposed mechanical model for each failure mode, namely tie, cone break-out, pull-out, buckling, punching and piercing failures, are compared to the experimental results of the wall tie connections tests in terms of force capacity by grouping the results per type of connection and loading (monotonic and cyclic), as shown in Table 5.2.

Table 5.2 Predicted and average experimental failure modes and capacities of the tested wall tie connections.

Typology		Tie Failure	Cone Break-out Failure	Pull-out Failure	Buckling Failure	Punching Failure	Piercing Failure
CS70	**Proposed Model**	4.18	4.25	2.04	1.69	3.09	2.17
	Experiment (Mono)	-	-	2.35	1.83	-	1.51
	Experiment (Cyclic)	-	-	1.88	1.78	-	1.63
CB50	**Proposed Model**	4.18	5.28	3.19	1.69	5.70	1.94
	Experiment (Mono)	4.22	-	3.43	1.83	-	-
	Experiment (Cyclic)	3.95	-	3.32	1.60	-	-
CS50	**Proposed Model**	4.18	2.40	1.77	1.69	6.73	2.91
	Experiment (Mono)	-	-	1.87	1.80	-	-
	Experiment (Cyclic)	-	-	1.62	1.90	-	-
CS70-15D	**Proposed Model**	4.18	4.25	2.27	1.42	3.09	2.17
	Experiment (Mono)	-	-	2.51	1.35	-	-
	Experiment (Cyclic)	-	-	2.07	1.44	-	-

As discussed in Chapter 3, pull-out failure under tension and buckling under compressive loading are the most common failure modes observed during the experimental campaign: 92% of the specimens undergo pull-out failure in tension and 92% of buckling failure in compression. The predictions obtained with the proposed model agree satisfactorily with the experimental results. Also, the mean peak force is computed with adequate accuracy, as shown in Figure 5.12; the error between the experimental results and the proposed mechanical model for the pull-out and buckling failure is never larger than 13% for monotonic loading and 11% for cyclic loading. The error is computed as the difference between the mean experimental result and the proposed mechanical model divided by the mean experimental result. The error can be calculated by using Eq. (5-16):

$$error = \frac{N_p - N_e}{N_e} \quad (5\text{-}16)$$

where N_e is the mean experimental result, and N_p is the result from the proposed mechanical model. As shown in Figure 5.12, in the underperformed part, the brackets indicate the number of specimens that are below the predicted value of the proposed mechanical model for each failure mode compared to the total number of specimens tested for each corresponding variation. Conversely, the bracket shows the number of specimens above the predicted value for each corresponding variation in the outperformed part.

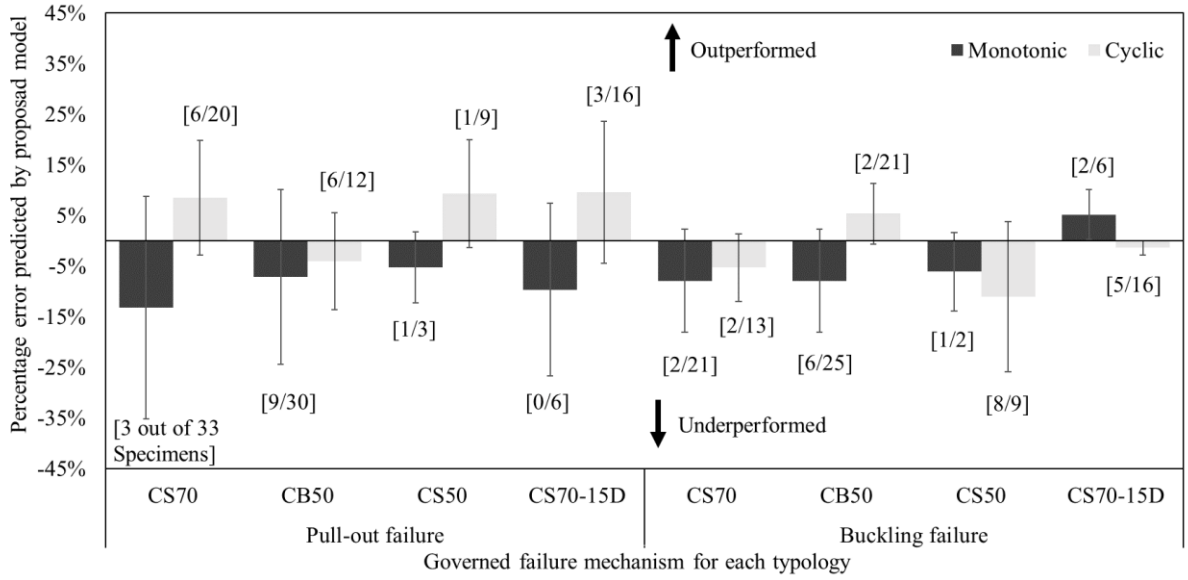

Figure 5.12 Error for the predicted values using the proposed mechanical model versus the experimental data. Error bars indicate standard deviation.

5.1.6 Accuracy and limitations of the results of mechanical model

This section provides a discussion based on the calibration of the proposed mechanical model. There are some cases in which the experimental failure does not always correspond to the lowest predicted capacity. The unexpected results of the model can be summarised as follow:

- The failure mode of CS70, CS50, CS70-15D in tension, and CB-50, CS50, CS70-15D is correctly predicted.
- Regarding CS70 in compression, two different failure modes were observed during the experiment. The model predicts the most frequent failure mode (buckling) correctly as the lowest predicted capacity. In contrast, the experimental capacity for piercing obtained in the case of this failure mode is lower than the one indicated by the proposed model. The observed piercing capacity was low in the experimental

campaign because the straightening of the hooked end of the tie resulted in a smaller load-bearing area of the head.

- Regarding CB50 in tension, there were two different observed failure modes from the experiment, namely tie failure and pull-out failure. The values predicted by the model are close to the strength measured at failure for both modes. However, in a few cases, the specimens had larger pull-out strength, possibly due to unexpected interlocking between tie and mortar, determining eventually the failure of the tie in place of the pull-out failure (which is predicted by the proposed model as the lowest capacity).

It should be noted that, particularly for punching failure, although not observed in the experiments as discussed in Chapter 3, a combination of failure modes may also occur in some cases. One of the reasons why such a combination was not captured experimentally may be the fact that once a failure mode is activated, the localisation of damage accelerates the development of that failure mode.

After the mechanical model, the study was intended to conduct a parametric study using the proposed mechanical model to evaluate the effects of untested configurations of cavity wall tie connections, as explained in the following section.

5.1.7 Parametric study

The experimental campaign on cavity wall ties considered a large number of variations which were seen in common construction practice, such as two different embedment lengths, two different tie geometries, four pre-compression levels, and five different testing protocols. More parameters can influence the behaviour of the cavity wall tie connections, but it is impractical to conduct an experimental campaign considering all the possible influence parameters. Hence, a consistent sensitivity study of the key parameters was performed, making use of the proposed mechanical model. The following additional variations of the parameters are considered: (i) a different (15 MPa) mortar strength for CS couplets, (ii) a shorter (60mm) cavity depth, (iii) a different (70 mm) embedment depth for CB walls and (iv) solid brick for CB. All the studied parameters are summarised in Table 5.3. The parameters described below are varied individually.

Table 5.3 The studied parameters for the extension of the proposed model.

Type	Mortar Strength		Embedment depth		Type of Brick		Cavity width
	CB Leaf	CS Leaf	CB Leaf	CS Leaf	CB Leaf	CS Leaf	
Tested combination	M5	M5	50mm	70mm	Perforated CB brick	CS	70 mm
P1 - 15 MPa CS mortar	M5	M15	50mm	70mm	Perforated CB brick	CS	70 mm
P2 - 60 mm Cavity width	M5	M5	50mm	70mm	Perforated CB brick	CS	60 mm
P3 - 70mm embedded CB	M5	M5	70mm	50mm	Perforated CB brick	CS	70 mm
P4 – Solid Clay Brick	M5	M5	50mm	70mm	Solid CB brick	CS	70 mm

5.1.7.1 Mortar with higher strength class

The majority of the masonry buildings in the Netherlands were mainly made of low-quality mortar [83]. For the parametric study, a higher mortar strength (15 MPa) is chosen for the CS specimens. Figure 5.13 shows how the strength of the connection is predicted to change for each failure mode and for each specimen type when the new higher value of the mortar strength is considered. As expected, an increase in the mortar strength leads to an increase in break-out, pull-out, punching and piercing strength. On the other hand, the increase in the mortar strength does not influence the buckling capacity or the steel rupture failure. As a consequence, the use of stronger mortar leads to more frequent steel rupture failure in tension and buckling failure in compression.

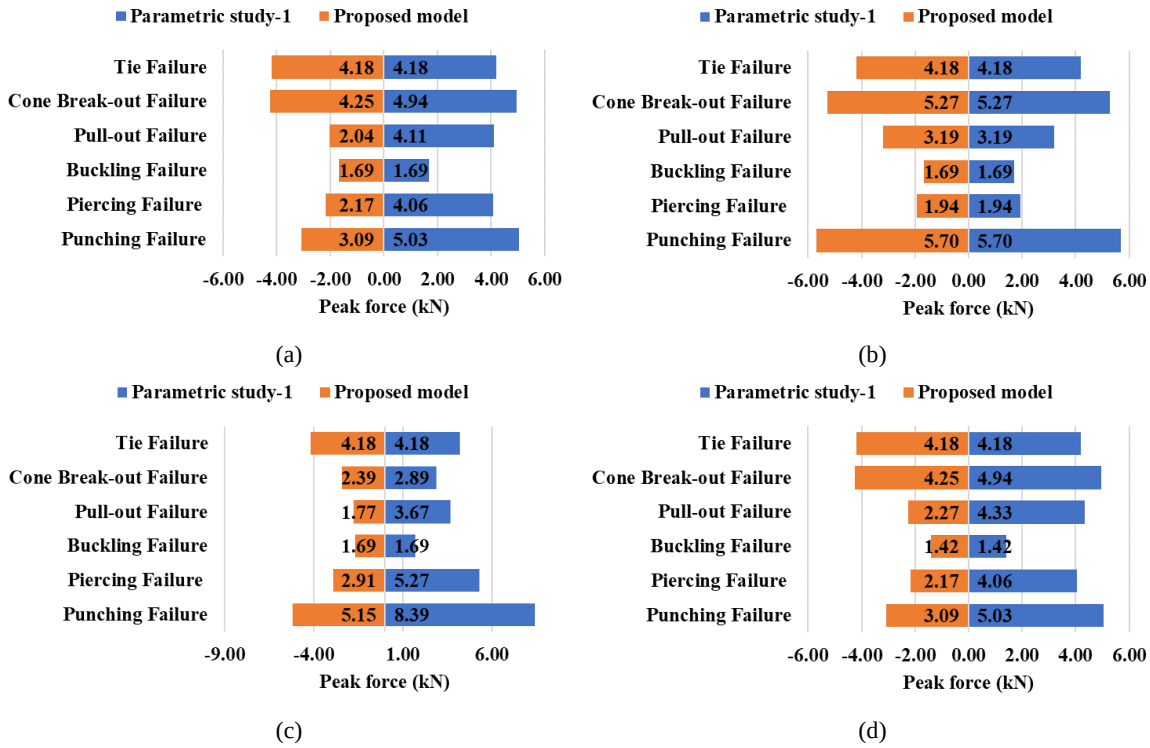

Figure 5.13 Comparison between the proposed model and the parametric study-1: CS70 (a), CB50 (b), CS50 (c) and CS70-15D (d).

5.1.7.2 Reduced cavity width

A cavity width of 60 mm is considered an alternative to the more usual value of 80 mm to consider potential errors and inaccuracies in the construction practice. Figure 5.14 shows the variation of the predicted strength for each failure mode and each specimen type. It is noted that the predicted strength for the cavity width of 60 mm is conducted without changing other parameters, such as the embedment length of CB or CS.

A change in the cavity width affects only the buckling capacity of the ties in compression since a decrease in the gap between the two leaves leads to an increase in the buckling capacity (Figure 5.14). Therefore, the reduced width of the cavity may affect the governing failure mode in compression.

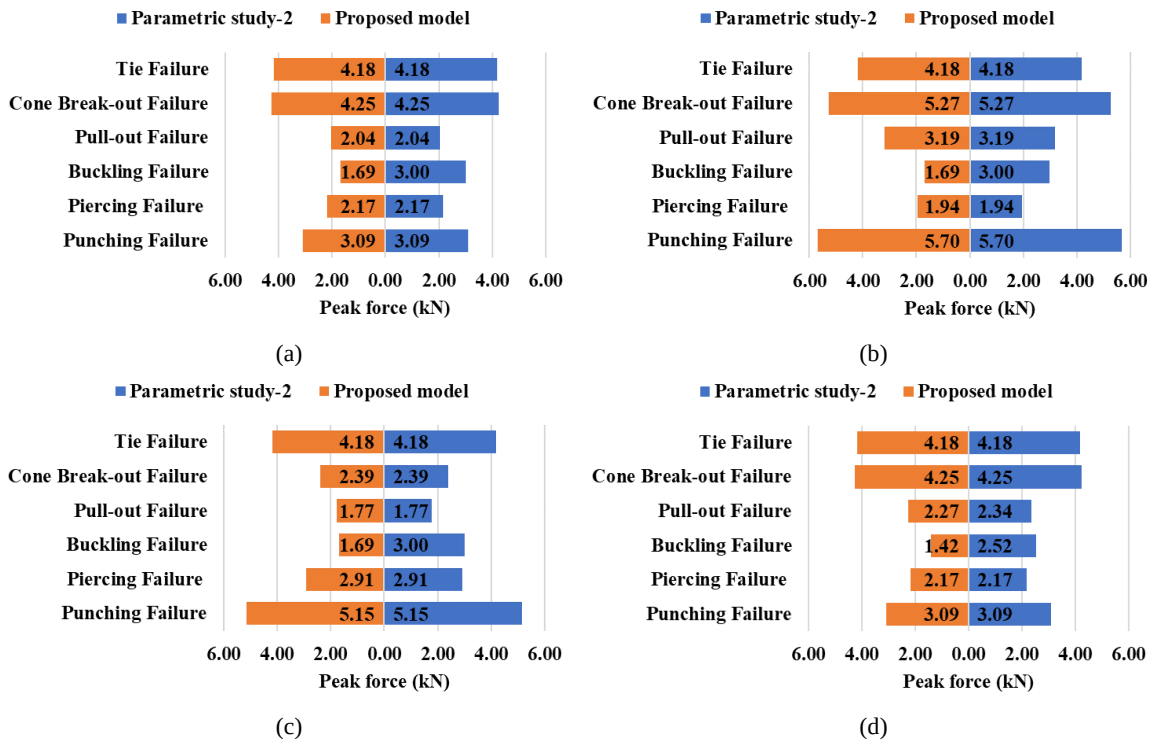

Figure 5.14 Comparison between the values of peak force computed via the proposed model for the original value of the parameters and for the parametric study-2: specimens CS70 (a), CB50 (b), CS50 (c) and CS70-15D (d).

5.1.7.3 Longer embedment depth for CB

In the experimental campaign, discussed in Chapter 3, the CS specimens were investigated under two different embedment depths (50 mm or 70 mm), but only a length of 50 mm was considered for the embedment of the ties in the CB specimens. In this section, the effects of an increased embedment length of 70mm in CB walls (which may be due to an imperfect application) are evaluated.

An increase in the embedment depth in the CB specimens determines a higher strength capacity in cone break-out and pull-out failure and a lower strength for punching and piercing failure (Figure 5.15).

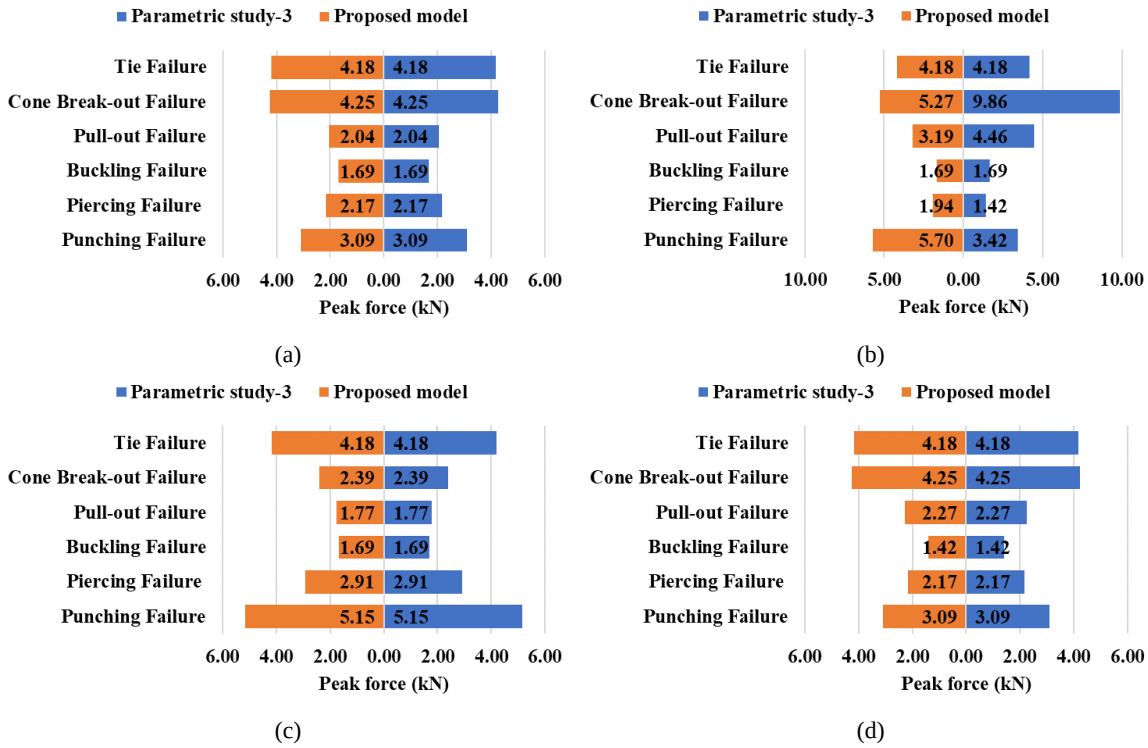

Figure 5.15 Comparison between the values of peak force computed via the proposed model for the original value of the parameters and for the parametric study-3: specimens CS70 (a), CB50 (b), CS50 (c) and CS70-15D (d).

5.1.7.4 Solid clay bricks

As already mentioned, perforated bricks were used for the clay masonry outer leaf. In addition, the embedment in solid clay brick masonry for cavity walls is conducted to provide a better representative result for cavity walls. Jafari et al. [140] provide the initial shear parameters, including initial shear strength and coefficient of friction for the solid brick for CB specimens, which are employed for the parametric study. A comparison between the proposed model and the studied parameter is shown in Figure 5.16. Due to the absence of the dowel effect, cone breakout failure is more likely to be observed.

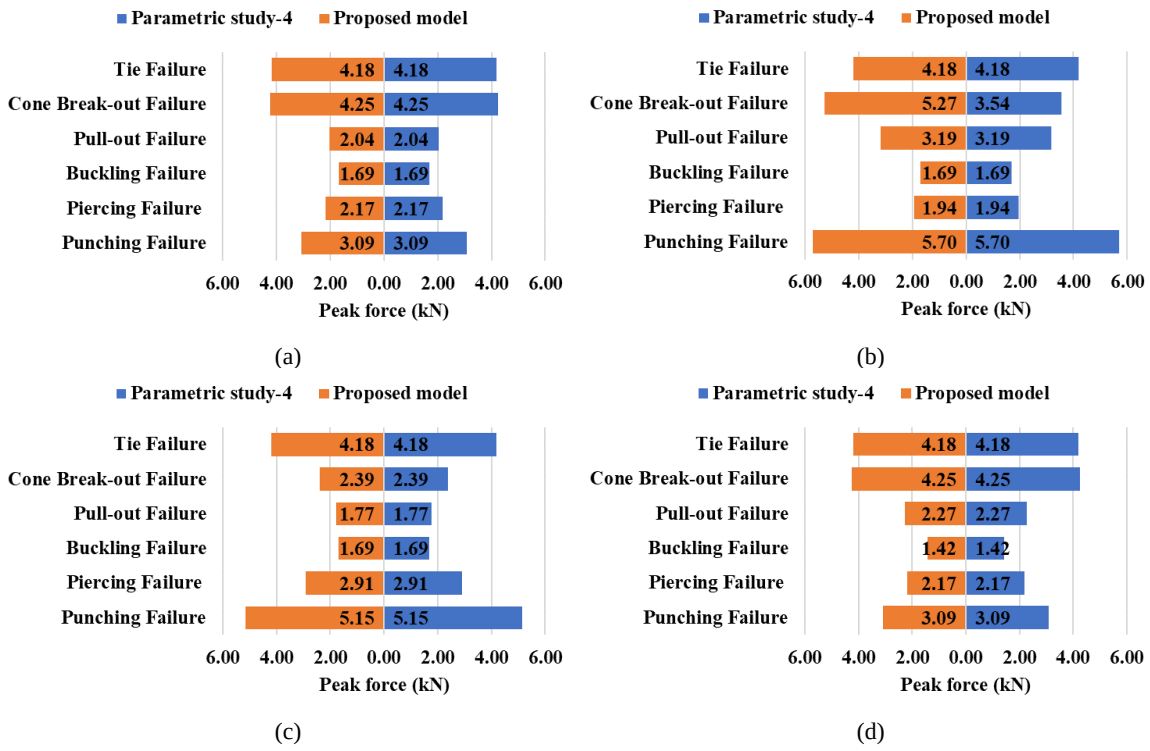

Figure 5.16 Comparison between the values of peak force computed via the proposed model for the original value of the parameters and for the parametric study-4: specimens CS70 (a), CB50 (b), CS50 (c) and CS70-15D (d).

5.1.7.5 Summary of the failure modes for all the different configurations studies

A summary of the results obtained via the parametric study is reported in Figure 5.17 and Table 5.4. Overall, the parametric analysis showed that the governing failure mode, marked in bold letters in Table 5.4, can change due to the variation of the parameters, as expected. Nevertheless, the most frequent failure modes remain pull-out under tension and buckling in compression. A different mortar strength for CS couplets affects the failure mode due to the development of a more efficient bonding between the mortar and tie in tension, while it does not have an influence on compression since the buckling failure is governed. Due to the shorter cavity depth, which leads to an increase in the buckling strength, the failure mode changes to piercing failure. A different embedment depth for CB walls may change the governing failure mode in both tension and compression due to the reduced distance to the edge, so that the connection may be vulnerable to piercing failure. Finally, the use of solid clay bricks does not have a significant influence on the governing failure mode, neither in tension nor in compression.

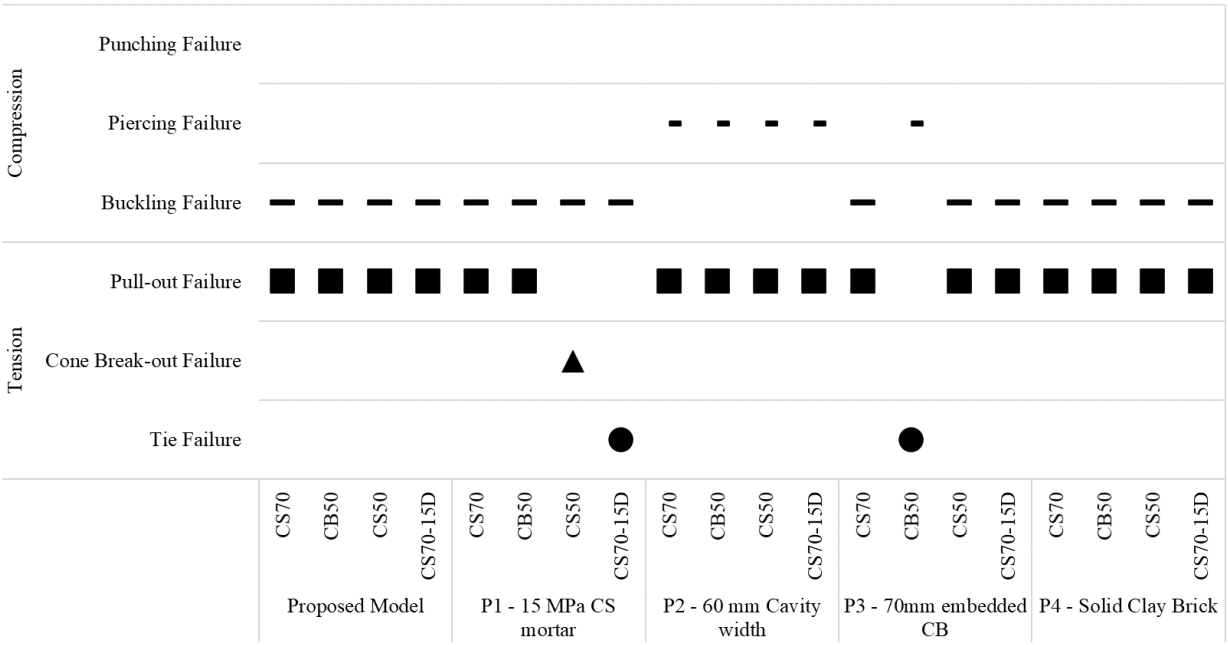

Figure 5.17 Governing failure modes predicted by the parametric study.

Table 5.4 Force capacity of the connections predicted by the parametric study (the governing failure mode is marked in bold letters).

Parametric study	Typology	Tension			Compression		
		Tie Failure (kN)	Cone Break-out Failure (kN)	Pull-out Failure (kN)	Buckling Failure (kN)	Piercing Failure (kN)	Punching Failure (kN)
P1- 15 MPa CS mortar	CS70	4.18	4.94	**4.11**	**-1.69**	-4.06	-5.03
	CB50	4.18	5.27	**3.19**	**-1.69**	-1.94	-5.70
	CS50	4.18	**2.89**	3.67	**-1.69**	-5.27	-10.97
	CS70-15D	**4.18**	4.94	4.33	**-1.42**	-4.06	-5.03
P2- 60 mm Cavity width	CS70	4.18	4.25	**2.04**	-3.00	**-2.17**	-3.09
	CB50	4.18	5.27	**3.19**	-3.00	**-1.94**	-5.70
	CS50	4.18	2.39	**1.77**	-3.00	**-2.91**	-6.73
	CS70-15D	4.18	4.25	**2.34**	-2.52	**-2.17**	-3.09
P3- 70mm embedded CB	CS70	4.18	4.25	**2.04**	**-1.69**	-2.17	-3.09
	CB50	**4.18**	9.86	4.46	-1.69	**-1.42**	-3.42
	CS50	4.18	2.39	**1.77**	**-1.69**	-2.91	-6.73
	CS70-15D	4.18	4.25	**2.27**	**-1.42**	-2.17	-3.09
P4- Solid Clay Brick	CS70	4.18	4.25	**2.04**	**-1.69**	-2.17	-3.09
	CB50	4.18	3.54	**3.19**	**-1.69**	-1.94	-5.70
	CS50	4.18	2.39	**1.77**	**-1.69**	-2.91	-6.73
	CS70-15D	4.18	4.25	**2.27**	**-1.42**	-2.17	-3.09

5.2 Constitutive modelling for numerical analyses of cavity wall tie connections

The experimental campaign on the wall tie connection tests is used to calibrate a hysteretic model in OpenSees [146]. The nonlinear behaviour of metal ties is modelled in terms of pinching behaviour, strength and stiffness degradation. The model is based on the quantitative evaluation of the force-displacement curve obtained during the experiment in order to simulate the cyclic behaviour of the cavity wall metal tie connections.

5.2.1 Review of Past Research on numerical modelling

The Pinching4 constitutive law in OpenSees [147] is often adopted since it is capable of the nonlinear hysteretic response in terms of pinching, strength and stiffness degradation [148–151]. The Pinching4 material was developed by Lowes et al. [152] to simulate the inelastic response of typical beam-column joints under reversed-cyclic loading. The constitutive material is developed to define the load-deformation response of the joint with respect to material, geometric and design parameters.

A comparison between two hysteretic models from OpenSees was conducted by Shen et al. [149]. Pinching4 and Saws materials were calibrated in order to simulate the output of a series of monotonic and cyclic loading tests on CLT shear walls and different bracket connections conducted by Schneider [153]. The configuration of the CLT shear wall and connections can be seen in Figure 5.18. In the experimental campaign, it was mentioned that the behaviour of the CLT wall samples was governed by the connections due to their inherent energy dissipation and ductility [153]. The connections were modelled using Pinching4 and Saws uniaxial material models. After that, Pinching4 and Saw models were compared with the experimental results, and the Pinching4 model exhibited better performance than the Saws model due to the capability of Pinching4 in terms of pinching effect and degradation in strength and stiffness.

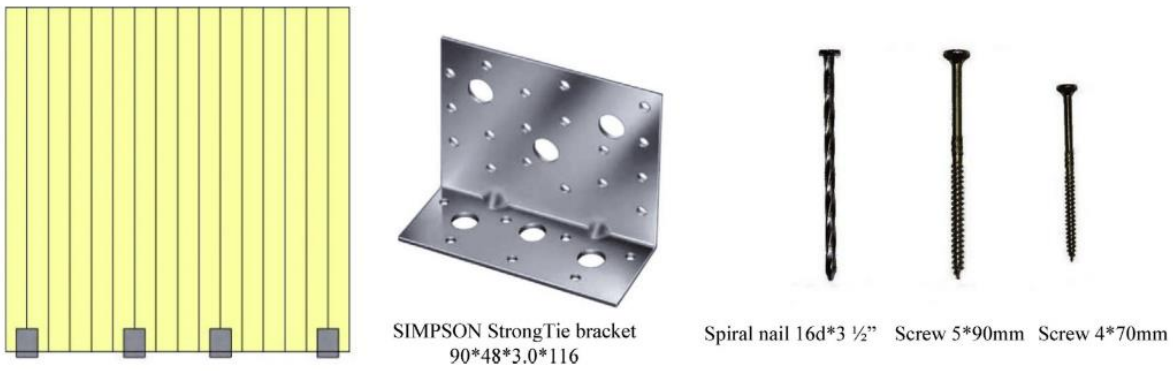

Figure 5.18 Tested wall and connection configuration from Shen et al. [149].

Reneckis and LaFave [113] utilised the test data from Choi and Lafave [76] to develop and calibrate nonlinear finite element models that represented the full-scale experimental brick veneer wall panel specimens. They mentioned that the tie could be modelled by axial links with nonlinear inelastic material properties in order to capture different tie connection features based on the observations of the test (Figure 5.19). It was concluded that brick veneer wall damage could be captured at various stages by examining whether the tie connections at key locations in the models exceeded their ultimate load and/or specific displacement capacities.

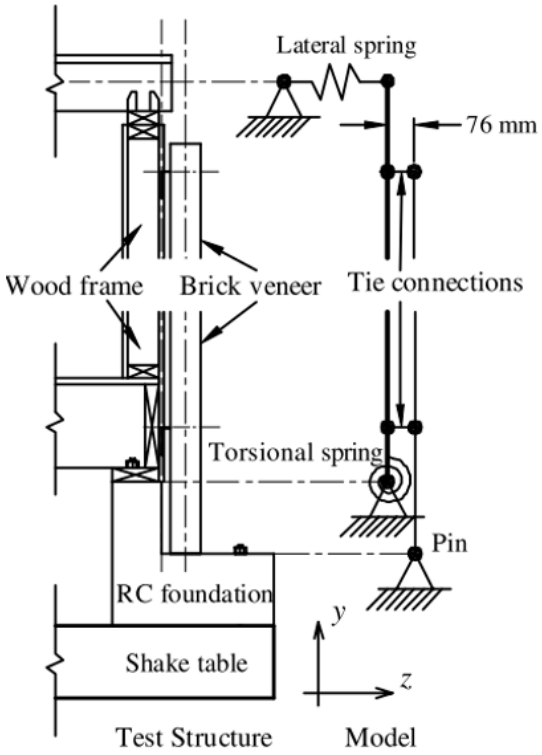

Figure 5.19 Model geometry from Reneckis and LaFave [113].

Jo [154] developed a simplified finite element model in OpenSees that was calibrated using the test results conducted by the author to represent the in-plane and out-of-plane wall system behaviour of concrete masonry unit-tie-masonry veneer wall systems. The ties were modelled as truss elements with general hysteretic material behaviour (Figure 5.20). He mentioned that the OOP response of walls was governed by the axial behaviour of the connections between the clay masonry veneer and the backing system (wood-stud frames or reinforced concrete masonry).

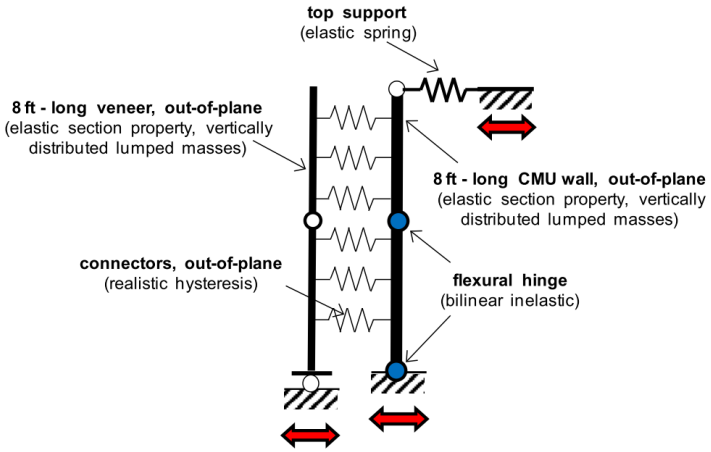

Figure 5.20 OpenSees model for OOP behaviour from Jo [154].

Okail et al. [155] developed a series of OpenSees models to simulate the seismic behaviour of brick veneers connected to a wood frame by means of metal ties. Beam-column elements with fibre cross-section were used to model the masonry veneer, whereas the wood shear walls were simulated through elastic beam elements. The metal tie connections were modelled via nonlinear truss elements. A proper hysteretic model was selected to simulate the cyclic behaviour of the metal ties. The numerical model showed a good match with the experimental data. Based on the results, it was found that the connection force distribution was dependent on the cracking of the veneer.

The current study aims at a computationally efficient approach to simulate the experimental results of wall connections in cavity walls under cyclic loading representative of earthquake motions. The study is supported by the experimental work explained in Chapter 3. The open code OpenSees software [146] has been used in this study.

5.2.2 Hysteretic model for cavity wall tie connections

The experimental results of tie response in CS and CB units explained in Chapter 3 have been simulated in this work within the OpenSees environment [146]. In order to do that, the average experimental curves were fitted into zero-length element backbone curves, as explained below.

The "Pinching4" model [152] was chosen as a material model due to the pinching effect and the degradation in strength and stiffness under cyclic loading. The properties of the Pinching4 material in Opensees are shown in Figure 5.21 and define a backbone curve, the unloading-reloading path that represents the pinching behaviour, and the parameters for strength and stiffness degradation. The curve proposed in this section is hence created by inserting appropriate variables into the Pinching4 material in OpenSees.

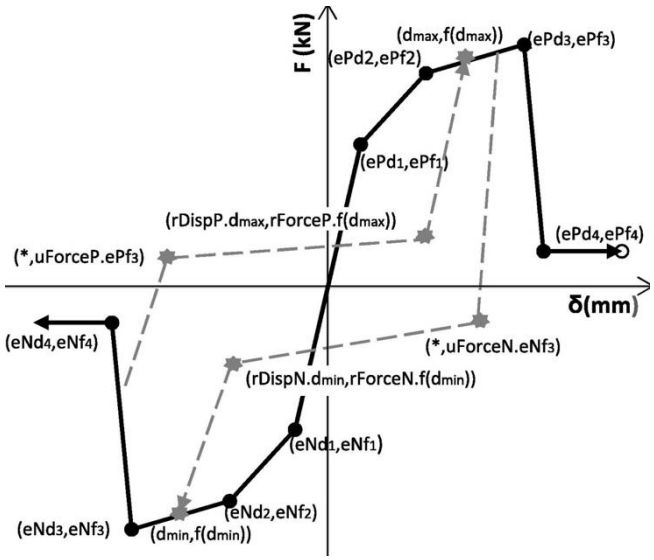

Figure 5.21 Pinching Material model from OpenSees [156].

The Pinching4 constitutive law described above was used in zero-length elements to simulate the wall connection behaviour. The zero-length elements considered for this simulation correspond to springs with only one degree of freedom (DOF), i.e., the axial response, having a hysteretic response that is defined by using the calibrated Pinching4 material. The other DOFs in the model are left constrained.

The tension backbone curves differ from the compression backbone curves for each tested typology due to the different failure modes in tension and compression. Therefore, the backbone curve should be defined separately in tension and compression for each typology in Pinching4 material. However, the strength and stiffness degradation parameters cannot be defined separately in tension and compression due to the limitation of the Pinching4

constitutive law. The material parameters were hence calibrated in order to match the overall simulated responses from the experimental results.

Due to its flexible format, the Pinching4 material can actually successfully fit a wide variety of experimental results. The point of this study is to propose a general model by using an averaging procedure. In order to do this, the backbone shape given in Fig. 2 has been fitted to every tested typology individually and the input parameters have been found for the best fit. As an example, an experimental hysteresis was chosen from one of those typologies to validate the numerical model with the experimental data (Figure 5.22).

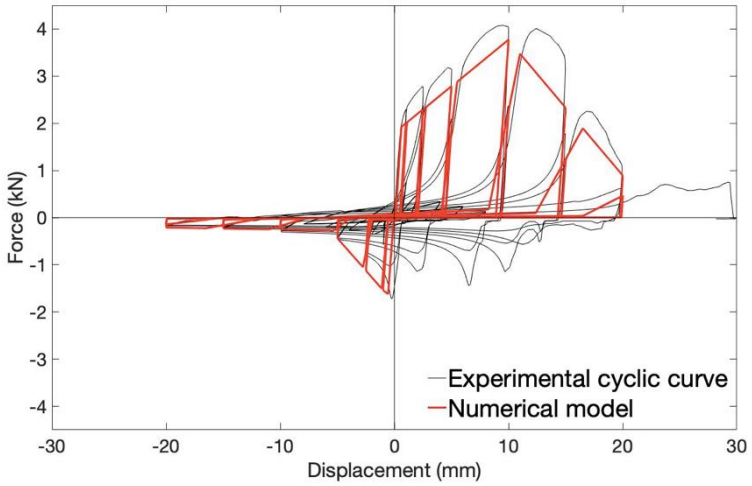

Figure 5.22 Comparison between experimental and numerical result.

Additional parameters of the Pinching4 model define the cyclic response. Two parameters, rDisp and fForce, define the ratio of the deformation/force at which the reloading starts to the maximum deformation/force demand of the previous cycle in the loading direction of interest for positive and negative. The uForce parameter defines the ratio of strength developed after unloading from the negative/positive load to the maximum strength developed under monotonic loading. The cyclic deterioration for unloading, reloading stiffness and strength are controlled with gKLim, gDLim, and gFLim, respectively. The values of cyclic degradation parameters (gKLim, gDLim, and gFLim) and pinching parameters (rDispP, rDispN, rForceP, rForceN, uForceP and uForceN) simulate the force-deformation history for selected specimens. The values suggested for all these parameters are reported in Table 5.1.

Table 5.5 Suggested values of the modelling parameters for OpenSees Pinching4 material based on experiments and mechanical model (number of the equation from the mechanical model between brackets).

Parameters	Suggested Values CS70	Suggested Values CB50	Suggested Values CS70-15D	Suggested Values CS50
Positive backbone				
ePf_1 (kN)	0.77	2.16	0.77	0.60
ePf_2 (kN)	1.89	3.32	2.15	1.72
ePf_3 (kN)	1.51	2.66	1.72	1.38
ePf_4 (kN)	0.80	0.50	1.50	0.90
ePd_1 (m)	0.001	0.001	0.001	0.001
ePd_2 (m)	0.01	0.01	0.01	0.01
ePd_3 (m)	0.011	0.011	0.011	0.011
ePd_4 (m)	0.011	0.025	0.04	0.011
Negative backbone				
eNf_1 (kN)	-1.68	-1.68	-1.42	-1.68
eNf_2 (kN)	-1.34	-1.34	-1.10	-1.34
eNf_3 (kN)	-0.60	-0.30	-0.60	-0.60
eNf_4 (kN)	-0.10	-0.10	-0.10	-0.10
eNd_1 (m)	-0.003	-0.001	-0.003	-0.003
eNd_2 (m)	-0.004	-0.003	-0.004	-0.004
eNd_3 (m)	-0.005	-0.0056	-0.005	-0.005
eNd_4 (m)	-0.04	-0.050	-0.040	-0.040
Pinching				
rDispP	0.95	0.53	0.53	0.53
fForceP	0.22	0.20	0.20	0.20
uForceP	0.04	0.05	0.09	0.09
rDispN	0.80	0.70	0.76	0.76
fForceN	0.53	0.66	0.66	0.66
uForceN	0.04	0.70	0.94	0.90
Unloading stiffness degradation				
gK_1	0.15	0	0	0
gK_2	0.15	0.1	0.1	0.1
gK_3	0.15		0	0
gK_4	0.15	0.1	0.1	0.1
gKLim	0	0.2	0.1	0.1
Reloading stiffness degradation				
gD_1	0.1	0.2	0.1	0.1
gD_2	0.2	0.2	0.1	0.1
gD_3	0.1	0.2	0.1	0.1
gD_4	0.2	0.2	0.1	0.1
gDLim	0.1	0.1	0.1	0.1
Strength degradation				
gF_1	0	0	0	0
gF_2	0	0	0	0
gF_3	0	0	0	0
gF_4	0	0	0	0
gFLim	0	0	0	0
Energy degradation (gE)	10	10	10	10
Damage type	Cycle	Cycle	Cycle	Cycle

The average cyclic hysteresis curves, obtained following the procedure and using the parameters described above, are presented in Figure 5.23 for each tested typology of wall connections. The figure shows that the results obtained with numerical analyses have a fairly good match with the average experimental curves. The calibrated hysteretic models are capable of capturing important aspects of the tie response, such as the initial stiffness, strength, sudden drop of strength and cyclic response in the degradation part of the response. However, the Pinching4 material has no input parameter to capture buckling deformation besides the abovementioned aspects. Hence, it is a phenomenological model due to mainly aiming to reproduce not only the overall behaviour of the tie but also different embedment lengths and tie geometries. Also, it is said by Mazzoni and Scott [157] and among others [158,159] that phenomenological models are expected to be computationally faster but less accurate than mechanical laws.

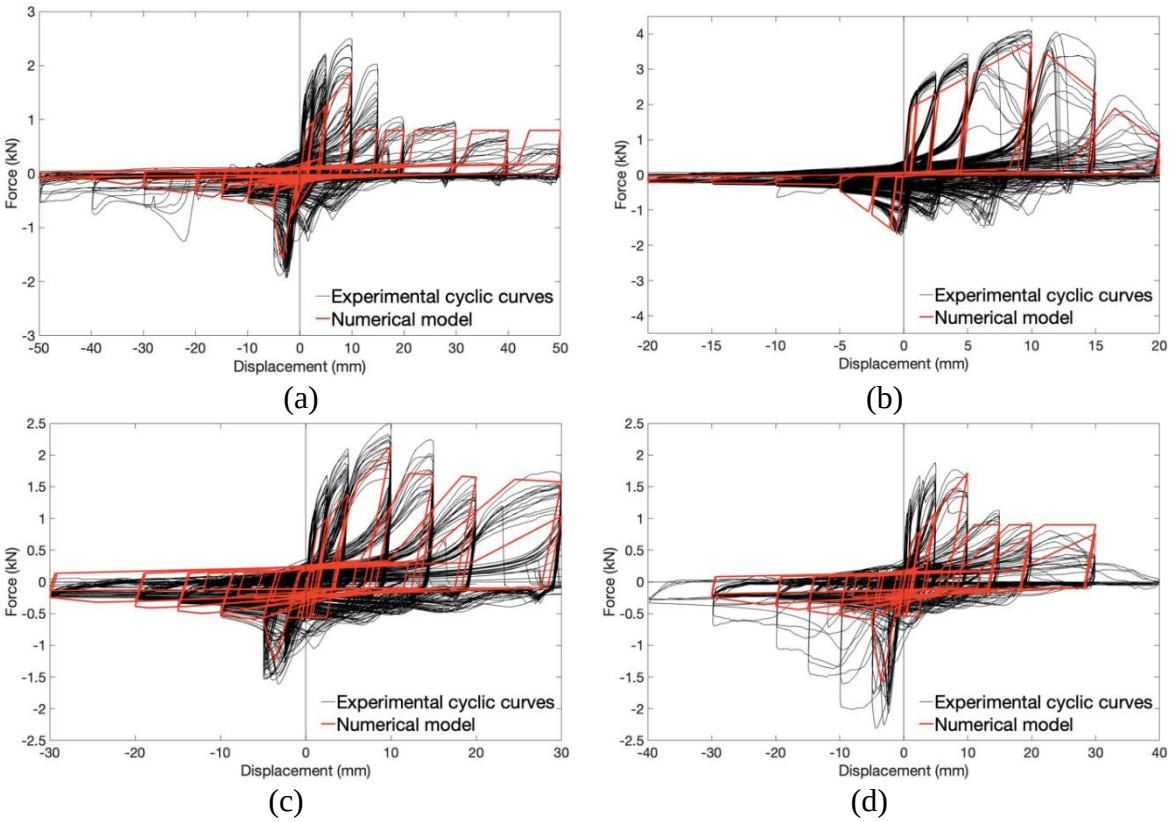

Figure 5.23 Simulated and experimental response for CS70 (a), CB50 (b), CS70-15D (c) and CS50 (d).

A comparison of the accumulated hysteretic energy (i.e., the area within the hysteresis loop) is given in Figure 5.24, where it can be seen that the proposed numerical model performs

well in terms of hysteretic energy dissipated by the wall connection. The numerical model dissipates more energy per cycle for smaller displacements, whereas smaller energy dissipation is observed for larger displacements compared to the experimental results. This can be attributed to the lack of ability of the model to simulate the unloading-reloading path from tension to compression accurately after the buckling of the tie, as mentioned above, that determines the compressive peaks for positive displacements, which the Pinching4 constitutive model does not capture. At the end of the tests, the total energy dissipation for the numerical model is very close to the average peak energy dissipation for each tested typology.

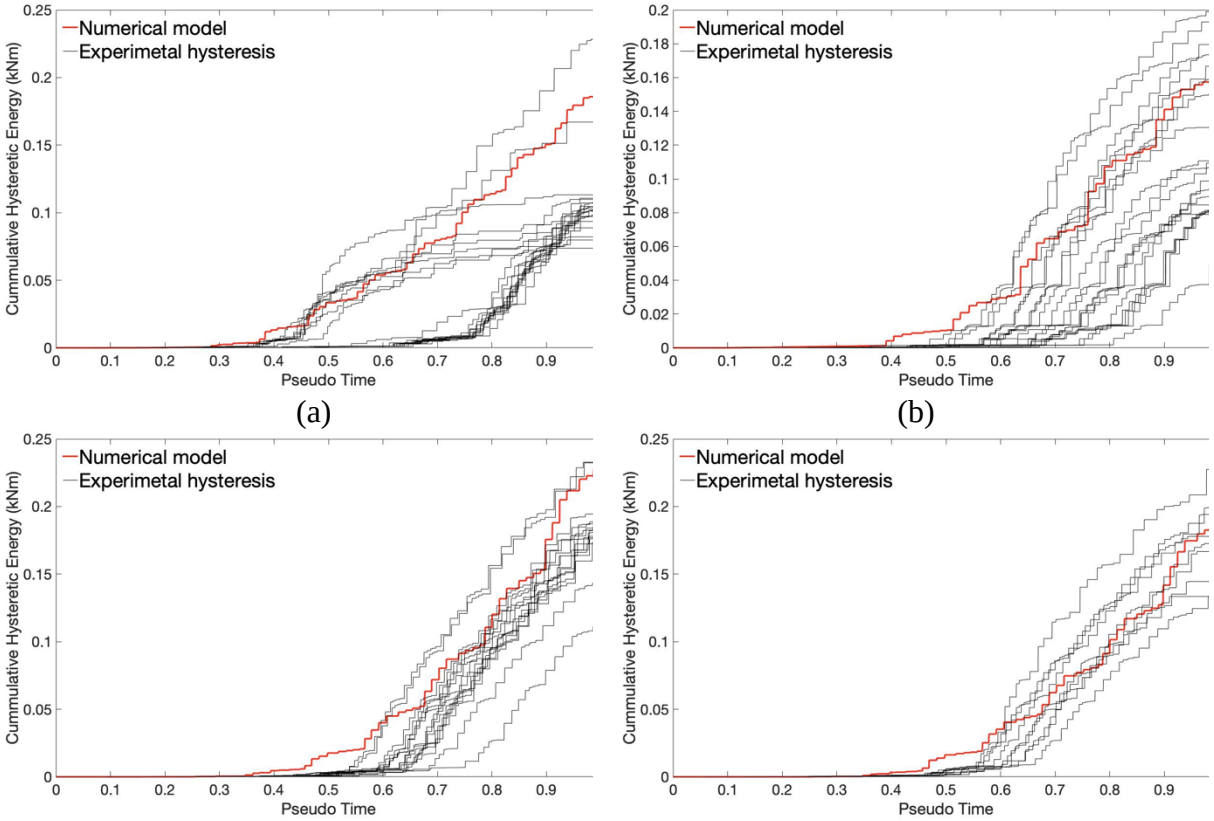

Figure 5.24 Cumulative hysteretic energy for experiments and numerical simulations for specimens CS70 (a), CB50 (b), CS70-15D (c), and CS50 (d).

5.3 Conclusions

This chapter aims to develop a mechanical model to predict the failure mode and the strength capacity of wall metal tie connections in masonry cavity walls and a constitutive model to simulate the experimental results of cavity wall tie connections. In the first part of the chapter, the study investigates connections embedded in double-leaf cavity walls composed of an inner load-bearing leaf made of calcium silicate brick masonry and an outer leaf made of perforated

clay brick masonry, while in the second part, the study utilises the results of the experimental campaign discussed in Chapter 3 to calibrate a hysteretic numerical model that represents the cyclic axial response of cavity wall tie connections.

The proposed mechanical model for the cavity wall tie connection considers six possible failure modes, which are tie failure, cone break-out failure, pull-out failure, buckling failure, punching failure and piercing failure. The prediction of one of these failure modes is based on the characteristics of the used materials, type of bricks and ties, embedment length, different tie geometries, mortar quality and bond strength between tie and mortar. A good agreement between the experiments and the proposed model is found in terms of both identification of the failure mode and the determination of the peak capacity of the connection.

The following results are reported:

- The proposed mechanical model is capable of predicting the failure modes observed during the experimental campaign, which are pull-out and buckling failure. When two different failure modes were observed in the experiments for a specific type of connection (CS70 in compression and CB50 in tension), the model predicted the most frequent failure mode correctly.
- The model accurately predicts the strength capacity of the cavity wall ties. The ratio between the experimental results and mechanical model ($N_{Test}/N_{Predicted}$) for pull-out and buckling failure is determined as 1.04 and 1.04 with standard deviations of 0.15 and 0.10, respectively.
- The parametric analysis showed that the studied parameters, which are mortar with higher strength, reduced cavity width, longer embedment depth and a different type of brick, moderately influence the failure type and the corresponding capacity of metal tie connections between the leaves in a cavity wall. A higher mortar strength has an impact on the tensile behaviour of the connection as it increases the bond between the mortar and the tie; conversely, for compression, the failure mode is not affected by the mortar strength since the governing failure mode depends exclusively on the properties of the metal tie. A decrease in the cavity width increases the critical buckling load, leading to a different failure mode in compression; however, in tension, the strength capacity of the metal tie connection does not change.

The experimental results of the aforementioned experimental campaign are used to develop a general load-deformation hysteretic numerical model for different typologies of cavity wall connections. The numerical simulations make use of nonlinear zero-length spring elements,

whose axial response is defined by a constitutive law (Pinching4) already implemented in the open code OpenSees. Alternatively, similar procedures can be adopted in other structural analysis software used in earthquake engineering. The material parameters of the Pinching4 law are derived from the experimental tests. The strength degradation, stiffness degradation and pinching behaviour of the load-deformation responses are modelled differently for each typology. The phenomenological model can mainly reproduce the observed experimental force-displacement curves except for the buckling response of the ties.

The presented mechanical model can be adopted by structural engineers, particularly estimating each contribution of the studied mechanism in case to have at least one of these mechanisms and to assess the performance of such connections during seismic events in masonry cavity walls with the characteristic considered, whereas other construction techniques and/or materials would require specific studies. In addition, the hysteretic model can be employed by structural engineers for accurate modelling of the response of wall-to-wall connections under dynamic earthquake loading.

Chapter 6: Mechanical modelling of timber-masonry connections

In the following chapter, two mechanical models are introduced to examine different failure modes in timber-joist connections within masonry cavity walls. One model focuses on the joist-sliding failure mode, where the Coulomb friction model [160] is adopted and further extended to include the arching effect using the model proposed by Paulay and Priestley [161]. The other model investigates the rocking failure mode, applying the model proposed by Tomassetti et al. [162] to predict the strength capacity of the connections (whose experimental performance is presented in Chapter 4). The study aims at identifying the contributions of various resisting mechanisms to the force capacity of the connection.

The adopted mechanical model examines two different failure modes: joist-sliding with partial wall-joist interaction and out-of-plane (OOP) rocking behaviour of the masonry walls. Section 6.1 reviews the past research on the mechanical modelling of the frictional and rocking mechanisms. Sections 6.2 and 6.3 present the adopted mechanical modelling for joist-sliding with joist-to-wall interaction and rocking failure modes, respectively. Section 6.4 compares the values of the force capacity of the connections predicted via the mechanical model with the experimental results by grouping the results per type of connection in both unstrengthened and strengthened conditions. Section 6.5 discusses the accuracy and limitations of the considered mechanical model.

6.1 Review of past research on mechanical modelling of timber joist to masonry connections

In the experimental campaign on timber-masonry connections reported in Chapter 4, two different failure modes were observed: joist-sliding, which includes partial joist-to-wall interaction, and OOP rocking failure mode. The joist-sliding failure with the partial joist-to-wall interaction mechanism was governing weak joist-masonry connections. Otherwise, when the connection was over-resistant due to retrofitting, failure occurred due to the OOP rocking of the wallet. The former mechanism depended on cohesion and friction between joist and masonry, as well as by the arch effect activated due to the joist-to-wall interaction, whereas the

latter was characterised by the rocking behaviour of either one or both leaves of the wallet. Considering the observed failure modes, a summary of the models proposed in the literature to describe the frictional behaviour of the joist-wallet interface and the rocking behaviour of the wall is discussed in the following paragraphs.

6.1.1 Literature review on Frictional behaviour of joist

Friction and cohesion at the masonry-joist interface play an important role in predicting the governing failure mode for timber-joist connections. When the applied shear force at the interface of the embedded part of the joist exceeds the frictional capacity, sliding of the joist occurs. Friction is the force resisting the relative motion between two surfaces, such as solid surfaces sliding against each other and producing heat and resisting to this movement. Coulomb (1736-1806) classified two types of friction as follows: (i) static friction, which is the resistance until starting the relative motion and (ii) dynamic friction, which concerns the resistance when the surfaces move with respect to one another.

The static friction coefficient can be computed as the maximum tangential force that develops before the onset of the sliding mechanism divided by the normal load acting on the interface. In contrast, the resisting force due to dynamic friction can be described in terms of the residual resisting force, which is achieved after the force drop due to the activation of sliding. In the study of Suh & Turner [163], static and dynamic friction were compared for the dry materials. It was concluded that the dynamic friction coefficient was less than the static friction coefficient, generally of the order of 25%. Another study by Doherty [95], evaluated the performance of unreinforced masonry (URM) connections containing damp proof course (DPC) membranes under dynamic loading in order to assess their seismic integrity. In addition, he compared the dynamic friction coefficient determined from the experiments conducted by the author with the quasi-static friction coefficient determined by Griffith & Page [164]. It was highlighted that the quasi-static friction coefficient was not more than 20% higher than the dynamic friction coefficient.

Casapulla et al. [165] conducted a study on the simple overturning mechanism of a masonry wall weakly connected to the timber diaphragm. They defined a priori failure mode based on the frictional resistance at the support of the timber diaphragm. This was represented as a cohesionless Coulomb's law, as seen in Figure 6.1, so that the connection is limited by a horizontal friction force as follows:

$$F_Q = Q \cdot \mu \tag{6-1}$$

where μ is the beam-wall friction coefficient, and Q is the vertical load transferred to the wall. The physical characteristics of the contact surfaces can affect cohesion and friction. Therefore, the value of friction coefficient of 0.1 representing light horizontal diaphragms, 0.3 for intermediate diaphragms, and 0.6 for heavy diaphragms have been chosen for the contact surface in order to investigate the stabilising role of the frictional resistance due to the presence of a simply inserted horizontal diaphragm. Finally, for the rocking mechanism, the sensitivity of the load multiplier with respect to the studied friction coefficients was defined. Casapulla et al. [165] found that when a joist is inserted in a masonry pocket, an increase in the seismic masses associated with heavier floors reduces the load multiplier. Hence, the friction contribution has a significant influence on the horizontal loads related to the floor masses.

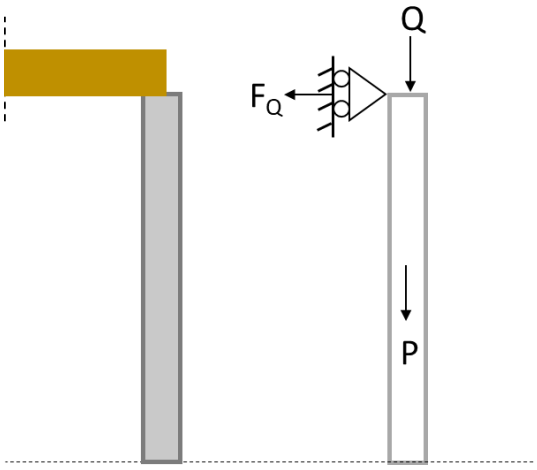

Figure 6.1 Schematic view of the specimen with a masonry pocket connection (adopted from Casapulla et al. [165]*).*

The joist-sliding failure mode was recently studied by Almeida et al. [101], who conducted an experimental campaign with cyclic friction triplet tests between mortar and timber units. Friction was described as a surface force that restrained the sliding motion of bodies and was categorised into three types: (i) independent of the normal area of contact, (ii) proportional to the normal force and (iii) independent of the sliding speed. Dry friction or Coulomb friction (which is the friction coefficient caused by surface roughness) was derived without considering the contribution of cohesion. The coefficient of friction was defined as follows:

$$\mu = \frac{F_{friction}}{2 \cdot N_{contact}} \tag{6-2}$$

where the contact force, $N_{contact}$, is multiplied by 2 due to the two friction surfaces of the tested specimen. The static friction force was characterised by a maximum shear force, which developed before the onset of sliding of the joist. In contrast, the resisting force due to dynamic friction can be described in terms of the residual resisting force, which was achieved after the force drop due to the activation of sliding. In their study, it was found that the dynamic and static friction coefficients were similar for mortar-timber specimens.

Apart from friction, cohesion is another contribution to the interface between timber and masonry. Cohesion plays an important role in the force-displacement property, including peak force and post-cracking hysteric behaviour [108]. Although the cohesion bond between brick and mortar was commonly studied in the literature [62,166,167], a few studies have focused on the contribution of cohesion between timber and masonry [168,169]. A Coulomb type of representation can be adopted to determine the friction and cohesion bond between masonry and timber (Figure 6.2a). The Coulomb friction criterion [160] is based on a linear failure envelope to determine the critical combination of shear and normal stress that will cause failure. The ultimate shear strength at the interface between timber and masonry at a particular level of normal stress can be calculated by the Coulomb criterion (6-3), as seen in Figure 6.2b. The post-peak phase is characterised by cohesion softening, followed by a plateau representing residual dry friction.

$$\tau = c + \mu \cdot \sigma_N \tag{6-3}$$

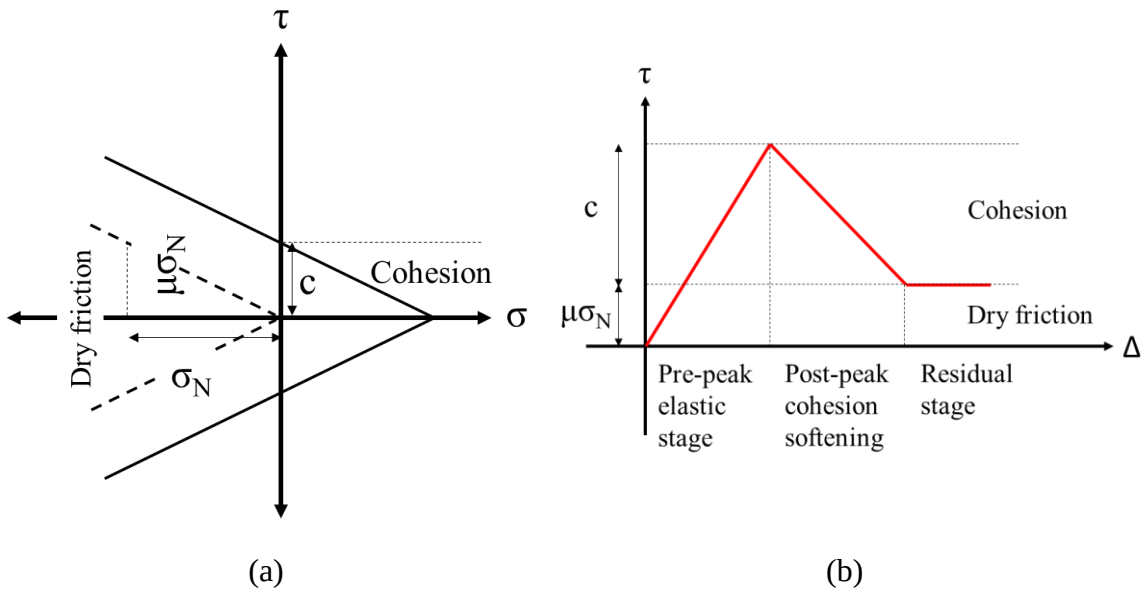

(a) (b)

Figure 6.2 Definition of cohesive-frictional behaviour in shear: Coulomb friction law (a), Coulomb friction and cohesion softening for interfaces subjected to shear and compression.

As mentioned earlier, the observed joist-sliding failure mode included a partial joist-to-wall interaction; hence a second-order geometric effect was activated. The second-order effect introduces the arch effect, increasing overburden and, hence affecting frictional behaviour. No studies in the literature focused on frictional behaviour with the second-order effect regarding the mechanical behaviour of timber-masonry connections. However, the second-order effect on masonry structures and how it may affect the force capacity of the walls have been studied extensively in the literature [108,170–172].

The strength capacity of masonry walls can be affected by second-order geometrical effects when large displacements dominate the out-of-plane behaviour. Several factors play an essential role in activating the second-order effects, including limited or zero tensile strength, the effect of creep deformation and boundary conditions. Regarding the limited or zero tensile strength, in the attainment of cracking, there will be no contribution to the stiffness due to the cracked zone on the section. While regarding the boundary condition, the second order can be activated in the fixed-fixed boundary condition since the vertical displacement is restrained. Magenes [173] said that the first analytical model for the compressive response of URM walls under vertical loading could be considered the base for the arch effect caused by the second-order effect going back to 1937 and was proposed by Nils Royen. Similar approaches have been followed by other authors in the following decades [174–177].

Paulay and Priestley [161] proposed a simplified procedure based on elastic buckling behaviour for the OOP response of masonry walls, particularly for one-way vertical spanning URM walls, based on the exact solution for the compressive response of masonry walls conducted by Sahlin [176]. The simplified analytical model was developed to define the load-deflection (P-Δ) relationship for the masonry wall, taking into account the second-order geometric effect. Figure 6.3 shows the behaviour of a slender unreinforced wall under the eccentricity of the applied vertical load.

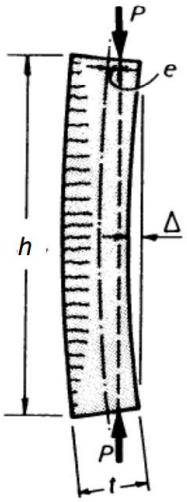

Figure 6.3 Schematic presentation for the second-order effect in masonry walls from Paulay and Priestley [161].

The vertical load, *P*, and corresponding displacement, *Δ*, can be computed according to Paulay and Priestley [161], as follows:

$$\Delta = 0.5 \cdot t_w \cdot \left(y - \sqrt{y^2 - \frac{f_s}{6E}\left(\frac{h}{t_w}\right)^2} \right) \tag{6-4}$$

$$P = 0.75 \cdot f_s \cdot t_w \cdot \left(y + \sqrt{y^2 - \frac{f_s}{6E}\left(\frac{h}{t_w}\right)^2} \right) \tag{6-5}$$

$$y = \frac{1}{2} - \frac{e}{t_w} \tag{6-6}$$

where t_w is the thickness of the wall, y is the dimensionless distance from the extreme compression fibre at the top and bottom sections of the wall to the line of action of the load, *P*, *h* is the height of the wall, and *e* is the eccentricity of the axial load. An increase in the lateral displacement, *Δ*, leads to an increase in the bending moment at midspan. It should be noted that the lateral displacement, *Δ*, or the load, *P*, can be obtained by using Eq. (6-4) or (6-5), respectively, for a given stress value at the extreme compression fibre at mid-height, f_s.

In the following, a mechanical model that takes into account the frictional behaviour and second-order effect is selected amongst the models described in the literature. The adopted model is based on the Coulomb criterion with the contribution of a second-order effect due to the joist-to-wall interaction. This mode will be used in the following sections to predict the joist-sliding capacity of the cavity wall systems whose experimental outcomes are reported in Chapter 4.

6.1.2 Literature review on Rocking behaviour

The rocking behaviour of rigid blocks or assemblies has been widely studied in the literature [162,170,178–180] since it is one of the most common out-of-plane (OOP) failure mechanisms. The type and quality of masonry, geometry of the wall and vertical load can influence the rocking failure mechanism [181]. URM cantilever walls subjected to out-of-plane loading first crack along the base of the wall and then undergo rocking behaviour. For URM cantilevers, the overturning force can be simply computed assuming zero tensile strength as follows:

$$W = \gamma_m \cdot t_w \cdot h \cdot l \tag{6-7}$$

$$N_O = \frac{W \cdot t_w}{2 \cdot h_b} \tag{6-8}$$

where W is the weight of the wall, γ_m is the density of the wall, and N_o is the overturning force at the height, h_b. Regarding fixed-fixed URM walls, the resulting force due to vertical bending moment in vertical-spanning action at a specific height of wall can be calculated using a formula in the Australian Masonry Standards, AS3700 [182], as follows:

$$N_B = \frac{f_w \cdot Z_d + f_d \cdot Z_d}{h_b} \tag{6-9}$$

where f_w is the flexural tensile strength of the wall, Z_d is the section modulus of the bedded area, f_d is compressive stress acting on the bed joint due to vertical load and h_b is the height of the applied force.

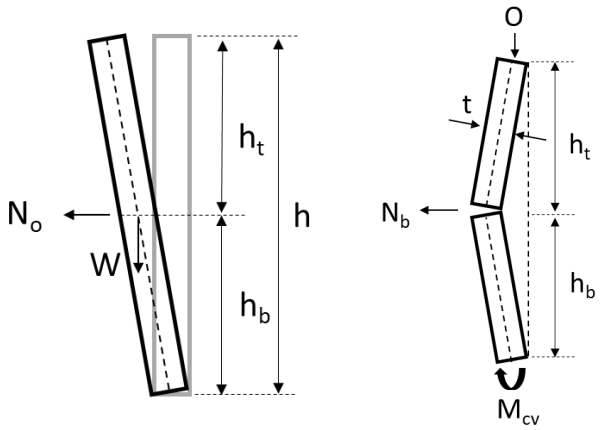

Figure 6.4 Out-of-plane failure mechanism: cantilever wall (a) and fixed-fixed boundary conditions with an applied vertical force.

The assessment of the out-of-plane behaviour has been studied mostly for single-leaf walls [95,178,183–186]. An example of bi-linear curve proposed by Doherty [95] by assuming infinite material stiffness for the rigid bodies can be seen in Figure 6.5.

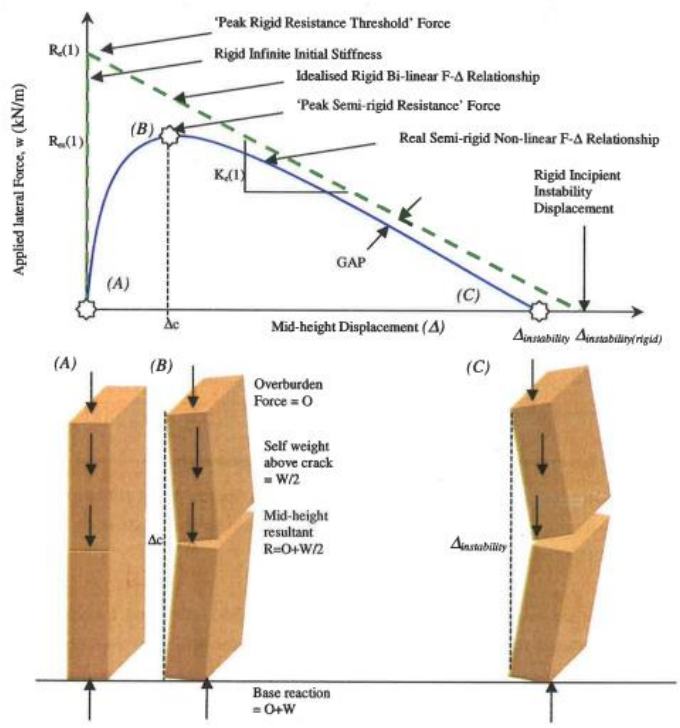

Figure 6.5 Semi-rigid non-linear force-displacement relationship from Doherty [95].

Griffith et al. [185] performed an experimental program to provide experimental evidence to support the proposed model by Doherty et al. [95]. In this experimental campaign, a total of 14 one-way vertically spanning URM wall panels were tested. The load was applied from at mid-height of the wall by means of an actuator. The boundary conditions represent a simply supported wall with a vertical load at the edge of the wall face. Force-displacement relationships are computed via the Linear elastic theory and the Rigid body theory. The linear elastic strength of the load-bearing wall is calculated by using the following equation:

$$F_{LE} = \frac{4}{h} Z(f_w + f_d) \tag{6-10}$$

where Z is the section modulus for the wall cross-section, h is wall height, f_w is the tensile bond strength, and f_d is the compressive stress at the middle height of the wall due to the vertical load applied at its top plus the weight of the upper half of the wall. The strength using rigid body theorem proposed by Doherty et al. [95] is as follows:

$$F_{RB} = \frac{3t}{h} W(1 + \psi) \tag{6-11}$$

where W is the weight of the wall, h is the height of the wall, t is the wall thickness and ψ is ratio of the applied vertical load to the weight of the upper half of the wall. Both equations consider only a single wall since cavity walls have a complex dynamic behaviour due to the presence of the load-bearing leaf and the non-load-bearing leaf connected by cavity wall ties. Hence, a static force-displacement (F-u) relationship is proposed for the OOP analysis of one-way vertical spanning strip cavity walls [162], assuming that the cavity wall ties provide sufficient axial stiffness and bonding between two leaves [68]. Since the experimental campaign described in Chapter 4 considers cavity walls with efficient wall ties, the model proposed by Tomassetti et al. [162] will be used in the following sections to predict the rocking capacity of the cavity wall system.

6.2 Joist-sliding failure mode including joist-to-wall interaction

As mentioned in Chapter 4, it was observed that an additional vertical force was introduced at the joist-wallet interface. This affected the capacity of the connection. In the test setup, the horizontal top and bottom edges of the specimens were fixed. Hence, when the middle of the wallet was displaced in the out-of-plane (OOP) direction, the deformation of the specimen and the uplifting resulting from cracking caused an increase in the axial vertical force (due to confinement) and consequently affected the frictional mechanism. It should be noted that this phenomenon can only be observed when the boundary condition of the specimen restricts vertical displacements at the top of the wallet, meaning that the vertical movement of the wall is fully or partially restrained. The additional resistance depended on the upward force related to the horizontal displacement of the cracked middle section of the wallet. Since the vertical movement was restrained, cracking due to the horizontal displacement led to a migration of the neutral axis of bending and hence introduced an elongation along the centroidal axis resulting in greater compressive forces. The elongation is computed based on the corresponding horizontal displacement where the joist was inserted in the pocket through simple geometric observations.

It is worth emphasising that the arching effect may not be taken into account if a structure is characterised by load-bearing URM walls with flexible diaphragms since the vertical motion of the wall is not restrained [190–192]. However, it would be a case not for the upper level of

a masonry building but for the lower floor level since the structural weight is higher at the lower floor level, causing to larger overburden on the masonry wall, thus, may cause arching action. Besides, as highlighted by Magenes [193], the strength capacity of URM buildings subjected to lateral loading is derived through vertical compression, apparent flexural strength in one- or two-way bending and arching action. In the current research, not only due to the presence of restrained overburden loads at the top of the wallet representing a concrete ring beam or a bounded wall condition etc., in a real building but also the filling with mortar between the joist and wallet allowing the arch force to be transferred at the interface, it is essential to compute the strength capacity of URM building in terms of each possible contribution including vertical compression, flexural strength or thrust action.

The additional resistance determined by the second-order effect is schematically illustrated in Figure 6.6. The curve expresses the relation between the horizontal force transferred by the timber joist to the masonry and the relative displacement between the joist and wall. Without any additional resistance due to the boundary condition, a curve based on Coulomb's law consisting of cohesion and friction (H_C+H_V), highlighted in red, would be expected. In the case of vertically restrained conditions, a modified Coulomb envelope curve is proposed to incorporate the contribution of arching (H_S) at the joist-masonry wall interface. This modified curve, highlighted in blue, exhibits increased stiffness and peak force (H_M) compared to the unrestricted conditions. The additional vertical arching force is proportional to the OOP displacement at the mid-height of the inner leaf. For this reason, it is related to the level of connectivity between the joist and masonry. When joist and wall are well connected, such as in the initial elastic branch, the OOP displacement at the mid-height of the inner leaf corresponds to the horizontal displacement of the timber joist. For this reason, the maximum contribution of the second-order effect is obtained at the peak load. After the peak, the level of connectivity between joist and wall decreases and relative displacements due to sliding rise between the two structural elements. The OOP displacements of the wall become then gradually smaller than those of the joist, reducing then the effect of the arching force. The post-peak phase of the proposed curve is therefore characterised by a softening behaviour attributed to the cohesion softening behaviour and the disappearance of the second-order effect, followed by a plateau due to dry friction.

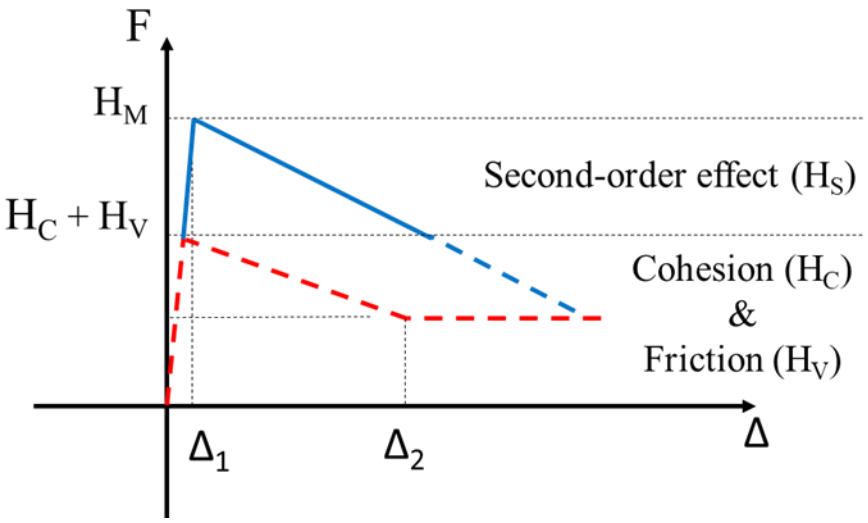

Figure 6.6 Proposed envelope curve compared to the conventional Coulomb model. The vertical axis indicates OOP force transferred by the timber joist to the wall, while the horizontal axis indicates the relative displacement between the joist and wall.

The conditions for the activation of the second-order effect are illustrated in Figure 6.7In this schematic illustration, the height of the thrust line, *h'*, is the path followed by the resultant of the forces acting on an arch across its span. When a unique displacement, *u*, of joist and inner leaf is observed thanks to the initial strong bond between masonry and timber, the second-order effect is activated, introducing an elongation along the centroidal axis and hence leading to additional compressive normal stresses at the joist-wall interface. This increases the frictional capacity of the joist-masonry connection. The sliding of the joist starts when this force is exceeded due to the absence of additional anchors.

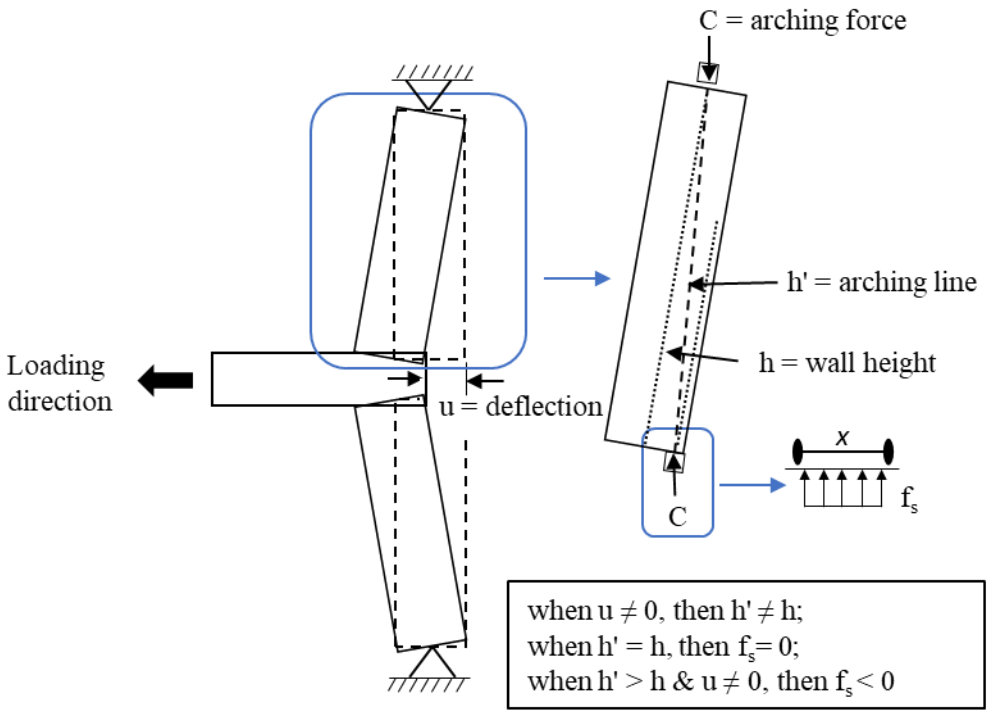

Figure 6.7 Schematic representation of the conditions that determine the activation of the arching effect.

The arching effect described here above was evident in the experimental results. In Figure 6.8, it can be clearly seen that the sliding force exponentially increases with the displacement of the wall as well as the wall-to-joist relative displacement increases. Considering a simple friction mechanism between the timber joist and the wall, the only effect that can highly nonlinearly increase the resisting force is the arching effect. The progression of this arching effect with the increasing displacement is shown in an example in Figure 6.8 for a singled-out example cycle from the experiments.

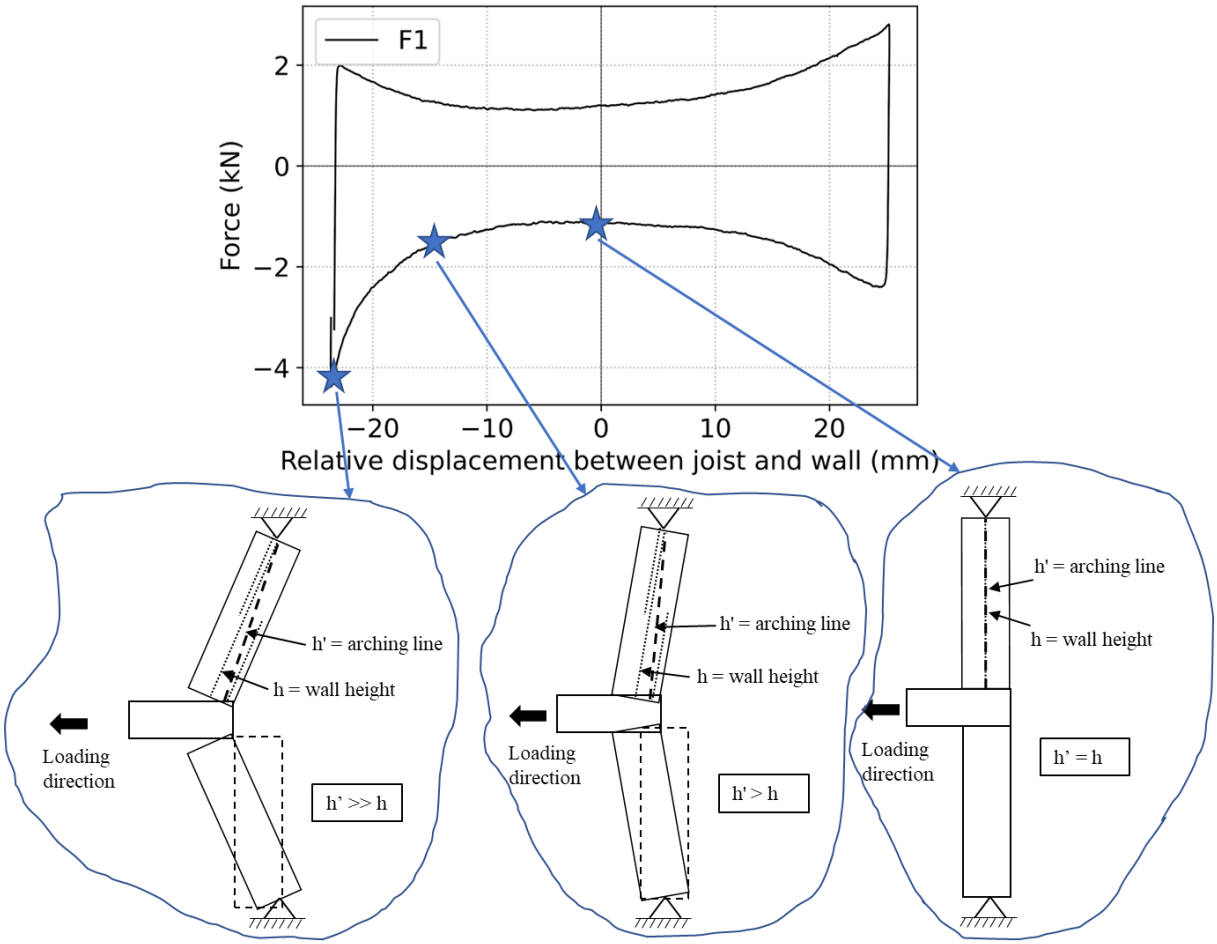

Figure 6.8 Example cycle from the force-displacement curve of Specimen F1 with the deformed configurations at three different positions of the inner leaf. The example highlights how the nonlinearity of the cavity wall system and the specific boundary conditions resulted in the arching effect.

This arching effect was previously reported in the literature [172,187] and Eurocode 6 [188]. To quantify the increase of resistance determined by the arching effect (H_S) a mechanical model already reported in the literature that includes both the Coulomb friction and second-order contributions is considered. The model is also used to analyse the contributions of these two mechanisms to the masonry pocket connections. In this model, the total frictional capacity consists of the cohesion and friction between timber and masonry and the additional out-of-plane strength (arching force) caused by the activation of the second-order effect. A number of parameters are required to compute the total capacity:

- friction coefficient,
- cohesion,
- normal force acting on the topside and underside of the embedded part of the joist,

- the arching force due to the OOP displacement of the inner leaf. This force, too, determines an additional normal force at the interface between the masonry and the joist.

Regarding the specimens in the as-built conditions, the cohesion contributed to the reaction force until the peak force, assuming that the interface between the joist and mortar was not cracked. Therefore, the measured force up to the peak, H_E, is divided by the upside and downside contact surface between the joist and the mortar, $2 \cdot t_w \cdot t_j$, in order to compute the interface shear strength. The shear strength, according to Coulomb's law, is obtained as follows:

$$\tau = \frac{H_E}{2 \cdot t_w \cdot t_j} = c + \mu \cdot \sigma_N + \mu \cdot \sigma_S \quad (6\text{-}12)$$

where τ is the shear strength, c is the cohesion, μ is the friction coefficient, σ_N is the normal stress at the interface due to the initial imposed axial load and σ_S is the normal stress at the interface due to the arching effect. The normal stress σ_N is computed as the sum of the initial forces imposed at the top of the wallet, N_V, divided by the contact area. The stress due to arching, σ_S, is computed as the additional vertical force due to the arching action in the inner leaf, N_S, again divided by the contact area.

$$\sigma_N = \frac{N_V}{t_w \cdot t_J} \quad (6\text{-}13)$$

$$\sigma_S = \frac{N_S}{t_w \cdot t_J} \quad (6\text{-}14)$$

where t_w is the thickness of the inner leaf and t_j is the thickness of the joist. The aforementioned three contributions are introduced in the following subparagraphs:

(1) Initial pre-compression load (N_V)

The initial force acting on the contact areas between the joist and the masonry was determined by the weight of the masonry, the overburden force above the joist and the applied vertical load at the middle of the joist. It should be noted that the joist deflected during the experiment because one extreme of the joist was fixed in the testing machine and could not displace vertically nor rotate, while the other extreme displaced vertically due to the OOP rocking of the inner leaf and the sliding of the joist in the pocket, as shown in Figure 6.9 (the out-of-plane rocking of the wall is amplified to provide a clearer visualization of the vertical displacement). However, the vertical deformation was very limited due to the vertical confinement of the wall caused by the applied boundary conditions. Hence, the shear force that would be caused by the

elastic deformation of the timber joist can be considered negligible and was not included in the proposed mechanical formula. An example of computing the vertical deformation and corresponding shear force due to the flexural and shear stiffness of the element is provided in Annex C.

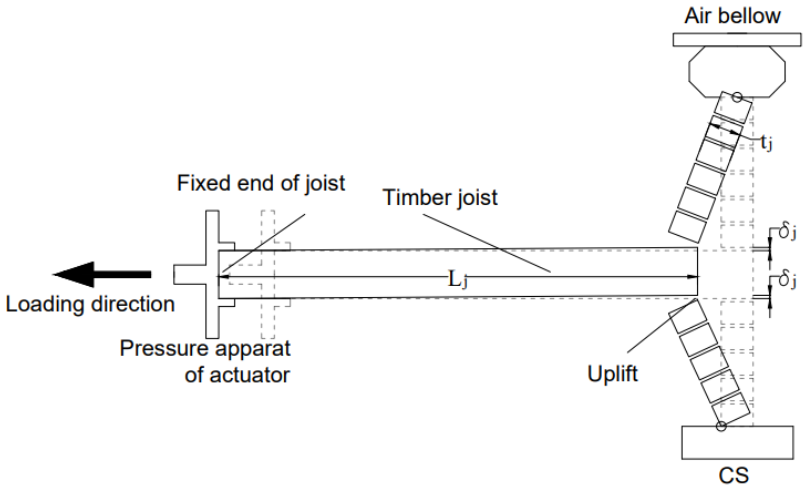

Figure 6.9 Amplified schematic representation of the OOP rocking of the inner leaf.

(2) Additional vertical force due to the arching effect (N_S)

The tilting of the wall induced additional compressive stress at the contact point between the joist and the masonry due to the arching effect within the masonry wallet, which determines an increase in the frictional force at the timber-masonry interface. The additional compressive stress was due to the rotation of wall blocks, behaving as rigid bodies. As these blocks rotated, the contact area between the joist and masonry reduced. In order to compute the arching force, N_s, firstly, the additional compressive stress, f_s, and the corresponding effective section depth, x, should be calculated. The additional compressive stress at the contact area between the joist and the masonry due to the arching effect, f_s, was determined based on the study of Paulay and Priestley [161] by using Eq. (6-4) for a given OOP displacement of the inner, u. While, the effective section depth, x, for the corresponding OOP displacement of the inner can be computed as follows:

$$x = 3\left(\frac{t_w}{2} - e - u\right) \tag{6-15}$$

where e is the eccentricity, and u is the OOP displacement of the inner, in which used to calculate the additional compressive stress. The arching force on the joist was computed, assuming a triangular stress profile as described in [161], as follows:

$$C = \frac{f_s \cdot x}{2} \tag{6-16}$$

$$N_S = C \cdot t_j \tag{6-17}$$

where C is the thrust force per unit width of the joist and t_j is the width of the joist. A schematic representation of arching effect is illustrated in Figure 6.10. It is important to note that the peak OOP deflection of the inner leaf was observed until the failure of bonding between joist and masonry followed by a decrease in the deflection and the sliding of the joist.

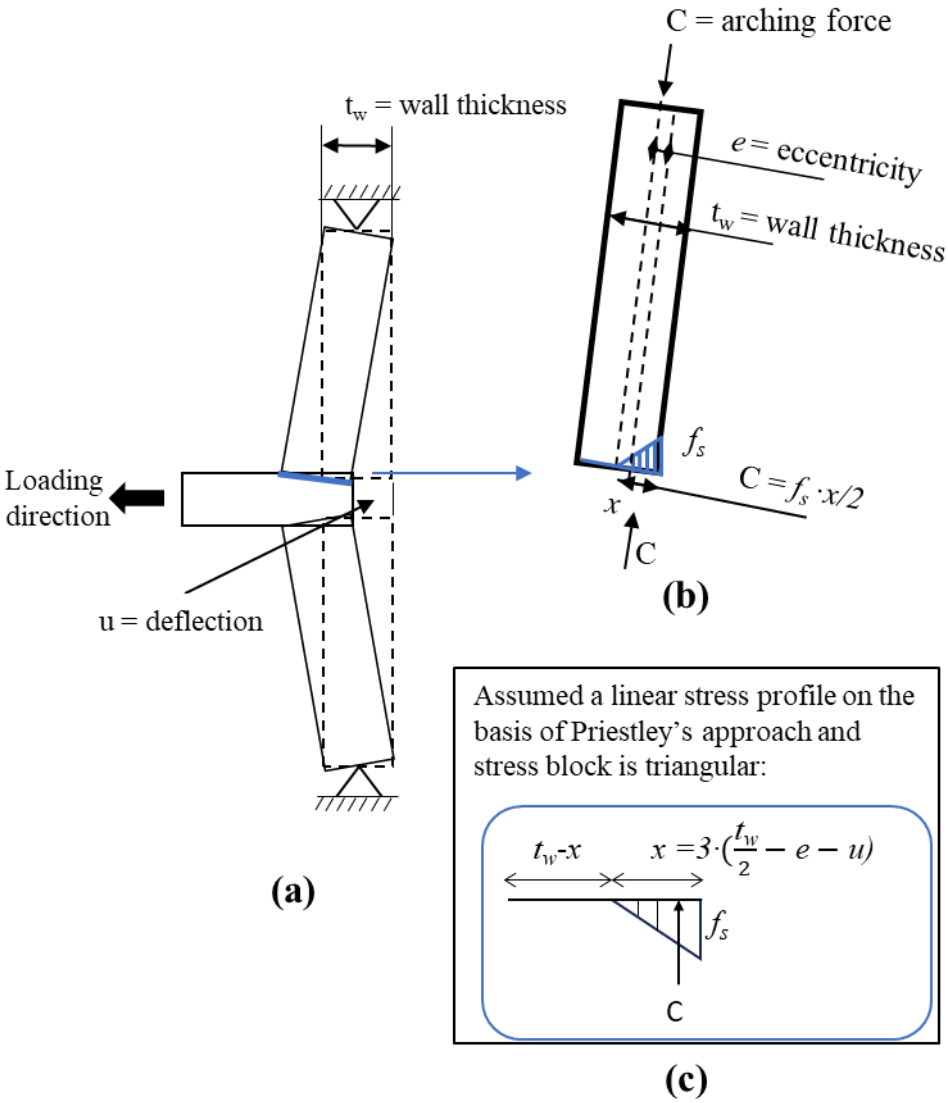

Figure 6.10 Schematic view illustrating the arching effect: cavity wall with timber joist subjected to OOP displacement (a), idealized wall segment (b) and triangular stress block of masonry based on Paulay and Priestley [161](c).

After computing the vertical forces on the joist due to initial pre-compression load, N_V, cohesion, c, and arching force, N_S, the contribution of pre-compression load, H_V, cohesion, H_C, and arching force, H_S, with respect to the horizontal direction and the OOP force as the sum of these contributions, H_M, are computed according to the following equation, as can seen in Figure 6.11:

$$H_M = H_V + H_S + H_C \tag{6-18}$$

$$H_V = 2 \cdot \mu \cdot N_V \tag{6-19}$$

$$H_S = 2 \cdot \mu \cdot N_S \tag{6-20}$$

$$H_C = 2 \cdot c \cdot A_J \tag{6-21}$$

where A_J is the contact area of the joist, computed as *tw*tj*.

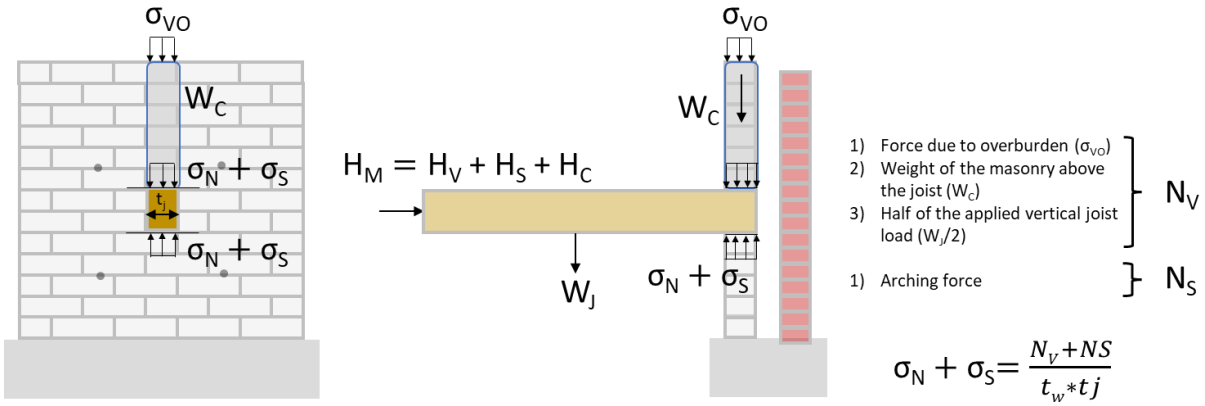

Figure 6.11 Schematic used to compute the normal force acting at the interface between masonry and joist.

6.3 Wall rocking failure mode due to joist movement

As explained in the previous section, in the case of the specimens with masonry pocket connection, the bond between the joist and wall is weak, not enough to create cracks in the wall itself. When an additional connection is present, such as a hook anchor or other strengthening solutions, the interaction between the wall and joist increases significantly, eventually leading to the failure of the wall itself due to OOP rocking. An example of a specimen with strengthened cavity wall anchors and timber joist-masonry connection by means of timber blocks at the failure can be seen in Figure 6.12. As evident from the figure, both leaves were

damaged severely, and the failure mode was governed by the OOP rocking behaviour of both leaves of the wallet.

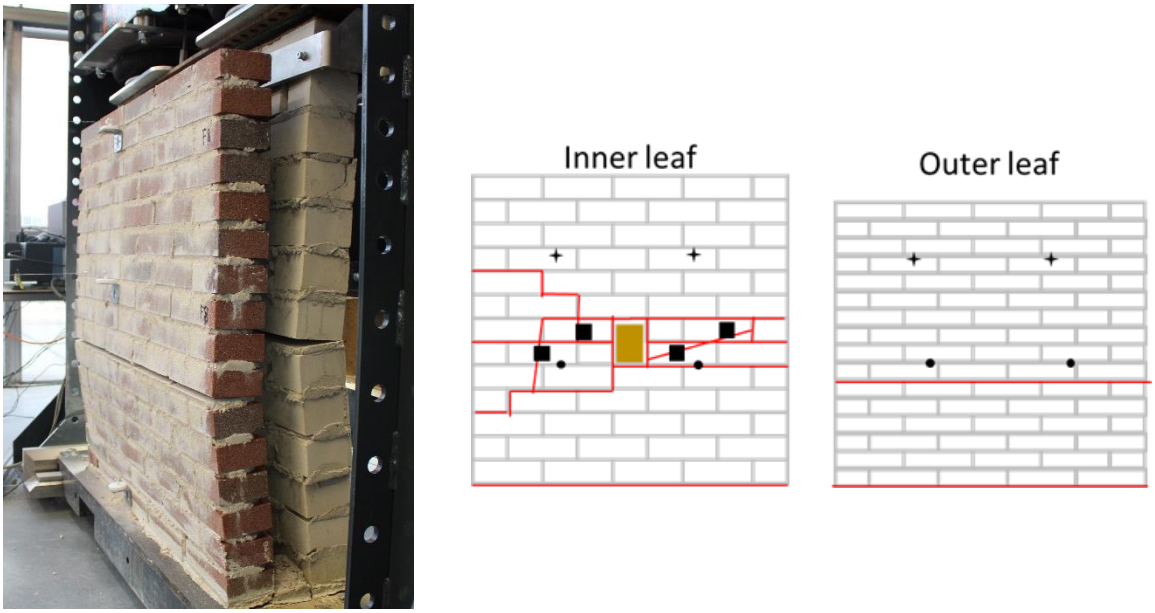

(a) (b)

Figure 6.12 Rocking behaviour of a strengthened specimen: observed view at the failure (a) and corresponding crack patterns (b).

As discussed in Section 6.2, the arching effect activated due to the joist-to-wall interaction should also be taken into account for the rocking behaviour. However, it is complex to determine the additional force for the full wall width because of the lack of experimental data supporting this in the OOP rocking, not only the nonlinearity of the problem but also the change in lateral deflection from the resting till the instability displacement of a leaf. Hence in this section, although known to exist to some degree, the additional overburden coming from the arching effect to the full wall width is omitted.

As a result, the simplified envelope curve illustrated in Figure 6.6 is updated by adding the OOP rocking failure mode, as shown in Figure 6.13. The vertical axis indicates OOP force transferred by the timber joist to the wall, while the horizontal axis indicates the relative displacement between the joist and wall. A bi-linear idealisation is used to define the rocking F-Δ curve. Since the additional overburden due to the arching effect determined an increase of the frictional capacity, the final failure of the system should be close to the OOP rocking capacity. It should be noted that, in reality, the size of the wall is bigger than those tested in this experimental campaign, and more joists will be inserted in the wall. Since the size effect

is not included in this study, the strength capacity may differ with increasing wall size. Hence, the results of the rocking failure mode are constrained by the dimensions of the specimens.

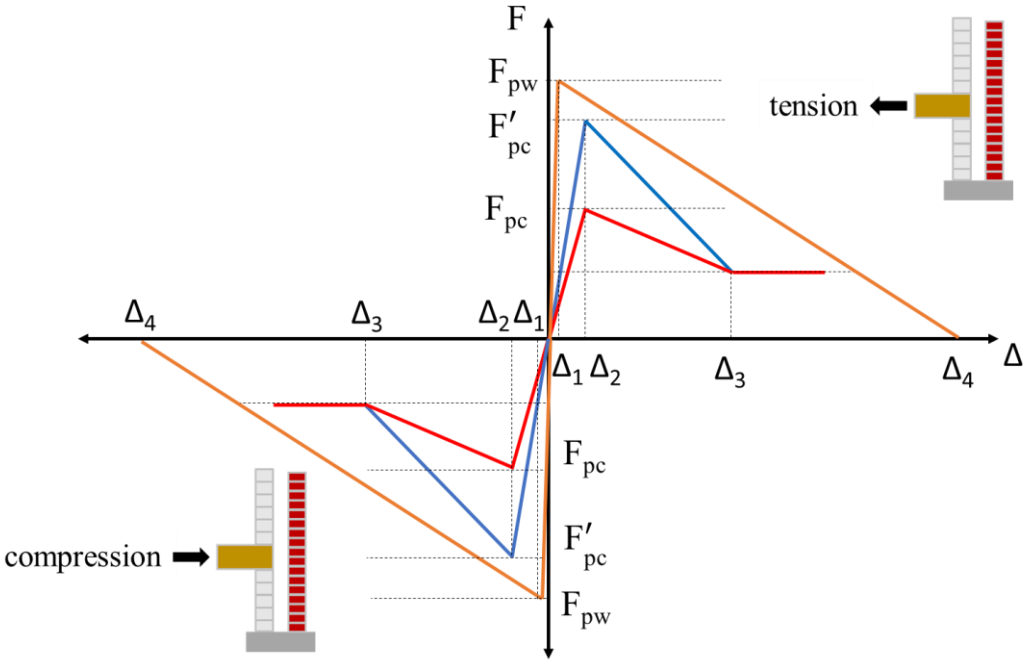

Figure 6.13 Simplified envelope curve for both failure modes: the red line indicates the Coulomb friction law. The blue line is the proposed curve to predict the joist-sliding failure mode, including the Coulomb friction criterion and the arching effect. The orange line is the bilinear curve to predict the rocking capacity of the cavity wall system.

In the study of Tomassetti et al. [162], the seismic behaviour of vertically spanning URM cavity walls subjected to out-of-plane movements was defined by the bilinear force-displacement model. The simplified force-displacement model was derived from a nonlinear rigid-body kinematic analysis of the cavity wall. The model represented an upper bound of the OOP static resistance of a masonry cavity wall. The bilinear model of nonlinear rocking behaviour yielded the two parameters of the model, which were the total rigid force (F_c+$F_{0,iw}$+$F_{0,ow}$) associated with the sum of the two rigid body mechanism forces of the two walls and the coupling force contribution of the embedded ties, and the instability displacement, u_{ins}, the maximum wall displacement.

The cavity walls initially exhibited a linear response controlled by the masonry flexural stiffness. The initial elastic phase of one-way vertical spanning strip walls was evaluated according to the boundary conditions. Since the exact boundary conditions were difficult to be defined, double fixed and double pinned configurations were considered as two limit configurations, as shown in Figure 6.14. In order to compute the pre-cracking phase, two different factors, a_t and a_b, corresponding to the type of bottom and top boundary conditions,

respectively, are defined. As mentioned in Chapter 4, the boundary condition of the inner leaf is defined as a pinned-pinned configuration, while the outer leaf is considered a cantilever wall. Hence, a_t and a_b are set equal to 0, which indicates the development of the full cracking moment only in the middle of the wall. In this case, as seen in Figure 6.14, for the pinned-pinned condition, the rocking behaviour develops simply with cracking at the middle of the wall (Point A*), and β is equal to a value of 5.

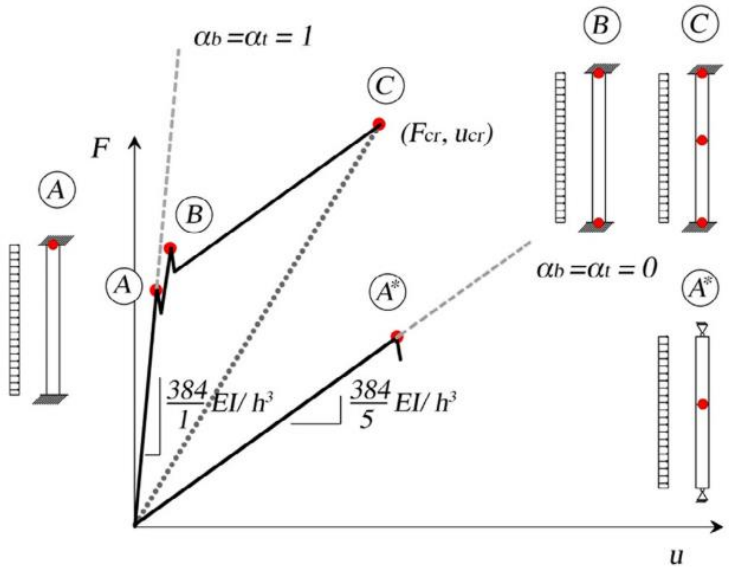

Figure 6.14 Pre-cracking phase for one-way vertical spanning strip walls considering the two limit boundary condition situations, which are fixed-fixed (A-B-C) and pinned-pinned (A) from Tomassetti et al.* [162].

The linear elastic response of the OOP plane one-way bending is computed by adopting the equilibrium method according to plastic analysis principles. Before computing the cracking force, F_{cr}, the top and bottom cracking moments, M_t, and, M_b, need to be defined based on the identified boundary conditions. Hence, only one level of stiffness is associated with computing the cracking force due to the formation of one hinge for the pinned-pinned condition. The linear elastic response of the OOP plane one-way bending, cracking force, F_{cr}, cracking displacement, u_{cr}, panel height, h_1, can be computed as follows:

$$F_{cr} = \frac{\zeta + \sqrt{\zeta - \frac{W^2}{4 \cdot {t_w}^2} - \frac{(a_b \cdot M_b - a_t \cdot M_t)}{{t_w}^3} - \frac{(a_b \cdot M_b - a_t \cdot M_t)^2}{{t_w}^4}}}{\frac{3}{2} \cdot \frac{h}{{t_w}^2}} \quad (6\text{-}22)$$

$$\zeta = f_w + \frac{1}{t_w}\left(\frac{W}{2} + \sigma_{v0} \cdot t_w + \frac{3 \cdot (a_b \cdot M_b - a_t \cdot M_t)}{t_w}\right) \quad (6\text{-}23)$$

$$M_b = \left(f_w + \frac{W + \sigma_{v0} \cdot t_w}{t_w}\right)\frac{{t_w}^2}{6} \tag{6-24}$$

$$M_t = \left(f_w + \frac{\sigma_{v0} \cdot t_w}{t_w}\right)\frac{{t_w}^2}{6} \tag{6-25}$$

$$u_{cr} = \frac{\beta}{384}\frac{F_{cr} \cdot h^3}{E_w \cdot I_w} \tag{6-26}$$

$$\frac{h_1}{h} = \frac{1}{2} + \frac{1}{h \cdot F_{cr}}\left(\frac{W \cdot t_w}{6} + (a_b \cdot M_b - a_t \cdot M_t)\right) \tag{6-27}$$

where W is the weight of the wall, t_w is the wall thickness, f_w is the masonry flexural strength, a_t and a_b are factors varying from 0 to 1 to define the degree of moment restrained associated with the related top and bottom extremities, h is the height of the wall, and h_1 is the panel height where the maximum tensile stress equals the masonry flexural strength.

After the formation of the horizontal crack at mid-height of the wall, the rocking behaviour fully developed. The formation of three hinges which are at the wall bottom (*A-A'*), mid-height (*B-B'*) and top (*C-C'*) can be seen in Figure 6.15. The rigid bodies rotated around the pivot points *A'*, *B* and *C'*. a_1 and a_2 represent the geometric angles for defining the slenderness of the two rigid bodies above and below the mid-height crack of the wall. W_1 and W_2 are the weight of the two rigid bodies below and above, respectively. σ_{vo} is the vertical overburden stress applied with eccentricity *e*. h_1 and h_2 are the height of the two rigid bodies below and above, respectively.

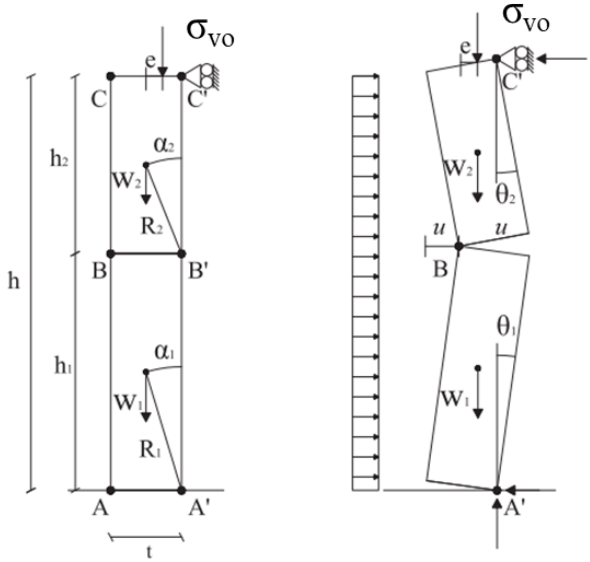

Figure 6.15 Rocking behaviour for a one-way vertical spanning strip walls: geometry at rest (left) and deformed shape (right) from Tomassetti et al. [162].

Due to the hinges, the wall can undergo large displacement. The proposed model also considers the eccentricity due to the migration of the top resultant overburden force along the top edge of the wall. Regarding the bilinear curve, as seen in Figure 6.16, rigid force, F_o, and the instability displacement, u_{ins}, are computed by using the following equations, respectively:

$$F_0 = \frac{2}{h_1}(W + \sigma_{v0} \cdot t_w) \cdot t_w + \frac{\sigma_{v0} \cdot t_w}{h - h_1}(t_w + 2e) \tag{6-28}$$

$$u_{ins} = \frac{\frac{2}{h_1(W + \sigma_{v0} \cdot t_w)t_w} + \frac{\sigma_{v0} \cdot t_w(t_w + 2e)}{h - h_1}}{\frac{2}{h_1(W + \sigma_{v0} \cdot t_w)} + \frac{2 \cdot \sigma_{v0} \cdot t_w}{h - h_1}} \tag{6-29}$$

where h_1 is the panel height where the maximum tensile stress equals the masonry flexural strength, $\sigma_{v0} \cdot t_w$ is the overburden force, W is the weight of masonry, t_w is the thickness of the masonry and e is eccentricity. The coupling force contribution of ties in cavity wall can be computed as follows:

$$F_c = 2 \cdot V_t \cdot t_w \cdot \frac{h}{h_1 \cdot h_2} + 2 \cdot M_t \frac{h}{h_1 \cdot h_2} \tag{6-30}$$

$$V_t = \sum_1^n V_i \tag{6-31}$$

$$M_t = \sum_1^n M_i \tag{6-32}$$

where V_t and M_t are the sum of the n tie plastic moments and the corresponding shears at the inner leaf edge interfaces, respectively. As shown in Figure 6.16, the force capacity of the cavity wall specimens can be defined as the sum of the cracking force of the two leaves (considered independent of one another) and the coupling force:

$$F = F_{0,iw} + F_{0,ow} + F_c \tag{6-33}$$

The formulation, based on the rigid body theorem, can be used to define an upper bound for the experimental results discussed in Chapter 4 on the as-built and strengthened timber joist-cavity wall specimens. This assumption is used for both the strengthening solutions described in Section 4.5 and Section 4.6.

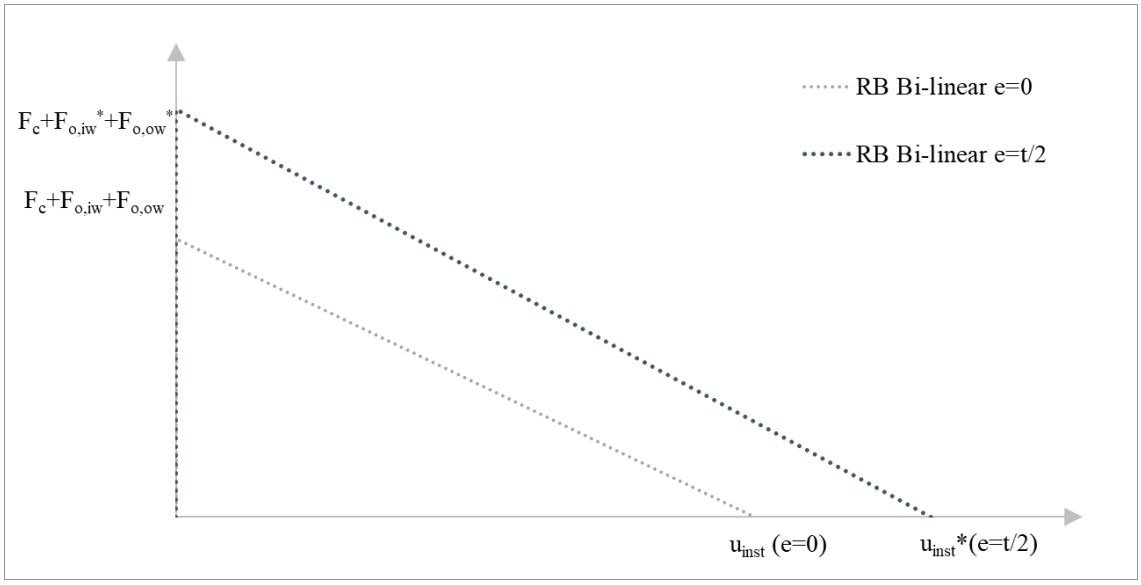

Figure 6.16 Bilinear envelope curve for the force-displacement curve of a one-way spanning wall, proposed by Tomassetti et al. [162].

6.4 Comparison of predictions with the experimental tests

The values of the force capacity predicted via the analytical models described in the previous sections are compared to the experimental results. The comparison is presented by grouping the results per type of connection: namely, joists with no anchors, joists with a hook anchor, and strengthened specimens. The horizontal displacement of the middle height of each leaf (CS and CB) and the peak force in pulling and pushing are shown in Figure 6.17 to highlight the initial rocking behaviour due to bonding and friction between the joist and masonry. It is essential to define the out-of-plane displacement of the inner leaf in order to compute the additional vertical force due to the arching action in the inner leaf (N_S).

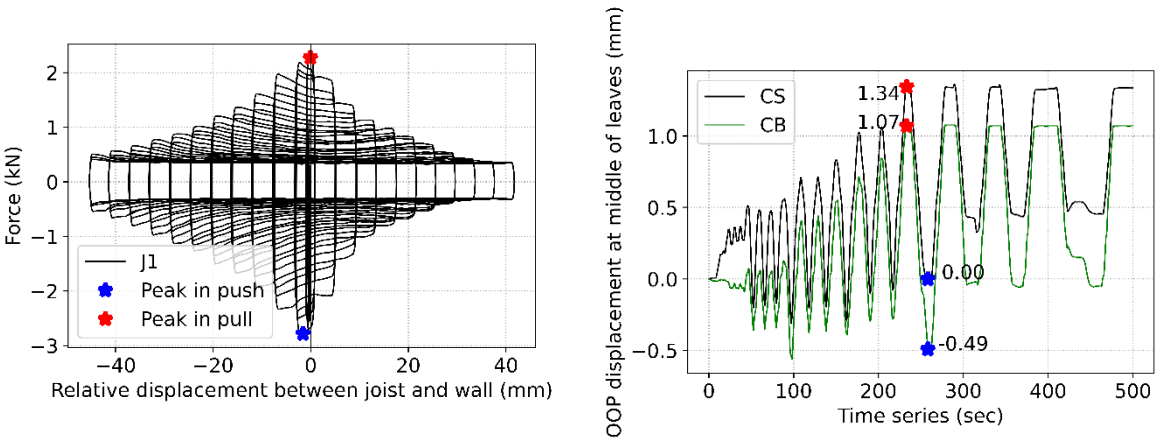
Force (kN)
Relative displacement between joist and wall (mm)
J1
Peak in push
Peak in pull
OOP displacement at middle of leaves (mm)
Time series (sec)
CS
CB
1.34
1.07
0.00
-0.49

(a)

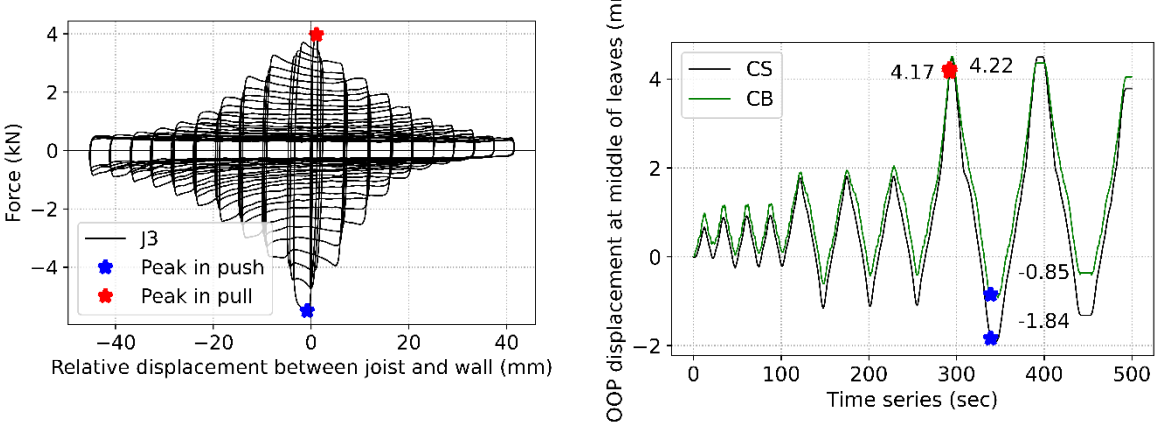
Force (kN)
Relative displacement between joist and wall (mm)
J3
Peak in push
Peak in pull
OOP displacement at middle of leaves (mm)
Time series (sec)
CS
CB
4.17
4.22
-0.85
-1.84

(b)

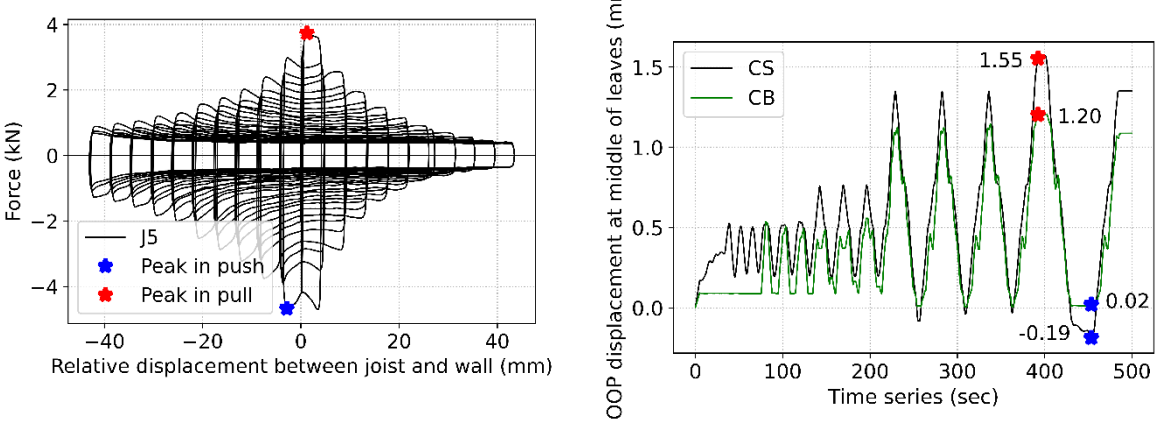
Force (kN)
Relative displacement between joist and wall (mm)
J5
Peak in push
Peak in pull
OOP displacement at middle of leaves (mm)
Time series (sec)
CS
CB
1.55
1.20
0.02
-0.19

(c)

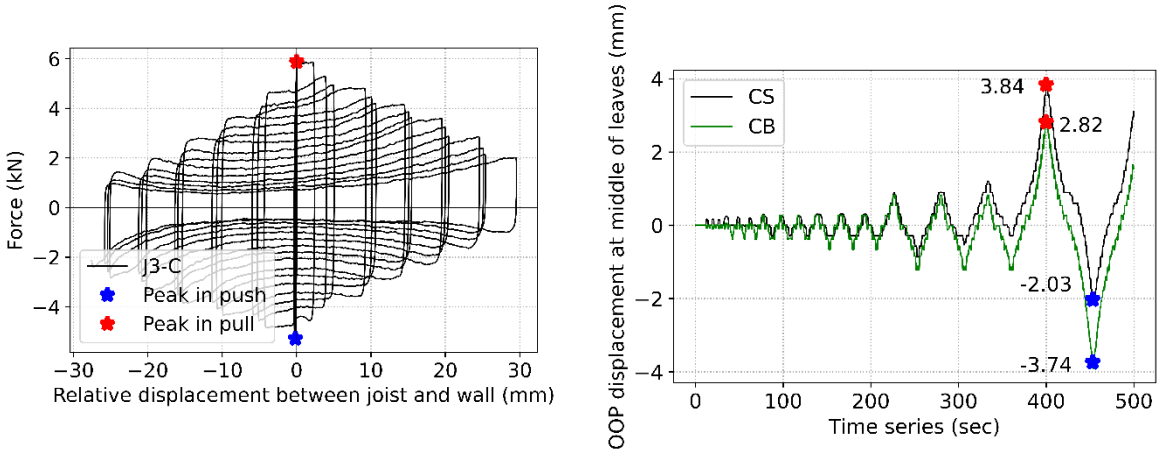

(d)

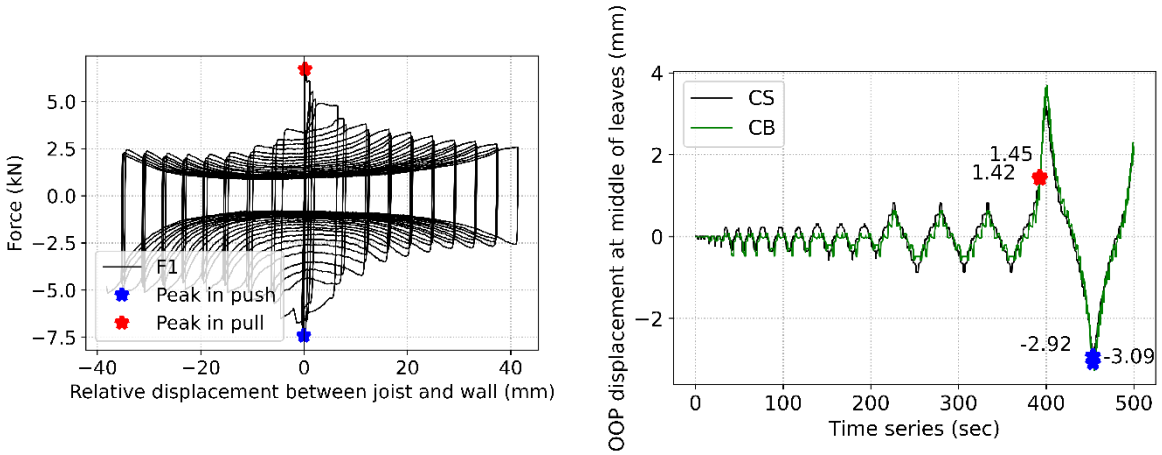

(e)

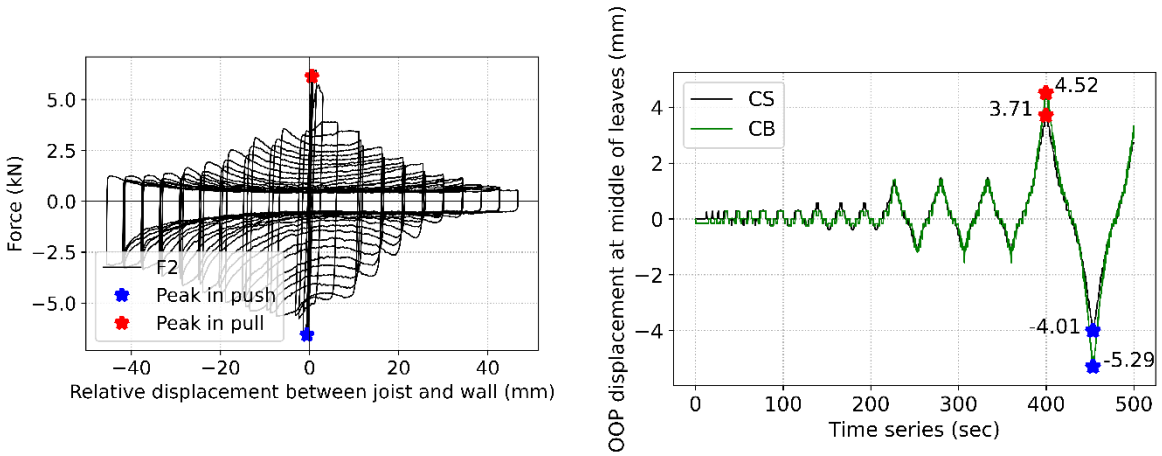

(f)

Figure 6.17 Hysteresis curve for the tested specimens (left) with the corresponding OOP displacement at the middle of the inner and outer leaves (right), for specimens J1 (a), J3 (b), J5 (c), J3-C (d), F1 (e) and F2 (f). Red and blue stars highlight the peak force in both the pulling and pushing directions, respectively.

With the aim to define the friction coefficient between joist and masonry, the joists with no anchors were used since the capacity of the connection was mainly governed by the friction

between the joist and the mortar towards the end of the loading cycle where the plastic plateau occurred. Hence, the friction coefficient is computed based on the last cycles of loading at the plastic plateau for both loading directions, and its result is equal to a value of 0.6. It should be noted that the coefficient of friction for the rest of the specimens is set to a friction coefficient equal to 0.6 since the specimens with masonry pocket connections are based on frictional capacity. The cohesion, according to Coulomb's law, is obtained by using Eq. (6-12). It should be noted that the cohesion is firstly obtained for both directions, and the average of these two values is taken.

The obtained values for shear stress are summarised in Table 6.1. The shear stress, τ, is defined as the peak force (as measured experimentally) in pulling or pushing divided by the contact area at the interface between the mortar and joist. The reason why the shear stress in pulling (column (1)) and pushing (column (2)) was separately computed is due to the asymmetric behaviour of the test results. The asymmetric behaviour is attributed to the nonlinearity of the cavity wall system with the test setup, causing additional vertical forces due to the arching action in the inner leaf and the deflection of the joist caused by the displacement of the point supported. Due to the same reason, the normal stress acting on the joist and the arching stress are defined separately. As expected, the normal stresses in pulling and pushing are equal, shown in column (3), and computed according to Eq. (6-13). The arching stresses in pulling (column (4)) and pushing (column (5)) are defined as the additional force acting on the joist in the vertical direction divided by the contact area at the interface between the mortar and joist. Finally, cohesion is computed according to Eq. (6-12) for pulling and pushing separately. After that, the mean value of cohesion in pulling and pushing was defined. Hence, the cohesion (column (6)) is the same value in pulling and pushing. It should be noted that an example of the calculation of the joist-sliding failure mode is presented in Annex C.

Table 6.1 Stress values acting at the interface between masonry and timber joist.

	(1)	(2)	(3)	(4)	(5)	(6)
	Shear Stress (MPa) [τ]		Normal Stress (MPa) [σ_N]	Arching Stress (MPa) [σ_S]		Cohesion (MPa) [c]
	Pulling	Pushing	Pulling & pushing	Pulling	Pushing	Pulling & pushing
J1	0.19	0.26	0.15	0	0.10	0.10
J3	0.33	0.47	0.11	0.23	0.42	0.11
J5	0.31	0.41	0.35	0.03	0.20	0.08
J3-C	0.49	0.44	0.15	0.40	0.37	0.14
F1	0.56	0.62	0.15	0.38	0.51	0.23
F2	0.51	0.56	0.15	0.41	0.44	0.19

After computing the shear stress, the total resistance due to cohesion and friction can be estimated via Eq. (6-19). Such value is compared to the measured peak force obtained in the experiments, as seen in Table 6.2. An error of up to 5% is found, which can be considered acceptable due to the nonlinearity of the system. The error is computed as the difference between the mechanical model and the experimental result divided by the experimental result.

Table 6.2 Comparison between the peak forces measured experimentally and predicted by means of the proposed mechanical model. The different components contributing to the total force (cohesive force and friction force due to both the initial normal force and the arching effect) are identified.

	(1)	(2)	(3)	(4)	(5)	(6)	(7)	(8)	(9)	(10)
	Pulling					Pushing				
	Exp.	Prediction			Error	Exp.	Prediction			Error
	Peak Force (kN)	Cohesion (kN)	Friction forces			Peak Force (kN)	Cohesion (kN)	Friction forces		
			Initial force (kN)	Arching effect (kN)				Initial force (kN)	Arching effect (kN)	
J1	2.29	1.19	1.09	-	-0.4%	3.13	1.19	1.09	0.73	-2.1%
J3	4.02	1.35	1.09	1.66	2.1%	5.59	1.35	1.09	3.05	-1.7%
J5	3.77	0.97	2.53	0.20	-1.8%	4.89	0.97	2.53	1.43	1.0%
J3C	5.87	1.73	1.09	2.89	-2.8%	5.28	1.73	1.09	2.63	3.3%
F1	6.71	2.80	1.09	2.74	-1.1%	7.49	2.80	1.09	3.67	1.0%
F2	6.45	2.26	1.09	2.96	-2.1%	6.68	2.26	1.09	3.18	-2.3%

Note: in the table, columns (2)-(4) and (7)-(9) are computed according to Eq. (6-19).

Regarding the rocking failure mode, the parameters of the bilinear curve are determined by means of Eq. (6-28)-(6-30) can be seen in Table 6.3. The values were obtained for each configuration. An increase at the pre-compression level leads to a significant increase of rigid

force obtained as the sum of the forces associated with the rigid body mechanisms of the two leaves. Besides, a higher mortar strength quality has an impact on the rigid forces, as can be seen from Specimen F1-F8. It should be noted that an example of the calculation of the rocking failure mode is presented in Annex C.

Table 6.3 Parameters used to define the bilinear curves for rocking failure.

Specimen	F_{cr} (kN)	u_{cr} (mm)	h_1/h	F_0 (kN)	F_0*(kN)	F_c (kN)	u_{ins} (mm)	u_{ins}*(mm)
J1-J2 TJ1-TJ2	6.19	0.13	0.51	6.81	8.66	0.2	76.5	100
J3-J4-J3C-J4C TJ3-TJ4	6.39	0.13	0.51	7.01	8.86	0.4	76.5	100
J5-J6 TJ5-TJ6	8.80	0.13	0.51	17.84	23.31	0.4	75.4	100
F1-F8	8.27	0.11	0.51	6.64	8.48	0.2	76.5	100

The failure of the specimens with a hook anchor was governed by rocking behaviour. Therefore, the force associated with the sum of the two rigid body mechanism forces of two leaves is compared to the experimental force-displacement curves. The bilinear curves were plotted versus the OOP displacement at the middle height of the inner and outer leaves, as seen in Figure 6.18a and b, respectively. The bilinear curves are computed as described in section 6.3, either considering the eccentricity of the top axial load equal to zero (RB Mechanism) or to half of the wall thickness (RB* Mechanism). Although the specimens with hook anchors exhibited rocking behaviour, the limited contribution due to the hook anchor to the inner and outer leaves can be seen in Figure 6.18a and b; hence, the obtained test results do not exceed the bilinear curves. It should be noted that the bilinear curve is defined only for the weakest configuration, which has a pre-compression level of 0.1 MPa and two cavity wall ties, because the test results are already below the rigid body mechanism of that configuration.

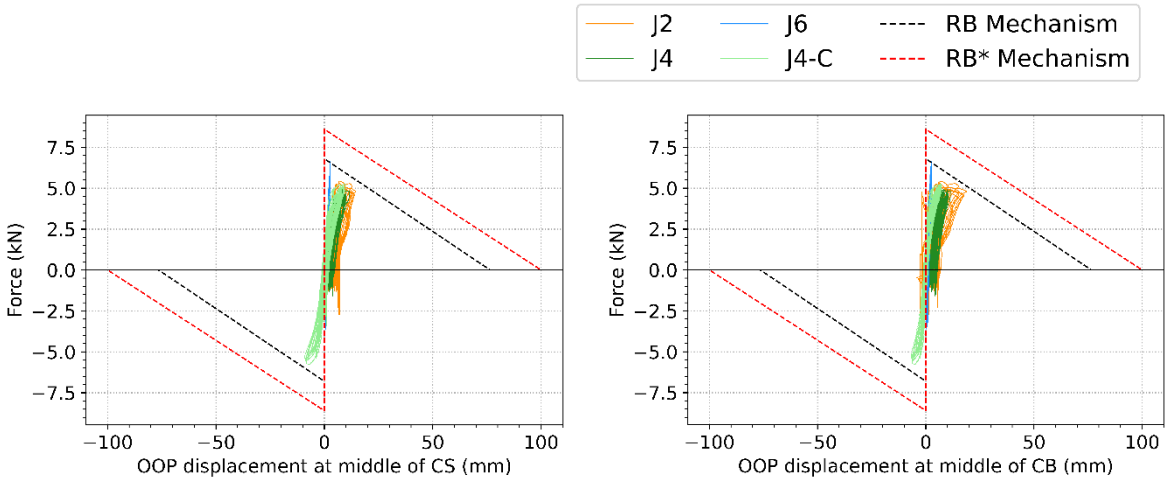

(a) (b)

Figure 6.18 Comparison between the test results of hook anchor specimens and the corresponding bilinear curves: force versus the OOP displacement at the middle height of the CS (a) and of the CB (b) leaves.

All the tested specimens, namely J1 to J6, were retrofitted and retested, labelled as TJ1-TJ6. After the application of the strengthening measures, rocking failure mode occurred. It should be noted that the forces measured during the tests with a pre-compression level of 0.3 MPa do not exceed the predicted rigid body force associated with a pre-compression level of 0.1 MPa and 2 ties/m^2 (Figure 6.19). The value for each configuration is reported in Table 6.3. The final collapse of the retested specimens is due to the instability displacement of the outer leaf, as seen in Figure 6.19.

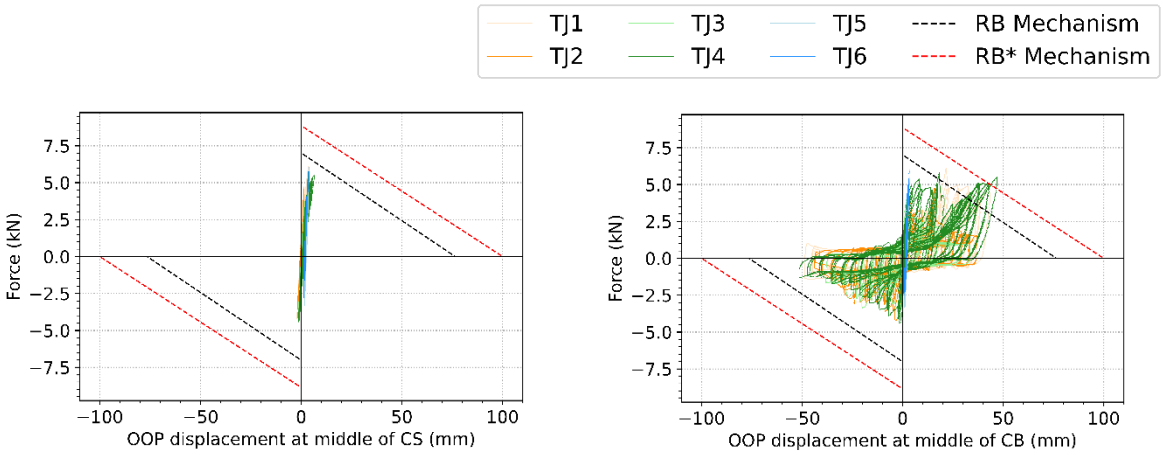

(a) (b)

Figure 6.19 Comparison between the test results of retested specimens and the corresponding bilinear curves: force versus the OOP displacement at the middle height of the CS (a) and of the CB (b) leaves.

As seen in Figure 6.19, the hysteresis curves exceed the envelope of the rocking mechanism, particularly the specimens with hook anchors in the pulling direction. Although the arch effect is omitted for the specimens that exhibited rocking behaviour, the specimens with the hook anchor in pulling exhibit plateau show that the continuation of OOP displacement in CS leaf causes the arching effect. A slight increase in capacity is observed regarding the retested specimens due to the helical bars. Besides, the OOP displacement of the inner leaf was very limited since the anchor fastened to the outer leaf.

With the aim of improving the displacement capacity of both leaves in both directions, the timber joist-masonry connection was strengthened by means of timber blocks. In addition, the retrofitting anchors were also used. The bilinear curves are plotted for the inner and outer leaves, as shown in Figure 6.20a and b, respectively. The rocking of both the inner and outer leaf is the governing failure mode for the specimens strengthened with the timber blocks since this measure provides a very strong connection between the joist and the wall. Hence, similarly to the retested specimens, the hysteresis curves are either very close or exceed the envelope of the rocking mechanism due to the arch effect.

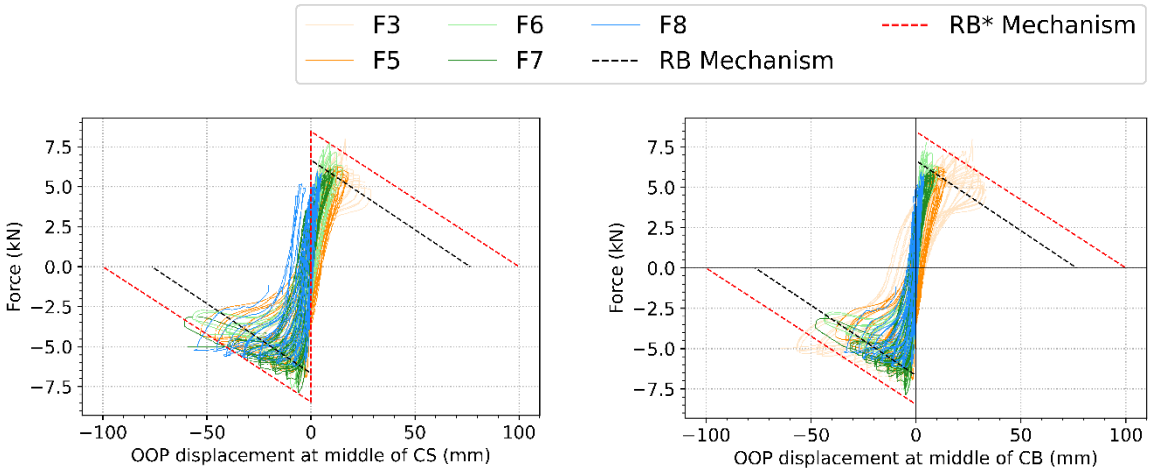

(a) (b)

Figure 6.20 Comparison between the test results of specimens strengthened with timber blocks and the corresponding bilinear curves: force versus the OOP displacement at the middle height of the CS (a) and of the CB (b) leaves.

The properties derived from the tests used in the mechanical model are summarised in Table 6.4.

Table 6.4 Summary of the joist-masonry connection properties.

Material Characteristic	Joist	CS	Solid clay brick	Perforated clay brick
Elastic modulus from Jafari [62] (MPa)	12000	2749	5019	5201
Friction coefficient between joist and masonry	-	0.6	-	-
Masonry weight above the joist (kN)	-	0.06	-	-
Overburden force above the joist (kN)	-	0.6	-	-
Height of wall (mm)	-	1030	950	950
Width of wall (mm)	-	930	930	930
Thickness of wall (mm)	-	100	100	100
Compressive strength of wall from Jafari [62] (MPa)	-	5.93	-	-
Flexural strength of wall (MPa)	-	0.1	0.28	0.42
Density of wall (kg/m3)	-	1683	1740	1250

6.5 Conclusions

This chapter aims to identify the contribution of different resisting mechanisms to the force capacity of timber-joist connections. The adopted mechanical model examines two distinct failure modes: joist-sliding with partial wall-joist interaction and out-of-plane (OOP) rocking behaviour of the masonry walls.

The joist-sliding failure, which involves a partial joist-to-wall interaction mechanism, governs weak joist-masonry connections. Regarding the OOP rocking failure mode, the failure mechanism shifts from the connection to the wall system. If the joist-masonry connection is strong, i.e., the connection retrofitted or characterised by high strength, the failure mode is characterised by the rocking behaviour of either one or both leaves of the wallet.

An interesting finding was that, due to the OOP displacement of the wall leaves rocking over the timber joist, an arching effect was activated, causing additional friction. The total joist push/pull capacity is computed as the sum of two contributions according to this: initial friction force and the additional friction caused by the arching effects.

The considered model presented here is capable of accurately predicting the peak capacity of the joist connection. Based on the results of the modelling of timber-masonry connections, the following observations have been made:

- The studied analytical model successfully defines the contribution of each mechanism in terms of the resistance at the failure for the joist-sliding failure mode.

Regarding the rocking behaviour, the bilinear curve effectively predicts the capacity of the wallet.

- The error between the analytical model and the experimental results for the specimens without hook anchors amounts to approximately 5% in terms of peak forces in pulling and pushing.
- Due to the variations in the configurations, different results in strength were observed when comparing the experimental results of unstrengthened and strengthened connections. When comparing the experimental results of the as-built masonry pocket connection with two ties to the same configuration but strengthened with helical bars in terms of peak load, an average increase of 13% in pulling and 12% in pushing is observed. Similarly, when comparing the experimental results of the as-built masonry pocket connection with two ties to the same configuration but strengthened using the timber blocks and post-installed cavity wall tie anchors in terms of peak load, an average increase of 5% in pulling and 9% in pushing is observed.

This chapter addressed two crucial factors: frictional behaviour and arching effect. These factors are present in real buildings and hence should be taken into account. Frictional behaviour pertains to the resistance between the timber joists and the masonry wall interface. In the latter case, even when the vertical displacement of walls is not restrained, the arching effect due to the out-of-plane behaviour of masonry walls, especially at lower levels, needs to be evaluated. This is due to the increased structural load, resulting in greater vertical pressure and possible arching effect.

The author believes that the presented model can be utilised by structural engineers to estimate each contribution of the analysed mechanism in case they have at least one of these mechanisms. In addition to that, it can be used to assess the performance of such connections during seismic events in masonry cavity walls with the characteristic under investigation, whereas other alternative construction methods and/or materials would necessitate dedicated research.

Chapter 7: Conclusions and recommendations for future research

7.1 Conclusions

The research presented in this thesis aims to investigate the seismic response of wall-to-wall tie connections and wall-to-floor timber-masonry connections commonly used for cavity walls in the traditional Dutch construction practice, specifically in the Groningen province. A series of how-to questions are formulated in the introduction section (Chapter 1) to fulfil the overall objective. To this end, the research has been structured in three phases: (i) An inventory of existing buildings and connections in the Groningen area is set up (Chapter 2); (ii) The mechanical behaviour of the prevalent connection typologies identified in the inventory for cavity walls is characterised experimentally: first, wall-to-wall tie connections are simulated by means of a metal tie embedded in the mortar of a masonry couplet (Chapter 3). Second, wall-to-floor connections are simulated by means of masonry wallets and timber joists (Chapter 4); and (iii) Mechanical models are proposed and validated against the performed experiments for the studied connections, namely the wall-to-wall tie connections (Chapter 5) and the wall-to-floor connections (Chapter 6).

Chapter 2 presents a dataset of buildings and connection details in the Groningen area with the purpose of identifying the most prevalent connection typologies used in buildings with cavity walls. A total of 267 addresses and 59 inspection reports received from Nationaal Coördinator Groningen (NCG) were processed, and the following structural characteristics were identified:

- The preferred construction type in the area before World War II was the detached house. However, after World War II, the terraced house became increasingly popular, accounting for over 65% of the buildings in the inventory constructed after that date.
- From the studied dataset, a similar number of detached houses with solid walls and timber floors and detached houses with cavity walls and timber floors was found.
- Approximately 20% of the URM buildings have timber floors, while around 26% of the inventory comprises attic floors made of timber.

- The dimensions of a cavity wall vary from building to building, with median values of 100 mm for the inner leaf, 80 mm for the cavity, and 100 mm for the outer leaf.
- Hook anchors are the most commonly documented as-built connections between timber floors and masonry walls.

It was observed not only in the studied dataset but also from the literature that World War II was a milestone in terms of construction technique. Consequently, after the war, not only the cavity-wall terraced house typology became predominant in the region but also the cavity-wall construction technique was used in the construction of newly built detached houses. Hence, cavity walls and flexible timber diaphragms have been selected as representative of the Dutch construction practice in typical terraced and detached houses. In this thesis, the following structural characteristics are identified for traditional Groningen houses:

- Cavity walls consist of an inner 102-mm-thick load-bearing leaf made of calcium silicate (CS) bricks and an outer 100-mm-thick external veneer made of clay bricks (CB) separated by a cavity of 80 mm. The inner leaf is constructed using solid bricks, while both solid and perforated clay bricks are commonly employed for the veneer.
- Regarding wall-to-wall connections (the connections between the two leaves), L-shaped ties with a diameter of 3.6 mm and a total length of 200 mm are selected. The ties are embedded in the mortar joint of both the CS and CB leaves: the zigzag end of the tie is embedded in the CB leaf, while the L-shaped hooked end is embedded in the inner CS wall.
- The connection between a flexible floor and a masonry wall consists of a timber joist with a size of 55x155 mm (L x H) connected to the inner leaf of the cavity wall either by masonry pocket connection or hook anchor connection.

Two experimental campaigns have been conducted to study the structural configurations described above. The first experimental campaign was conducted at the laboratory at Delft University of Technology and provided a complete characterisation of the axial behaviour of traditional wall tie connections in cavity walls (Chapter 3). The tested specimens consisted of masonry couplets (two stacked bricks connected by means of mortar) and a metal wall tie embedded in the mortar joint at one end. The connection between the metal tie and the masonry couplet was then tested. The embedment in the CS and the CB couplets was tested separately. Couplets with perforated CB were used to represent the external veneer. Several variations were considered: two embedment lengths (50 mm and 70 mm), four pre-compression levels of the couplets (0 MPa, 0.1 MPa, 0.3 MPa and 0.6 MPa), two different tie geometries (the zigzag

end embedded in CB and the L-shaped hooked end embedded in CS), and five different loading protocols, including monotonic and cyclic loading. Regarding the loading protocols, monotonic tests were conducted to obtain the maximum strength capacity of connection under tension and compression. In addition, a cyclic loading protocol was also considered to capture any strength and stiffness degradation.

The following failure modes were observed: sliding failure (the tie slides along the tie-mortar interface), tie failure (the tie first yields and then fractures), buckling failure (the tie buckles), and expulsion failure (failure is achieved by piercing and expulsion of the cone of mortar around the tie). The most common types of failure were observed as sliding during tensile loading and buckling during compressive loading, which was observed in 92% of the tested specimens for both tension and compression. The experimental results also showed that the force capacity of the connection was strongly influenced by the embedment length and the geometry of the tie, depending on whether the zigzag end or the L-shaped hooked end was embedded in the mortar. In contrast, the level of pre-compression applied to the couplets and the loading rate did not significantly affect the force capacity.

Specifically, the following conclusions are drawn based on the performance of cavity wall tie tests on couplets:

- Monotonic tests show, on average, a 19% larger peak load than cyclic tests for the CS specimens. A comparable increase is also observed for the CB specimens.
- In tension, the strength capacity of the tie embedded in clay couplets is approximately 70% higher than when embedded in calcium silicate couplets; such high capacity can be attributed to the dowel action of the mortar in the brick holes of clay bricks which provides extra confinement to the mortar and, hence, resistance.
- In compression, the large majority of the couplets exhibit buckling failure due to the buckling of the tie. Therefore, the strength capacity is similar for the CS and CB specimens.
- Overall, despite testing the embedment of the tie in CS and CB couplets separately, it can be concluded that in the case of cavity walls in real construction practice with a CS inner leaf and a CB veneer, the behaviour and performance of the studied wall-tie connection is mainly governed by the tie embedment in the CS leaf.

The second experimental campaign took place at the laboratory of the Hanze University of Applied Sciences. The campaign involved quasi-static cyclic tests conducted on both as-built and strengthened sub-assemblages consisting of a cavity-wall masonry wallet with a timber

joist pocketed in the wallet, as described in Chapter 4. A total of twenty-two specimens were tested, with varying configurations in terms of two different tie distributions, two pre-compression levels, two as-built connection details, and two strengthening solutions. The as-built connections involved either the timber joist pocketed in the masonry or a hook anchor bearing against the exterior surface of the inner leaf. Two different failure modes were observed for the as-built connections: specimens with a masonry pocket connection exhibited joist-sliding failure mode and joist-to-wall interaction, while specimens with the hook anchor exhibited the rocking behaviour of the wallet.

Regarding the strengthened specimens, two different strengthening approaches were considered: (i) connecting the joist and the outer leaf by means of helical bars and (ii) strengthening the connection between the joist and the inner leaf via timber blocks. The tests on the former strengthening solution were conducted after completing the testing of the as-built specimens; the helical bars were then drilled through the outer leaf and the timber joist, and the specimens were retested. The latter strengthening solution was applied to newly built specimens. Besides, a different mortar quality was used for the inner leaf for validation purposes since a parametric study was conducted, as explained in Chapter 5. Both the strengthened specimens with helical bars and timber blocks exhibited rocking failure mode.

During the tests, the arching effect contributed to the capacity of the wall-to-floor connection since the top horizontal edge of the inner leaf was restrained against vertical translation. The arching effect generated an additional confining force at the timber-masonry interface and increased with larger horizontal displacements, eventually leading to higher frictional force at the interface between joist and masonry.

The assessment of both unstrengthened and strengthened specimens yielded the following conclusions:

- The joist-sliding failure is governed by cohesion and friction between timber and masonry.
- The capacity of the connection is sensitive to material parameters and boundary conditions. Higher values of the axial load in the wallet lead to larger friction forces. Similarly, higher mortar strength quality improves the cohesion between timber and masonry.
- Hook anchors or other strengthening measures ensure a good connection between the joist and the masonry wallet. The failure of the sub-assemblage is then due

to rocking and is governed by the geometry of the wallet and the tensile strength of the masonry.

- Comparing the experimental results of the as-built and strengthened connections in terms of peak load, the strengthened specimens exhibit an average peak load increase of approximately 5% in pulling and 9% in pushing. The increase is limited due to the arching effect that enhances the capacity of the as-built connections and to the activation of the rocking failure mode, which constitutes an upper bound for the capacity of the sub-assemblage.
- Regarding the strengthened specimens, post-installed cavity wall anchors may act as stress concentrators, resulting in splitting cracks around the anchors, especially if the installation process is not executed with utmost care. Hence, the specimens that had as-built wall ties retrofitted with timber blocks showed higher strength capacity than the specimens that lacked as-built wall ties and were retrofitted via timber blocks and post-installed cavity wall ties.

When both the conducted experimental campaigns are considered, i.e., testing of cavity wall tie and timber joist-masonry connections, the observed failure mode shows similarities. First, bonding plays an essential role in connections. Higher bonding capacity at the local level (tie-mortar or timber-mortar) may lead to different failure modes: the failure modes change from pull-out failure to cone break-out failure for cavity wall tie connections and from joist-sliding failure to rocking failure for the timber joist-masonry connections. Second, improving connections is important to prevent the out-of-plane (OOP) overturning of masonry walls, but it may lead to a different response and failure mode of the structure, which is not always favourable. I.e., strengthened cavity wall anchors exhibit brittle behaviour, while for the strengthened timber joist connections, the failure mode shifts from the local connection failure to the rocking of the wallet. On the other hand, shifting the failure mode by strengthening connections may be beneficial in identifying the second weak link in URM failure patterns. This can provide a comprehensive insight into the behaviour of connections in masonry buildings.

The two testing campaigns also highlighted differences in the structural response of the connections. The most remarkable one regards the contribution of the arching action to the capacity of the connections. Unlike timber joist-masonry connections, the arching action does not affect the performance of a cavity wall tie connection, as the variation of the levels of pre-compression has negligible influence on the capacity of such connection.

Mechanical and constitutive models were proposed to predict the structural response of the wall-to-wall tie connections and wall-to-floor connections. The experimental results presented in Chapter 3 and Chapter 4 were used as a benchmark for validation. Chapter 5 presents a mechanical model that is capable of predicting the failure mode and the strength capacity of wall metal tie connections in masonry cavity walls. A computationally efficient approach to simulate numerically the experimental results is also provided. The proposed mechanical model for the cavity wall tie considers six possible failure modes: tie failure, cone break-out failure, pull-out failure, buckling failure, punching failure, and piercing failure. Although cone break-out and punching failure modes were not observed during the experimental campaign, a combination of failure modes, in this case between either the cone and bond failure or the piercing and punching failure, may occur in some cases.

The proposed mechanical model of cavity wall tie connections accurately predicts the most frequent failure mode in both loading directions, which are pull-out and buckling failure. The ratio between the experimental results and the outcomes of the mechanical model for pull-out and buckling failure is computed as equal to 1.04 and 1.04, with standard deviations of 0.15 and 0.10, respectively.

In order to predict the connection behaviour for untested configurations, a parametric analysis was conducted using the proposed mechanical model. The proposed model highlights the sensitivity of the connections to the examined parameters, and five different failure modes are observed. Specifically, a different mortar strength for CS couplets affects the failure in tension, except for the pull-out failure, cone break-out and tie failures were also observed. A shorter cavity depth changes the failure mode in compression from buckling failure to piercing failure. A different embedment depth for CB walls changes the governing failure mode from pull-out failure to tie failure in tension and buckling failure to piercing failure in compression. On the contrary, the use of solid clay bricks does not have a significant influence on the governing failure mode, neither in tension nor in compression.

The experimental results of the cavity wall tie tests were used to develop a general load-deformation hysteretic numerical model for different typologies of cavity wall connections. A constitutive material model, Pinching4 with zero-length element, already available in the library of the open-source software OpenSees, was chosen due to the pinching effect and the degradation in strength and stiffness observed during the experimental campaign conducted on the cavity wall tie connections. The material parameters of the Pinching4 law were calibrated from the experimental tests. The strength degradation, stiffness degradation and pinching

behaviour of the load-deformation responses were modelled differently for each typology. The final models were able to reproduce the observed experimental force-displacement curves adequately.

Finally, Chapter 6 analyses the main contributions of the resisting mechanisms to the force capacity in timber joist-masonry connections. The two observed failure modes, namely joist-sliding and wallet rocking, are considered in the mechanical model. Regarding the joist-sliding mechanism, the model is capable of predicting the different contributions observed during the experimental campaign: namely, cohesion, initial axial force imposed at the top of the wallet, and additional axial force due to the arching effect, with the last two affecting friction at the interface between joist and wallet. The total joist capacity is then computed as the sum of these contributions. Regarding the rocking behaviour, a mechanical model already reported in the literature is able to predict the capacity of the wallet. Overall, the mechanical model shows good agreement when adequately calibrated, as an error of up to 5% is estimated with respect to the experimental results.

It should be noted that although the mechanical model was based on two models already proposed in the literature, the combination of these models to compute the joist capacity generates a novel approach.

The presented mechanical models can be adopted by structural engineers to predict the peak force capacity of wall tie connections and estimate the contribution of each mechanism to the overall connection capacity of timber joist-masonry connections. This will allow the engineers to determine whether strengthening is needed and what type of intervention should be adopted. Finally, the numerical modelling of cavity wall tie connections can also be used within nonlinear finite element analyses of full-scale structures for accurate modelling of the response of wall-to-wall connections under dynamic earthquake loading.

The studies carried out and reported in this thesis provide comprehensive insight into the behaviour of cavity wall tie and timber-masonry connections not only for URM buildings in the Netherlands but also in other regions of the world, such as Australia, New Zealand, and North America, as well as in various parts of northern Europe. The research improves the knowledge of the cavity wall tie and timber joist-masonry connections, which serves to improve the design and assessment methods, as well as to identify adequate retrofit interventions.

7.2 Recommendations for further research

The study presented in this thesis sheds light on the characterisation of wall tie and wall-to-floor connections. Some areas of this work that deserve further research attention include the following:

(a) *Conducting an extended inventory of existing buildings and connections in the Groningen area based on one or multiple additional inspection surveys*. The inventory conducted in this study was limited to a small number of addresses (267) and represents, therefore, only a preliminary investigation; there is a need for a larger scale inventory to assign more typologies since the area consists of more than 250.000 buildings. An inspection survey may be undertaken to validate the inventory regarding the identified connections.

(b) *Continuing the experimental campaign on cavity wall tie connections*. In addition to the variations considered during the experimental campaign, the following should be investigated: solid clay bricks for the load-bearing leaf, the same mortar for both cavity leaves and the use of corrugated metal wall ties. Additionally, the performance of corroded ties should also be assessed.

(c) *Conducting in-situ quasi-static tests for cavity wall tie and timber-joist connections in the Groningen area*. The specimens from the experimental campaigns were replicated in the laboratory; hence, conducting in-situ testing on connections could enhance the pool of experimental data as well as provide new insights into understanding and assessing the performance of the connections.

(d) *Developing a numerical model by implementing the proposed mechanical models for the cavity wall tie and timber joist-masonry connections*. The proposed mechanical models for both connection types can be used as a basis to develop a general load-deformation hysteretic numerical model.

(e) *Implementing the experimental results for modelling the structural behaviour of complete full-scale unreinforced masonry walls*. The presented results can be used in numerical models that aim to model full-scale masonry cavity walls with a timber diaphragm in which the connection details are explicitly taken into account. Additionally, those numerical models can be extended to a complete building.

Bibliography

[1] K. van Thienen-Visser, J.N. Breunese, Induced seismicity of the Groningen gas field: History and recent developments, Lead. Edge. 34 (2015) 664–671. https://doi.org/10.1190/tle34060664.1.

[2] W.L. Ellsworth, Injection-Induced Earthquakes, Science (80-.). 341 (2013) 250–260. https://doi.org/10.1126/science.1225942.

[3] J.J. Bommer, J. van Elk, Comment on "The Maximum Possible and the Maximum Expected Earthquake Magnitude for Production-Induced Earthquakes at the Gas Field in Groningen, The Netherlands" by Gert Zöller and Matthias Holschneider, Bull. Seismol. Soc. Am. 107 (2017) 1564–1567. https://doi.org/10.1785/0120170040.

[4] B. Dost, E. Ruigrok, J. Spetzler, Development of seismicity and probabilistic hazard assessment for the Groningen gas field, Geol. En Mijnbouw/Netherlands J. Geosci. 96 (2017) s235–s245. https://doi.org/10.1017/njg.2017.20.

[5] İ.E. Bal, E. Smyrou, D. Dais, Comparison of polarity in Groningen data with that of other natural and induced seismicity records, and implications in hazard and risk models, Bull. Earthq. Eng. 17 (2019) 4457–4474. https://doi.org/10.1007/s10518-018-0517-3.

[6] B. Dost, B. Edwards, J.J. Bommer, The relationship between M and ML: A review and application to induced seismicity in the groningen gas field, the Netherlands, Seismol. Res. Lett. 89 (2018) 1062–1074. https://doi.org/10.1785/02201700247.

[7] D. Dempsey, J. Suckale, Physics-based forecasting of induced seismicity at Groningen gas field, the Netherlands, Geophys. Res. Lett. 44 (2017) 7773–7782. https://doi.org/10.1002/2017GL073878.

[8] S.J. Bourne, S.J. Oates, J. van Elk, The exponential rise of induced seismicity with increasing stress levels in the Groningen gas field and its implications for controlling seismic risk, Geophys. J. Int. 213 (2018) 1693–1700. https://doi.org/10.1093/gji/ggy084.

[9] KNMI, Aardbevingen door gaswinning, (2020). https://www.knmi.nl/kennis-en-datacentrum/uitleg/aardbevingen-door-gaswinning.

[10] H. Crowley, J. Uilenreef, R. Scheefhals, Exposure Database V7, 2020.

[11] S. Kallioras, G. Guerrini, U. Tomassetti, B. Marchesi, A. Penna, F. Graziotti, G. Magenes, Experimental seismic performance of a full-scale unreinforced clay-masonry building with flexible timber diaphragms, Eng. Struct. 161 (2018) 231–249. https://doi.org/10.1016/j.engstruct.2018.02.016.

[12] S. Kallioras, A.A. Correia, F. Graziotti, A. Penna, G. Magenes, Collapse shake-table testing of a clay-URM building with chimneys, Bull. Earthq. Eng. 18 (2020) 1009–1048. https://doi.org/10.1007/s10518-019-00730-0.

[13] F. Graziotti, U. Tomassetti, S. Kallioras, A. Penna, G. Magenes, Shaking table test on a full scale URM cavity wall building, Bull. Earthq. Eng. 15 (2017) 5329–5364. https://doi.org/10.1007/s10518-017-0185-8.

[14] U. Tomassetti, A.A. Correia, P.X. Candeias, F. Graziotti, A. Campos Costa, Two-way bending out-of-plane collapse of a full-scale URM building tested on a shake table, Bull. Earthq. Eng. 17 (2019) 2165–2198. https://doi.org/10.1007/s10518-018-0507-5.

[15] C. Chandrakumar, S.J. McLaren, D. Dowdell, R. Jaques, A science-based approach to setting climate targets for buildings: The case of a New Zealand detached house, Build. Environ. 169 (2020) 106560. https://doi.org/10.1016/j.buildenv.2019.106560.

[16] T. Pakkala, Assessment of the Climate Change Effects on Finnish Concrete Facades and

Balconies., Tampere University, 2020. http://urn.fi/URN:ISBN:978-952-03-1423-1.
[17] M. Reynolds, M. Wulff, E. Healy, Why don't small households live in small dwellings?: disentangling a planning dilemma., People Place. 12(1), 58– (2004). https://doi.org/https://search.informit.org/doi/10.3316/ielapa.200403974.
[18] G. Guerrini, F. Graziotti, A. Penna, G. Magenes, Dynamic shake-table tests on two full-scale, unreinforced masonry buildings subjected to induced seismicity, Lect. Notes Civ. Eng. 5 (2018) 376–387. https://doi.org/10.1007/978-3-319-67443-8_32.
[19] R. Esposito, F. Messali, G.J.P. Ravenshorst, H.R. Schipper, J.G. Rots, Seismic assessment of a lab-tested two-storey unreinforced masonry Dutch terraced house, Bull. Earthq. Eng. 17 (2019) 4601–4623. https://doi.org/10.1007/s10518-019-00572-w.
[20] P. Nicholson, Encyclopædia of architecture., Ed. by Edward Lomax Thomas Gunyon, London. (1852).
[21] S.B. Hamilton, The history of hollow bricks, Br. Ceram. Soc. Vol. 58, N (1959).
[22] N. Khattak, H. Derakhshan, D.P. Thambiratnam, N.J. Perera, Typological characterisation of vintage unreinforced masonry buildings of Queensland, Australia, Structures. 41 (2022) 99–116. https://doi.org/10.1016/j.istruc.2022.04.095.
[23] M. Giaretton, D.Y. Dizhur, F. da Porto, J.M. Ingham, Construction Details and Observed Earthquake Performance of Unreinforced Clay Brick Masonry Cavity-walls, Structures. 6 (2016) 159–169. https://doi.org/10.1016/j.istruc.2016.04.004.
[24] D.Y. Dizhur, X. Jiang, Q. Chengliang, N. Almesfer, J.M. Ingham, Historical development and observed earthquake performance of unreinforced clay brick masonry cavity-walls, Struct. Eng. Soc. J. - SESOC. 28 (2015) 55–67.
[25] Ritchie.T, NOTES ON THE HISTORY OF HOLLOW MASONRY WALL, Bull. Assoc. Preserv. Technol. 5 (1973) 40–49. https://www.jstor.org/stable/1493439.
[26] P.B. Lourenço, N. Mendes, L.F. Ramos, D. V. Oliveira, Analysis of Masonry Structures Without Box Behavior, Int. J. Archit. Herit. 5 (2011) 369–382. https://doi.org/10.1080/15583058.2010.528824.
[27] M. Tomazevic, M. Lutman, P. Weiss, Seismic Upgrading of Old Brick-Masonry Urban Houses: Tying of Walls with Steel Ties, Earthq. Spectra. 12 (1996) 599–622. https://doi.org/10.1193/1.1585898.
[28] M. Tomazevic, Earthquake-Resistant Design of Masonry Buildings, PUBLISHED BY IMPERIAL COLLEGE PRESS AND DISTRIBUTED BY WORLD SCIENTIFIC PUBLISHING CO., 1999. https://doi.org/10.1142/p055.
[29] C. Blasi, A. Borri, S. Di Pasquale, P. Malesani, G. Nigro, A. Parducci, G. Tampone, Manuale per la riabilitazione e la ricostruzione sismica degli edifici — Regione dell'Umbria, DEI Tipografia del Genio Civile, Roma (in Italian), 1999.
[30] D.F. D'Ayala, S. Paganoni, Assessment and analysis of damage in L'Aquila historic city centre after 6th April 2009, Bull. Earthq. Eng. 9 (2011) 81–104. https://doi.org/10.1007/s10518-010-9224-4.
[31] L. Moon, D.Y. Dizhur, I. Senaldi, H. Derakhshan, M.C. Griffith, G. Magenes, J.M. Ingham, The Demise of the URM Building Stock in Christchurch during the 2010–2011 Canterbury Earthquake Sequence, Earthq. Spectra. 30 (2014) 253–276. https://doi.org/10.1193/022113EQS044M.
[32] D.Y. Dizhur, R.P. Dhakal, J. Bothara, J.M. Ingham, Building typologies and failure modes observed in the 2015 Gorkha (Nepal) earthquake, Bull. New Zeal. Soc. Earthq. Eng. 49 (2016) 211–232. https://doi.org/10.5459/bnzsee.49.2.211-232.
[33] K.Q. Walsh, D.Y. Dizhur, J. Shafaei, H. Derakhshan, J.M. Ingham, Out-of-Plane In-Situ Testing of Masonry Cavity Walls in As-Built and Improved Conditions, in: Aust. Earthq. Eng. Soc. 2014 Conf., 2014: pp. 187–199. https://doi.org/10.13140/2.1.4434.0804.

[34] D. Reneckis, J.M. LaFave, Out-of-plane seismic performance and detailing of brick veneer walls, J. Struct. Eng. 136 (2010) 781–794. https://doi.org/10.1061/(ASCE)ST.1943-541X.0000169.
[35] BSI (British Standards Institution), Recommendations for the design of masonry structures to BS EN 1996-1-1 and BS EN 1996-2, 2010.
[36] R. Esposito, K.C. Terwel, H.R. Schipper, F. Messali, J.G. Rots, Cyclic pushover test on an unreinforced masinry structure ressembling a typical Dutch terraced house, 16th World Conf. Earthq. (2017) Paper N° 4752.
[37] F. Messali, R. Esposito, S. Jafari, G.J.P. Ravenshorst, P. Korswagen Eguren, J.G. Rots, A multiscale experimental characterisation of Dutch unreinforced masonry buildings, in: Proc. 16th Eur. Conf. Earthq. Eng., Thessaloniki, Greece, 2018: pp. 1–12.
[38] S. Mertens, A. Smits, Y. Grégoire, Experimental parametric study on the performance of wall ties, Int. Mason. Conf. 2014. (2014) 1–11.
[39] G. Skroumpelou, F. Messali, R. Esposito, J.G. Rots, Mechanical characterization of wall tie connection in cavity walls, 10th Aust. Mason. Conf. (2018).
[40] M. Giaretton, D.Y. Dizhur, J.M. Ingham, Shaking table testing of as-built and retrofitted clay brick URM cavity-walls, Eng. Struct. 125 (2016) 70–79. https://doi.org/10.1016/j.engstruct.2016.06.032.
[41] F. Messali, G.J.P. Ravenshorst, R. Esposito, J.G. Rots, Large-scale testing program for the seismic characterization of Dutch masonry walls, 16th World Conf. Earthq. (2017) Paper N° 4753. https://repository.tudelft.nl/islandora/object/uuid%3A7f4baaa0-b1d4-49ad-b41c-584f324c102e.
[42] G.J.P. Ravenshorst, M. Mirra, Cyclic behavior of replicated timber-joist connections, 2018.
[43] O. Arslan, F. Messali, E. Smyrou, İ.E. Bal, J.G. Rots, Experimental characterization of the axial behavior of traditional masonry wall metal tie connections in cavity walls, Constr. Build. Mater. 266 (2021) 121141. https://doi.org/10.1016/j.conbuildmat.2020.121141.
[44] O. Arslan, F. Messali, E. Smyrou, İ.E. Bal, J.G. Rots, Mechanical modelling of the axial behaviour of traditional masonry wall metal tie connections in cavity walls, Constr. Build. Mater. 310 (2021) 125205. https://doi.org/10.1016/j.conbuildmat.2021.125205.
[45] O. Arslan, F. Messali, J.G. Rots, E. Smyrou, İ.E. Bal, NUMERICAL MODELLING OF CAVITY WALL METAL TIES, 17th World Conf. Earthq. Eng. (2020) 491–498. https://doi.org/10.1201/9781003098508-67.
[46] H. Crowley, R. Pinho, F. Cavalieri, Report on the v6 Fragility and Consequence Models for the Groningen Field, 2019.
[47] Arup, Seismic Risk Study - Earthquake Scenario-Based Risk Assessment, 2013.
[48] M. Polese, M. Di Ludovico, M. Gaetani d'Aragona, A. Prota, G. Manfredi, Regional vulnerability and risk assessment accounting for local building typologies, Int. J. Disaster Risk Reduct. 43 (2020) 101400. https://doi.org/10.1016/j.ijdrr.2019.101400.
[49] M. Vettore, M. Donà, P. Carpanese, V. Follador, F. da Porto, M.R. Valluzzi, A Multilevel Procedure at Urban Scale to Assess the Vulnerability and the Exposure of Residential Masonry Buildings: The Case Study of Pordenone, Northeast Italy, Heritage. 3 (2020) 1433–1468. https://doi.org/10.3390/heritage3040080.
[50] A. Altindal, S. Karimzadeh, M.A. Erberik, A. Askan, O. Anil, M.K. Kockar, M. Sahmaran, A case study for probabilistic seismic risk assessment of earthquake-prone old urban centers, Int. J. Disaster Risk Reduct. 61 (2021) 102376. https://doi.org/10.1016/j.ijdrr.2021.102376.
[51] G. Brando, G. Cianchino, D. Rapone, E. Spacone, S. Biondi, A CARTIS-based method

for the rapid seismic vulnerability assessment of minor Italian historical centres, Int. J. Disaster Risk Reduct. 63 (2021) 102478. https://doi.org/10.1016/j.ijdrr.2021.102478.
[52] M. Giaretton, Earthquake performance and securing of unreinforced masonry components, (2016) 277. https://doi.org/10.13140/RG.2.1.4639.1923.
[53] K.Q. Walsh, Inventory and seismic assessment of earthquake - vulnerable masonry and concrete buildings, The University of Auckland, 2015.
[54] P.P. Kruiver, E. van Dedem, R. Romijn, G. de Lange, M. Korff, J. Stafleu, J.L. Gunnink, A. Rodriguez-Marek, J.J. Bommer, J. van Elk, D. Doornhof, An integrated shear-wave velocity model for the Groningen gas field, The Netherlands, Bull. Earthq. Eng. 15 (2017) 3555–3580. https://doi.org/10.1007/s10518-017-0105-y.
[55] E. van Wijnbergen, Seismic retrofit - an architectural approach for the situation in Groningen, TU Delft, 2015.
[56] Arup, Structural Upgrading Study (REP/229746/SU003)., Amsterdam, The Netherlands, 2013.
[57] A.P. Russell, J.M. Ingham, Prevalence of New Zealand's unreinforced masonry buildings, Bull. New Zeal. Soc. Earthq. Eng. 43 (2010) 182–201. https://doi.org/10.5459/bnzsee.43.3.182-201.
[58] N. Ismail, K. McGrannachan, G. Hazelton, Characterisation and seismic vulnerability assessment of unreinforced masonry buildings in Dunedin CBD, Bull. New Zeal. Soc. Earthq. Eng. 46 (2013) 131–140. https://doi.org/10.5459/bnzsee.46.3.131-140.
[59] A. Masi, L. Chiauzzi, C. Samela, L. Tosco, M. Vona, SURVEY OF DWELLING BUILDINGS FOR SEISMIC LOSS ASSESSMENT AT URBAN SCALE: THE CASE STUDY OF 18 VILLAGES IN VAL D'AGRI, ITALY, Environ. Eng. Manag. J. 13 (2014) 471–486. https://doi.org/10.30638/eemj.2014.051.
[60] Arup, EDB V6 data documentation, 2019.
[61] S. Brzev, C. Scawthorn, A.W. Charleson, L. Allen, M. Greene, K. Jaiswal, V. Silva, GEM Building Taxonomy Version 2.0, GEM Tech. Rep. 02 (2013) 188.
[62] S. Jafari, Material characterisation of existing masonry: A strategy to determine strength, stiffness and toughness properties for structural analysis, 2021. https://doi.org/10.4233/uuid:3bcbbc72-0212-44e9-ac86-2fdc54ec5987.
[63] R.G. Drysdale, A.A. Hamid, L.R. Baker, Masonry structures : behavior and design, Englewood Cliffs, N.J: Prentice Hall, 1994.
[64] H.O. Sugo, A.W. Page, B. Moghtaderi, A comparative study of the thermal performance of cavity and brick veneer construction, 13th Int. Brick Block Mason. Conf. - IBMAC. (2004) 767–776.
[65] M.F. Williams, B.L. Williams, A Case Study of the Performance and Repair of a Masonry Veneer Cavity Wall Construction, in: 4th Int. Mason. Conf., 1995.
[66] R. Van Der Pluijm, A. Vermeersch, Lateral load capacity of a cavity wall with a thin outer leave, Proc. Int. Mason. Soc. Conf. 0 (2018) 255–266.
[67] H. Derakhshan, W. Lucas, P. Visintin, M.C. Griffith, Out-of-plane Strength of Existing Two-way Spanning Solid and Cavity Unreinforced Masonry Walls, Structures. 13 (2018) 88–101. https://doi.org/10.1016/j.istruc.2017.11.002.
[68] F. Graziotti, U. Tomassetti, A. Penna, G. Magenes, Out-of-plane shaking table tests on URM single leaf and cavity walls, Eng. Struct. 125 (2016) 455–470. https://doi.org/10.1016/j.engstruct.2016.07.011.
[69] F. Messali, G.J.P. Ravenshorst, Database of connections: characteristics and properties, 2019.
[70] NEN, NPR 9998, 2015 (2015).
[71] NEN-NPR, Assessment of structural safety of buildings in case of erection,

reconstruction and disapproval- induced earthquake - Basis of design, actions and resistances, NPR 9998:2020, 2020.
[72] F. Graziotti, A. Penna, G. Magenes, A comprehensive in situ and laboratory testing programme supporting seismic risk analysis of URM buildings subjected to induced earthquakes, Bull. Earthq. Eng. 17 (2019) 4575–4599. https://doi.org/10.1007/s10518-018-0478-6.
[73] F. Graziotti, U. Tomassetti, S. Sharma, L. Grottoli, G. Magenes, Experimental response of URM single leaf and cavity walls in out-of-plane two-way bending generated by seismic excitation, Constr. Build. Mater. 195 (2019) 650–670. https://doi.org/10.1016/j.conbuildmat.2018.10.076.
[74] D. Reneckis, J.M. LaFave, W.M. Clarke, Out-of-plane performance of brick veneer walls on wood frame construction, Eng. Struct. 26 (2004) 1027–1042. https://doi.org/10.1016/j.engstruct.2004.02.013.
[75] H. Derakhshan, W. Lucas, P. Visintin, M.C. Griffith, Laboratory Testing of Strengthened Cavity Unreinforced Masonry Walls, J. Struct. Eng. 144 (2018) 04018005. https://doi.org/10.1061/(ASCE)ST.1943-541X.0001987.
[76] Y.-H. Choi, J.M. LaFave, Performance of Corrugated Metal Ties for Brick Veneer Wall Systems, J. Mater. Civ. Eng. 16 (2004) 202–211. https://doi.org/10.1061/(ASCE)0899-1561(2004)16:3(202).
[77] D. Reneckis, J.M. LaFave, Seismic Performance of Anchored Brick Veneer, 2009.
[78] A. Martins, G. Vasconcelos, A. Campos Costa, Experimental assessment of the mechanical behaviour of ties on brick veneers anchored to brick masonry infills, Constr. Build. Mater. 156 (2017) 515–531. https://doi.org/10.1016/j.conbuildmat.2017.09.013.
[79] Nederlands Normalisatie-instituit (NEN)., NEN-EN 1015-3: Methods of test for mortar for masonry - Part 3: Determination of consistence of fresh mortar (by flow table), (1999).
[80] Nederlands Normalisatie-instituit (NEN), NEN-EN 845-1 + A1: Specification for ancillary components for masonry - Part 1: Wall ties, tension straps, hangers and brackets, (2013).
[81] Nederlands Normalisatie-instituit (NEN)., NEN-EN 846-5: Methods of test for ancillary components for masonry - Part 5: Determination of tensile and compressive load capacity and load displacement characteristics of wall ties (couplet test), (2010).
[82] Nederlands Normalisatie-instituit (NEN), NEN-EN 1015-11: Methods of test for mortar for masonry - Part 11: Determination of flexural and compressive strength of hardened mortar, (1999).
[83] Eucentre, P&P, TU Delft, TU Eindhoven, Material Characterization, 2015.
[84] Nederlands Normalisatie-instituit (NEN), Nen-en 1052-5: Methods of test for masonry - Part 5: Determination of bond strength by the bond wrench method, (2005).
[85] ASTM, Standard Test Methods for Tension Testing of Metallic Materials - ASTM E8/E8M-21, 2021.
[86] ASTM, Standard Test Methods of Compression Testing of Metallic Materials at Room Temperature - ASTM E9-19, 2019.
[87] S. Moreira, L.F. Ramos, D. V. Oliveira, P.B. Lourenço, Experimental behavior of masonry wall-to-timber elements connections strengthened with injection anchors, Eng. Struct. 81 (2014) 98–109. https://doi.org/10.1016/j.engstruct.2014.09.034.
[88] FEMA 965, Quantification of Building Seismic Performance Factors, 2009.
[89] M.N. Fardis, Seismic Design, Assessment and Retrofitting of Concrete Buildings, Springer Netherlands, Dordrecht, 2009. https://doi.org/10.1007/978-1-4020-9842-0.
[90] ASTM E2126-119, Standard test methods for cyclic (reversed) load test for shear

resistance of vertical elements of the lateral force resisting systems for buildings., 2019. https://doi.org/10.1520/E2126-19.
[91] O. Arslan, Supplementary data for the Research on Experimental Characterization of Wall Tie Connections in Cavity Walls (Version 1), 4TU.ResearchData. (2019). https://doi.org/10.4121/uuid:429e07ad-50e8-48e1-a610-461332e6267b.
[92] A. Wibowo, Performance of Brick Veneer Ties Under Cyclic Loadings, THE UNIVERSITY OF BRITISH COLUMBIA, 2001.
[93] A. Martins, Seismic behaviour of masonry veneer walls, Universidade do Minho, 2018. http://hdl.handle.net/1822/59015.
[94] T.J. Lin, J.M. LaFave, Experimental structural behavior of wall-diaphragm connections for older masonry buildings, Constr. Build. Mater. 26 (2012) 180–189. https://doi.org/10.1016/j.conbuildmat.2011.06.008.
[95] K. Doherty, An investigation of the weak links in the seismic load path of unreinforced masonary buildings, (2000) 354.
[96] J.K. Bothara, R.P. Dhakal, J.B. Mander, Seismic performance of an unreinforced masonry building: An experimental investigation, Earthq. Eng. Struct. Dyn. (2009) n/a-n/a. https://doi.org/10.1002/eqe.932.
[97] G. Magenes, A. Penna, I.E. Senaldi, M. Rota, A. Galasco, Shaking Table Test of a Strengthened Full-Scale Stone Masonry Building with Flexible Diaphragms, Int. J. Archit. Herit. 8 (2014) 349–375. https://doi.org/10.1080/15583058.2013.826299.
[98] G. Magenes, A. Penna, A. Galasco, A full-scale shaking table test on a two-storey stone masonry building, 14th Eur. Conf. Earthq. Eng. (2010) 384.
[99] T. Yi, Experimental Investigation and Numerical Simulation of an Unreinforced Masonry Structure with Flexible Diaphragms, Georgia Institute of Technology, 2004. https://linkinghub.elsevier.com/retrieve/pii/S1090780710000546.
[100] M. Miglietta, L. Mazzella, L. Grottoli, G. Guerrini, F. Graziotti, Full-scale shaking table test on a Dutch URM cavity-wall terraced-house end unit – EUC-BUILD-6, Res. Rep. EUC160/2018U. (2019).
[101] J.P. Almeida, K. Beyer, R. Brunner, T. Wenk, Characterization of mortar–timber and timber–timber cyclic friction in timber floor connections of masonry buildings, Mater. Struct. 53 (2020) 51. https://doi.org/10.1617/s11527-020-01483-y.
[102] M. Merriman, American Civil Engineer's Handbook., New York: John Wiley & Sons, Inc., 1920.
[103] M. Mirra, G.J.P. Ravenshorst, Seismic characterization of timber-masonry connections based on experimental results, 2019.
[104] F. Solarino, D. V. Oliveira, L. Giresini, Wall-to-horizontal diaphragm connections in historical buildings: A state-of-the-art review, Eng. Struct. 199 (2019) 109559. https://doi.org/10.1016/j.engstruct.2019.109559.
[105] N. Damiani, M. Miglietta, L. Mazzella, L. Grottoli, G. Guerrini, F. Graziotti, Full-scale shaking table test on a Dutch URM cavity-wall terraced-house end unit – A retrofit solution with strong-backs and OSB boards – EUC-BUILD-7, Pavia, Italy, 2019.
[106] M. Bruneau, State-of-the-Art Report on Seismic Performance of Unreinforced Masonry Buildings, J. Struct. Eng. 120 (1994) 230–251. https://doi.org/10.1061/(ASCE)0733-9445(1994)120:1(230).
[107] HeliBar, Website of the HeliFix, (2014). http://www.helifix.com/products/retrofit-products/dryfix/.
[108] P. Morandi, Second order effects in out-of-plane strength of URM walls subjected to bending and compression, ROSE SCHOOL, 2006. https://doi.org/10.13140/RG.2.2.19870.64326.

[109] ISO 16670:2003, Timber structures - Joints made with mechanical fasteners - Quasi-static reversed-cyclic test method. International Organization for Standardization (ISO)., 2003.
[110] J. Vaculik, M.C. Griffith, Out-of-plane shaketable testing of unreinforced masonry walls in two-way bending, Springer Netherlands, 2018. https://doi.org/10.1007/s10518-017-0282-8.
[111] N. V. Zisi, R.M. Bennett, Shear Behavior of Corrugated Tie Connections in Anchored Brick Veneer–Wood Frame Wall Systems, J. Mater. Civ. Eng. 23 (2011) 120–130. https://doi.org/10.1061/(ASCE)MT.1943-5533.0000143.
[112] A. Martins, G. Vasconcelos, A. Campos Costa, Experimental study on the mechanical performance of steel ties for brick masonry veneers, (2016) 1723–1731.
[113] D. Reneckis, J.M. LaFave, Analysis of brick veneer walls on wood frame construction subjected to out-of-plane loads, Constr. Build. Mater. 19 (2005) 430–447. https://doi.org/10.1016/j.conbuildmat.2004.08.006.
[114] V.P. Paton-Cole, E.F. Gad, C. Clifton, N.T.K. Lam, C. Davies, S. Hicks, Out-of-plane performance of a brick veneer steel-framed house subjected to seismic loads, Constr. Build. Mater. 28 (2012) 779–790. https://doi.org/10.1016/j.conbuildmat.2011.10.033.
[115] W.M. McGinley, S. Hamoush, Seismic masonry veneer: quazi-static testing of wood stud backed clay masonry veneer walls, Proc. 2008 Struct. Congr. - Struct. Congr. 2008 Crossing Borders. 314 (2008). https://doi.org/10.1061/41016(314)220.
[116] M. Hatzinikolas, J. Longworth, J. Warwaruk, Strength and behaviour of anchor bolts embedded in concrete masonry, Alberta Masonry Institute, [Edmonton], 1979.
[117] R.H. Brown, A.R. Whitlock, Strength of Anchor Bolts in Grouted Concrete Masonry, J. Struct. Eng. 109 (1983) 1362–1374. https://doi.org/10.1061/(ASCE)0733-9445(1983)109:6(1362).
[118] J.B. Tubbs, D.G. Pollock, D.I. McLean, Testing of anchor bolts in concrete block masonry, Mason. Soc. J. 18 (2000) 81/92.
[119] W.M. McGinley, S. Singleton, J. Greenwald, J. Thompson, CAPACITY OF ANCHOR BOLTS IN CONCRETE MASONRY, 2004.
[120] H. Krenchel, S.P. Shah, Fracture analysis of the pullout test, Mater. Struct. 18 (1985) 439–446. https://doi.org/10.1007/BF02498746.
[121] G. Rehm, J. Schlaich, K. Schäfer, R. Eligehausen, Fritz-Leonhardt-Kolloquium 1984. 15. Forschungskolloquium des Deutschen Ausschusses für Stahlbeton (Teil 1)., 1985. https://doi.org/10.1002/best.198500310.
[122] H. Bode, K. Roik, Headed Studs--Embedded in Concrete and Loaded in Tension, Spec. Publ. 103 (1987) 61–88. https://doi.org/10.14359/1671.
[123] G. Rehm, R. Eligehausen, R. Mallée, Befestigungstechnik : Sonderdruck aus dem Beton-Kalender 1992, 1991. https://doi.org/http://dx.doi.org/10.18419/opus-657.
[124] W. Fuchs, R. Eligehausen, J.E. Breen, Concrete Capacity Design (CCD) Approach for Fastening to Concrete, ACI Struct. J. 92 (1995) 794–802.
[125] W. Fuchs, R. Eligehausen, Das CC-Verfahren für die Berechnung der Betonausbruchlast von Verankerungen., Beton- Und Stahlbetonbau. 90 (1995) 6–9. https://doi.org/10.1002/best.199500020.
[126] U. Kuhlmann, F. Wald, J. Hofmann, Š. Bečková, F. Gentili, H. Gervásio, J. Henriques, M. Krimpmann, A. Ožbolt, J. Ruopp, I. Schwarz, A. Sharma, L.S. da Silva, J. van Kann, Design of Steel-to-Concrete Joints. Design Manual II, 2014.
[127] F. Arifovic, M.P. Nielsen, Strength of anchors in masonry, Byg Rapport, No. R-134, 2006.
[128] L.Z. Hansen, K. Findsen, M.P. Nielsen, Beregning af indlimede ankre i murede vaegge,

2004. http://www.byg.dtu.dk/publications/rapporter/byg-.
[129] M.P. Nielsen, L.C. Hoang, Limit analysis and concrete plasticity, 2016.
[130] MSJC, Building Code Requirements and Specification for Masonry Structures, Mason. Stand. Jt. Comm. (2013).
[131] J. Moe, Shearing strength of reinforced concrete slabs and footings under concentrated loads, Portl. Cem. Assoc. (1961).
[132] ACI Committee 318, Commentary on Building Code Requirements for Structural Concrete (ACI 318R-19), Am. Concr. Inst. (2019).
[133] E.A. Toubia, J. Lintz, In-Plane Loading of Brick Veneer over Wood Shear Walls, Mason. Soc. J. 31 (2013).
[134] Australian Standard., AS 3700-2018: Masonry Structures, (2018).
[135] A.W. Page, J. Kautto, P.W. Kleeman, A Design Procedure for Cavity and Veneer Wall Ties, (1996).
[136] A.W. Page, G. Simundic, M. Masia, A Study of Wall Tie Force Distribution in Veneer Wall, J. Ind. Econ. LV (2007) 0022–1821.
[137] K. HØISETH, A.M.Y. Hamed, T. Kvande, Evaluation of Seismic Code Regulations on Typical Veneer Walls, Int. Mason. Conf. 2014. (2014) 1–10.
[138] D.P. Kuhn, F.A. Shaikh, Slip-Pullout Strength of Hooked Anchors, Res. Report, Univ. Wisconsin-Milwaukee, Submitt. to Natl. Codes Stand. Counc. (1996).
[139] MSJC, Building Code Requirements for Masonry Structures (TMS 402-11/ACI 530-11/ASCE 5-11), 2011.
[140] S. Jafari, J.G. Rots, R. Esposito, F. Messali, Characterizing the Material Properties of Dutch Unreinforced Masonry, Procedia Eng. 193 (2017) 250–257. https://doi.org/10.1016/j.proeng.2017.06.211.
[141] G.M. Verderame, G. De Carlo, P. Ricci, G. Fabbrocino, Cyclic bond behaviour of plain bars. Part II: Analytical investigation, Constr. Build. Mater. 23 (2009) 3512–3522. https://doi.org/10.1016/j.conbuildmat.2009.07.001.
[142] G.M. Verderame, P. Ricci, An empirical approach for nonlinear modelling and deformation capacity assessment of RC columns with plain bars, Eng. Struct. 176 (2018) 539–554. https://doi.org/10.1016/j.engstruct.2018.09.022.
[143] L. Euler, Methodus inveniendi lineas curvas maximi minimive proprietate gaudentes sive solutio problematis isoperimetrici latissimo sensu accepti, Opera Omnia. Vol. 24 (1744).
[144] Column Research Council (U.S.), B.G. Johnston, Guide to Stability Design Criteria for Metal Structures, John Wiley & Sons, Inc., Hoboken, NJ, USA, 2010. https://doi.org/10.1002/9780470549087.
[145] N.M. Hawkins, The bearing strength of concrete loaded through rigid plates, Mag. Concr. Res. 21 (1969) 225–227. https://doi.org/10.1680/macr.1969.21.69.225.
[146] F. McKenna, M.H. Scott, G.L. Fenves, Nonlinear Finite-Element Analysis Software Architecture Using Object Composition, J. Comput. Civ. Eng. 24 (2010) 95–107. https://doi.org/10.1061/(ASCE)CP.1943-5487.0000002.
[147] S. Mazzoni, F. McKenna, M.H. Scott, G.L. Fenves, OpenSees Command Language Manual, Berkeley, California, 2006.
[148] L.N. Lowes, A. Altoontash, Modeling reinforced-concrete beam-column joints subjected to cyclic loading, J. Struct. Eng. 129 (2003) 1686–1697. https://doi.org/10.1061/(ASCE)0733-9445(2003)129:12(1686).
[149] Y.-L. Shen, J. Schneider, S. Tesfamariam, S.F. Stiemer, Z.-G. Mu, Hysteresis behavior of bracket connection in cross-laminated-timber shear walls, Constr. Build. Mater. 48 (2013) 980–991. https://doi.org/10.1016/j.conbuildmat.2013.07.050.

[150] H. Crowley, R. Pinho, B. Polidoro, P. Stafford, Development of V2 fragility and consequence functions for the Groningen Field, 2015.
[151] N. Mohammad Noh, L. Liberatore, F. Mollaioli, S. Tesfamariam, Modelling of masonry infilled RC frames subjected to cyclic loads: State of the art review and modelling with OpenSees, Eng. Struct. 150 (2017) 599–621. https://doi.org/10.1016/j.engstruct.2017.07.002.
[152] L.N. Lowes, N. Mitra, A. Altoontash, A Beam-Column Joint Model for Simulating the Earthquake Response of Reinforced Concrete Frames, 2003. http://dx.doi.org/10.1016/j.compstruc.2009.08.001%5Cnhttp://hdl.handle.net/2047/d20003280%5Cnhttp://www.stanford.edu/~bakerjw/Publications/Baker (2007) Record scaling, 8PCEE.pdf%5Cnpapers2://publication/uuid/1498A307-A88B-4AAF-B3F7-E6B4B14F87C2.
[153] J. Schneider, Connections in cross-laminated-timber shear walls considering the behaviour under monotonic and cyclic lateral loading, Univ. Stuttgart, 2009.
[154] S. Jo, Seismic Behavior and Design of Low-rise Reinforced Concrete Masonry with Clay Masonry Veneer, The University of Texas, 2010.
[155] H. Okail, Experimental and Analytical Investigation of the Seismic Performance of low-rise masonry veneer buildings, 2010.
[156] S. Mazzoni, F. McKenna, M.H. Scott, G.L. Fenves, Open System for Earthquake Engineering Simulation User Command-Language Manual, OpenSees Version 2.0, Berkeley, California, 2009.
[157] S. Mazzoni, M.H. Scott, Weekly meeting on the topic of OpenSees, (2023).
[158] N. Vaiana, S. Sessa, F. Marmo, L. Rosati, An accurate and computationally efficient uniaxial phenomenological model for steel and fiber reinforced elastomeric bearings, Compos. Struct. 211 (2019) 196–212. https://doi.org/10.1016/j.compstruct.2018.12.017.
[159] M. Terrenzi, E. Spacone, G. Camata, Comparison Between Phenomenological and Fiber-Section Non-linear Models, Front. Built Environ. 6 (2020). https://doi.org/10.3389/fbuil.2020.00038.
[160] C. Coulomb, Sur une application des regles maximis et minimis a quelques problems de statique, relatives a l'architecture, Acad Sci Paris Mem Math Phys 7343–382. (1776).
[161] T. Paulay, M.J.N. Priestly, Seismic Design of Reinforced Concrete and Masonry Buildings, John Wiley & Sons, Inc., Hoboken, NJ, USA, 1992. https://doi.org/10.1002/9780470172841.
[162] U. Tomassetti, F. Graziotti, A. Penna, G. Magenes, Modelling one-way out-of-plane response of single-leaf and cavity walls, Eng. Struct. 167 (2018) 241–255. https://doi.org/10.1016/j.engstruct.2018.04.007.
[163] N.P. Suh, P.L. Turner, Elements of the Mechanical Behaviour of solids, Scripta Book Co, 1975.
[164] M. Griffith, A. Page, On the seismic capacity of typical DPC and slip joints in unreinforced masonry buildings, Aust J Struct Eng. 1. 133-140. (1998).
[165] C. Casapulla, L. Argiento, F. da porto, D. Bonaldo, The relevance of frictional resistances in out-of-plane mechanisms of block masonry structures, in: Proc. 16th Int. Brick Block Mason. Conf., CRC Press, Padova, Italy, 2016: pp. 145–154. https://www.taylorfrancis.com/books/9781498795920/chapters/10.1201/b21889-16.
[166] A. Rahman, T. Ueda, Experimental Investigation and Numerical Modeling of Peak Shear Stress of Brick Masonry Mortar Joint under Compression, J. Mater. Civ. Eng. 26 (2014). https://doi.org/10.1061/(ASCE)MT.1943-5533.0000958.
[167] L. Pelà, K. Kasioumi, P. Roca, Experimental evaluation of the shear strength of aerial

lime mortar brickwork by standard tests on triplets and non-standard tests on core samples, Eng. Struct. 136 (2017) 441–453. https://doi.org/10.1016/j.engstruct.2017.01.028.
[168] S. Kallioras, Numerical simulation of shaking table tests on a URM cavity-wall building., Mason Int. 30(2) (2017).
[169] Y. Endo, Y. Kondo, G. Iwanami, Adaptative Pushover Analyses of a Heritage Structure: Application to a Multi-Tiered Pagoda Temple, (2021). https://doi.org/10.23967/sahc.2021.020.
[170] M.J.N. Priestley, Seismic behaviour of unreinforced masonry walls, Bull. New Zeal. Soc. Earthq. Eng. 18 (1985) 191–205. https://doi.org/10.5459/bnzsee.18.2.191-205.
[171] M. Donà, P. Morandi, M. Minotto, C.F. Manzini, F. da Porto, G. Magenes, Second-order effects in URM walls subjected to compression and out-of-plane bending: From numerical evaluation to proposal of design procedures, Eng. Struct. 209 (2020) 110130. https://doi.org/10.1016/j.engstruct.2019.110130.
[172] P. Morandi, G. Magenes, M.C. Griffith, Second order effects in out-of-plane strength of unreinforced masonry walls subjected to bending and compression, Aust. J. Struct. Eng. 8 (2008) 133–144. https://doi.org/10.1080/13287982.2008.11464993.
[173] G. Magenes, Lecture on masonry structures (14.01.2020), Lecture, (2020).
[174] K. Angervo, Über die Knickung und Tragfähigkeit eines exzentrisch gedrückten Pfeilers ohne Zugfestigkeit unter- und oberhalb der Proportionalitätsgrenze mit besonderer Berücksichtigung des rechteckigen Quer- schnitts, (1954).
[175] K. Angervo, A.I. Putkonen, U. Attila, Erweiter- ung der Theorie der Biegung eines Pfeilers ohne Zugfestigkeit und ihre Anwendung zur Berechnung von Rahmentragwerken mit unbewehrten Stielen, (1957).
[176] S. Sahlin, Structural masonry., Prentice-Hall, 1971.
[177] J.C. CHAPMAN, J. SLATFORD, THE ELASTIC BUCKLING OF BRITTLE COLUMNS. (INCLUDES APPENDICES)., Proc. Inst. Civ. Eng. 6 (1957) 107–125. https://doi.org/10.1680/iicep.1957.12395.
[178] M.C. Griffith, G. Magenes, G. MELIS, L. PICCHI, EVALUATION OF OUT-OF-PLANE STABILITY OF UNREINFORCED MASONRY WALLS SUBJECTED TO SEISMIC EXCITATION, J. Earthq. Eng. 7 (2003) 141–169. https://doi.org/10.1080/13632460309350476.
[179] H. Derakhshan, M.C. Griffith, J.M. Ingham, Airbag testing of multi-leaf unreinforced masonry walls subjected to one-way bending, Eng. Struct. 57 (2013) 512–522. https://doi.org/10.1016/j.engstruct.2013.10.006.
[180] M. Godio, K. Beyer, Analytical model for the out-of-plane response of vertically spanning unreinforced masonry walls, Earthq. Eng. Struct. Dyn. 46 (2017) 2757–2776. https://doi.org/10.1002/eqe.2929.
[181] M. Tomaževič, Some considerations on testing and experimental simulation of seismic behaviour of masonry walls and buildings, in: Proc. 16th Int. Brick Block Mason. Conf., CRC Press, Padova, Italy, 2016: pp. 65–70. https://www.taylorfrancis.com/books/9781498795920/chapters/10.1201/b21889-6.
[182] Standards Australia, Masonry Structures - AS3700-2001, 2018.
[183] K. Doherty, M.C. Griffith, N.T.K. Lam, J. Wilson, Displacement-based seismic analysis for out-of-plane bending of unreinforced masonry walls, Earthq. Eng. Struct. Dyn. 31 (2002) 833–850. https://doi.org/10.1002/eqe.126.
[184] C.C. Simsir, M.A. Aschheim, D.P. Abrams, Out-of-plane dynamic response of unreinforced bearing walls attached to flexible diaphragms, Proc. 13th World Conf. Earthq. Eng. (2004) 15.

[185] M.C. Griffith, N.T.K. Lam, J.L. Wilson, K. Doherty, Experimental Investigation of Unreinforced Brick Masonry Walls in Flexure, J. Struct. Eng. 130 (2004) 423–432. https://doi.org/10.1061/(asce)0733-9445(2004)130:3(423).
[186] J. Vaculik, E. Lumantarna, M.C. Griffith, N.T.K. Lam, J. Wilson, Dynamic Response Behaviour of Unreinforced Masonry Walls Subject to Out of Plane Loading, Aust. Earthq. Eng. Soc. Conf. (2007).
[187] E.L. McDowell, K.E. McKee, E. Sevin, Arching Action Theory of Masonry Walls, J. Struct. Div. 82 (1956). https://doi.org/10.1061/JSDEAG.0000019.
[188] EN 1996-1-1-2005, Eurocode 6 – Design of masonry structures – Part 1-1: General rules for reinforced and unreinforced masonry structures, (2005).
[189] H.R. Hodgkinson, B.A. Haseltine, H.W.H. West, Preliminary tests on the effect of arching in laterally loaded walls, 1976.
[190] L. Sorrentino, R. Masiani, M.C. Griffith, The vertical spanning strip wall as a coupled rocking rigid body assembly, Struct. Eng. Mech. 29 (2008) 433–453. https://doi.org/10.12989/sem.2008.29.4.433.
[191] K. Walsh, D.Y. Dizhur, I. Giongo, H. Derakhshan, J.M. Ingham, Predicted Versus Experimental Out-of-plane Force-displacement Behaviour of Unreinforced Masonry Walls, Structures. 15 (2018) 292–306. https://doi.org/10.1016/j.istruc.2018.07.012.
[192] ASCE/Sei 41-13, Seismic Evaluation and Retrofit of Existing Buildings, American Society of Civil Engineers, Reston, VA, 2014. https://doi.org/10.1061/9780784412855.
[193] G. Magenes, Masonry Building Design in Seismic Areas: recent experiences and prospects from a European standpoint, 1st Eur. Conf. Earthq. Eng. Seismol. (2006) Keynote 9.

Annex A

This annex reports all the results obtained in terms of the force-displacement curve for each group of tests performed. The corresponding data of the force-displacement curves of the experiments response are accessible in open source data storage [91].

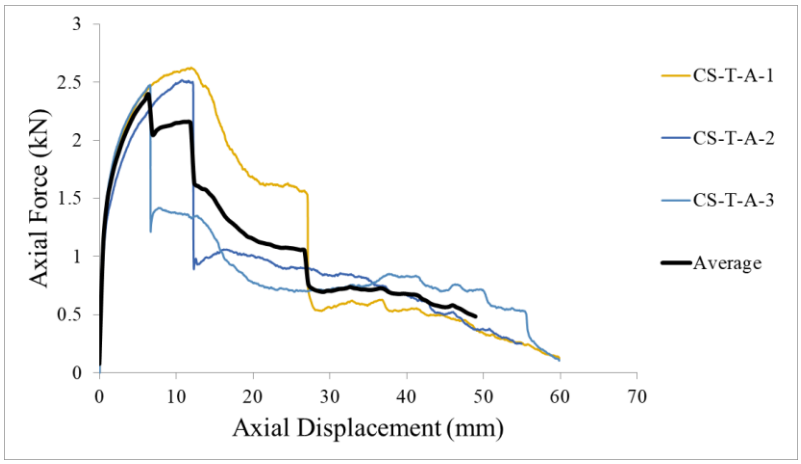

Figure A.1 Experimental results of CS70 specimens in tension for a pre-compression level of 0 MPa.

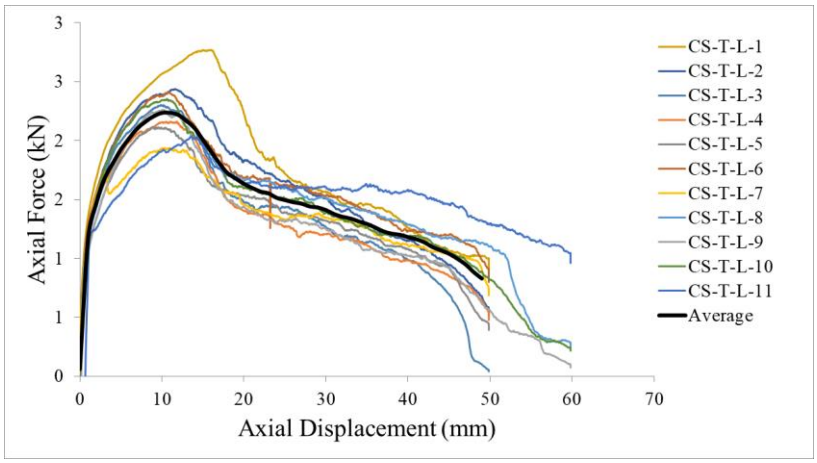

Figure A.2 Experimental results of CS70 specimens in tension for a pre-compression level of 0.1 MPa.

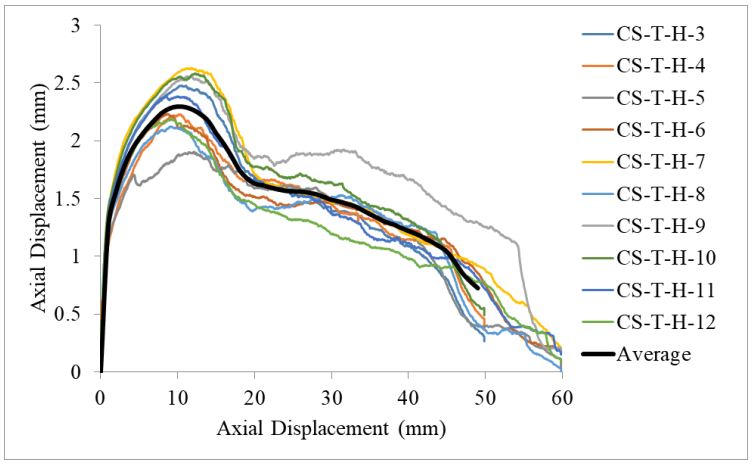

Figure A.3 Experimental results of CS70 specimens in tension for a pre-compression level of 0.3 MPa.

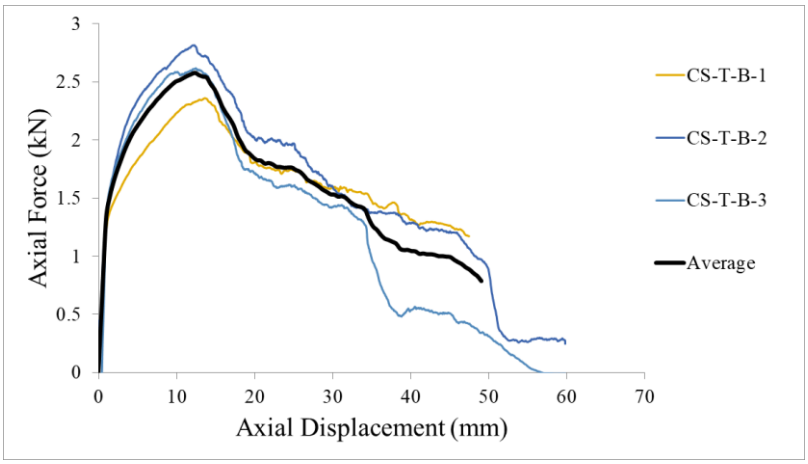

Figure A.4 Experimental results of CS70 specimens in tension for a pre-compression level of 0.6 MPa.

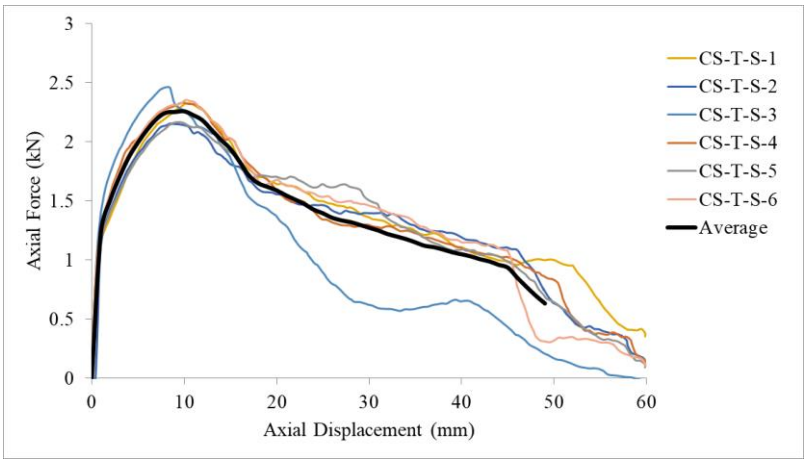

Figure A.5 Experimental results of CS70 specimens in tension for a pre-compression level of 0.1 MPa with a high-speed rate.

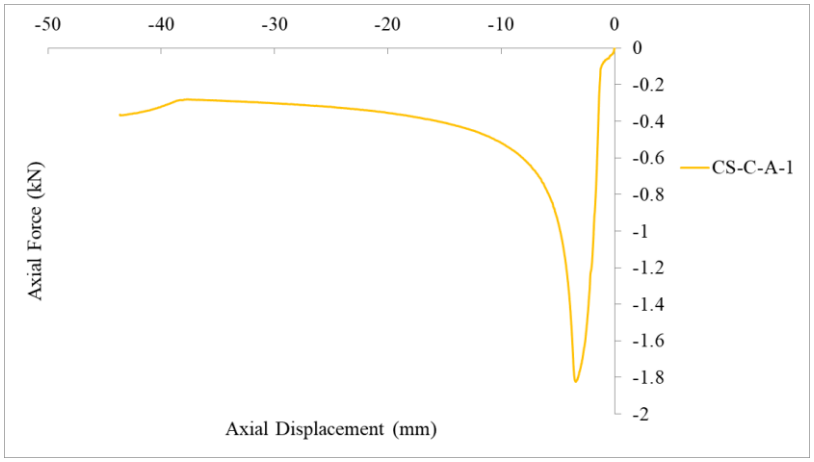

Figure A.6 Experimental result of CS70 specimens in compression for a pre-compression level of 0 MPa.

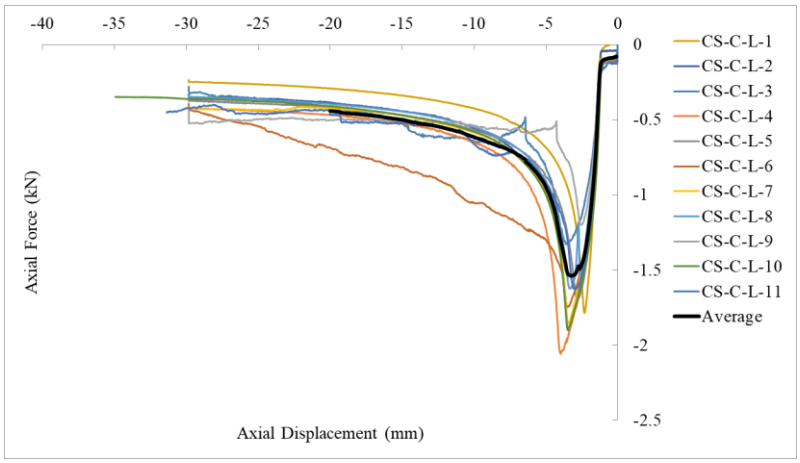

Figure A.7 Experimental results of CS70 specimens in compression for a pre-compression level of 0.1 MPa.

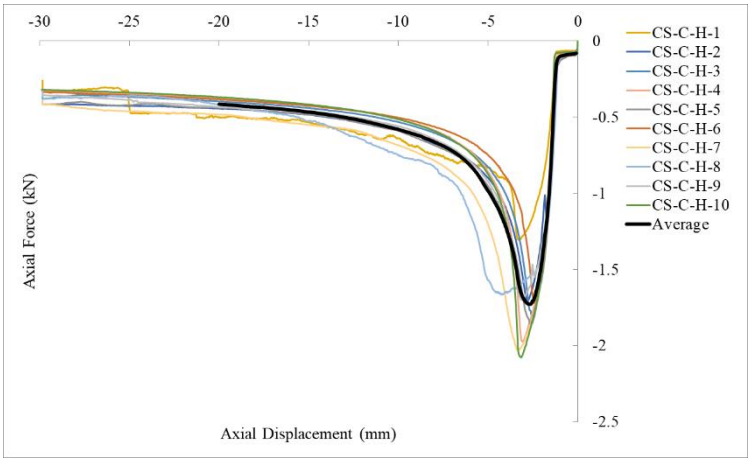

Figure A.8 Experimental results of CS70 specimens in compression for a pre-compression level of 0.3 MPa.

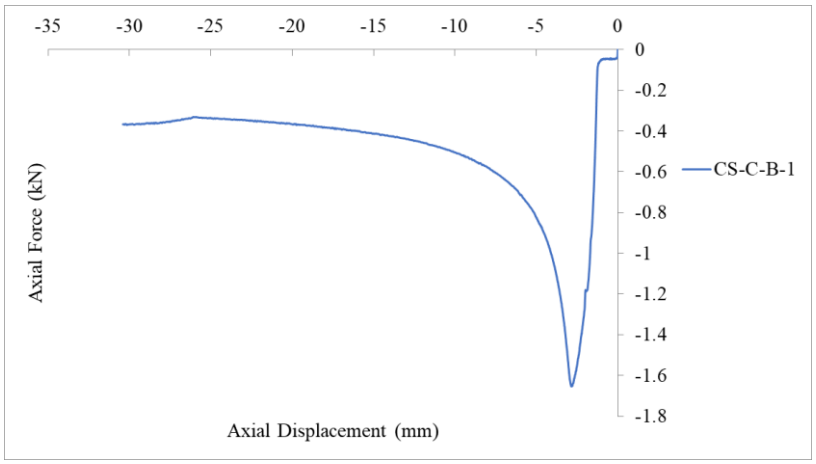

Figure A.9 Experimental results of CS70 specimens in compression for a pre-compression level of 0.6 MPa.

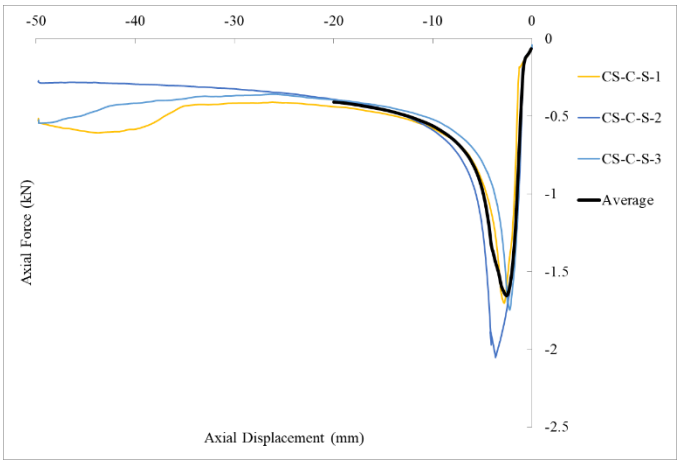

Figure A.10 Experimental results of CS70 specimens in compression for a pre-compression level of 0.1 MPa with a high-speed rate.

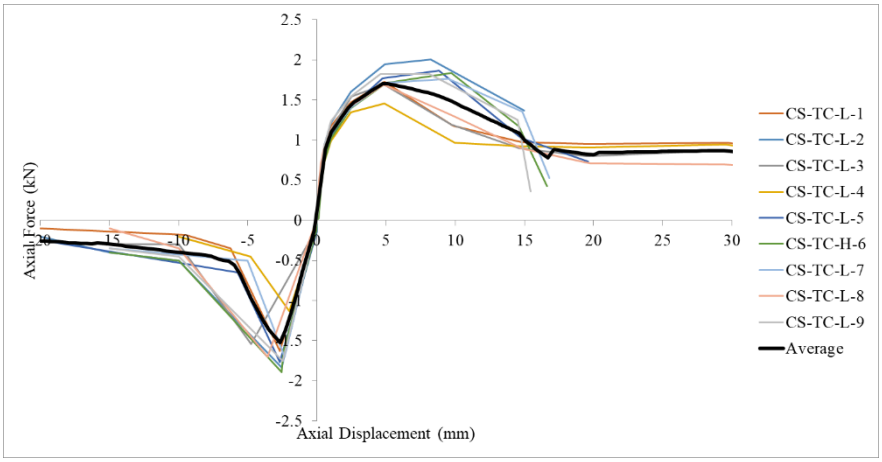

Figure A.11 Experimental results of CS70 specimens for cyclic loading for a pre-compression level of 0.1 MPa.

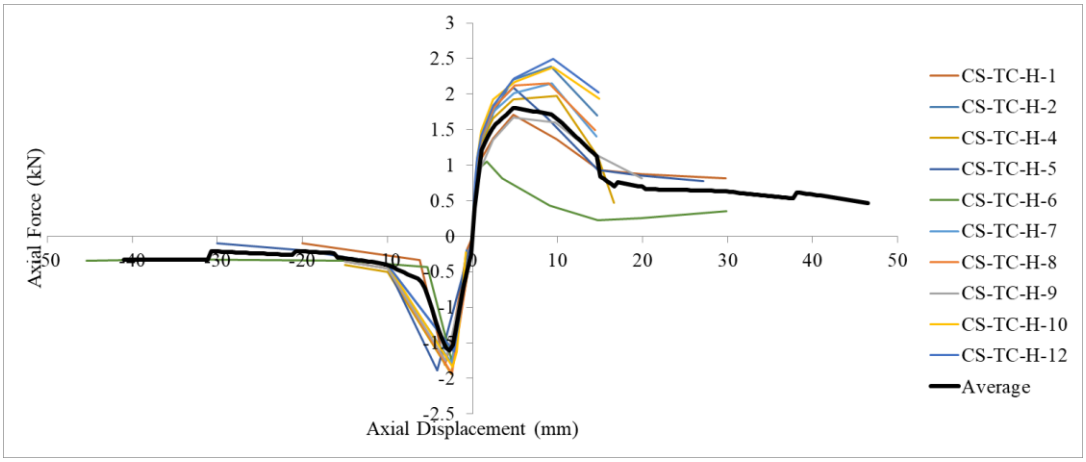

Figure A.12 Experimental results of CS70 specimens for cyclic loading for a pre-compression level of 0.3 MPa.

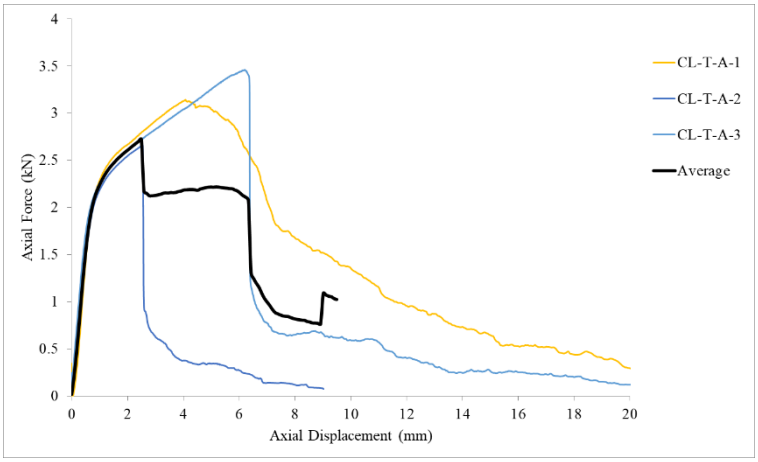

Figure A.13 Experimental results of CB50 specimens in tension for a pre-compression level of 0 MPa.

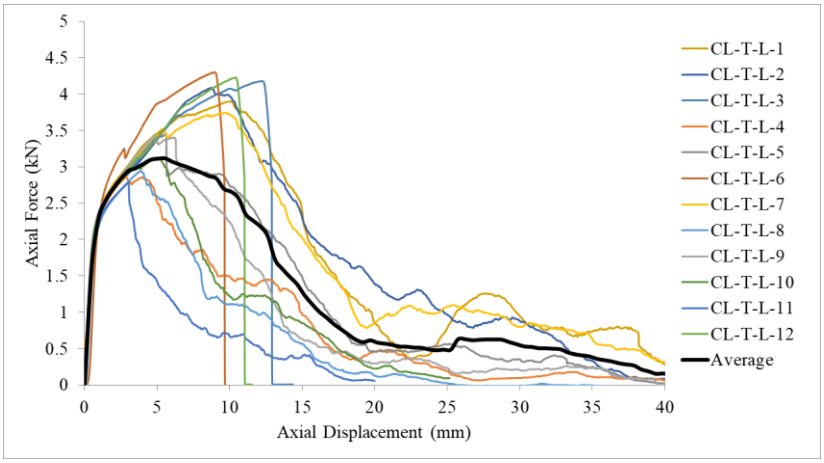

Figure A.14 Experimental results of CB50 specimens in tension for a pre-compression level of 0.1 MPa.

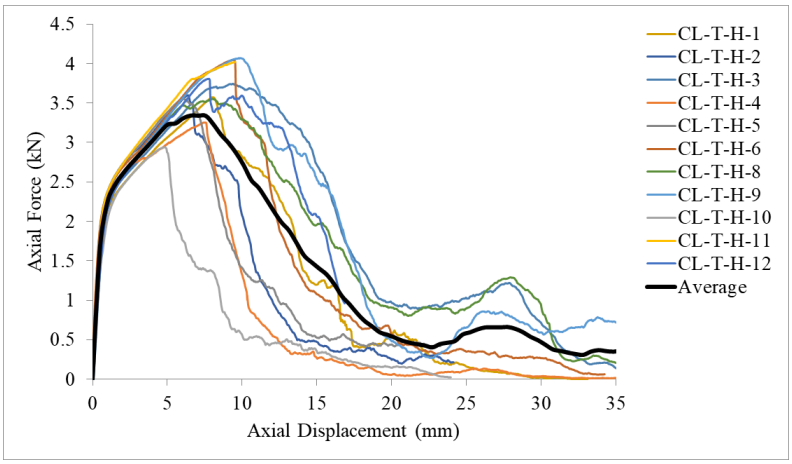

Figure A.15 Experimental results of CB50 specimens in tension for a pre-compression level of 0.3 MPa.

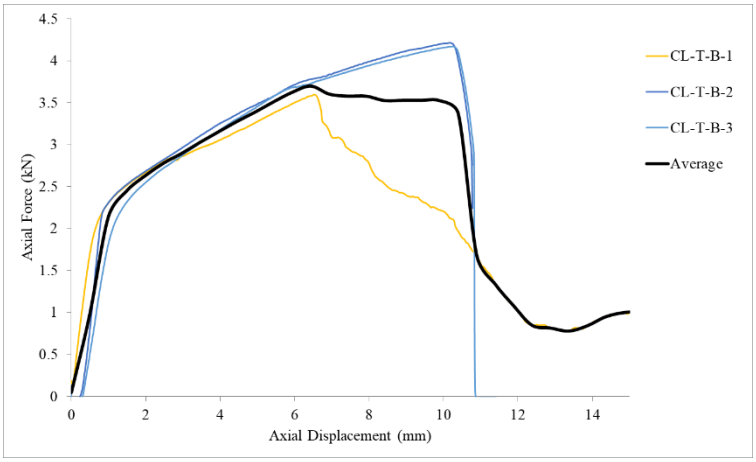

Figure A.16 Experimental results of CB50 specimens in tension for a pre-compression level of 0.6 MPa.

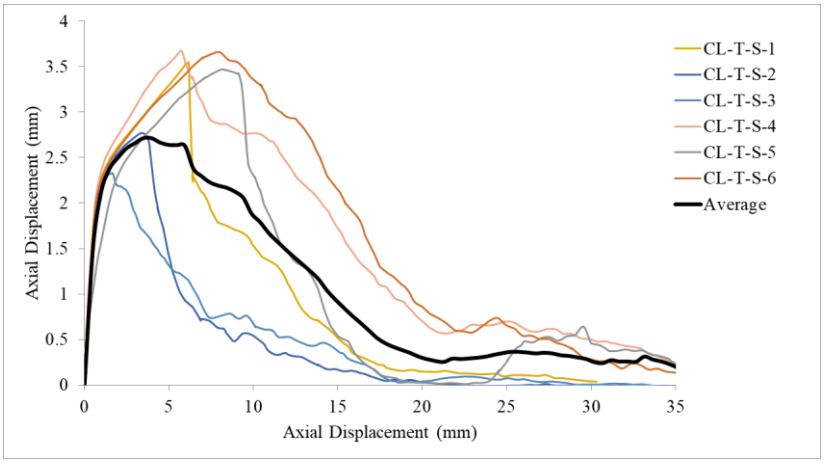

Figure A.17 Experimental results of CB50 specimens in tension for a pre-compression level of 0.1 MPa with a high-speed rate.

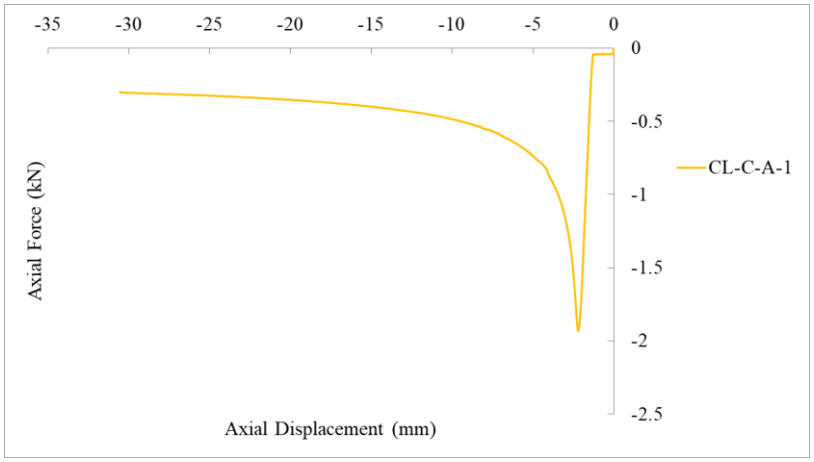

Figure A.18 Experimental result of CB50 specimens in compression for a pre-compression level of 0 MPa.

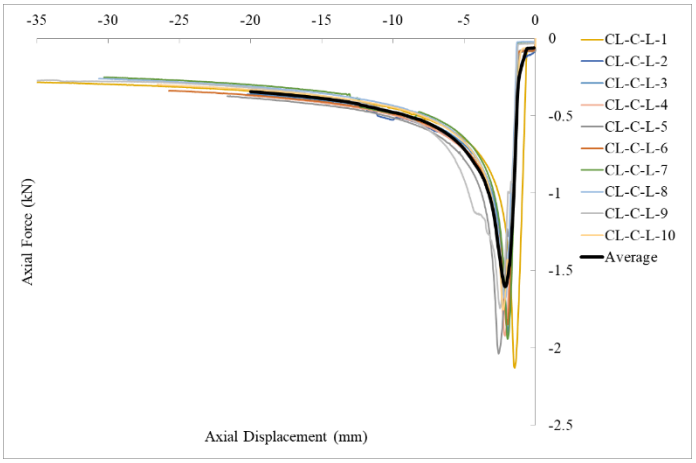

Figure A.19 Experimental results of CB50 specimens in compression for a pre-compression level of 0.1 MPa.

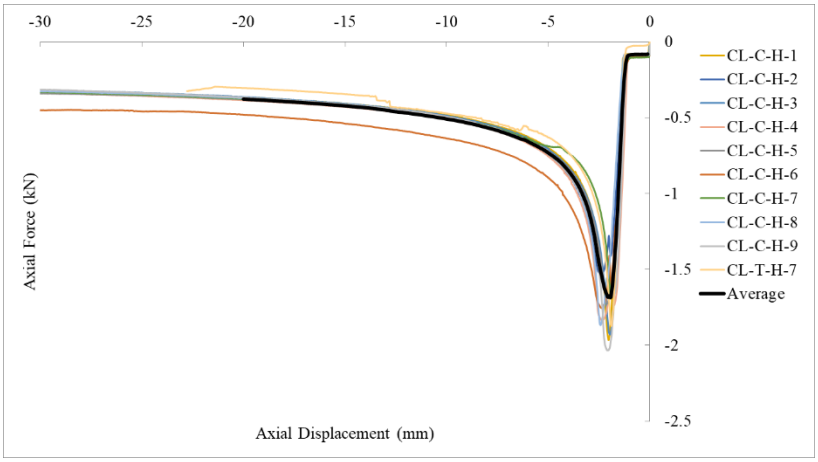

Figure A.20 Experimental results of CB50 specimens in compression for a pre-compression level of 0.3 MPa.

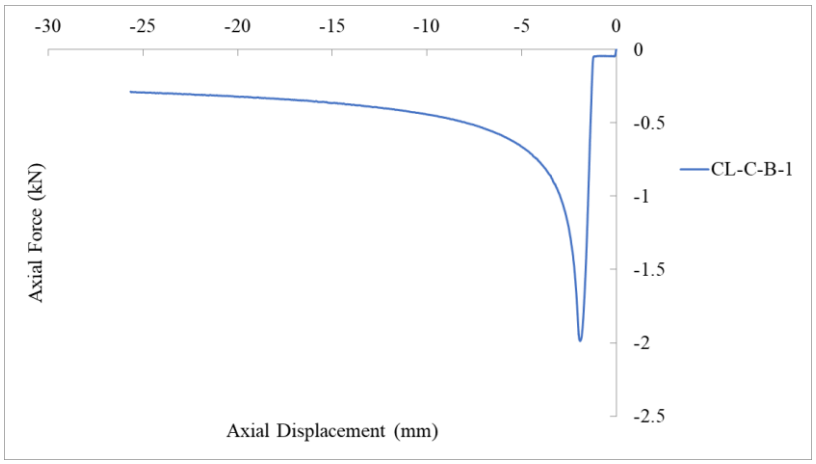

Figure A.21 Experimental result of CB50 specimens in compression for a pre-compression level of 0.6 MPa.

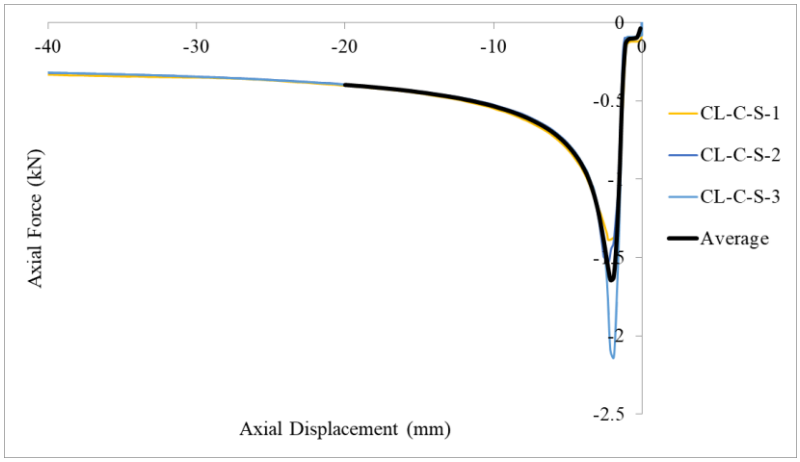

Figure A.22 Experimental results of CB50 specimens in compression for a pre-compression level of 0.1 MPa with a high-speed rate.

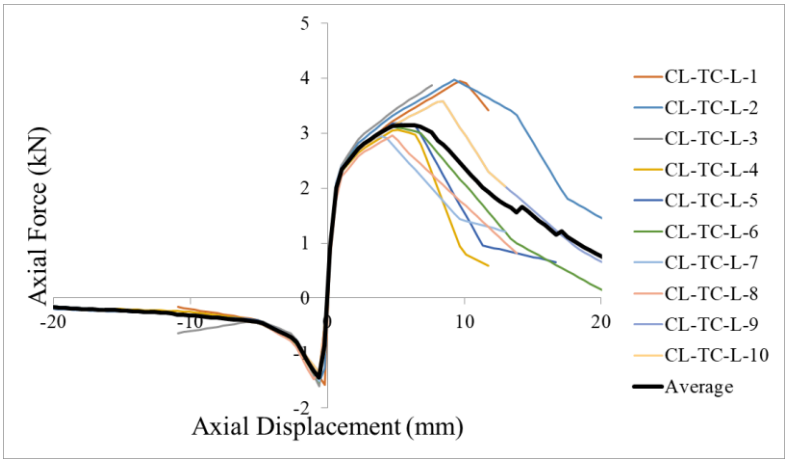

Figure A.23 Experimental results of CB50 specimens for cyclic loading for a pre-compression level of 0.1 MPa.

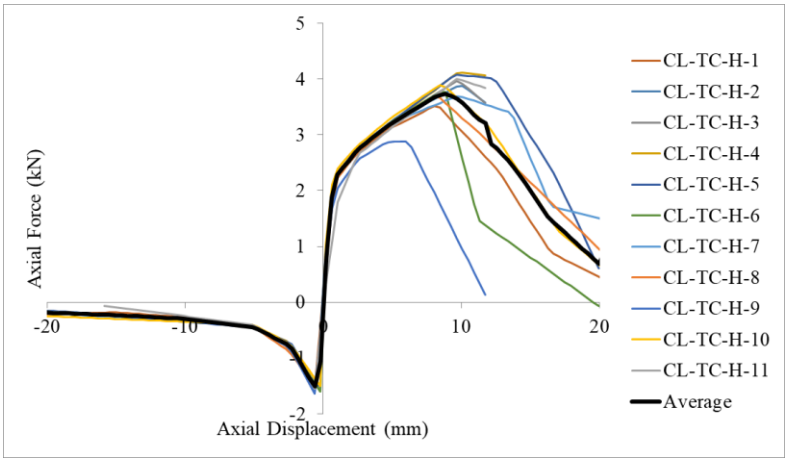

Figure A.24 Experimental results of CB50 specimens for cyclic loading for a pre-compression level of 0.3 MPa.

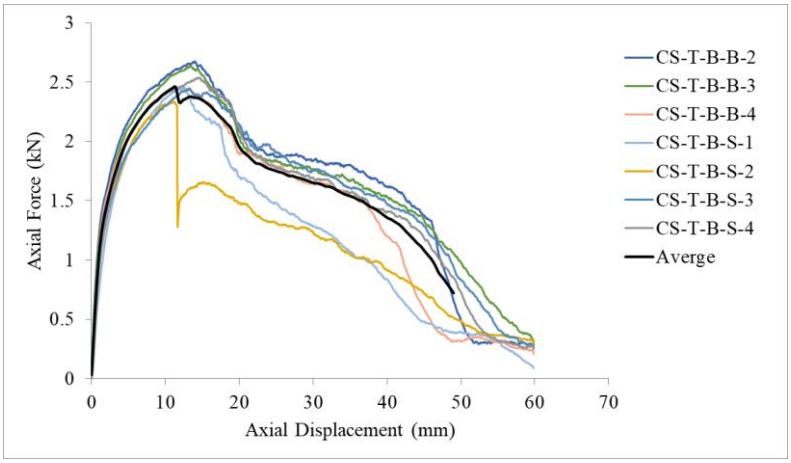

Figure A.25 Experimental results of CS70-15D (bent tie) specimens in tension for a pre-compression level of 0.1 MPa.

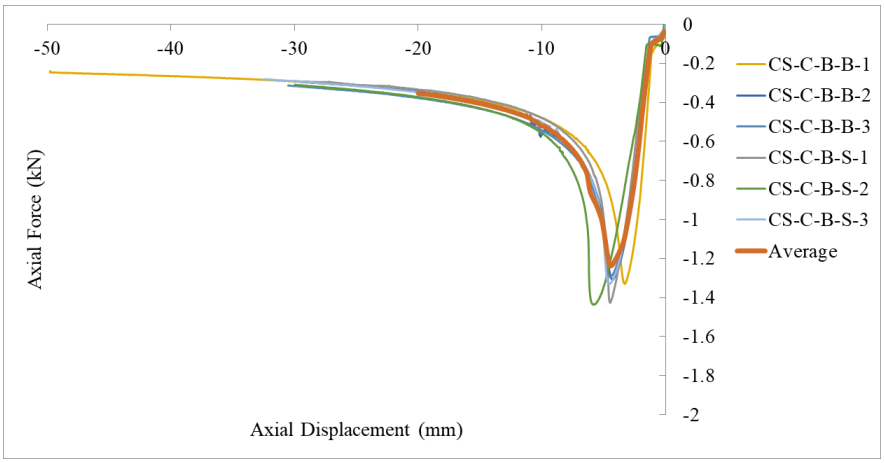

Figure A.26 Experimental results of CS70-15D (bent tie) specimens in compression for a pre-compression level of 0.1 MPa.

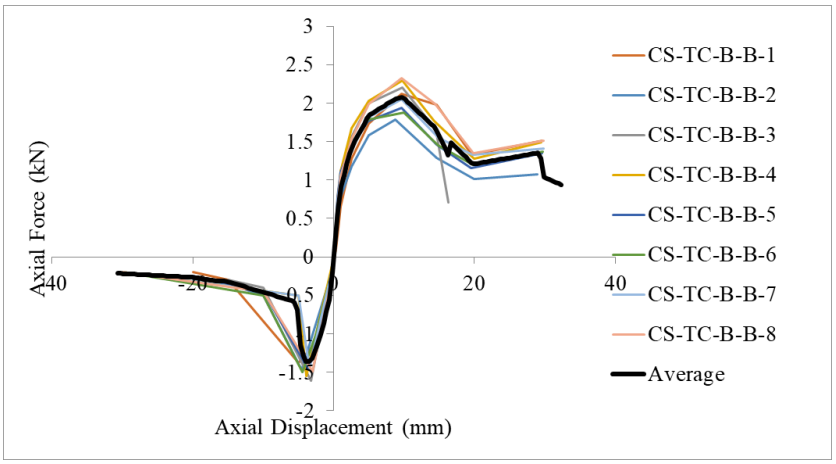

Figure A.27 Experimental results of CS70-15D (bent tie) specimens for cyclic loading for a pre-compression level of 0.1 MPa.

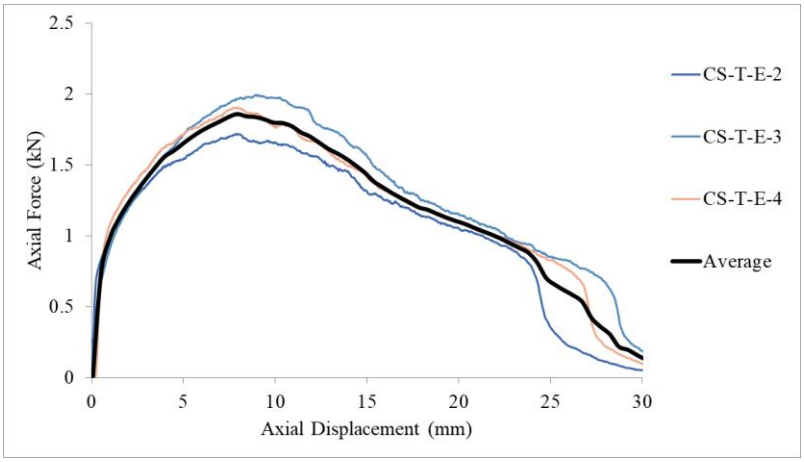

Figure A.28 Experimental results of CS50 specimens in tension for a pre-compression level of 0.1 MPa.

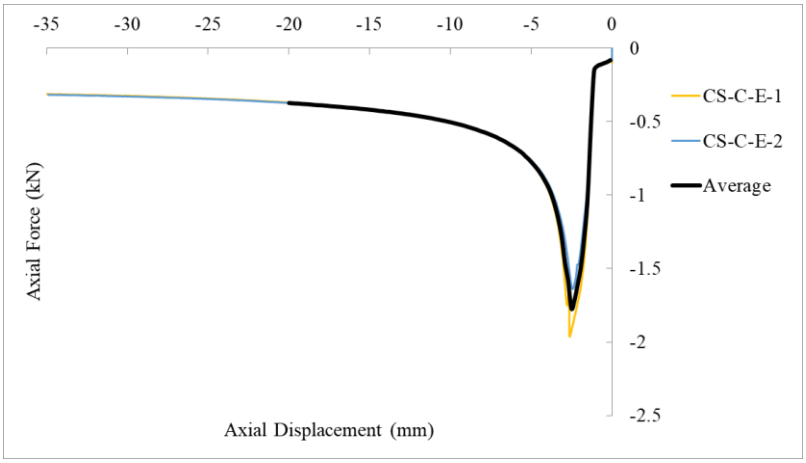

Figure A.29 Experimental results of CS50 specimens in compression for a pre-compression level of 0.1 MPa.

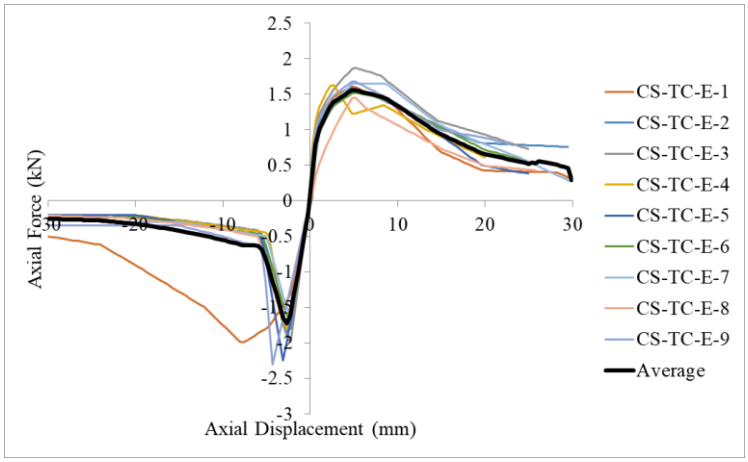

Figure A.30 Experimental results of CS50 specimens for cyclic loading for a pre-compression level of 0.1 MPa.

Annex B

This annex provides the crack pattern of the specimens with strengthened timber joist-masonry connection by means of helical bars and the corresponding deformed shape with maximum displacement in positive and negative directions (Figure B.1) and a comparison between each corresponding group's as-built and strengthened conditions (Figure B.2).

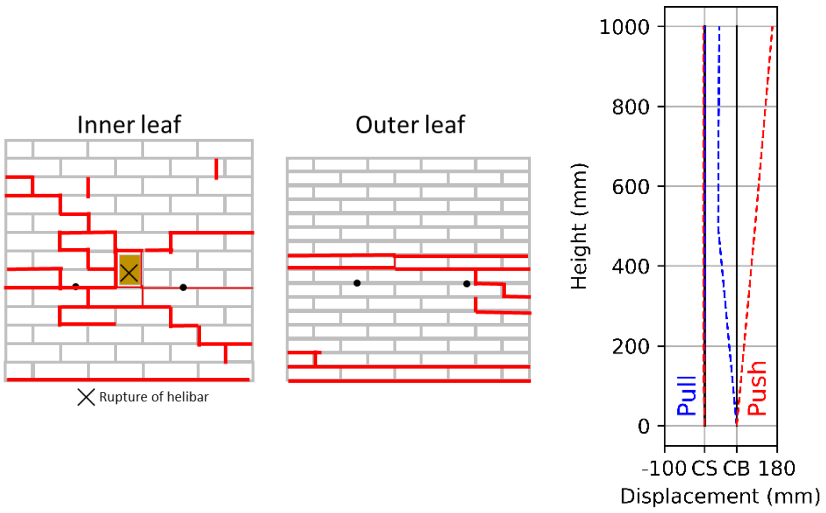

(a) TJ1 (σ_{VO} =0.1 MPa)

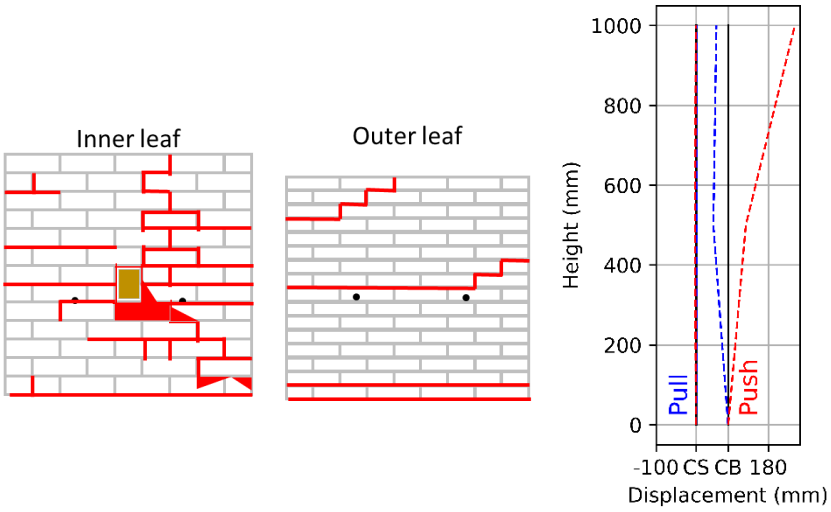

(b) TJ2 (σ_{VO} =0.1 MPa)

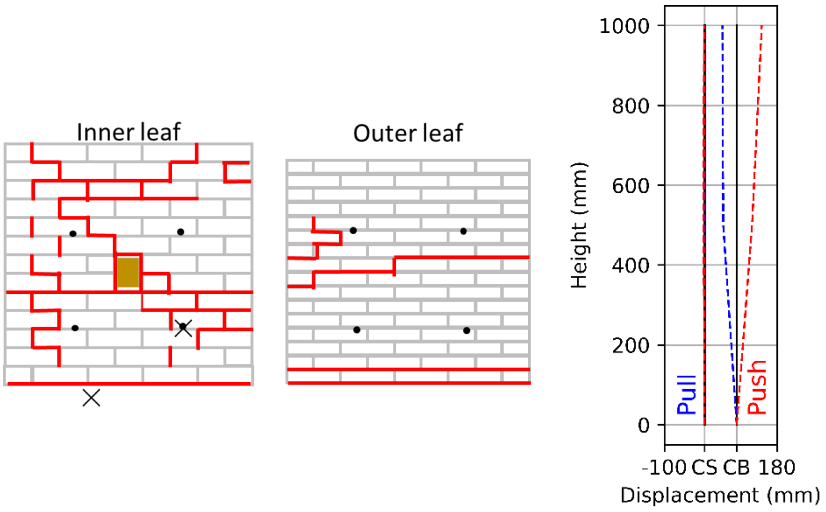

(c) TJ3 (σ_{VO} =0.1 MPa)

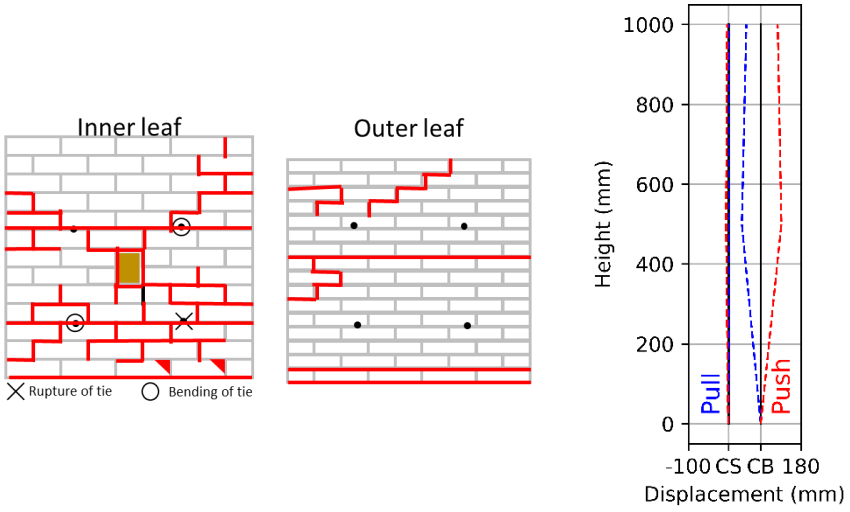

(d) TJ4 (σ_{VO} =0.1 MPa)

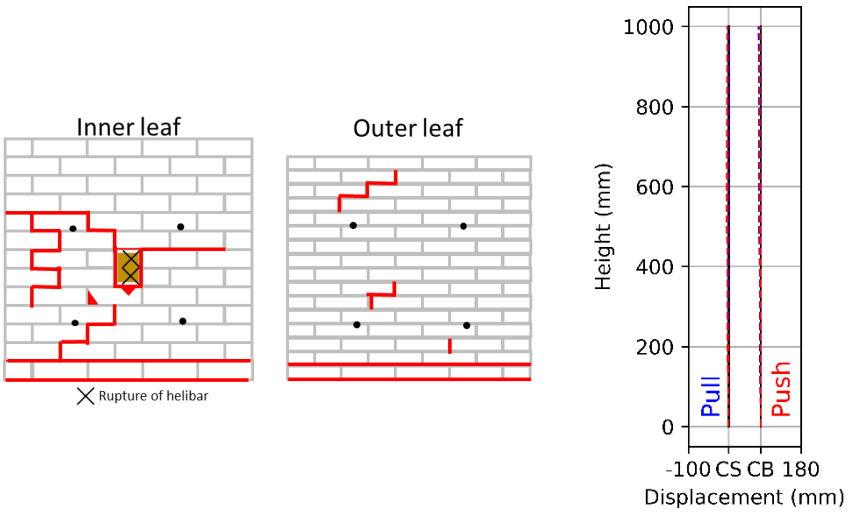

(e) TJ5 (σ_{VO} =0.3 MPa)

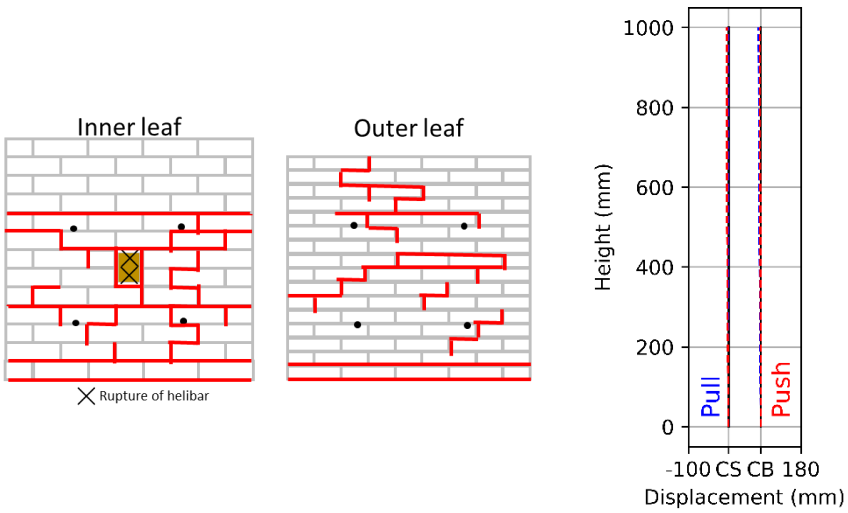

(f) TJ6 (σ_{VO} =0.3 MPa)

Figure B.1 Crack patterns and deformed shapes of the specimens with strengthened timber joist-masonry connection by means of helical bars. The left diagram for each specimen shows the crack pattern at the conclusion of the test. The right diagram indicates the deform shape.

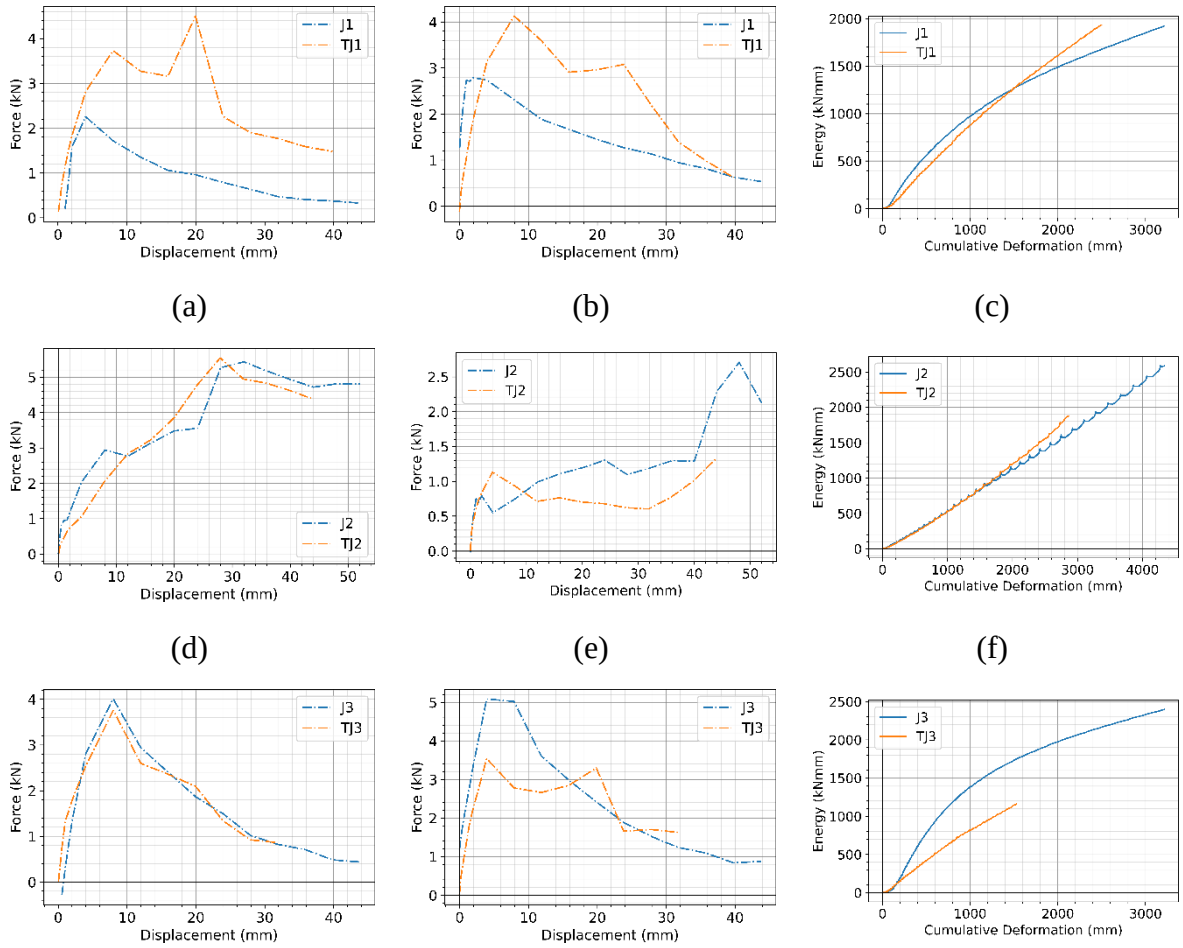

(a) (b) (c)

(d) (e) (f)

(g) (h) (i)

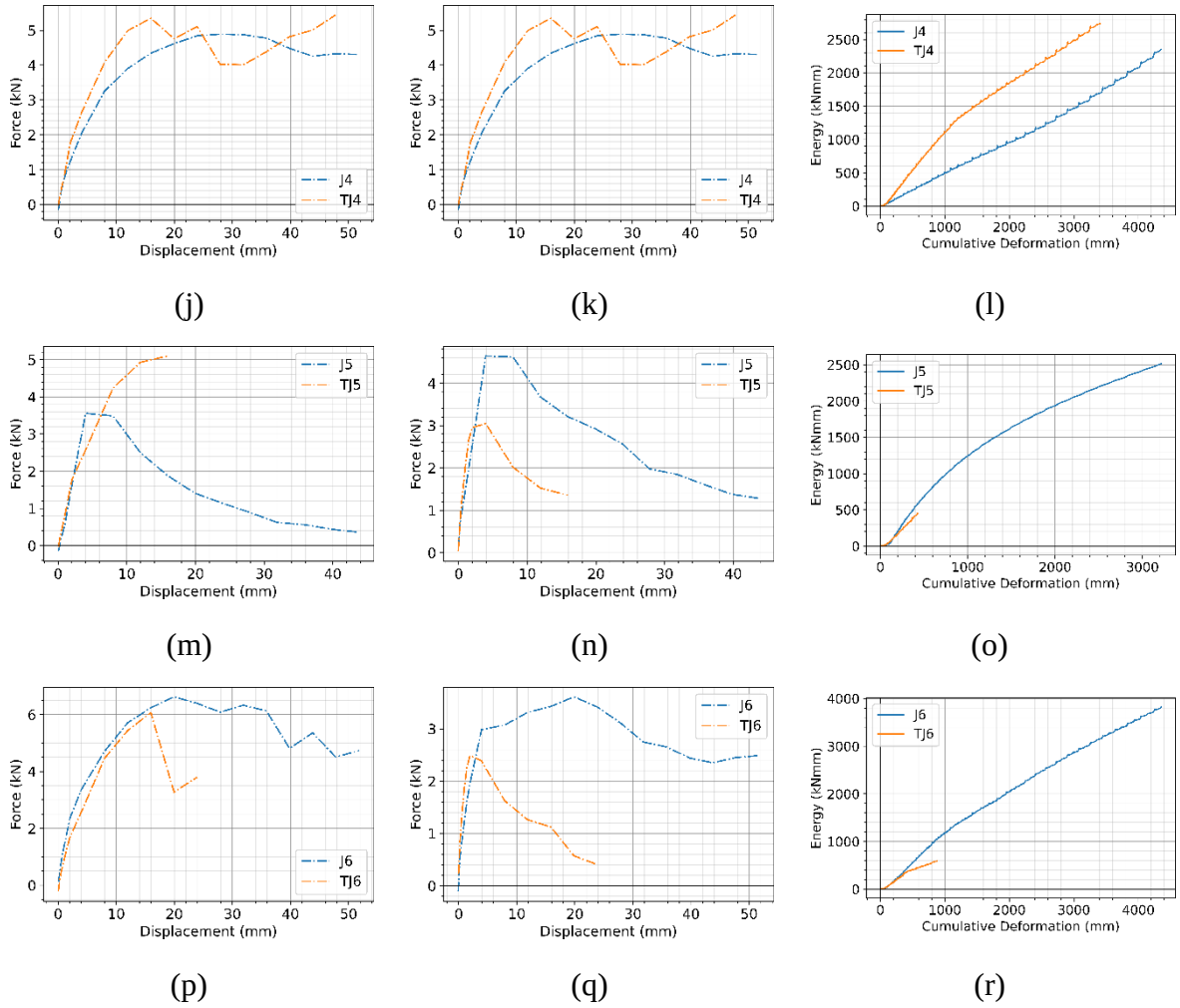

Figure B.2 Comparison of each specimen in as-built condition with corresponding strengthened specimen in terms of average envelope curves in tension (left diagrams) and compression (in the middle of diagrams), and cumulative hysteretic energy (right diagrams).

Annex C

In this annex, the detailed calculations used in the mechanical model of timber-masonry connections (Chapter 6) are presented. The first part concerns the calculation of the joist-sliding failure mode including joist-to-wall interaction, while the second part of this annex deals with the calculation of the force associated with triggering of wall rocking failure mode due to joist movement.

C.1 Joist-sliding failure mode

An example of the calculation of joist-sliding failure mode including joist-to-wall interaction for a specimen with masonry pocket connection, in this case, it is Specimen J1, is shown. Input data of the mechanical model is as follows:

- Thickness of inner leaf t_w: 100 mm
- Thickness of joist t_j: 60 mm
- Density of inner leaf masonry ρ_{CS}: 1683 kg/m^3
- Applied vertical dead load to joist W_J: 100 kg
- Elastic modulus of joist E_j: 12000 MPa
- Elastic modulus of inner leaf masonry (CS) E_{CS}: 12000 MPa
- Total length of joist L_j: 1550 mm
- Wallet height h: 1030 mm
- Parameter for the internal lever arm γ: 0.9

The obtained values for the shear stress for J1 can be seen in Table C.1. The sequence of calculations used to produce the values is traced from (1) to (6). The calculations for each sequence, line by line, are given below the table.

Table C.1 Cohesion values for Specimen J1.

	(1)	(2)	(3)	(4)	(5)	(6)
	Shear Stress (MPa) [τ]		Normal Stress (MPa) [σ_N]	Arching Stress (MPa) [σ_S]		Cohesion (MPa) [c]
	Pulling	Pushing	Pulling & Pushing	Pulling	Pushing	Pulling & Pushing
J1	0.19	0.26	0.15	0	0.10	0.10

Sequence (1) represents the shear stress in pulling. The peak force in pulling, $H_{E,Pull}$, is obtained from the test as a value of 2.29 kN at 4 mm. Determination of the shear stress is as follows:

$$\tau = \frac{H_E}{2 \cdot t_w \cdot t_j} = \frac{2290}{2 \cdot 100 \cdot 60} = 0.19\ MPa$$

Sequence (2) refers to the shear stress in pushing. The peak force is obtained from the test as a value of 3.13 kN at displacement of 4 mm. Determination of the shear stress is as follows:

$$\tau = \frac{H_E}{2 \cdot t_w \cdot t_j} = \frac{3130}{2 \cdot 100 \cdot 60} = 0.26\ MPa$$

Sequence (3) shows the normal stress on the joist in pulling and pushing (σ_N) due to the normal force (N_V).

The initial force (N_V) consists of three parts which are the weight of the masonry above the joist (i), overburden force above the joist (ii) and the applied vertical joist load at the middle of the joist (iii). Hence, the aforementioned parts are calculated as follows:

(i) Determination of the force due to weight of the masonry above the joist:

0.48 m * 0.10 m * 0.06 m = 0.00288 m^3 (the volume of the masonry above the joist)

0.00288 m^3 * 1683 kg/m^3 = 4.85 kg (the weight of the masonry above the joist)

4.85 kg * 9.807 m/s^2 = 50 N = 0.05 kN (force due to the weight)

(ii) Determination of the force due to overburden:

0.1 N/mm^2 * 60 mm * 100 mm= 0.6 kN (the applied overburden is 0.1 MPa)

(iii) Determination of the force due to the applied vertical joist load, representing dead load of the joist:

100 kg / 2 / 2 / 9.807 m/s^2 = 245.2 N = 0.25 kN (The vertical dead load is applied only at the joist's lower contact surface, hence divided by two to consider an average vertical load on the joist, taking into account the lower and upper surfaces of the joist.)

The normal force on the joist (Nv) is the sum of the three parameters which is equal to 0.91 kN.

Determination of the normal stress on the joist (σ_N) in pulling and pushing is as follows:

$$\sigma_N = \frac{N_V}{t_w * t_J} = \frac{910}{60 * 100} = 0.15\ MPa$$

Sequence (4) refers to the arching stress on the joist (σ_N) in pulling due to arching force (N_S). In order to compute the additional vertical force due to the arching effect, N_S, the

compressive stress at the contact area between the joist and masonry (σ_s) due to the arching effect needs to be obtained for the corresponding horizontal displacement of the inner leaf at mid-height. The horizontal displacement of the inner leaf at mid-height at the attainment of the peak force is measured as zero. Hence, N_S is equal to zero, exhibiting no arching effect in tension.

Sequence (5) refers to the arching stress on the joist (σ_N) in the pushing direction. Similarly to what has been done for Sequence (4), the OOP displacement of the inner leaf at mid-height needs to be defined. In order to compute the additional vertical force due to the arching effect, N_S, firstly, the compressive stress at the contact area between the joist and masonry (σ_s) due to the arching effect is obtained for the corresponding horizontal displacement of the inner leaf at mid-height at the attainment of the peak force.

$$y = \frac{1}{2} - \frac{e}{t_w} = \frac{1}{2} - \frac{30}{100} = 0.2$$

$$\Delta = 0.5 \times t_w \times \left(y - \sqrt{y^2 - \frac{f_s}{6E}\left(\frac{h}{t_w}\right)^2} \right) = 1.34 = 0.5 \times 100 \times \left(0.5 - \sqrt{0.5^2 - \frac{f_s}{6 \cdot 2749}\left(\frac{1030}{100}\right)^2} \right)$$

$$P = 0.75 \times fs \times t_w \times \left(y + \sqrt{y^2 - \frac{f_s}{6E}\left(\frac{h}{t_w}\right)^2} \right) = 10.88\ N/mm$$

In which f_s is computed as a value of 0.39 MPa. Finally, the additional vertical force due to the arching effect can be computed as follows:

$$N_S = P \cdot t_j = 10.9 \cdot 60 = 653\ N = 0.65\ kN$$

Determination of the normal stress on the joist (σ_N) in pushing is as follows:

$$\sigma_N = \frac{N_S}{t_w * t_J} = \frac{0.65}{60 * 100} = 0.10\ MPa$$

Sequence (6) represents the cohesion. Cohesion is considered same in both directions, pulling and pushing. Hence, it is determined for both loading directions as follows. Determination of the cohesion (c) is as follows:

$$\tau = c + \mu \cdot (\sigma_N + \sigma_S) = 0.19 = c + 0.6 \cdot 0.15$$

Cohesion in pulling is equal to 0.099 MPa. While in pushing,

$$\tau = c + \mu \cdot (\sigma_N + \sigma_S) = 0.26 = c + 0.6 \cdot 0.26$$

c is equal to 0.104 MPa. Hence, cohesion can be chosen as a value of 0.10.

It should be noted that, as mentioned in Chapter 4, the joist deformed during the experiment because one extreme of the joist was fixed in the testing machine and cannot displace vertically, while, the other extreme moved due to the overturning of the inner leaf and the sliding of the joist in the pocket. The deflection of the joist introduced then an additional shear force due to

the flexural and shear stiffness of the element. Although the shear force due to the joist deflection is very limited, an example of computing the vertical deformation and corresponding shear force is explained below.

In order to compute the shear force due to the joist deflection, uplift or lowering of the contact point between the joist and the masonry due to the OOP rocking, δ_j, needs to be determined. During the experiments, only the horizontal displacements were obtained by sensors. However, the vertical displacement of the joist due to the OOP rocking of the inner leaf can be calculated by using a simple geometrical approach "triangle similarity" (Figure C.1) since the horizontal displacement of the inner leaf is very limited in the range of 0 mm – 5.29 mm (see Figure 6.17).

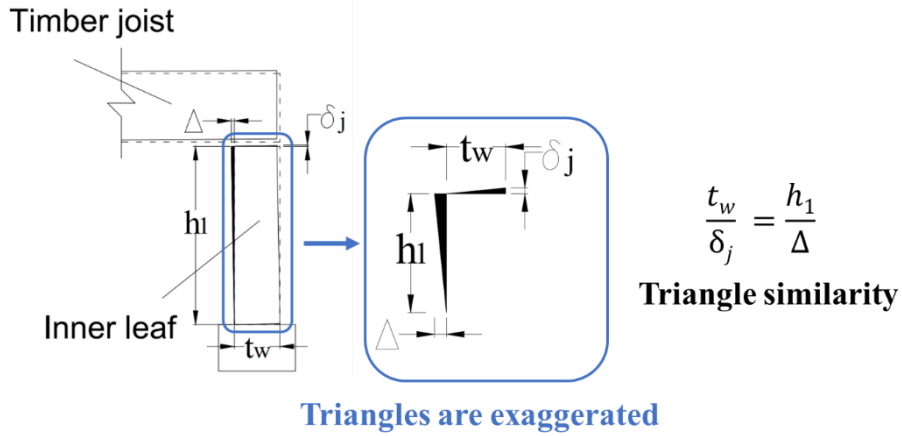

Figure C.1 rotation of the inner leaf due to the joist movement.

Specimen J1 in pushing exhibits an OOP displacement of 1.34 mm, Δ. By using the triangle similarity, the vertical displacement, δj, can be calculated as follows:

$$\frac{t_w}{\delta_j} = \frac{h_1}{\Delta} = \frac{100}{\delta_j} = \frac{300}{1.34}$$

In which δj is equal to 0.45 mm. Finally, the additional vertical force due to the deflection of the joist, N_J, is as follows:

$$N_J = \frac{\delta_j 3E_j I_j}{L_j^3} = \frac{0.45 \cdot 3 \cdot 12000 \cdot 18619375}{3723875000} = 0.08\ kN$$

After completing the calculation of normal stress and cohesion, the contribution of each parameter to the peak force, which are cohesion, initial normal force, and arching effect, can be determined. The obtained values of such contributions for J1 can be seen in Table C.2. The sequence of calculations used to produce the values is traced from (1) to (10). The calculations for each sequence, line by line, are given below the table.

Table C.2 Cohesion and friction force values for Specimen J1.

	(1)	(2)	(3)	(4)	(5)	(6)	(7)	(8)	(9)	(10)
	Tension					Compression				
	Exp.	Mechanical			Error	Exp.	Mechanical			Error
	Peak Force (kN)	Cohesion (kN)	Friction forces			Peak Force (kN)	Cohesion (kN)	Friction forces		
			Initial normal force (kN)	Arching effect (kN)				Initial normal force (kN)	Arching effect (kN)	
J1	2.29	1.19	1.09	-	-0.4%	3.13	1.19	1.09	0.73	-2.1%

It should be noted that from sequence (1) to (5) the values are obtained in pulling. Sequence (1) is obtained during the experiment. $H_{E,Pull}$ is equal to 2.29 kN. Sequence (2) refers to the resistance force due to cohesion acting on the contact surface, which is in between timber joist and mortar.

$$H_C = 2 \cdot c \cdot A = 2 \cdot 0.10 \cdot 60 \cdot 100 = 1.19\ kN$$

Sequence (3) refers to the initial normal force observed due to friction.

$$H_V = 2 \cdot \mu \cdot N_V = 2 \cdot 0.6 \cdot 0.91 = 1.09\ kN$$

Sequence (4) is equal to zero since there was no horizontal displacement on the inner leaf due to the joist. Finally, the peak force obtained by the mechanical model can be computed as follows:

$$H_M = H_V + H_J + H_S = 1.19 + 1.09 + 0 = 2.28\ kN$$

Sequence (5) represents the error between the experimental results and the studied mechanical model in pulling. The error is computed as the difference between the mechanical model and the experimental result divided by the experimental result.

$$Error = \frac{H_M - H_E}{H_E} = \frac{(1.19 + 1.09) - 2.29}{2.29} = -0.4\%$$

It should be noted that from sequence (6) to (10) the values are obtained in pushing. Sequence (6) is obtained during the experiment. $H_{E,Push}$ is equal to 3.13 kN. Sequence (7) refers to the resistance force due to cohesion acting on the contact surface.

$$H_C = 2 \cdot c \cdot A = 2 \cdot 0.10 \cdot 60 \cdot 100 = 1.19\ kN$$

Sequence (8) refers to the initial normal force observed due to friction.

$$H_V = 2 \cdot \mu \cdot N_V = 2 \cdot 0.6 \cdot 0.91 = 1.09\ kN$$

Sequence (9) refers to the force due to the arching effect.

$$H_A = 2 \cdot \mu \cdot N_A = 2 \cdot 0.6 \cdot 0.65 = 0.78\ kN$$

Finally, the peak force obtained by the mechanical model can be computed as follows:

$$H_M = H_V + H_J + H_S = 1.19 + 1.09 + 0.78 = 3.06\ kN$$

Sequence (10) represents the error between the experimental results and the studied mechanical model in pushing. The error is computed as the difference between the mechanical model and the experimental result divided by the experimental result.

$$Error = \frac{H_M - H_E}{H_E} = \frac{(1.19 + 1.09 + 0.78) - 3.13}{3.13} = -2.1\%$$

C.2 Rocking failure mode

An example of the calculation of forces associated with triggering of rocking failure mode for Specimen J1 is shown below. Firstly, the pre-activation mechanism phase is computed. The cracking force, Fcr, can be calculated by employing Eq. (6-22). As seen in the equation, the cracking force of the cavity walls is computed as the sum of each leaf cracking force. Hence, the cracking force for the inner and outer leaves are determined, respectively. Cracking force of inner leaf, $F_{cr,iw}$, is as follows:

$$M_b = \left(f_w + \frac{W + \sigma_{v0} \cdot t_w}{t_w}\right)\frac{{t_w}^2}{6} = \left(0.1 + \frac{1.78 + 10}{100}\right)\frac{100^2}{6} = 361.7$$

$$M_t = \left(f_w + \frac{\sigma_{v0} \cdot t_w}{t_w}\right)\frac{{t_w}^2}{6} = \left(0.1 + \frac{10}{100}\right)\frac{100^2}{6} = 333.33$$

$$\zeta = f_w + \frac{1}{t_w}\left(\frac{W}{2} + \sigma_{v0} \cdot t_w + \frac{3 \cdot (a_b \cdot m_b - a_t \cdot m_t)}{t_w}\right)$$

$$= 0.1 + \frac{1}{100}\left(\frac{1.78}{2} + 10 + \frac{3 \cdot (0 \cdot 363.05 - 0 \cdot 333.33)}{100}\right) = 0.21$$

$$F_{cr,iw} = \frac{\zeta + \sqrt{\zeta - \frac{W^2}{4 \cdot {t_w}^2} - \frac{(a_b \cdot m_b - a_t \cdot m_t)}{{t_w}^3} - \frac{(a_b \cdot m_b - a_t \cdot m_t)^2}{{t_w}^4}}}{\frac{3}{2} \cdot \frac{h}{{t_w}^2}}$$

$$= \frac{0.21 + \sqrt{0.21 - \frac{1.78^2}{4 \cdot 100^2} - \frac{(0 \cdot 363.05 - 0 \cdot 333.33)}{100^3} - \frac{(0 \cdot 363.05 - 0 \cdot 333.33)^2}{100^4}}}{\frac{3}{2} \cdot \frac{1030}{100^2}}$$

$$= 2.70$$

$F_{cr,iw}$ is equal to 2.70 kN for the inner leaf. Cracking force of outer leaf, $F_{cr,ow}$, is computed as follows:

$$M_b = \left(f_w + \frac{W + \sigma_{v0} \cdot t_w}{t_w}\right)\frac{{t_w}^2}{6} = \left(0.28 + \frac{1.84 + 10}{100}\right)\frac{100^2}{6} = 496$$

$$M_t = \left(f_w + \frac{\sigma_{v0} \cdot t_w}{t_w}\right)\frac{{t_w}^2}{6} = \left(0.28 + \frac{10}{100}\right)\frac{100^2}{6} = 466.7$$

$$\zeta = f_w + \frac{1}{t_w}\left(\frac{W}{2} + \sigma_{v0} \cdot t_w + \frac{3 \cdot (a_b \cdot m_b - a_t \cdot m_t)}{t_w}\right)$$

$$= 0.28 + \frac{1}{100}\left(\frac{1.84}{2} + 10 + \frac{3 \cdot (1 \cdot 497.39 - 0 \cdot 466.67)}{100}\right) = 0.29$$

$$F_{cr,ow} = \frac{\zeta + \sqrt{\zeta - \frac{W^2}{4 \cdot {t_w}^2} - \frac{(a_b \cdot m_b - a_t \cdot m_t)}{{t_w}^3} - \frac{(a_b \cdot m_b - a_t \cdot m_t)^2}{{t_w}^4}}}{\frac{3}{2} \cdot \frac{h}{{t_w}^2}}$$

$$= \frac{0.29 + \sqrt{0.29 - \frac{1.84^2}{4 \cdot 100^2} - \frac{(0 \cdot 497.39)}{100^3} - \frac{(0 \cdot 497.39)^2}{100^4}}}{\frac{3}{2} \cdot \frac{1030}{100^2}} = 3.74$$

In order to compute the total cracking force (F_c+$F_{cr,iw}$+$F_{cr,ow}$), the coupling force associated with the contribution of embedded ties needs to be obtained. The coupling force can be computed by employing Eq. (6-30) as follows:

$$V_t = \sum_1^n V_i = \sum_1^2 100 = 200$$

$$M_t = \sum_1^n M_i = \sum_1^2 3000 = 6000$$

$$F_c = 2 \cdot V_t \cdot t_w \cdot \frac{h}{h_1 \cdot h_2} + 2 \cdot M_t \frac{h}{h_1 \cdot h_2} = 2 \cdot 200 \cdot 100 \cdot \frac{1030}{526 \cdot 504} + 2 \cdot 6000 \frac{1030}{526 \cdot 504}$$

$$= 0.2$$

$$F_{cr} = F_{cr,iw} + F_{cr,ow} + F_c = 2.51 + 3.48 + 0.2 = 6.19$$

The cracking displacement is obtained as the lesser of the ones associated with the two leaves (inner and outer leaves). The cracking displacement of inner leaf is determined as follows:

$$u_{cr} = \frac{\beta}{384}\frac{F_{cr} \cdot h^3}{E_w \cdot I_w} = \frac{5}{384}\frac{2.70 \cdot 1030^3}{2749 \cdot 83333.33} = 0.17$$

The cracking displacement of outer leaf is determined as follows:

$$u_{cr} = \frac{\beta}{384}\frac{F_{cr} \cdot h^3}{E_w \cdot I_w} = \frac{5}{384}\frac{3.74 \cdot 1030^3}{5019 \cdot 83333.33} = 0.13$$

Hence, the cracking displacement is equal to 0.13 mm. The location along the wallet height where the middle crack (h_1) occurs can be computed by employing Eq. (6-27). h_1 for the inner leaf can be computed as follows:

$$\frac{h_1}{h} = \frac{1}{2} + \frac{1}{h \cdot F_{cr}}\left(\frac{W \cdot t_w}{6} + (a_b \cdot m_b - a_t \cdot m_t)\right) = \frac{h_1}{1030}$$

$$= \frac{1}{2} + \frac{1}{1030 \cdot 5.16}\left(\frac{1.78 \cdot 100}{6} + (0 \cdot 363.05 - 0 \cdot 333.33)\right)$$

h_1 is equal to 526 mm for the inner leaf. While h_1 for the outer leaf can calculated as follows:

$$\frac{h_1}{h} = \frac{1}{2} + \frac{1}{h \cdot F_{cr}}\left(\frac{W \cdot t_w}{6} + (a_b \cdot m_b - a_t \cdot m_t)\right) = \frac{h_1}{1030}$$

$$= \frac{1}{2} + \frac{1}{1030 \cdot 5.39}\left(\frac{1.84 \cdot 100}{6} + (0 \cdot 497.39)\right)$$

h_1 is equal to 523 mm for the outer leaf. After defining the pre-activation mechanism phase of the wallet, the activation of the OOP mechanism phase was obtained for the same specimen. Rigid force, F_0, is defined for the inner and outer leaf, separately. Rigid force of the inner leaf, $F_{o,iw}$ can computed as follow:

$$F_{O,iw} = \frac{2}{h_1}(W + \sigma_{v0} \cdot t_w) \cdot t_w + \frac{\sigma_{v0} \cdot t_w}{h - h_1}(t_w + 2e)$$

$$= \frac{2}{526}(1.78 + 10) \cdot 100 + \frac{10}{1030 - 526}(100 + 0) = 6.44$$

Rigid force of the outer leaf, $F_{0,ow}$ can computed as follow:

$$F_{0,ow} = \frac{2}{h_1}(W + \sigma_{v0} \cdot t_w) \cdot t_w + \frac{\sigma_{v0} \cdot t_w}{h - h_1}(t_w + 2e)$$

$$= \frac{2}{523}(1.84 + 0) \cdot 100 + \frac{0}{1030 - 523}(100 + 0) = 0.67$$

$$F_0 = F_{0,iw} + F_{0,ow} + F_c = 5.98 + 0.63 + 0.2 = 6.81$$

The total rigid force is equal to 6.7 kN. The instability displacement, u_{ins}, can be computed by employing Eq. (6-29). It is obtained only for the inner leaf.

$$u_{ins} = \frac{\frac{2}{h_1(W + \sigma_{v0} \cdot t_w)t_w} + \frac{\sigma_{v0} \cdot t_w(t_w + 2e)}{h - h_1}}{\frac{2}{h_1(W + \sigma_{v0} \cdot t_w)} + \frac{2\sigma_{v0} \cdot t_w}{h - h_1}} = \frac{\frac{2}{526(1.78 + 10)100} + \frac{10(100 + 0)}{1030 - 526}}{\frac{2}{526(1.78 + 10)} + \frac{20}{1030 - 526}}$$

$$= 76.5$$

List of publications

Journal publication

Arslan, O., Messali, F., Smyrou, E., Bal, I. E. & Rots, J., (2021). Mechanical modelling of the axial behaviour of traditional masonry wall metal tie connections in cavity walls. Construction & building materials.

Arslan, O., Messali, F., Smyrou, E., Bal, I. E. & Rots, J., (2020). Experimental characterization of the axial behavior of traditional masonry wall metal tie connections in cavity walls. Construction & building materials.

Conference publication

Arslan, O., Messali, F., Smyrou, E., Bal, I. E. & Rots, J., (2022). Experimental characterization of timber joist-masonry connections. 3rd European Conference on Earthquake Engineering & Seismology, Bucharest, Romania.

Smyrou, E., Arslan, O., Moshfeghi, A. & Bal, I. E. (2022). Shake table tests on Groningen-type masonry walls in out-of-plane direction. 3rd European Conference on Earthquake Engineering & Seismology, Bucharest, Romania.

Smyrou, E., Arslan, O., Moshfeghi, A. & Bal, I. E. (2022). Out-of-plane Shake Table Tests on Masonry Walls Representing Groningen Houses. 12th National Conference on Earthquake Engineering, Salt Lake City, Utah, USA.

Arslan, O., Messali, F., Smyrou, E., Bal, I. E. & Rots, J., (2020). Numerical modelling of cavity wall metal ties. *17th World Conference* on Earthquake Engineering, Sendai, Japan.

Arslan, O., Messali, F., Smyrou, E., Bal, I. E. & Rots, J., (2020). Mechanical modelling of cavity wall metal ties. 17th International Brick and Block Masonry Conference - From Historical to Sustainable Masonry, Krakow, Poland.

Propositions accompanying the dissertation:

Experimental characterisation and mechanical modelling of connection details in traditional Groningen houses

Onur Arslan

1. Sufficient connections between structural elements promote the so-called “box behaviour” and, therefore, can prevent the collapse of buildings. Embracing box-type behaviour is key to working effectively against global societal problems, including global warming, wars, earthquakes, and other natural disasters.
2. The habits of people must change to reduce the impact of climate change. Science must have a steering role in changing people's habits.
3. The current economic policy of the Turkish government is based on the assumption that lower interest rates will lead to lower inflation. However, this conflicts with scientific facts indicating that rising interest rates will bring inflation down once it is too high. It is crucial to consistently defend science in this regard.
4. Earthquakes do not kill people; inadequately designed and poorly constructed buildings do.
5. Conducting favouritism can be seen as one of the differences between the Eastern and Western worlds. However, both the Western and Eastern worlds exploit favouritism while denying its existence.
6. Although cavity ties are very tiny elements, their contribution to the safety of buildings can be major. (This proposition pertains to this dissertation.)
7. A simple improvement to a local connection may substantially improve the global behaviour of a structure. (This proposition pertains to this dissertation.)
8. Even if a timber joist is simply pocketed into the masonry wall, there may be additional contributions to the connection capacity that goes beyond frictional behaviour, such as the arching effect. (This proposition pertains to this dissertation.)
9. All weak links in a building need to be identified to prevent potential failure. (This proposition pertains to this dissertation.)
10. Answering questions does not prevent the rise of new questions; rather, providing good answers should encourage more questions.

These propositions are considered opposable and defendable and have been approved by the promotor, Prof. dr. ir. Jan G. Rots, the copromotor, Dr. Francesco Messali, and the external advisor, Dr. Ihsan E. Bal and.

About the author

Onur Arslan was born in Istanbul, Türkiye. He obtained his B.Sc in Civil Engineering from Anadolu University (now Eskisehir Technical University) in 2011. He received his M.Sc. in Civil Engineering with a specialization in Earthquake Engineering from Istanbul Technical University. His master thesis entitled “Seismic performance evaluation of an existing RC building considering the earthquake code regulations” was published in 2015. From September 2013 to September 2017, he worked as a production engineer at Yapi Merkezi on Eurasia Tunnel and the 3rd Bosporus Bridge projects.

In September 2017, he started a PhD project under the supervision of Prof. Jan Rots, Dr Ihsan Engin Bal and Dr Francesco Messali in the Applied Mechanics section of the Faculty of Civil Engineering and Geosciences at Delft University of Technology, the Netherlands, where he conducted research on the seismic response of the most common connection details used in the traditional Dutch construction practice, and specifically in the Groningen area. Since September 2017, he has worked as a researcher in the Research Group on Earthquake Resistant Structures at Hanze University of Applied Sciences, Groningen, the Netherlands. In addition, he is also a lecturer at SOFE at Hanze University of Applied Sciences since September 2022.

Acknowledgements

My six-year-long doctoral journey could not have been possible without some people who supported me in achieving my goal. I would like to express my gratitude to those people who, either directly or indirectly, have contributed to this long journey.

I would like to express my sincere gratitude to my promotor Prof. Jan Rots who provided me with the opportunity to be in his research group as a PhD candidate at TU Delft and supported me through these years. I would like to express my warmest appreciation to my copromotor Dr Francesco Messali for his patience, effortless help, and suggestions throughout the PhD. I am deeply grateful to thank my copromotor Dr Ihsan Engin Bal, who paved the way to my research at Hanze UAS, who also inspired, encouraged, and generously supported my development. I would especially like to acknowledge Dr Eleni Smyrou, who guided and helped me gain academic confidence and critical thinking.

I would like to graciously acknowledge Hanze University of Applied Sciences, particularly Kenniscentrum NoorderRuimte, for funding this research. Special gratitude goes to Liesbeth Jorritsma, Janny Slagter, and Jelle Pama. Also, thanks to all the other staff members of Kenniscentrum NoorderRuimte, particularly the people of the programma office, for allowing this research to become true, for making this research possible. I am also thankful to my colleague Bert van Veen from the laboratory of Hanze University, BuildinG, for his excellent cooperation in completing the tests. I would like to express my gratitude to Totalwall and Marten de Jong for their support in providing the materials used for the specimens with strengthened timber joist-masonry connections using helical bars during the experimental campaign on timber joist connections.

In my PhD, one experimental campaign was conducted at the Macrolab/Stevin laboratory of TU Delft. My sincere appreciation goes to Dr Geert Ravenshorst, Dr Rita Esposito and the colleagues from the laboratory. I would also like to thank my kind and supportive colleagues Chang Langzi, Georgios Stamoulis, Iris Nederdof-van Woggelum, Jaap Meijer, Lucia Licciardello, Manimaran Pari, Maria Belen Gaggero, Marianthi Sousamli, Michele Longo, Michele Mirra, Paul Korswagen Eguren, and Samira Jafari.

I am very thankful that I had the privilege to the course “Masonry Structures” from Prof. Guido Magenes and increase my scope. Also, thank you to Kerim Efe Ozcanli for collaborating throughout this course. Special thanks to the people from OpenSees Cafe, whom we met biweekly, particularly Dr Silvia Mazzoni and Prof. Michael Scott, who have helped me improve my skills and capabilities in different parts of my speciality. I would also like to express my gratitude to Trijnie and Henk Jan Oudenampsen, my lifelong teachers.

I would like to thank my previous colleagues from the company of Yapi Merkezi, Giray Arslan, Ismail Girgin, Mesut Yurdakul, Oncu Gonenc, and Orhan Manzak, even if they are far; they have always been here whenever I needed them. I am also grateful to all my friends, Alvand Moshfghi, Bensen Unluoglu, Berk Kavak, Egemen Kesler, Eray Saglam, Firat Yilmaz, Ibrahim Acar, Merve Coruh Kavak, Onur Kargioglu, and Sertac Sefer, and who were next to me during this journey.

Finally, I would like to thank my girlfriend, Dimitra Fratzeskou, for being part of my life and being there from the beginning to the end of every journey we undertake; the journey with her is a reward. Most of all, I am deeply grateful for my family, Gul Arslan, Feyzullah Arslan, Elif Arslan Gungor, Mithat Gungor, Eylul Kiraz and Elife Arslan, who selflessly have always been next to me in every step I have taken.

Onur Arslan

Groningen, November 2023